Department of Physics and Astronomy

Heidelberg University

Master thesis

in Physics

submitted by

Mathurin Arthur Choblet

born in Lich

2022

Reconstructing climate fields of the last millennium with data from terrestrial climate archives and isotope-enabled GCMs using Data Assimilation

This Master thesis has been carried out by Mathurin Arthur Choblet

at the

Institute of Environmental Physics

under the supervision of

Prof. Dr. André Butz and Prof. Dr. Kira Rehfeld

Abstract

Data Assimilation in the field of paleoclimatology (PaleoDA) is an original method that has been used in several climate reconstructions for the last millennium. By fusing information from both climate proxies and general circulation models (GCMs), PaleoDA provides statistical estimates of climate fields that are dynamically consistent. However, existing reconstructions mostly rely on calibrated tree ring data and assimilate proxy records on a single, annual time scale. Ice cores and speleothems, which record past variations in the oxygen isotope ratio of precipitation, often have a lower and irregular time resolution, but reliably record climate variations on decadal to centennial time scales. Here I implemented a computationally efficient DA algorithm that enables the assimilation of proxy records on multiple timescales. The algorithm has been applied to speleothem and ice core records from the SISALv2 and Iso2k database and five isotope-enabled GCMs. Reconstructions of global mean temperature changes during the last millennium compare well in both amplitude and uncertainty to recent studies. The potential of incorporating speleothems is shown with a reconstruction of hydroclimatic changes in tropical South America, where speleothems represent the most abundant type of hydroclimate archive. The experiments performed in this thesis also suggest an increased reconstructed decadal to centennial variability by using proxy records on multiple timescales. Making use of different climate models manifested the influence of model biases on the reconstructions. Future PaleoDA studies will profit from more proxy records and the multiple time scale approach to provide a globally complete picture of past climate changes in both mean state and variability.

Zusammenfassung

Datenassimilation in der Paläoklimatologie (PaleoDA) ist eine Methode, die in mehreren Klimarekonstruktionen des letzten Jahrtausends verwendet wurde. Durch das Verbinden von Informationen aus Klimaproxies und Klimamodellen berechnet PaleoDA statistische Schätzungen von Klimafeldern, welche dynamisch konsistent sind. Bestehende Rekonstruktionen stützen sich jedoch zumeist auf kalibrierte Baumringdaten und assimilieren Klimaproxies auf einer einzigen, jährlichen Zeitskala. Eisbohrkerne und Speläotheme, welche Veränderungen im Sauerstoffisotopenverhältnis des Niederschlags aufzeichnen, haben oft eine geringere und unregelmäßigere zeitliche Auflösung, Sie erfassen jedoch zuverlässig Klimaveränderungen auf dekadischen bis hundertjährigen Zeitskalen. Für diese Arbeit implementierte ich einen effizienten DA-Algorithmus, welcher die Assimilation von Proxydaten auf mehreren Zeitskalen ermöglicht. Für die Anwendung des Algorithmus wurden Speläothem- und Eisbohrkerndaten aus den SISALv2 und Iso2k-Datenbanken sowie fünf Klimamodelle, welche auch die Isotopenverhältnisse simulieren, verwendet. Die Rekonstruktionen der globalen mittleren Temperaturveränderungen während des letzten Jahrtausends sind in Amplitude und statistischer Unischerheit mit neueren Rekonstruktionen gut vergleichbar. Das Potenzial der Einbeziehung von Speläothemen verdeutliche ich anhand einer Rekonstruktion der hydroklimatischen Veränderungen im tropischen Südamerika, wo Speläotheme ein häufig vorliegendes Hydroklimaarchiv darstellen. Die durchgeführten Experimente deuten zudem darauf hin, dass die Rekonstruktion der dekadischen bis hundertjährigen Variabilität durch die Verwendung von Proxydaten auf mehreren Zeitskalen verbessert werden kann. Durch die Verwendung verschiedener Klimamodelle wurde der Einfluss von systematischen Fehlern in den Klimamodellen auf die Rekonstruktionen veranschaulicht. Künftige PaleoDA-Studien werden von mehr Proxydaten und der Assimilierung auf mehreren Zeitskalen profitieren um ein umfassenderes Bild der Klimaveränderungen in der Vergangenheit zu berechnen, sowohl für den mittleren Zustand des Klimas als auch für seine Variabilität.

Contents

List of Figures

List of Tables

List of Abbreviations and Symbols

AR Assessment report issued by the IPCC
BP Before present (1950CE)
CE Coefficient of Efficiency or Common Era, depending on the context
CFR Climate field reconstructions
Corr Pearson correlation
CPS Composite plus scaling. CFR method in Neukom et al. (2019a)
CWP Current warm period (1850CE-present)
DA Data assimilation
DAISIM Data Assimilation with Isotopes recorded by Speleothems and Ice cores on Multiple time scales. Name for reconstructions performed in this thesis.
ECHAM ECHAM5/MPI-OM climate model
EKF Extended Kalman Filter
EnKF Ensemble Kalman Filter
EnSRF Ensemble Square Root Kalman Filter
Erb-2022 Erb et al. (2022)
ETKF Ensemble Transform Kalman Filter
ESTKF Error-subspace Transform Kalman Filter
EVD Eigenvalue Decomposition
GCM General Circulation Model
GISS Goddard Institute for Space Studies atmospheric general circulation model
GHG Greenhouse gas
iCESM isotope-enabled version of the Community Earth System Model
iHadCM3 isotope-enabled version of the Hadley Centre Coupled Model
IPCC Intergovernmental Panel on Climate Change of the United Nations
Iso2k Database of water isotope values for the past two millennia (Konecky et al., 2020)
isoGSM Isotopes-incorporated Global Spectral Model
ITCZ Intertropical Convergence Zone
SACZ South Atlantic Convergence Zone
K Kelvin
KF Kalman Filter
LIA Little Ice Age
lh latent heat
LMR Last Millennium Reanalysis (Hakim et al., 2016)
MCA Medieval climate anomaly
MME Multi-model ensemble
NAN Not a number
PAI Pairwise comparison CFR method included in Neukom et al. (2019a)
PAGES2k Database for temperature proxies during the last two millennia (Ahmed et al., 2013; Emile-Geay et al., 2017)

PaleoDA Paleoclimate data assimilation
PI Pre-industrial period (before 1850CE)
PF Particle Filter
PHYDA Paleo Hydrodynamics Data Assimilation product (Steiger et al., 2018)
PPE Pseudoproxy experiments
prec Precipitation
PRYSM Proxy system modeling framework by Dee et al. (2015)
PSD Power spectral density
PSM Proxy system model (Evans et al., 2013)
RE Reduction of error
RMSE Root mean square error
SH-2016 Steiger and Hakim (2016)
SISALv2 Second version of the SISAL speleothem database (Comas-Bru et al., 2020)
SNR Signal-to-noise ratio
SVD Singular Value Decomposition
tsurf Surface temperature

Dimensions

N_e number of ensemble members
N_x number of state variables
N_y number of observations

Operators, sub and superscripts

$\overline{\mathbf{X}}$ Ensemble/Temporal mean
$\mathbb{E}$ Expected value
cov Covariance
var Variance
σ Standard deviation
$\mathbf{x}^f$ forecast (prior)
$\hat{\mathbf{x}}$ estimate
$\mathbf{X}'$ deviation from the mean
$\mathbf{X}^{-1}$ Inverse of a matrix $\mathbf{X}$
$\mathbf{X}^T$ Transpose of a matrix $\mathbf{X}$
$\mathbf{k}$ Time step index in sequential KF
$\mathbf{i}$ Observation enumeration index in serial KF
$\overline{\mathbf{X}}$ Ensemble or temporal mean depending on the context
$\mathcal{O}$ Computational complexity (Big O notation)

Matrices and vectors

$\mathbf{I}$ Identity matrix
$\mathbf{y}$ Observation vector
$\mathbf{H}$ **or** $\mathcal{H}$ Observation operator
$\mathbf{x}$ Prior state vector
$\mathbf{X}^f$ Prior ensemble matrix
$\mathbf{X}$ Posterior ensemble matrix

$\mathcal{H}\mathbf{X}^f$ Observation estimates from prior
$\overline{\mathcal{H}\mathbf{X}^f}$ Ensemble mean of observation estimates
$\mathbf{X}^{f\prime}$ Ensemble matrix of prior deviations from ensemble mean
$\mathbf{X}'$ Ensemble matrix of posterior deviations from ensemble mean
$\overline{\mathbf{X}}$ Mean of forecast ensemble
$\mathbf{d}$ Innovation ($\mathbf{y} - \overline{\mathcal{H}\mathbf{X}^f}$)
$\mathbf{M}$ Transition matrix of linear model
$\mathbf{K}$ Kalman gain
$\tilde{\mathbf{K}}$ Perturbation Kalman gain
$\mathbf{R}$ Covariance matrix of observation error
$\mathbf{v}$ Measurement error vector
$\mathbf{n}$ Model error vector
$\mathbf{Q}$ Covariance matrix of model error
$\mathbf{P}$ Error covariance matrix of posterior state estimate
$\mathbf{P}^f$ Error covariance matrix of prior state estimate
$\overline{\mathbf{w}}$ Weight vector for transforming $\overline{\mathbf{X}}$ in the EnSRF
$\mathbf{W}'$ Perturbation weight matrix for transforming $\mathbf{X}'$ in the EnSRF
$\mathbf{A}$ Averaging kernel or some matrix used in the derivations (with specific characteristics)

Chapter 1

Introduction

Paleoclimatology is the study of Earth's past climates before the onset of the period of instrumental climate measurements in the 19th century. It aims at understanding how the climate system has evolved in response to external and internal forcing factors (Bradley, 2015). The main forcings are the orbital configuration of Earth, the amount of solar irradiance, volcanic aerosol, greenhouse gas, and sulphate aerosol concentrations, land use changes as well as internal variability (e.g. El Niño-Southern Oscillation or the North Atlantic Oscillation). The induced changes in both mean state and variability occur over a wide range of timescales, ranging from millennia for orbital changes to days and hours for weather processes (Peixoto and Oort, 1992). Studying the inherent mechanisms which are governing Earth's climate is essential for framing the currently experienced anthropogenic warming and assessing possible impacts under different scenarios. Since its founding, the Intergovernmental Panel on Climate Change (IPCC) dedicates parts of its assessment reports to new insights from the field of paleoclimatology. One of the best known paleoclimate reconstructions that drew the attention of the broad public to paleoclimatology, was the temperature reconstruction by Mann et al. (1998). Its key finding about global mean temperature over the past six centuries, including the current warming, resulted in a simple curve, coined the *hockey stick* due to its horizontal handle and upward blade form. Heavily contested and criticized in an infamous debate at first, the exceptionality of the current warming has since been confirmed in numerous studies and has been shown to be unprecedented over the last 120,000 years (Gulev et al., 2021; Kaufman and McKay, 2022).

The importance of past climates goes far beyond the study of global mean temperature. Climate is characterized by spatially and temporally heterogeneous and multivariate phenomena. Paleoclimatology also studies changes in the hydroclimate, the biosphere, circulation patterns, and extreme climate and weather events, like droughts and floods. These changes, which are are of societal importance due to their direct and indirect impacts, are not only characterised by changes in the mean states of the climate, but also by the variability around the mean states. Understanding how the variability of climate has changed in the past and how it is affected by the anthropogenic warming is a fundamental topic of investigation, which also has very practical implications. For assessing the frequency of climate extremes for instance, it is assumed that changes in variability are more relevant than changes in the mean state (Katz and Brown, 1992).

To investigate the mean climate state and its variability, time series of specific variables of interest are studied. However, climate variables like temperature and precipitation have only been recorded systematically and globally for the last 150 years. Thus, information has to be inferred from so-called *climate proxies*. Proxy variations are preserved by natural climate archives, which indirectly record their climatic environment. Examples of climate archives are tree rings, varves (annual layers of lake and marine sediments), corals, foraminifera, ice cores, speleothems, boreholes, sediments, deposits, and to a small extent also ancient documents. Whereas archives

as tree rings can represent information on the annual scale, speleothems or sediments capture climate variables on decadal to millennial time scales. Climate archives are imperfect recorders of climate-related phenomena by their biological, chemical, or physical nature (Jones and Mann, 2004). It causes them to archive a filtered version of the climate signal, which is obfuscated by noise and non-climatic influences. Understanding the signal-to-noise content of proxy records is an essential task in paleoclimatology.

One important climate proxy type is the ratio of stable water isotopes. Water consists of different isotopes, mainly the lighter $H_2{}^{16}O$ and the heavier and less abundant $H_2{}^{18}O$. The concentration of the oxygen isotope ^{18}O is used as a climate proxy for past atmospherical conditions. The ratio of both oxygen isotopes in a sample, which is given relative to a normed standard, is named $\delta^{18}O$.

$$\delta^{18}O = \left(\frac{\frac{^{18}O}{^{16}O\,\text{sample}}}{\frac{^{18}O}{^{16}O\,\text{standard}}} - 1 \right) \cdot 1000‰ \tag{1.1}$$

$\delta^{18}O$ is considered a valuable climate proxy because it can be interpreted in terms of temperature, precipitation amount and moisture fluxes (Bradley, 2015). This is because throughout the global water cycle, water undergoes several phase transitions. Heavier water molecules are less likely to evaporate and more likely to condense compared to lighter molecules, such that at each of these transitions the $\delta^{18}O$ ratio is altered. As empirically formulated in the seminal paper by Dansgaard (1964), the fractionation processes relate the $\delta^{18}O$ of precipitation to air temperature, precipitation amount, altitude, latitude and distance from the coast. Speleothems and ice cores are both archives of $\delta^{18}O$. Speleothems are geological cave formations created by accumulating layers of calcite transported by drip water. Ice cores are created from snow which becomes ice through compaction. Both archives can thus record the $\delta^{18}O$ of precipitation up to thousands of years, although especially speleothems are rarely dated annually.

Individual proxy records can be strong indicators of past climate changes. Although they can indicate that something has happened, especially at the regional level, alone they are not able to exhaustively inform why changes have happened and how these changes are related to the global climate system. To overcome this fundamental limitation, spatially complete *climate field reconstructions* (CFR) are performed for variables such as temperature, precipitation, sea level pressure, and drought conditions (Jones and Mann, 2004). CFRs provide statistical estimates, and thus always comprise uncertainties associated to the reconstructed fields.
To inform such reconstructions, proxy records are compiled into *proxy networks* of global coverage over a specified time period. For the last two millennia, the PAGES2k database (Emile-Geay et al., 2017) provides a large collection of climate proxy record with a significant correlation to local temperature. As there are numerous ways to interpret and extrapolate information from such networks, a variety of CFR techniques have been developed and applied. For instance, Neukom et al. (2019a) and Neukom et al. (2019b) use a range of established CFR techniques with the PAGES2k database to reconstruct climate variability and refute the existence of globally coherent warm and cold periods over the last two millennia.

Another important tool to study past climates are climate models. Climate models are simplified and discretized representations of Earth's climate and its components. They solve the basic equations of fluid dynamics and thermodynamics on varying levels of complexity for the atmosphere, ocean and biosphere. Climate models are used to test hypotheses about the climate system under different boundary conditions (forcings). Since models provide climate fields for a multitude of climate variables, they can inform why changes happen and how the changes are connected to the global climate system. In this thesis, the output from Atmosphere-Ocean

general circulation models (GCM) with a water cycle that includes the simulation of water isotopes is used. Such *isotope-enabled models* represent an important advancement in the field of climate modeling, because they take into account the fractionation effects which occur at phase changes as evaporation from land and ocean surfaces and condensation during cloud formation and precipitation (Werner, 2010). Isotope-enabled models have the potential of enhancing model-data comparison. The simulated values for δ^{18}O of precipitation can be compared to the δ^{18}O from climate archives like ice cores and speleothems without the need of calibrating δ^{18}O to temperature or precipitation. Climate models run independently of climate archive observations. They are only constrained by boundary conditions as e.g. greenhouse gas concentrations, orography and solar irradiance. In contrast, CFRs usually rely entirely on proxy record data without using climate models.

In this thesis, a novel approach, which fuses information from both proxy records and climate models, is investigated. The concept is called *Data Assimilation* (DA). DA uses observations to refine statistical state estimates provided by models. It is an extremely versatile concept, which is applied in a wide range of fields, from navigation and positioning systems in engineering, oceanography, numerical weather prediction to paleoclimatology. DA in the field of paleoclimatology, which is termed PaleoDA in this thesis, has been applied in particular to reconstruct the climate of the last millennium (Franke et al., 2017; Franke et al., 2020; Hakim et al., 2016; Shoji et al., 2022; Steiger et al., 2018; Tardif et al., 2019) but also for time periods farther back in time as the last glacial maximum (Annan et al., 2022; Tierney et al., 2020) or the paleocene–eocene thermal maximum (Tierney et al., 2022). Climate reconstructions using PaleoDA have been used to investigate mechanisms of the climate, for instance, Steiger et al. (2021) demonstrated how medieval megadroughts in the North American Southwest were connected to oceanic conditions in the Pacific and the Atlantic.

Two popular PaleoDA reconstructions for the last millennium, LMR (Hakim et al., 2016; Tardif et al., 2019) and PHYDA (Steiger et al., 2018), which have been used in many subsequent data-analysis studies, rely on non-isotope-enabled models. They use the PAGES2k proxy network and additional tree-ring data from Breitenmoser et al. (2014) as observational data. This data consists of proxy records that are dated annually, thus only a fraction of potentially available ice cores and speleothems. While containing a comparably large set of data, the proxy networks used by LMR and PHYDA need to be calibrated to climate variables such as temperature and precipitation because these are the climate variables simulated by conventional, non-isotope-enabled GCMs. This type of calibration is performed on data from the instrumental period and is a standard procedure for tree-ring-widths, which is the largest climate proxy type in the PAGES2k database, but is less suited for other climate proxies. Indeed, for δ^{18}O of precipitation in the low-latitudes the correlation to precipitation is stronger than for temperature (LeGrande and Schmidt, 2006). Speleothems and ice cores from such regions, in particular South America, could contribute to improving reconstructions of regional hydroclimate. In addition, proxy networks are often biased towards the mid-latitudes of the northern hemisphere because historically most climate proxy data has been collected in Europe and North America. Another issue is the suppressed multi-decadal to centennial climate variability in the PHYDA and LMR reconstructions (Neukom et al., 2019a). This effect can be caused by a variety of factors. First, trees are known to capture climate variability on the seasonal and annual scale, but underestimate long-term climate variability on decadal to centennial time scales (Bradley, 2015). Furthermore, climate models also underestimate regional climate variability on multi-decadal and longer time scales in comparison to long-term climate proxy records (Bühler et al., 2022; Laepple and Huybers, 2014). On top of that, PaleoDA in itself is a reconstruction method, that suppresses long-term climate variability in comparison to other CFR methods when using the PAGES2k database as observational data (see Figure 1 in Neukom et al. (2019a)). A way

to improve the representation of climate variability could lie in explicitly assimilating archives that reliably capture long-term climate variability, like speleothems and ice cores. To that end, isotope-enabled models are needed. Although they have been employed for instance in Okazaki and Yoshimura (2017), Shoji et al. (2022), and Steiger et al. (2017), these studies focused on the instrumental era and did not incorporate speleothems, a prominent archive of δ^{18}O.

The overarching goal of this thesis is to reconstruct climate fields for the last millennium from isotope-enabled GCMs and speleothem and ice core δ^{18}O proxy records using DA. The last millennium is commonly defined as the time period between 850-1850CE. The orbit of Earth and ice masses being relatively unchanged during that period, the last millennium is considered to be a stable climatic period. It is marked by a millennial cooling trend of –0.18 °C/kyrs. Warm and cold multi-decadal periods were not globally synchronized and occurred at different times (Gulev et al., 2021). Climate variability during the last millennium was mainly caused by irradiation changes, volcanic eruptions and internal climate variability (Jones and Mann, 2004). As the density of available proxy records is higher than during every other pre-instrumental period, it makes for an ideal testbed to study Earth's natural climate variability.
The proxy record data used in this thesis is provided by the speleothem database SISALv2 (Comas-Bru et al., 2020) and the δ^{18}O database Iso2k (Konecky et al., 2020), which contains hundreds of ice core records. The chosen DA method is the *stationary offline Ensemble Kalman Filter*. To that end, a code framework that allows for the assimilation of δ^{18}O, taking into account archive characteristics, in particular the low temporal resolution of paleoclimate records, is developed. The limitations, methodological choices and uncertainties underlying PaleoDA are elaborated.

The scientific questions that are addressed in this thesis are as follows:

1. What are the characteristics of reconstructed temperature and hydroclimate time series for the last millennium, globally as well as regionally? How do these reconstructions compare to existing reconstructions? An interesting test case is the South American Summer Monsoon region, where existing PaleoDA reconstructions use few local proxy records.

2. How do the speleothem and ice core records contribute to the climate reconstructions?

3. What is the temporal variability of the CFRs?

4. Five different isotope-enabled models are going to be used in this project. How do inter-model differences and model-biases affect the PaleoDA reconstructions?

To answer these questions, this thesis adopts the following structure.

Chapter 2 covers the mathematical basics of the DA method that is used in this thesis, namely the Ensemble Kalman Filter. It is comprehensively derived, including how the different algorithms proceed to calculate the equations efficiently. Furthermore, this chapter bridges the gap of the general Ensemble Kalman Filter to its application in PaleoDA.
Chapter 3 describes the climate models and the speleothem and ice core proxy record data used for the Data Assimilation.
Chapter 4 documents the specific implementation of the PaleoDA method for this thesis, possible methodological choices and how the existing PaleoDA algorithm is adapted to reconstruct climate fields on multiple timescales.
Chapter 5 pre-assesses and validates the developed framework with prior data-analysis and by performing experiments based on simulated observational data (pseudoproxies).
Chapter 6 is dedicated to the application of the framework to real proxy data for reconstructing climate fields for the last millennium. Besides reconstructed global mean values, regional

fields over South America are analysed and compared to existing last millennium reconstructions.
Chapter 7 discusses the results obtained in this thesis and **chapter 8** provides a conclusion.

The appendix of this thesis comprises a detailed algorithm sketch and the full mathematical calculations and proofs required for the (Ensemble) Kalman Filter. Moreover, additional figures for the experiments are provided.

Chapter 2

Mathematical background

The Ensemble Kalman Filter is the Data Assimilation (DA) method used in this thesis. Here, I give a step-by-step introduction to it. This method builds on a Bayesian foundation (Section 2.1) and the original linear Kalman Filter (Section 2.2). I further elaborate on this linear approach by introducing the concept of serial observation treatment (Section 2.3), and finally enter the domain of non-linear problems with the Ensemble Kalman Filter. In the last section of this chapter I describe how the Ensemble Kalman Filter can be applied for performing CFRs. An overview of basic linear algebra/matrix calculation definitions used in the derivations can be found in Appendix C.

2.1 Bayes' Theorem and the basic iterative scheme

DA comprises different methods which are applied in a wide range of scientific fields. As stressed in the comprehensive DA review paper by Vetra-Carvalho et al. (2018), common ground for all DA methods is laid by Bayes' Theorem, a fundamental theorem of mathematics that was first published in 1763. Hence, I start by introducing the basic concept of DA via this theorem.
Bayes' Theorem states that given a prior state estimate X (e.g. provided by a climate model simulation) and a measurement Y (e.g. a climate proxy record), which are defined by their respective probability functions $P(X)$ and $P(Y)$, the conditional probability of the state estimate given the measurement is

$$P(X|Y) = \frac{P(Y|X) \cdot P(X)}{P(Y)} \tag{2.1}$$

where

$P(X)$ is the probability of X, called the *prior*,

$P(X|Y)$ is the conditional probability of X, given Y, called the *posterior*,

$P(Y|X)$ is the conditional probability of Y, given X, called the *likelihood*,

$P(Y)$ is the probability of Y, called the *marginal likelihood*.

In most cases, the probability distributions describing X and Y are assumed to be normal. Normal distributions are uniquely defined by their mean and variance. The variance or standard deviation is interpreted as the uncertainty of an estimate.

The case for combining models and measurements
In DA, Bayes' Theorem is used to fuse information from models and measurements to obtain a new estimate of a state. Doing so can enable reaching a better state estimate than would be obtained by relying exclusively on models and measurements. First of all, a description of a state,

or philosophically speaking, reality, that is not based on any measurements is obviously void of meaning. Measurements document *what* is happening, but they do not contain information on *why* things happen. To make sense of measurements, models are needed. Models are the cornerstone of our understanding of reality because they are mathematical descriptions of fundamental physical processes. They give a picture of reality, which is physically sound in terms of the underlying physical descriptions. By deliberately simplifying reality, models capture the scales that are relevant for the scientific hypotheses they are supposed to test. In the context of modeling Earth's climate, models can provide estimates for variables, for which no measurements are available or possible (e.g. the global mean temperature 1000 years ago), as well as forecasts of future states, which cannot be measured at the present moment. While models build on describing measurements, once developed they run independently of measurements.
Fusing information from models and measurements with DA combines the best of both worlds. DA provides state estimates that are based on model estimates, but which are continuously refined by measurements of reality.

The iterative scheme of DA
The essence of DA lies in applying Bayes' Theorem iteratively such that a prior state estimate can be updated when new information becomes available. Thus, DA introduces the dimension of time into Bayes' Theorem. It informs how to update a prior model estimate X^f, which I denote by the superscript f to mark its forecast nature[1]. The resulting posterior estimate, also called the analysis estimate, is simply denoted as X in the following.
A key assumption of DA is that a state estimate will only depend on the previous estimate, which is called the Markovian assumption in probability theory and statistics[2]. In consequence, Bayes' Theorem can be cycled through time and new information from observations can be fed into the state estimate as this information becomes available.
Not only do new observations affect the state estimates, but also the transition in time by itself. DA also requires the description of this time transition by a dynamical model M. In the case of a linear process, M is a transition matrix that describes how the state estimate changes during the time between the observations.
Repeating the incorporation of new information into the state estimates and the cycling of the model estimates through time are the essence of DA. This iterative DA scheme thus reduces to two basic steps.

1. An *analysis step*, in which a prior forecast estimate (including its uncertainty) is optimally updated given the available observations and their uncertainties.

2. A *forecast* step, in which the state estimate is projected onto the next time step via a dynamical model, where again the analysis equations from the first step are applied.

Throughout this thesis, I adopt the notion of discretized time steps. The notion of optimality in the analysis step depends on the transition model and the assumed probability distributions. Various DA methods have been developed to solve different kind of problems.

2.2 The Kalman Filter

The Kalman Filter (KF) has first been introduced by Rudolf Kalman in 1960 (Kalman, 1960). Although initially a purely mathematical description of an optimal solution for linear filtering, its practical value has been recognised quickly. For instance, it has been implemented in the

[1] Data Assimilation has been developed to a large extent in the field of Numerical Weather Forecasting, hence the name.

[2] This assumption also makes sense in the context of modeling weather and climate. The models simulate the next time step starting from the initial and boundary conditions of the present state

positioning system of the Apollo Guidance Computer, which made the moon landing possible. I start by introducing definitions and assumptions and mainly follow the steps presented in the classic textbook by Brown and Hwang (2012) (Chapters 5 and 6).

Notational conventions

In this first part, two dimensions are relevant:

- N_x is the number of variables describing a state (e.g.in the case of climate models, the number of cells of a discretized climate field).
- N_y is the number of measurements available for one time step (e.g. the number of available proxy records at a specific time)

Matrices are named by bold capitalized letters, whereas vectors are named by small bold letters in order to mark the difference to scalar quantities. The shape of variables is denoted in brackets when they are first introduced.

Process formulation and assumptions

The state estimate that is to be updated by DA is named $\mathbf{x}$. The current time step is denoted by a subscript k. How this state estimate changes through time is described by a dynamical process equation, which also incorporate uncertainties (noise). A noisy linear process can be described by the following type of transition equation

$$\mathbf{x}_{k+1} = \mathbf{M}_k \mathbf{x}_k + \mathbf{n}_k \tag{2.2}$$

for a discrete transition in time from step k to $k+1$, where

$\mathbf{x}_k$ is the state vector at time k $(N_x \times 1)$

$\mathbf{M}_k$ is the transition matrix $(N_x \times N_x)$

$\mathbf{n}_k$ is the normal noise $(N_x \times 1)$ of this model with zero mean and known covariance structure $\mathbf{Q}_k$ $(N_x \times N_x)$

In anticipation of the later application of the Kalman Filter for Paleoclimate DA, the focus in the presentation here lies solely on optimally updating the prior estimates. Hence, I do not elaborate further on the forward model $\mathbf{M}$, which has been introduced for the sake of completeness. A key assumption is that observations stem from the same distribution as the forecast estimate. Observing the process at step k can be described by applying the so called observation operator $\mathbf{H}$ to the state vector and adding a measurement error. Thus

$$\mathbf{y}_k = \mathbf{H}_k \mathbf{x}_k + \mathbf{v}_k \tag{2.3}$$

where

$\mathbf{y}_k$ is the measurement vector $(N_y \times 1)$, containing the measurements of the observed state.

$\mathbf{H}_k$ is the observation operator mapping the state vector into the measurement space $(N_y \times N_x)$,

$\mathbf{v}_k$ is the measurement error $(N_y \times 1)$ which is assumed to be normal with zero mean and known covariance structure $\mathbf{R}_k$ $(N_y \times N_y)$.

For the model and observation noise vectors $\mathbf{n}_k$ and $\mathbf{v}_k$, two additional assumptions are made. First, it is assumed that both are uncorrelated, which means that their shared expectation value vanishes

$$\mathbb{E}[\mathbf{n}_k \mathbf{v}_k] = 0, \tag{2.4}$$

and secondly, I assume that the errors are not correlated in time

$$\mathbb{E}[\mathbf{n}_k \mathbf{n}_j] = \begin{cases} \mathbf{Q}_k & k = j \\ 0 & k \neq j \end{cases} \tag{2.5}$$

$$\mathbb{E}[\mathbf{v}_k \mathbf{v}_j] = \begin{cases} \mathbf{R}_k & k = j \\ 0 & k \neq j \end{cases} \tag{2.6}$$

The true state $\mathbf{x}$ is not known, but inferred from a forecast estimate which we denote as $\hat{\mathbf{x}}^f$. To mark the difference to the true state estimates are denoted by a hat symbol. The superscript f denotes that this is the estimate before the incorporation of measurements. The prior estimate $\hat{\mathbf{x}}^f$ and the true state $\mathbf{x}$ are related through the prior estimation error $\mathbf{e}^f$

$$\mathbf{e}_k^f = \mathbf{x}_k - \hat{\mathbf{x}}_k^f. \tag{2.7}$$

The prior estimate is assumed to be an unbiased estimator, which means that the expectation value of the prior estimation error is zero

$$\mathbb{E}[\mathbf{e}_k^f] = \mathbb{E}[\mathbf{x}_k - \hat{\mathbf{x}}_k^f] = 0. \tag{2.8}$$

The prior estimation error $\mathbf{x} - \hat{\mathbf{x}}^f$ is characterized by its covariance matrix. The mean error is assumed to be zero, thus the covariance matrix is equal to the mean squared error[3]. I refer to the prior error covariance matrix as $\mathbf{P}_k^f$ $(N_x \times N_x)$.

$$\mathbf{P}_k^f = \mathbb{E}[\mathbf{e}_k^f (\mathbf{e}_k^f)^T] = \mathbb{E}[(\mathbf{x}_k - \hat{\mathbf{x}}_k^f)(\mathbf{x}_k - \hat{\mathbf{x}}_k^f)^T] \tag{2.9}$$

The Kalman Filter provides a new posterior estimate $\hat{\mathbf{x}}_k$. This new estimate is defined as a linear combination of the prior estimate $\hat{\mathbf{x}}_k^f$, the measurement $\mathbf{y}$ and the measurement according to the prior estimate, $\mathbf{H}\hat{\mathbf{x}}_k^f$

$$\hat{\mathbf{x}}_k = \hat{\mathbf{x}}_k^f + \mathbf{K}(\mathbf{y}_k - \mathbf{H}\hat{\mathbf{x}}_k^f). \tag{2.10}$$

where $\mathbf{K}$ $(N_x \times N_y)$ is the so called Kalman gain matrix. It's precise form will be derived in the following.
The posterior estimate $\hat{\mathbf{x}}_k$ has an error with respect to the true state $\mathbf{x}_k$. This error $\mathbf{e}_k$ is also assumed to have zero mean, thus to be unbiased.

$$\mathbf{e}_k = \mathbf{x}_k - \hat{\mathbf{x}}_k \tag{2.11}$$

$$\mathbb{E}[\mathbf{e}] = \mathbb{E}[\mathbf{x}_k - \hat{\mathbf{x}}_k] = 0 \tag{2.12}$$

This new estimate has a posterior error covariance with respect to the true state which we denote by $\mathbf{P}_k$ $(N_x \times N_x)$

$$\mathbf{P}_k = \mathbb{E}[\mathbf{e}_k \mathbf{e}_k^T] \tag{2.13}$$

$$= \mathbb{E}[(\mathbf{x}_k - \hat{\mathbf{x}}_k)(\mathbf{x}_k - \hat{\mathbf{x}}_k)^T]. \tag{2.14}$$

Finally, the Kalman Filter can be stated. To simplify the notation, the time step index k is dropped from the analysis equations.

[3]The Kalman Filter is in fact very closely related to the least squares method introduced by Carl Friedrich Gauß in 1795. See Sorenson (1970) for a discussion of this relationship.

The original Kalman Filter

Theorem 1. Given the aforementioned assumptions and definitions, the Kalman Filter provides the best linear unbiased estimate in form of the equation

$$\hat{\mathbf{x}} = \hat{\mathbf{x}}^f + \mathbf{K}(\mathbf{y} - \mathbf{H}\hat{\mathbf{x}}^f), \tag{2.15}$$

where the Kalman gain matrix,

$$\mathbf{K} = \mathbf{P}^f\mathbf{H}^T(\mathbf{H}\mathbf{P}^f\mathbf{H}^T + \mathbf{R})^{-1} \tag{2.16}$$

minimizes the posterior error covariance $\mathbf{P}$, which is given by

$$\mathbf{P} = (\mathbf{I} - \mathbf{K}\mathbf{H})\mathbf{P}^f(\mathbf{I} - \mathbf{K}\mathbf{H})^T + \mathbf{K}\mathbf{R}\mathbf{K}^T. \tag{2.17}$$

The difference between measurement and prior estimate of the measurement, $(\mathbf{y} - \mathbf{H}\hat{\mathbf{x}}^f)$ is also called the innovation, denoted by $\mathbf{d}$.

Proof See Appendix D.1.

Corollary The posterior covariance can also be written as

$$\mathbf{P} = (\mathbf{I} - \mathbf{K}\mathbf{H})\mathbf{P}^f \tag{2.18}$$

Proof See Appendix D.2.

Simple example of the Kalman Filter
For gaining a first intuition of the Kalman Filter it is useful to explicitely describe the scalar case, where the state vector contains only one variable and is updated by one measurement. The prior and posterior error estimate P^f and P are thus scalars, as is the observation uncertainty R. The state vector is projected into the measurement space via a linear function H. Here I simply assume it is the identity, 1. Then, the Kalman gain from equation 2.16 reduces to a fraction.

$$K = \frac{P^f}{P^f + R}. \tag{2.19}$$

Consider the two following extreme cases. First, $R \ll P^f$, which means that the observation uncertainty is small compared to the prior error. The Kalman Gain then becomes one, meaning that the prior estimate is replaced by the measurement y

$$\hat{x} = \hat{x}^f + K(y - \hat{x}^f) \approx \hat{x}^f + (y - \hat{x}^f) = y. \tag{2.20}$$

This intuitively makes sense. On the other hand, if $R \gg P^f$ the Kalman Gain is close to zero, meaning that the measurement will have no influence on the posterior estimate when the observation uncertainty is larger

$$\hat{x} \approx \hat{x}^f + 0 \cdot (y - \hat{x}^f) = \hat{x}^f. \tag{2.21}$$

This example can be extended to more dimensions, in which not all state estimate variables are covered by an observation ($N_x > N_y$). The Kalman Filter uses the relationship between different variables as captured by the error covariance to inform how one variable is changed by the measurement of another one.

Alternative formulation of the Kalman equations

The equations for the Kalman gain and posterior covariance can be rewritten in numerous ways. A popular formulation uses the inverse of the posterior error covariance matrix, $\mathbf{P}^{-1}$. This inverse, which is also called the precision, exists if the prior error covariance and the observation error covariance have an inverse. This is the case for positive definite matrices, a property that will be used extensively in Section 2.4.

$$\mathbf{P}^{-1} = (\mathbf{P}^f)^{-1} + \mathbf{H}^T\mathbf{R}^{-1}\mathbf{H} \tag{2.22}$$

$$\mathbf{K} = \mathbf{P}^f\mathbf{H}^T\mathbf{R}^{-1} \tag{2.23}$$

Proof See Appendix D.3.

Hence, $\mathbf{K}$ can also be computed from the posterior covariance $\mathbf{P}$, while the previous formulation proceeds in the other direction. For examples of practical applications where this is preferable see Brown and Hwang (2012). The formulation in equation 2.23 will be useful for deriving the serial Kalman Filter in Section 2.3 and Ensemble square root Kalman Filters in Section 2.4.2.

2.3 The serial Kalman Filter

A popular and intuitive implementation of the Kalman Filter involves the serial treatment of observations. Instead of assimilating all observations at one time step, the observations are treated serially one after another. As can be shown, this is possible when the observation errors are assumed to be uncorrelated. The method can be faster than computing the observations at once because it avoids the matrix inversion for computing the Kalman gain. In the sense of the iterative DA scheme presented in Section 2.1, the serial assimilation of observations can be seen as cycling through time steps of length zero, such that the dynamical model M does not be to be applied.
The concept of assimilating observations serially will be used in a modified form for the multi-timescale DA algorithm (Section 4.5). I consider it important to be aware of the formal equivalence of the serial formulation and the original formulation presented in Section 2.2 and thus also introduce the concept formally.

The serial Kalman Filter

Theorem 2. Assume the observations are treated as a vector consisting of a set of observations $\{1, \dots n\}$. Instead of assimilating the observation vector at once, each entry is assimilated one after another. The observation and its error at each assimilation step reduce to scalars. Each observation and term of the Kalman gain equations is denoted by an index i to indicate from which observation the terms stem.
The prior state estimate and error covariance have the index 0. They represent the state estimate before assimilating the first observation.

$$\mathbf{P}_0 = \mathbf{P}^f \tag{2.24}$$

$$\hat{\mathbf{x}}_0 = \hat{\mathbf{x}}^f \tag{2.25}$$

The updated state estimate gained by assimilating observation i is calculated recursively from the previously assimilated observations.

$$\hat{\mathbf{x}}_i = \hat{\mathbf{x}}^f_{i-1} + \mathbf{K_i}(y_i - \mathbf{H_i}\hat{\mathbf{x}}^f_{i-1}) \tag{2.26}$$

The Kalman gain matrix $\mathbf{K}_i$ is given by

$$\mathbf{K}_i = \mathbf{P}^f{}_{i-1}\mathbf{H}_i^T(\mathbf{H}_i\mathbf{P}^f{}_{i-1}\mathbf{H}_i{}^T + R_i)^{-1}. \tag{2.27}$$

The error covariance matrix at step i is defined as for the original Kalman Filter

$$\mathbf{P}_i = (\mathbf{I} - \mathbf{K}_i\mathbf{H})_i{\mathbf{P}^f}_{i-1}(\mathbf{I} - \mathbf{K}_i\mathbf{H}_i)^T + \mathbf{K}_i R_i {\mathbf{K}_i}^T. \tag{2.28}$$

After assimilating n observations, the final state estimate and posterior error covariance matrix are equal to the estimates from the non serial Kalman Filter.

$$\mathbf{x}_n = \hat{\mathbf{x}} \tag{2.29}$$

$$\mathbf{P}_n = \mathbf{P} \tag{2.30}$$

The equality holds when the observation errors are uncorrelated ($\mathbf{R}$ is a diagonal matrix) and is independent of the order in which observations are assimilated.

Proof The derivation of the serial Kalman Filter equations (with the index i for each individual assimilation step) above is equivalent to the normal Kalman Filter and is hence not performed. What needs to be proven is the equality of the posterior error covariances and the state estimates after assimilating all observations, which is not obvious. It requires rewriting the recursive formulas in a suited way (Appendix E).

2.4 Ensemble Kalman Filters

The original Kalman Filter faces several challenges which make it unfit for modelling weather, ocean and climate. It is restricted to linear observation operators $\mathbf{H}$ and transitions matrices $\mathbf{M}$ and most importantly requires an estimate of the prior covariance $\mathbf{P}^f$. For the case of non linear models and observation operators, the *Extended Kalman Filter (EKF)*, which uses linearised versions of model transition and measurement operators, was developed directly after the original Kalman Filter. This linearised technique has been applied extensively for oceanographic modelling, where it tends to produce instabilities and unphysical results (Evensen et al., 2022). A new, more flexible technique for non linear systems had to be found[4].
In the wake of more performant computer systems in the 1990s, Evensen (1994) proposed blending the Kalman Filter with a Monte Carlo method in form of the so called *Ensemble Kalman Filter (EnKF)*. The EnKF rapidly became the new standard in Data Assimilation, especially for numerical weather prediction and is the technique used in this thesis.
The main idea consists of approximating the error covariance estimates with an ensemble of estimates instead of one single prior state estimate, hence the state estimate vector $\hat{\mathbf{x}}$ becomes the ensemble matrix $\hat{\mathbf{X}}$. Each state variable is thus described by an ensemble of state estimates. The ensemble dimension N_e is introduced.
Consequently, the prior error covariance becomes

$$\mathbf{P}^f = \mathbb{E}[(\mathbf{x} - \hat{\mathbf{x}}^f)(\mathbf{x} - \hat{\mathbf{x}}^f)^T] \approx \mathbb{E}[(\mathbf{X}^f - \overline{\mathbf{X}}^f)(\mathbf{X}^f - \overline{\mathbf{X}}^f)^T]. \tag{2.31}$$

This practical approximation is the essence of the EnKF.
Using an ensemble of N_e state estimates, the covariances can be formulated either in sum or matrix notation. $\mathbf{X}'$ $(N_x \times N_e)$ denotes the anomaly from the ensemble mean $\overline{X}$ $(N_x \times 1)$. The state estimate ensemble mean $\overline{X}$ of dimension $N_x \times 1$ is often written with repeated columns as an $N_x \times N_e$ matrix $\overline{\mathbf{X}}$ such that it can be used in the matrix calculations.
The prior forecast error covariance is thus calculated from $\mathbf{X}^f$.

$$\mathbf{P}^f = \frac{1}{N_e - 1}\sum_{i=1}^{N_e}(\mathbf{X}_i^f - \overline{\mathbf{X}}^f)(\mathbf{X}_i^f - \overline{\mathbf{X}}^f)^T = \frac{\mathbf{X'}^f{\mathbf{X'}^f}^T}{N_e - 1} \tag{2.32}$$

[4]For the global positioning system (GPS), where the EKF performs well, it is still the standard.

Likewise, the terms $\mathbf{P}^f\mathbf{H}$ and $\mathbf{H}\mathbf{P}^f\mathbf{H}^T$ can be estimated through the ensemble matrix. The observation operator $\mathbf{H}$ is written as a function $\mathcal{H}$ in order to underline that also non linear functions for projecting the state estimation into observation space can be used.

$$\mathbf{P}^f\mathcal{H}^T \approx \frac{1}{N_e-1}\sum_{i=1}^{N_e}(\mathbf{X}_i - \overline{\mathbf{X}}^f)(\mathcal{H}\mathbf{X}_i - \overline{\mathcal{H}\mathbf{X}}^f)^T = \frac{\mathbf{X}'^f(\mathcal{H}\mathbf{X}'^f)^T}{N_e-1} \tag{2.33}$$

$$\mathcal{H}\mathbf{P}^f\mathcal{H}^T \approx \frac{1}{N_e-1}\sum_{i=1}^{N_e}(\mathcal{H}\mathbf{X}_i^f - \overline{\mathcal{H}\mathbf{X}}^f)(\mathcal{H}\mathbf{X}_i^f - \overline{\mathcal{H}\mathbf{X}^f})^T = \frac{\mathcal{H}\mathbf{X}'^f(\mathcal{H}\mathbf{X}'^f)^T}{N_e-1} \tag{2.34}$$

The EnKF is still based on the assumption of normal estimation and observation errors. However, it has proven to be a robust approximation also in case of non linear operators and non normal distributions (Evensen et al., 2022). In the following, the approximation sign is replaced by an equal sign to keep the notation simple.

2.4.1 The stochastic Ensemble Kalman Filter

The Ensemble Kalman Filter as proposed originally by Evensen (1994) had one shortcoming, which was realized subsequently to its publication (Burgers et al., 1998; Houtekamer and Mitchell, 1998). The original approach provides a too-small posterior ensemble covariance, also called filter inbreeding or under dispersiveness. A mathematically rigorous treatment of the problem was proposed by Leeuwen (1999). Burgers et al. (1998) propose to overcome the defect by adding random noise, according to the measurement uncertainty, to the observations $\mathbf{Y}$. This method has been called *perturbing* the observations and the resulting Kalman Filter the stochastic Ensemble Kalman Filter. The authors show that perturbing the observations leads to the correct posterior error covariance in the limit of infinite ensemble size. As the observations already contain measurement errors, Vetra-Carvalho et al. (2018) proposes the more intuitive notion that the observations from the prior estimate, $\mathcal{H}(\mathbf{X}^f)$, $\mathcal{H}\mathbf{X}^f$ are perturbed by observation noise $\mathbf{Y}'$ for each ensemble member. The ensemble of observation estimates then becomes

$$\mathbf{Y}^f = (\mathcal{H}(\mathbf{X}_1^f), \ldots, \mathcal{H}(\mathbf{X}_{N_e}^f)) + \mathbf{Y}'. \tag{2.35}$$

The last term denotes the perturbation matrix whose entries ϵ_i are noise vectors drawn from a normal distribution with mean zero and covariance $\mathbf{R}$.

$$\mathbf{Y}' = (\epsilon_\mathbf{1}, \ldots, \epsilon_{N_e})\,\epsilon\,\mathbf{R}^{N_y \times N_e} \tag{2.36}$$

For formulating the stochastic Ensemble Kalman Filter, the observation vector $\mathbf{y}$ $(N_y \times 1)$ is converted into an observation matrix $\mathbf{Y}$ with N_e identical columns. Then, the Kalman update equation becomes:

$$\mathbf{X} = \mathbf{X}^f + \mathbf{K}(\mathbf{Y} - \mathbf{Y}^f). \tag{2.37}$$

The Ensemble Kalman gain is

$$\mathbf{K} = \mathbf{P}^f\mathcal{H}^T(\mathcal{H}\mathbf{P}^f\mathcal{H}^T + \mathbf{R})^{-1} \tag{2.38}$$

$$= \frac{\mathbf{X}'^f(\mathcal{H}\mathbf{X}'^f)^T}{N_e-1}\left[\frac{\mathcal{H}\mathbf{X}'^f(\mathcal{H}\mathbf{X}'^f)^T}{N_e-1} + \mathbf{R}\right]^{-1} \tag{2.39}$$

2.4.2 Ensemble Square Root Kalman Filters (EnSRF)

At the same time as the statistical Ensemble Kalman Filter was proposed, a different Ensemble Kalman Filter technique was developed, the *Ensemble Square Root Kalman Filter (EnSRF)*. This technique does not require additional perturbation because it is explicitly designed to give the correct posterior error covariance. It has the advantage of not adding an additional error source in the form of sampling error and is therefore elaborated in the following.
Ensemble Square Root Kalman Filters conserve the equation

$$\mathbf{P} = (\mathbf{I} - \mathbf{KH})\mathbf{P}^f \tag{2.40}$$

and are therefore also called *deterministic* EnKFs in contrast to the *stochastic* EnKF presented in Section 2.4.1. To introduce the concept of *square root* filters and understand where the name comes from, I start by bringing $\mathbf{P}$ into a square root formulation following Vetra-Carvalho et al. (2018), who derive the different solutions of the problem using one consistent and intelligible notation.
I start from equation 2.40 using the ensemble representation of the covariances:

$$\mathbf{P} = (\mathbf{I} - \mathbf{KH})\mathbf{P}^f \tag{2.41}$$

$$\mathbf{X}'(\mathbf{X}')^T = (\mathbf{I} - \mathbf{P}^f\mathcal{H}^T[\mathcal{H}\mathbf{P}^f\mathcal{H}^T + \mathbf{R}]^{-1}\mathcal{H})\mathbf{X}'^f\mathbf{X}'^{fT} \tag{2.42}$$

$$= (\mathbf{X}'^f - \mathbf{X}'^f(\mathcal{H}\mathbf{X}'^f)^T(N_e-1)^{-1}[\mathcal{H}\mathbf{P}^f\mathcal{H}^T + \mathbf{R}]^{-1}\mathcal{H}\mathbf{X}'^f)\mathbf{X}'^{fT} \tag{2.43}$$

$$= \mathbf{X}'^f(\mathbf{I} - (\mathcal{H}\mathbf{X}'^f)^T[\mathcal{H}\mathbf{X}'^f(\mathcal{H}\mathbf{X}'^f)^T + \mathbf{R}(N_e-1)]^{-1}\mathcal{H}\mathbf{X}'^f)\mathbf{X}'^{fT} \tag{2.44}$$

Introducing the definitions $\mathbf{S} := \mathcal{H}\mathbf{X}'^f$ and $\mathbf{F} := \mathbf{S}\mathbf{S}^T + (N_e-1)\mathbf{R}$, the last equation can be written as

$$\mathbf{X}'(\mathbf{X}')^T = \mathbf{X}^{f\prime}(\mathbf{I} - \mathbf{S}^T\mathbf{F}^{-1}\mathbf{S})(\mathbf{X}'^f)^T. \tag{2.45}$$

Ensemble square root Kalman filter methods find the square root $\mathbf{T}$ of the term in brackets.

$$(\mathbf{I} - \mathbf{S}^T\mathbf{F}^{-1}\mathbf{S}) = \mathbf{T}\mathbf{T}^T \tag{2.46}$$

Hence the name *square root* filter.
The matrix $\mathbf{T}$ is not uniquely defined and different ways for solving the equations exist. The challenge lies in finding formulations where the number of elementary mathematical operations is reduced, for instance by making opportune transformations into subspaces. This is crucial to avoid the computationally expensive computation of the prior and posterior error covariance matrices $\mathbf{P}$ and $\mathbf{P}^f$, which are of dimension $N_x \times N_x$. As shown by the square root formulation of the Ensemble Kalman Filter derived above, it is sufficient to transform the ensemble perturbation $\mathbf{X}'^f$ $(N_x \times N_e)$ via the matrix $\mathbf{T}$, and not the full covariance.
A general formulation of the EnSRF consists of transforming the prior ensemble mean $\overline{\mathbf{X}}$ with a weight vector $\overline{\mathbf{w}}$ and the perturbations $\mathbf{X}'$ by a weight matrix $\mathbf{W}'$.

$$\overline{\mathbf{X}} = \overline{\mathbf{X}}^f + \mathbf{X}'^f\overline{\mathbf{w}} \tag{2.47}$$

$$\mathbf{X}' = \mathbf{X}'^f\mathbf{W}' \tag{2.48}$$

Bringing the mean update into the matrix form $\overline{\mathbf{W}} = (\overline{\mathbf{w}}, \ldots, \overline{\mathbf{w}})\,\epsilon\,\mathcal{R}^{N_x \times N_e}$ these equations can be formulated as one:

$$\mathbf{X} = \mathbf{X}^f + \mathbf{X}'^f(\overline{\mathbf{W}} + \mathbf{W}') \tag{2.49}$$

The perturbation weight matrix $\mathbf{W}'$ is derived from the square root equations, and the weight vector $\overline{\mathbf{w}}$ can then be computed from the ensemble Kalman gain (2.39) or also from the posterior error covariance as in the alternative Kalman gain formulation (2.23).
The Ensemble square root Kalman Filters which are derived from these equations and have been implemented for this thesis are listed in table 2.1.

2.4.3 Formulation of the EnSRF in terms of Kalman gains

In many PaleoDA publications which use the Ensemble Kalman Filter, (for instance King et al. (2021), Steiger et al. (2018), and Tierney et al. (2020)), one will find a particular formulation of the EnSRF which is usually not found in the original mathematics publications. They state the EnSRF in terms of the regular Kalman gain for the mean, $\mathbf{K}$ and a perturbation Kalman Gain $\tilde{\mathbf{K}}$ using explicit matrix square roots. I introduce the concept here in order to compare the efficiency of this approach to the regular EnKF formulations later.

$$\mathbf{K} = \mathbf{P}^f \mathcal{H}^T (\mathcal{H}\mathbf{P}^f \mathcal{H}^T + \mathbf{R})^{-1} \tag{2.50}$$

$$\tilde{\mathbf{K}} = \mathbf{P}^f \mathcal{H}^T [\sqrt{(\mathcal{H}\mathbf{P}^f \mathcal{H}^T + \mathbf{R})}^{-1}]^T [\sqrt{(\mathcal{H}\mathbf{P}^f \mathcal{H}^T + \mathbf{R})} + \sqrt{\mathbf{R}}]^{-1} \tag{2.51}$$

$\tilde{\mathbf{K}}$ is a solution of the posterior covariance error equation

$$\mathbf{P} = (\mathbf{I} - \tilde{\mathbf{K}}\mathcal{H})\mathbf{P}^f (\mathbf{I} - \tilde{\mathbf{K}}\mathcal{H})^T. \tag{2.52}$$

The proof of this relationship is shown in Appendix F.3.

The regular Kalman gain is then applied to the ensemble mean forecast

$$\overline{\mathbf{X}} = \overline{\mathbf{X}}^f + \mathbf{K}(\mathbf{Y} - \overline{\mathcal{H}\mathbf{X}^f}) \tag{2.53}$$

and the perturbation Kalman gain is used for updating the ensemble perturbations

$$\mathbf{X}' = \mathbf{X}'^f - \tilde{\mathbf{K}}(\mathcal{H}\mathbf{X}'^f). \tag{2.54}$$

The formulation has been introduced by Whitaker and Hamill (2002), where the equations are applied in form of serial observation treatment as presented in Section 2.3. PaleoDA studies solved these equations for all observations at once using square root computing functions of modern programming languages (as `scipy.linalg.sqrtm` in Python). It is the algorithm implemented in the public PaleoDA codebases PHYDA (Steiger et al., 2018) and DASH (King et al., 2021). This direct approach introduces additional numerical instabilities (in comparison to the singular value and eigen value decompositions used in the regular EnKFs). In Section 2.5 the computational efficiency of this approach will be compared to regular EnKFs.

2.4.4 Summary of the methods

The Ensemble Kalman Filters implemented for this thesis are listed in table 2.1 with a reference to the original publication and where the full derivation can be found in the appendix. Particularities are noted in the comment column. Python code for all the methods presented in this thesis can be found in the public repository github.com/mchoblet/ensemblefilters.
It is important to underline the differences and similarities of these approaches. All Ensemble Square Root Kalman Filters produce the same posterior ensemble mean and posterior error covariance due to the way how they are constructed. The stochastic EnKF produces the same mean estimate, but results in a different posterior error covariance estimate due to the additional noise. The differences are usually negligible. The direct EnSRF solver, called *EnSRF (PaleoDA*

Method	Publication	Derivation	Comment
Stochastic EnKF	Burgers et al. (1998)	2.4.1	
Ensemble Transform Kalman Filter (ETKF)	Bishop et al. (2001)	F.1	Two slightly different versions run under the name of ETKF.
Error-subspace Transform Kalman Filter (ESTKF)	Nerger et al. (2012)	F.5	
Ensemble square root Kalman filter (EnSRF)	Tippett et al. (2003) and Whitaker and Hamill (2002)	F.2	The first publication proposed an implementation only treating observations serially, whereas the second proposes a more general implementation.
EnSRF with serial observation treatment	Whitaker and Hamill (2002)	F.4	
EnSRF (PaleoDA version)	Steiger et al. (2018)	F.3	The authors solved the equations formulated by Whitaker and Hamill (2002) at once. In contrast to the implementation in the PHYDA code package, I changed the order of matrix calculation for means of efficiency.

Table 2.1: Overview of the Ensemble Kalman Filters tested in this thesis.

version) leads to a slightly different mean and covariance estimates due to the direct calculation of matrix square roots, which introduces negligible imaginary parts. The question of which algorithm to choose for performing PaleoDA reduces to the aspect of computational efficiency which is discussed in the next section.

2.5 Computational efficiency of the Ensemble Kalman Filters

The EnKF is the central algorithm of the CFRs performed for this thesis. As these equations are repeated thousands of times, understanding the speed limitations and optimizing the efficiency is a crucial task.

The rigorous way for deciding on which algorithm is best consists of performing a computational complexity analysis by counting the costs of all involved mathematical operations, including advanced operations as singular and eigenvalue decompositions. This is usually done with the Big $\mathcal{O}$ notation in terms of the problem dimensions N_e, N_y, N_x. Tippett et al. (2003) and Vetra-Carvalho et al. (2018) performed this type of analysis. Applying their results to a typical PaleoDA situation, in which there are orders of magnitude more state variables to determine than ensemble members and observations, $N_x \gg N_e \approx N_y$, gives a leading order of $\mathcal{O}(N_x \cdot N_e^2)$ for all algorithms. Hence, the algorithms should in theory be equally fast, but one must also be aware that the theoretical efficiency calculations cannot be transferred one to one to the Python implementation used in this thesis. In the `numpy` package for efficient matrix and vector calculations, some calculations are automatically parallelized whereas others are not.

To be able to decide which algorithm is the fastest I performed a non comprehensive test with typical PaleoDA dimensions on two different machines. The test data has the following dimensions:

- N_e=100, which corresponds to an ensemble size sufficiently large to capture the model covariance structure.
- N_y=100. The number of observations will in general fluctuate between a two and three digit number.

- N_x=50000. The number of grid cells in a typical simulated climate field, multiplied with the number of variables which are reconstructed, e.g. 3 for surface temperature, precipitation and δ^{18}O .

These dimensions define the size of the four involved matrices:

- $\mathbf{X}^f$, the ensemble of prior states ($N_x \times N_e$).
- $\mathbf{HX}^f$, the ensemble of prior observations estimates ($N_y \times N_e$).
- $\mathbf{Y}$, the vector containing the observations ($N_y \times 1$).
- $\mathbf{R}$, the error variance associated with the observations, which are assumed to be uncorrelated and hence given as a vector ($N_y \times 1$).

The workstations used for the tests are called *Ravenclaw* and *Gryffindor*. *Ravenclaw* has 8 available single-thread cores of the type *Intel(R) Core(TM) i7-9700K CPU* (2018) and *Gryffindor* 16 dual -thread core of the type *AMD Ryzen 9 5950X* (2020). Both offer a maximum frequency of up to 4.9 GHz. *Gryffindor* has more RAM (128gb instead of 64gb) and will thus be used for the CFRs in this thesis. For a statistical assessment of the algorithm speed, I use 10 samples, where each sample consists of 100 repeated calculations. The uncertainty is calculated from the standard deviation of the different sample means.

Method	Ravenclaw	Gryffindor
EnSRF	65.6 ± 2.0	46.7 ± 0.2
EnSRF (PaleoDA version, unoptimized)	133 ± 38	86.1 ± 0.2
EnSRF (PaleoDA version)	33.5 ± 0.9	34.1 ± 0.1
EnSRF (serial)	3310 ± 31	2900 ± 4
ESTKF	23.4 ± 0.2	23.0 ± 0.1
ETKF	23.3 ± 0.2	22.8 ± 0.1
ETKF (adaptation)	23.6 ± 0.2	23.4 ± 0.1
Stochastic EnKF	21.2 ± 0.4	19.1 ± 0.1

Table 2.2: Calculation time of the Ensemble Kalman Filter algorithms presented in Section 2.4 for two different machines, in [ms]. Machine specifications are presented in the text above this table.

On both machines, the stochastic EnKF is the fastest algorithm, closely followed by the ETKF and the ESTKF. The fact that *Gryffindor* has more available cores does not result in a significant speed increase for these algorithms. Surprisingly, the serial EnSRF is two orders of magnitude slower than the fastest algorithm, in spite of a having a similar theoretical complexity. As previously reported in Steiger et al. (2018), the direct solver of the EnSRF (PaleoDA version) is significantly faster than the serial assimilation. I suppose that the slowness of the serial assimilation comes from the fact, that the loop over all observations is slow in an interpreted language like Python, and that it can not easily be parallelized because the iterations are not independent. The serial EnSRF only computes on one core, whereas all other methods automatically use all available cores.
The table also contains the result for the PaleoDA EnSRF as used in Erb et al. (2022), denoted as *unoptimized*. The results show the pernicious effects that not optimally aligned matrix vector products can have. This code is two to three times slower than the rearranged version implemented for this thesis.

Due to the additional noise, I will not use the stochastic EnKF but the ETKF. One important aspect which has been not mentioned yet, is that for the covariance localization scheme presented in Section 4.4.2 the ETKF can not be used, and one has to rely either on the stochastic EnKF, the EnSRF (PaleoDA version) or the serial EnSRF.

2.6 Towards paleoclimate Data Assimilation

Up to this point, the description of the DA techniques has been kept general and close to its mathematical foundations. When applying DA for CFRs, adaptations and simplifications to the general methodology need to be performed. As a consequence, PaleoDA literature might appear confusing to the reader who knows the general formulations of the Ensemble Kalman Filter as presented in the previous chapter (Section 2.4) but has not been introduced to the peculiarities of PaleoDA. Therefore the aim of this section is to bridge the gap between general DA and PaleoDA by introducing the key methodological differences. In the next chapter, the concepts presented in this overview will be deepened and substantiated in the context of the data available for my project.

2.6.1 Assimilation of time-averaged quantities

A fundamental difference when assimilating paleoclimate data lies in the fact that the climate observations do not represent instantaneous values, but means over longer time resolutions. Depending on the climate archive type and the time studied, proxy records can represent mean values over a season, years, decades or centuries to millennia. In contrast, the EnKF as such is designed to instantaneously assimilate and update estimates in discrete time steps. The effect of treating observations as time-averaged values has been studied first in Dirren and Hakim (2005) who proposed extending the EnKF to averaging both observations and state variables. Subsequently Huntley and Hakim (2010) studied this approach with a more complicated atmospheric model and also mathematically showed the equivalence of the time averaging and instantaneous approach. The essence is that both the Kalman gain operator, which consists of covariance matrices, and the time averaging operator are linear and hence commute. As a result, assimilating time-averaged observations with time-averaged state variables leads to the same results as the instantaneous approach when the instantaneous estimates are averaged after the assimilation. Huntley and Hakim (2010) also showed, that if the averaged quantities and perturbations from the time averages do not covary, not only the assimilated time averages, but also the perturbations are equal for both approaches. This second part is not a necessary assumption for the DA performed here.
Some PaleoDA studies stress the fact that they assimilated time-averaged observations. Others tacitly assume the equivalence and do not mention the difference at all. To summarise, it can be said that assimilating time-averaged quantities is mathematically equivalent to assimilating instantaneous values. However, for real climate proxy records it is not unambiguous on what precise time scale they actually represent time-averaged values. This will be addressed in Section 4.5 when introducing the concept of multi-time scale DA.

2.6.2 Offline Data Assimilation

DA for CFRs can also be performed by using the mean model climatology for the ensemble covariance. The model climatology is not informed by the prior assimilation steps and the dynamical model/transition matrix $\mathbf{M}$ becomes irrelevant.
Dirren and Hakim (2005) and Huntley and Hakim (2010) tested this approach when investigating the effect of assimilating time-averaged quantities. They did so to evaluate the loss of forecasting skill for longer timescales and found that over longer averaging-times, the model climatology has as much forecasting skill as the forecasts based on updated initial conditions.

This issue is closely linked to the fundamental topic of predictability of the climate system. The term predictability can be understood as the inherent memory of the climate system, which is of chaotic nature. The less predictable a system is, the more important boundary conditions instead of initial values are to describe it properly. This is the case for the transition from the prediction of weather, which acts on hourly to daily timescales, to the prediction of decadal and centennial climate, as visualized in Figure 2.1

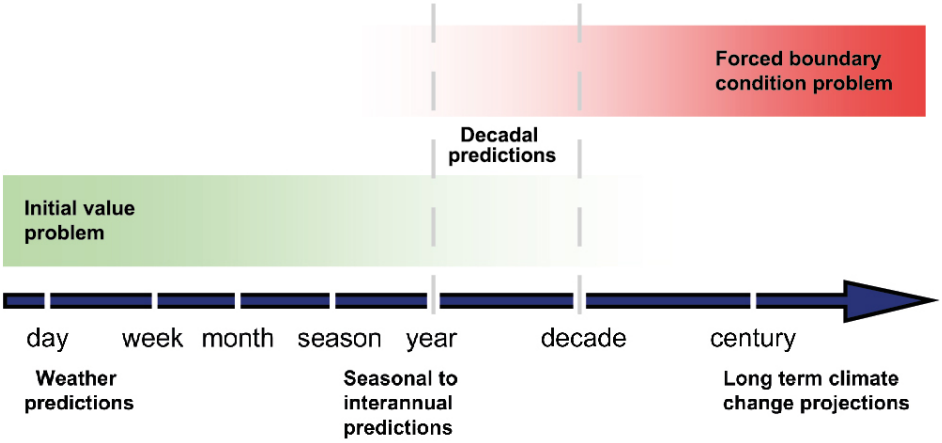

Figure 2.1: Visualization of the decreasing importance of initial values for long term climate predictions. Taken from AR5 of the IPCC (Kirtman et al., 2013).

In Huntley and Hakim (2010), in addition to using the mean climatology for the covariance, the authors propose that the forecasting step could be skipped when assimilating climate proxy records which are of annual or longer resolution. They argue, that due to the predictability limit the mean climatology can be a prior ensemble as reliable as the model forecast informed by prior measurements. Thus, constraining initial conditions of a climate simulation becomes irrelevant. A similar argument was brought forward independently by Bhend et al. (2012).
This approach saves a lot of computation time. Cycling an ensemble of complex climate models is extremely expensive and could at most be performed for models of intermediate complexity. The no cycling approach has been named *offline* DA, in contrast to regular *online* DA. It fundamentally changes DA as no information is propagated through time and initial conditions of a model simulation do not need to be adjusted. Data from already performed simulations, for instance taken from coupled Atmosphere-Ocean-GCM simulations can be applied directly to the observational data. For that reason, Offline Ensemble Kalman Filtering has also been called Ensemble Kalman Fitting (Bhend et al., 2012; Franke et al., 2020), which is a more precise name.
It is important to distinguish between two types of Offline Data Assimilation approaches that can be found in the literature. The terminology follows Okazaki et al. (2021).
In *stationary* offline DA, the prior is taken from a collection of climate states, which can stem from one to many model simulations. The prior is the same for each assimilation step and thus does not contain temporal information. It is computationally efficient because it does not require an ensemble run. *Transient* offline DA also does not require running an ensemble of climate models based on observations. However, it requires a large ensemble of different already ran simulations, for instance based on one model with a set of perturbed parameters. For each assimilation step the prior consist of the ensemble estimates for the current time of the assimilated proxies. Like this, temporal information from the models is kept. This approach has been followed in studies by Annan and Hargreaves (2012), Bhend et al. (2012), Franke et al. (2017), and Goosse et al. (2006).
Online Data Assimilation is rarely used in PaleoDA. It has been used in combination with

particle filters (selection of matching ensemble members, see Section 2.6.3) as by Dubinkina et al. (2011), Goosse et al. (2010), and Goosse et al. (2012). Matsikaris et al. (2015) compared a best matching ensemble member particle filter method which was performed online and offline and found no improvement for the online DA product. Yet, this study only used a simple DA method and not an advanced technique as the EnKF.
A recent study by Okazaki et al. (2021) re-elaborated the comparison of both with a model of intermediate complexity for the atmosphere, SPEEDY (Molteni, 2003) , coupled to a simple slab ocean model. In experiments with simulated observations, so-called pseudoproxies (see Section 4.3), they confirmed previous hypotheses that online DA outperforms offline DA when the time over which observations are averaged is shorter than the predictability of the climate model. For variables describing the ocean, the online DA product was closer to the truth than the offline DA product. Typical predictability timescales for the ocean are orders of magnitudes longer than for the atmosphere.
However, online PaleoDA is still in its very early stages. A promising method has recently been brought forward by Perkins and Hakim (2021). The authors emulated climate fields from a full GCM with a linear inverse model in order to add dynamical memory into the climate reconstruction.
Stationary offline DA is now a well established CFR method and is also computationally cheap to perform. Therefore it is the method used throughout this thesis. The construction of the prior is outlined in Section 4.7.

2.6.3 Other DA methods than the EnKF

Before the EnKF became the dominant method for PaleoDA, other DA concepts have been developed, and in part also been applied to paleoclimatic data. One recurring argument in favour of using DA for reconstructing past climates is the reconstruction of *dynamically/physically consistent fields*. However, it is important to stress that the meaning of this physical consistency actually depends on the applied method. For the EnKF it relates to the covariance structure provided by the simulation.
The first study to apply DA for paleoclimate reconstruction based on observations and simulations used pattern nudging technique (Storch, 2000). It was designed for reconstructing atmospheric circulation patterns close to prescribed target patterns. Another pioneering work introduced so-called forcing singular vectors (Barkmeijer et al., 2003). These methods have not been tested for climate variables as temperature and precipitation and have in general not been used in recent years.
A DA method commonly used for CFRs is the Particle Filter (PF). The idea behind PFs is simple. A cost function for comparing observations and simulated values is defined and based on it the best matching ensemble members are selected. The implementation can range from the simple selection of one best matching member to the calculation of a weighted mean of multiple ensemble members after applying an importance resampling technique. Studies as Goosse et al. (2010), Goosse et al. (2006), and Matsikaris et al. (2015) have used the simple best matching ensemble member approach, whereas Annan and Hargreaves (2012), Dalaiden et al. (2020), Dubinkina et al. (2011), and Goosse et al. (2012) implemented a sequential Monte Carlo method for estimating weights for a collection of best matching ensemble members. The PF has been used in both offline and online PaleoDA with climate models of intermediate complexity and also climate proxy records.
In principle, the PF is more versatile than the EnKF because it does not rely on the assumption of normal distributions. However, in practice so-called filter degeneracy, where one ensemble member gets all weight despite using a resampling technique, can occur. A consequence is that the posterior uncertainty is underestimated. Liu et al. (2017) compared PF and EnKF for simulated observations and found that the EnKF, in the respective experimental setting of that study, is more reliable and efficient than the PF.

2.6.4 Influence of proxy records and model priors in the Offline EnKF

This section is dedicated to emphasise the main mechanisms behind using the offline EnKF. Using a static prior ensemble for each assimilation step (typically yearly) means that in the reconstructed climate signal the temporal variability stems entirely from the measurements/climate proxy records.
The climate model prior is a collection of randomly selected climate states and its main purpose lies in providing representative observation estimates and a complete climate field. The Kalman gain is computed from the covariance between the observation estimates and the climate field. The relationship between the two informs how information from measurements are spread to all simulated climate variables, even to variables that are not directly measured. For instance, temperature and precipitation can be inferred from δ^{18}O via the covariance inherent to the model simulations. The covariances/correlations between remote locations usually monotonically decrease with geographic distance. However, long-ranging correlations, called *teleconnections* can exist even beyond continental length scales. Teleconnections are especially important when few climate observations are available. As will be presented in chapter 3, especially for the first half of the last millennium proxy records for less than 100 locations are available annually, whereas the total climate field is described by $\approx 10^6$ variables.
With respect to the influence of the proxies in the offline EnKF, recall that these appear in the innovation part of the Kalman Filter equations, $\mathbf{y} - \overline{\mathcal{H}\mathbf{X}^f}$. The observations are compared to the mean observation estimate from the climate model. To avoid being affected by climate model biases many PaleoDA studies do not assimilate absolute values, but anomalies. The implications of this choice will be discussed in more detail in 4.8.

In short, climate reconstructions with the offline EnKF are informed

1. temporally by the climate proxies
2. spatially by the climate model simulations used for the prior.

Stationary vs transient model covariance
An important methodological assumption is the temporal stationarity of the covariance patterns from the models. For a comparably stable period as the late Holocene, this is a reasonable assumption. For studies over longer timescales, e.g. transient periods like the last deglaciation, assuming a static covariance structure is less appropriate. Studies by Erb et al. (2022) and Osman et al. (2021) used a selection of climate states which move through time, allowing for the model covariance to change. Although close to *transient offline-DA* as described in Section 2.6.2, it is yet another approach because only one (respectively two) climate models were used as a prior.

The averaging kernel
In PaleoDA, it is not usual to estimate the potential influence of the prior and the proxy record locations on the reconstruction. In remote sensing, however, the concept of the *averaging kernel* $\mathbf{A}$ has been established (Rodgers, 2000). It is used to quantify how much the measurements of specific variables of the state vector can influence the other variables and how the posterior error uncertainty will be reduced. It is calculated from the Kalman gain and the observation operator.

$$\mathbf{A} = \mathbf{KH} = cov(\mathbf{X}^f, H\mathbf{X}^f)[cov(\mathbf{X}^f, H\mathbf{X}^f) + \mathbf{R}]^{-1}\mathbf{H} \tag{2.55}$$

In fact, one could also study the Kalman gain for each proxy record location. Recalling Equation 2.18 for the reduction of the posterior error covariance, we see that $\mathbf{I} - \mathbf{A}$ is the fraction of posterior to prior uncertainty. Thus the larger $\mathbf{A}$, the smaller the posterior uncertainty.

However, the averaging kernel is not directly applicable in the context of PaleoDA due to the peculiar way of applying the observation operator $\mathcal{H}$ (Section 2.6.5), for instance with non-linear functions (fractionation for speleothems) or the application to monthly instead of annual values for the precipitation and infiltration weighting. To make use of the concept one could assume that $\mathcal{H}$ is simply a vector with entries equal to one for the grid cells closest to the proxy record locations and zero for the rest. This way, each non-zero column of $\mathbf{A}$ represents one measurement location and how it influences the climate variables at each grid cell. Whereas this allows for studying the influence of each proxy record location on the reconstruction one after another, a more practical assessment of all proxy record locations at once consists of summing up the elements of each row of $\mathbf{A}$, which is called the area of the averaging kernel. It represents the response of each grid cell variable to a unit measurement at all proxy record locations.

2.6.5 Proxy System Models as observation operators

Until now, I generally referred to the function mapping the climate field from the model to the observation estimates as the observation operator $\mathcal{H}$ (as in Equation 2.3[5]). Initially, this mathematical operator which is applied to the state vector containing all climate state variables was assumed to be a simple linear operator. As discussed previously in Section 2.4, when using the EnKF it is a valuable approximation to use non-linear observation operators. PaleoDA goes beyond applying $\mathcal{H}$ to the model data at a specific time to obtain the observation estimate. For instance, $\mathcal{H}$ also processes information from other timescales like monthly data although in the end yearly means are assimilated, or when the low-pass filtering effects of climate archives are simulated information from various years is mixed. Given a prior climate state, which is represented by a discretized climate field for variables as temperature, precipitation and δ^{18}O , such an operator/function $\mathcal{H}$ has to answer the following question:
Which physical, chemical, biological and geological processes do we need to add to the simulated variables in order to reproduce the typical signal of a specific climate archive?
It is important to stress, that this approach is a forward approach instead of the inverse approach which is often used in order to translate a paleoclimatic observation into a climate variable, for instance by paleothermometers (e.g. in noble gas thermometry (Aeschbach-Hertig and Solomon, 2013)).

In Paleoclimatology the observation operators are called *proxy system models (PSM)*. PaleoDA is just one field of application of PSMs, which have been developed to better understand the climate signal captured by climate archives, their uncertainties and enhance model data comparison. Evans et al. (2013) introduced a general concept for PSMs. A PSM describes the different stages of influence on the climate signal, which are: *Environment*, *Sensor*, *Archive* and *Observation*.The environment is characterised by climate variables such as temperature, precipitation, humidity and pressure. This external influence is at first captured in direct response to it via a *sensor model*. The transformed climate signal is encoded into an archived form, a long-term signal via an *archive model*. At last, it needs to be reproduced how the climate archives are sampled by the researchers to obtain observation. The processes of measurement and dating uncertainties is captured by a separate *observation model*.

In recent years, many different PSMs have been proposed by the respective expert climate archive researchers, for instance for tree rings, corals, ice cores, boreholes, lake and marine sediments and speleothems. PSMs exist on various levels of complexity, which depend on the specific scientific questions and the climate variables which are available. An overview of var-

[5] $\mathcal{H}$ is also called a forward model in PaleoDA, although this terminology might cause confusion because in regular DA the forward operator denotes the dynamical model that projects the forecasts in time.

ious concrete PSMs and how they fit into the theoretical framework of PSMs can be found in Evans et al. (2013). Dee et al. (2015) and Okazaki and Yoshimura (2019) specifically assessed PSMs for water isotopes. Whereas PSMs in the field of tree rings have existed for decades, in the case of marine sediment proxies, PSMs have been developed only recently, see for instance Malevich et al. (2019), Tierney and Tingley (2015), Tierney and Tingley (2018), and Tierney et al. (2019). In the next chapter, PSMs for speleothem and icecore $\delta^{18}O$ will be introduced in detail. In PaleoDA practice, often PSMs of low-complexity are chosen. In fact, most PaleoDA studies even fall back to linear regression calibrations on data from the instrumental period, which is not directly physically motivated.

The role of PSMs in PaleoDA

In general, PSMs are meant to reproduce signal timing and the mean state of a proxy record, the spectral characteristics of a climate archive and its relationship to the global/local climate field (e.g. the covariance relationship to the climate at other locations).

For the specific purpose of *stationary offline EnKF* only two of these goals are relevant. As the assimilation is performed offline, the observation estimates from the model do not need to match the climate proxy in time. They provide an estimate of the range of values provided by the model for these proxies, their mean value is compared to the proxy in the innovation part of the Kalman Filter equations. Thus, only the mean state and not the signal timing is relevant. In case of assimilating climate anomalies with a static prior, this mean value will effectively be set to zero and hence not be relevant. Second, the observation estimates appear in the Kalman gain in the form of the covariance to the whole climate field. The covariance, which is weighted by the variance of the observation estimates and the proxy error (see Equation 2.16) informs the algorithm how the observation information is spread over the entire climate field. When evaluating the PSMs and performing reconstruction, these initial goals and mechanism need to be considered thoroughly. Furthermore these considerations serve to assess to which extent more realistic/precise PSMs are meaningful in PaleoDA.

2.6.6 Overview of climatic settings and phenomena studied with PaleoDA

After having mentioned a variety of PaleoDA studies with a primary focus on their methodology, I would now like to give a brief overview of the different temporal and spatial climate settings that have been investigated. PaleoDA using data from paleoclimate records has first been conducted for the climate of the last two millennia (Goosse et al., 2012; Hakim et al., 2016). This time period also represents the time frame targeted by most PaleoDA reconstructions due to the availability of large proxy networks as the PAGES2k database (Ahmed et al., 2013; Emile-Geay et al., 2017). Two outstanding (and methodologically similar) projects have provided climate fields for the last millennium and have been used in a number of subsequent data analysis studies. The Last Millennium Reanalysis (LMR) (Hakim et al., 2016) reconstructed temperature fields from the PAGES2k dataset, whereas the Paleo Hydrodynamics Data Assimilation product (PHYDA)(Steiger et al., 2018) in addition to temperature precipitation fields and various hydroclimatic indices, based on a different model prior and an extended proxy dataset. Three years after its original publication, the LMR obtained an update based on more elaborate PSMs, an extended proxy record database and also reconstructing precipitation and climate indices (Tardif et al., 2019). Both LMR and PHYDA did not use isotope-enabled models as a prior.

The reanalysis datasets have been used, inter alia, to look at the global response of the climate system in temperature and hydroclimate to volcanic eruptions (Tejedor et al., 2021a; Tejedor et al., 2021b; Zhu et al., 2020). A more regional, though globally important phenomenon that has been studied using these datasets/code frameworks is El Niño-Southern Oscillation (ENSO) (Dee et al., 2020; Dee and Steiger, 2022; Sanchez et al., 2021; Zhu et al., 2022). For reconstructing ENSO, which is also considered a central mode of internal climate variability

over the last millennium, proxies as corals which are near to the central pacific region are crucial. However, it is important to be aware of the fact that LMR and PHYDA mostly rely on hundreds of non curated tree ring records, where the applied statistical PSM (see Section 4.1.4) automatically selects meaningful records. The LMR and PHYDA reconstructions have been compared to other reconstruction methods and used for a multi-CFR-method mean to study climate variability (Neukom et al., 2019a) and reject the existence of global warm- and cold-periods over the last millennium (Neukom et al., 2019b).
Apart from LMR and PHYDA, reconstructions using only selected, high-quality networks of tree ring data (width and density) have been performed as in King et al. (2021). Due to their geographic locations, tree rings are particularly meaningful for reconstructing the climate on the Northern Hemisphere. Several studies also investigated the influence of seasonal biases inherent in these proxies on the reconstruction. Such high-quality, mostly tree-ring based datasets have also been used to reconstruct climate fields for the second half of the last millennium on a monthly instead of a yearly time scale by Franke et al. (2017), Franke et al. (2020), and Valler et al. (2019). These three studies used a transient offline EnKF rather than a stationary offline EnKF. Periods of specific interest in PaleoDA for the last millennium are the warm medieval climate anomaly, see for instance Goosse et al. (2012) and the so-called little ice age as studied in Neukom et al. (2019b). Recent studies have focussed on reconstructing the climate of polar regions, as done for Arctic Sea Ice (Brennan and Hakim, 2022) and surface air temperature in Antarctica using water isotopes and snow accumulation (Dalaiden et al., 2020).
Going back deeper in time, Badgeley et al. (2020) reconstructed temperature and precipitation over the Greenland ice sheet during the last 20000 thousand years. Erb et al. (2022) performed a global temperature reconstruction for the entire Holocene (the last 12,000 years) using terrestrial and marine sediment proxies. A PaleoDA reconstruction of the last 24,000 years, reaching back into the Last Glacial Maximum (LGM) was carried out by Osman et al. (2021) using marine sediments only. The aims of these two studies are, among others, reaching a better understanding of the mechanism of climate variability during the transition from the Last Glacial Maximum (LGM) to the Holocene and investigating the hypothesised mid-Holocene warming, which is also called the Holocene temperature conundrum (Liu et al., 2014). The alleged peak cooling of the LGM has been reconstructed globally with a single, isotope-enabled model prior in Tierney et al. (2020) and using a multi-model ensemble by Annan et al. (2022). These studies provide a single time reconstruction instead of a time series reconstruction. Besides elucidating the nature of this extreme climatic condition these reconstructions have also been used to estimate *Equilibrium Climate Sensitivity* (ECS), which is the warming of Earth's climate in response to a doubled CO_2 content in the atmosphere (from 260ppm to 520ppm). A similar single time fit has recently been presented for the Paleo-Eocene Thermal Maximum (PETM) and the period preceding it, 56 million years ago, which is also a valuable reference period for estimating ECS due to its higher temperature and CO_2 concentration (Tierney et al., 2022).

Classification of this thesis in the PaleoDA landscape
Although many PaleoDA reconstructions of the last millennia exist, none of them have incorporated the SISALv2 speleothem and the Iso2k water isotope databases (here I use the ice core records) and systematically worked with a variety of isotope-enabled simulations. The SISALv2 and Iso2k proxy networks could contribute meaningfully to temperature reconstructions, especially as they also capture long-term climate variability. Incorporating speleothem and ice core data into PaleoDA algorithms requires a careful and thought-out concept, which this thesis aims to provide. Speleothem and proxy records are also of particular interest for regions which are almost not covered by the proxy networks used in the PaleoDA studies mentioned above, for instance low-latitude regions like the Amazon region or high-latitude polar regions. Prototype regional reconstructions will be tested throughout this thesis, not only for temperature but also for the less understood hydroclimatic conditions over the last millennium.

Chapter 3

The Data

3.1 Isotope-enabled climate model simulations

The last millennium climate model simulations used in this project are ECHAM5/MPI-OM (short ECHAM), GISS, iCESM, isoGSM and iHadCM3. They are described in table 3.1. The simulations are the same as studied in Bühler et al. (2022). This publication also contains an extended description of the simulation runs. All models are coupled atmosphere- and ocean-GCMs, except for isoGSM. IsoGSM is an atmosphere-model which is forced by sea surface temperature and sea ice prescribed from a simulation run of the CCSM4 model.
The output of the simulations is provided in the form of monthly mean values, which are averaged to annual means in the PaleoDA algorithm. The simulated climate variables used in this thesis are surface temperature (tsurf), precipitation (prec), evaporation (evap), δ^{18}O of precipitation (δ^{18}O) and when available, sea level pressure (slp). In case only latent heat (lh) is provided, evaporation is computed via equation 4.4. Special preprocessing required for handling faulty δ^{18}O values is described in the next paragraph.

Preprocessing of model data δ^{18}O
A fraction of the simulated monthly δ^{18}O values exhibits two types of problems. First, unphysical δ^{18}O values are present, either extremely negative or positive. This problem is dealt with by defining global thresholds of $-60‰$ to $15‰$ and setting values that exceed these boundaries to not a number (NAN). In addition, for low latitudes within the boundaries of -50°S and -50°N, the valid range is refined to $-30‰$ to $15‰$. Also without this masking of extreme values, the data already contains NAN values. This makes sense if there is no precipitation in a grid cell during a month, but it also appears when there is precipitation. This effect is pronounced in arid regions like the Sahara or the Middle East and is usually a consequence of numerical instabilities caused by small evaporation and precipitation numbers. In the models ECHAM5, iCESM and iHadCM3 real values are missing over several years for these extreme regions.
NANs can constitute a problem when all months of a year are NAN, such that no yearly mean for a grid cell can be computed. NANs cause the PaleoDA algorithm to fail and explicitely skipping NANs in the algorithm would provide covariances based on too few values. To avoid these problems from the start, all NANs were replaced by spatially interpolated values. The last row of table 3.1 documents the percentage of monthly values that were interpolated. The approach used here can be considered a crude approach to deal with NANs. However, the percentage of replaced values is only small and in the end annual/seasonal means are computed. In the model iHadCM3 the values for all grid cells are missing, for the entire years 1426, 1427 and 1428. Spatial interpolation can thus not provide any values, and temporal interpolation of monthly values would also not be sensible. Incorporating an option to skip these years in the reconstruction code is incompatible with the multi-timescale reconstruction used in this thesis. Therefore, the values of year 1425 are simply copied three times when computing an-

Model	ECHAM5/MPI-OM	GISS ModelE2-R	iCESM1	isoGSM	iHadCM3
Reference	Sjolte et al. (2020) Werner et al. (2016)	Lewis and LeGrande (2015) Colose et al. (2016a) Colose et al. (2016b)	Brady et al. (2019) Stevenson et al. (2019)	Yoshimura et al. (2008)	Bühler et al. (2021) Tindall et al. (2009)
Spatial resolution	3.75° × 3.75°	2.5° × 2°	2.5° × 1.875°	1.875° × 1.875°	3.75° × 2.5°
Grid cells	96 × 48	140 × 90	144 × 96	192 × 94	96 × 73
Time (AD)	850-1849	850-1849	850-1850	851-1850	851-1850
Climate variables	tsurf, prec, δ^{18}O , evap	tsurf, prec, δ^{18}O , evap, slp	tsurf, prec, δ^{18}O , lh	tsurf, prec, δ^{18}O , lh	tsurf, prec, δ^{18}O , evap, slp
Interpolated δ^{18}O values [%]	3.8	0*	0.05	4.3	0.26
Reported biases	warm, wet and positive δ^{18}O bias over Antarctica	problems in convection changes, clouds and isotope kinetics over Antarctica	small negative δ^{18}O biases across the land surface, overestimated convection in mid-latitude oceans	underestimated isotopic deplection over Antarctica	overestimated local evaporation

Table 3.1: Brief description of last millennium simulations used in my project. This table is a reduced and adapted version of the table presented by Bühler et al. (2022). There, references to orbital parameters, GHG concentrations, vegetation, volcanic forcing and total solar irradiance configurations, as well as more detailed model descriptions can be found. The GISS model did not exhibit NAN values at first, but had to be detrended due to a significant drift. The procedure is described in the text.

nual/seasonal means. Three repeated values have little effect on the model covariances, which are computed from hundreds of simulation years.
The GISS simulation showed the peculiar behaviour of an extreme δ^{18}O drift over regions of Antarctica. This trend starts to be visible in the global mean after 300 years, but starts at different dates and accelerates towards the end of the simulation. The drift is visualised in Appendix B.1. Unfortunately, the authors of the simulation did not provide a simulation without this behaviour. The data was debiased with a fourth order polynomial to all grid cells which exhibit a trend for the δ^{18}O time series (detected with an augmented Dickey–Fuller test and a p value of 0.05). In future studies a GISS simulation with a less pronounced δ^{18}O drift should be used, especially if δ^{18}O values from Antarctica ice cores are assimilated.

3.2 Speleothem records

Speleothems are geological formations created by the accumulation of calcium carbonates like calcite and aragonite. This accumulation happens via drip water, which is precipitation water that has traveled through the soil above a cave and has become supersaturated in carbonates. Inside the cave this water then precipitates in form of speleothems (Bradley, 2015). By taking into account these processes, δ^{18}O measured in speleothems can thus be linked to δ^{18}O in precipitation. In Section 4.1.1 these processes are outlined in detail, which is crucial for making simulated δ^{18}O and measured δ^{18}O comparable. Speleothems grow over time scales of up to tens of thousands of years and can be precisely dated using uranium–thorium dating on seasonal to centennial scales.

3.2.1 The SISAL database

An international working group of speleothem experts affiliated to the Past Global Changes project (PAGES) have compiled hundreds of speleothem δ^{18}O and also δ^{13}C records into the well-documented and screened SISAL database (Atsawawaranunt et al., 2018; Comas-Bru et al., 2020). The collected records cover 130,000 years of past climatic history, from the last

interglacial over the last glacial maximum until the past two millennia. The database has been made easily accessible to enable regional climate reconstructions and model-data comparison. From the updated SISALv2 database, the δ^{18}O time series and corresponding measurement precision for records covering the years 0 until 2013 CE were extracted. The proxy record time series will be further cut in time in the PaleoDA algorithm. At first, the records are kept as long as possible for a more precise assesment of the time resultion. For the time axis, the original chronology (*interp_age*) was used. Dating uncertainties and alternative age models were not considered in this thesis. The proxy record time series are stored in a simple time-site data table, where non-existing values are denoted as NAN. I only kept speleothem records that have at least one sample measurement in the period from 1700 to 1800CE, because this period was later used as a reference period for the reconstruction of anomalies. I require that the speleothem records span at least 300 years. Besides the raw values, site metadata as the site_id, name, latitude, longitude, karst type (mineralogy) and elevation where saved for each cave.
After this preliminary procedure, the speleothem proxy data table reduces to 108 speleothem records. The speleothem record locations and their median time resolution are plotted in Figure 3.1. The selection offers a good coverage of the terrestrial low and mid-latitudes, except for the African continent. Most speleothem records are available for Central Europe, the low- to mid-latitudes of the Americas and
East Asia.
A bar plot of the median time resolutions and the availability of records per year are plotted in Figure 3.2. The number of annualy available speleothem records steadily increases from less than 20 in the first millennium to almost 40 in the 19th century, before dropping in the 20th century. The median time resolution of the speleothem records is broadly distributed, ranging from annual to multi-annual and multi-decadal resolutions.

3.3 Ice core records

Ice cores are created by the compaction of accumulated snowfall over large ice sheets, when the snow survives the ablation during the summer season. The δ^{18}O measured in ice cores can constitute a reliable climate proxy for past atmospheric conditions over up to hundred of thousands of years (Andersen et al., 2004; Augustin et al., 2004). Ice core layers can be dated down to years and seasons for the past millennia (Bradley, 2015). However, the dating is considered less precise than for speleothems due to the counting of snow layers relative to other layers. However, the interpretation of the ice core δ^{18}O signal is impeded by uncertainties in the relationship to other climate variables due to depositional and post-depositional processes. Processes which need to be taken into account are outlined in Section 4.1.1.

3.3.1 The Iso2k database

The ice core δ^{18}O proxy records used in this thesis are taken from the Iso2k database (Konecky et al., 2020), which is a global synthesis of water isotope values measured in a variety of climate archives covering the past two millennia. The ice core δ^{18}O time series provided in this database are dated to annual to centennial resolution. The speleothem records stored in Iso2k are a subset of records provided by the SISAL database and are thus not considered.
For selecting ice core records, I chose the δ^{18}O time series from the 'glacier ice' category which are denoted as the primary local time series and given in ‰. Iso2k provides one single date for the time stamps and does not provide measurement and dating uncertainties for the ice core records. As for the speleothem data table, the ice core time series were saved in a joint data table. The proxy record time series are stored in a simple time-site data table. Only records having at least one sample measurement in the period from 1700 to 1800 CE are kept. Furthermore, I require that the records have to span at least 300 years. Additional ice cores would be available

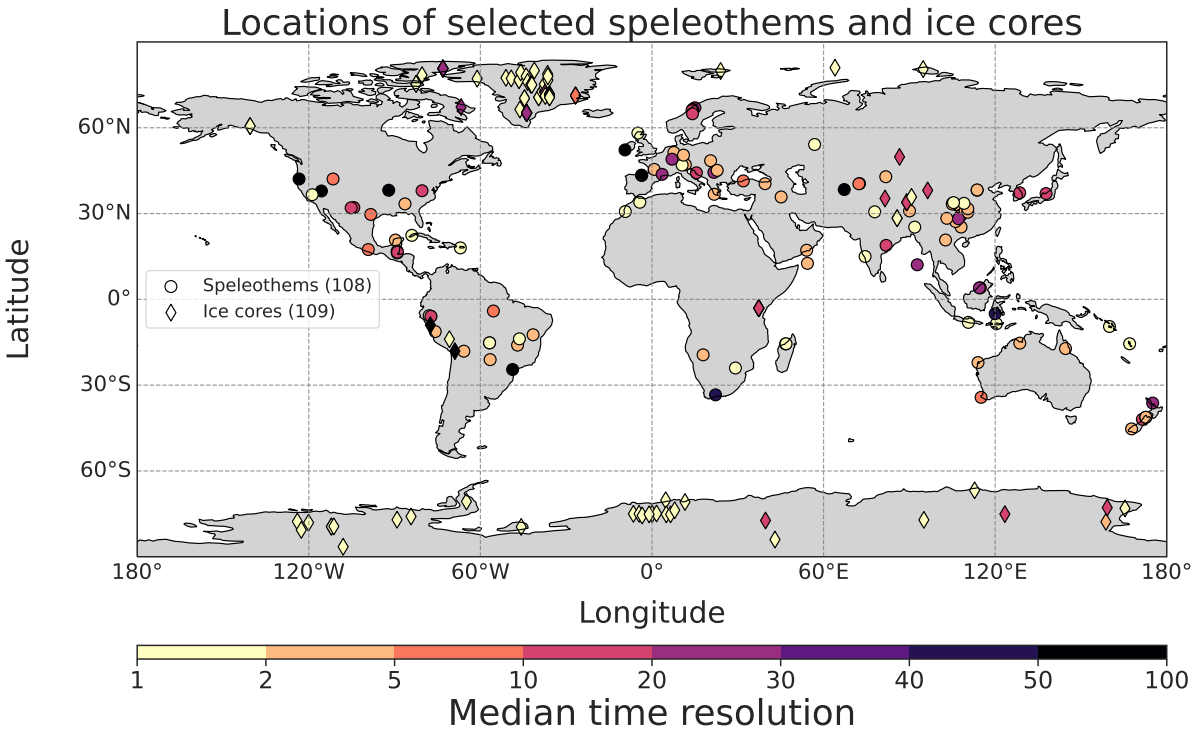

Figure 3.1: Locations of proxy records. Speleothem records from SISALv2 are marked with circles and ice core records with diamonds. The facecolors of the markers indicate the median resolution of each time series, which has been rounded to the next lowest resolution in a prescribed set of resolutions. The bins always include the left edge. The time resolutions are not spaced uniformly to better distinguish the resolutions of the high-resolution records .

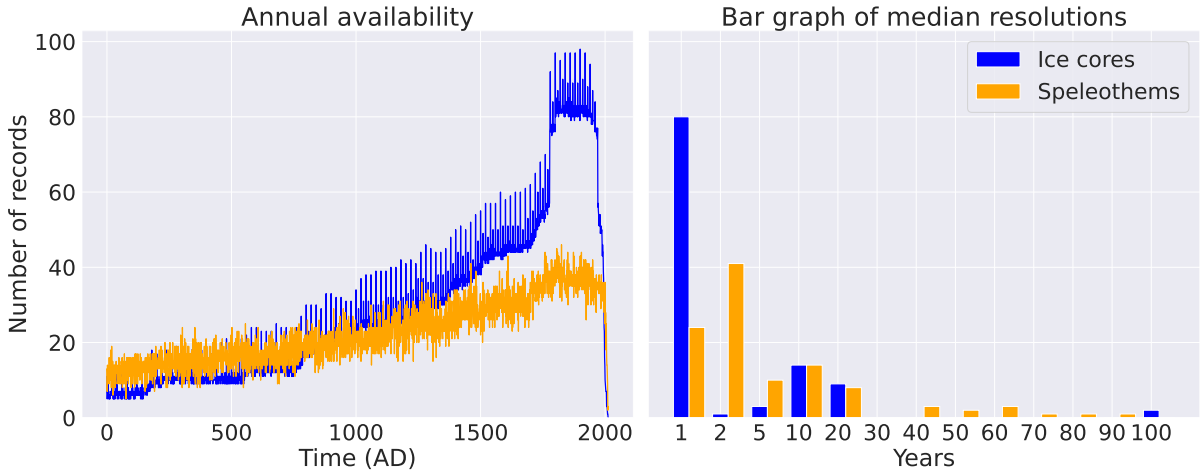

Figure 3.2: The left plot shows the annual availability of the speleothem and ice core record time series over the past two millennia. The comb-like form of the ice core curve stems from the ice cores which are resolved evenly with a 10- and 20-year resolution. The right plot shows the median resolutions as a bar plot.

from the end of the 18th century on, however for the annomaly reconstruction I chose to use longer records that span the entire 18th century. Record number 22 from Spitzbergen is dropped due to its extreme signal from -5 ‰ to -25‰ over the last millennium. This selection results in a final data table containing the time series for 109 sites. Metadata as the latitude, longitude, elevation and name of each site were also stored.
The ice core record locations and their median time resolution are plotted in Figure 3.1. The selection of ice core records is concentrated over Greenland and particular regions of Antarctica, especially around the region of 0° longitude. Furthermore, one record from Alaska, four from Nunavut (Canada) and three records from the Northeast Passage are available. Outside the polar regions, three records from the Andes, one from Mount Kilimanjaro and six records from central Asia and the Himalayas are part of the selection. A bar plot of the median time resolutions and the availability of records per year are plotted in Figure 3.2. The number of annualy available ice core records steadily increases from less than 20 in the first millennium to more than 80 in the 19th century before dropping in the 20th century. Most ice core records are of annual or (multi)-decadal resolution.

Chapter 4

Implementation of a Multi-Time scale and Multi-Archive PaleoDA framework

This chapter is dedicated to the concrete implementation of a PaleoDA framework which is adjusted to the data used for this thesis. The overall structure of the code is sketched in Figure 4.1. The code consists of two streamlines, one for preprocessing the model data (1., yellow) and one for preprocessing the proxy data (2., blue). Both are merged in the DA step (3., purple), which uses the Offline EnKF (see Section 2.6). In the first part of this chapter, proxy system models for converting simulated δ^{18}O into speleothem and ice core values, alternative calibrations, and the setting of observation uncertainty are outlined and discussed. The second part introduces the concept of *Pseudoproxy Experiments*. The third part is dedicated to possible enhancements of the reconstruction, namely the technique of augmenting the state vector and covariance localization and inflation. The fourth part presents how the PaleoDA algorithm is extended to perform reconstructions on multiple time scales. Finally, the methodological choices concerning the construction of the prior from one or multiple models, anomaly vs absolute value reconstruction, and a Monte Carlo technique are introduced. The code is publicly available in the repository github.com/mchoblet/paleoda, which also contains tutorials describing all configuration options.

4.1 Proxy System Models for speleothems and ice cores

This section corresponds to box 1.1 in Figure 4.1.

The first step of any kind of PSM consists of selecting the geographically nearest value in a simulated climate field with respect to the geographical location of a proxy. In the code, this is implemented as either taking the value of the nearest grid cell or computed via an inverse distance weighted mean using values and distances of the nearest four model grid cells.

The PSMs for speleothem and ice core δ^{18}O mainly follow the steps as outlined in Dee et al. (2015). The different steps of the PSMs are implemented in a way such that they can be turned on and off separately.
In terms of the general PSM framework outlined in Section 4.1.1, the *environment model* is performed already by the climate model, which simulates δ^{18}O given the external conditions as temperature, precipitation, pressure, and relative humidity (except for the height correction and infiltration/precipitation weighting). The *archive model* consists of the speleothem cave/ice core processes described in this section. An *observation model* would have to capture the dating

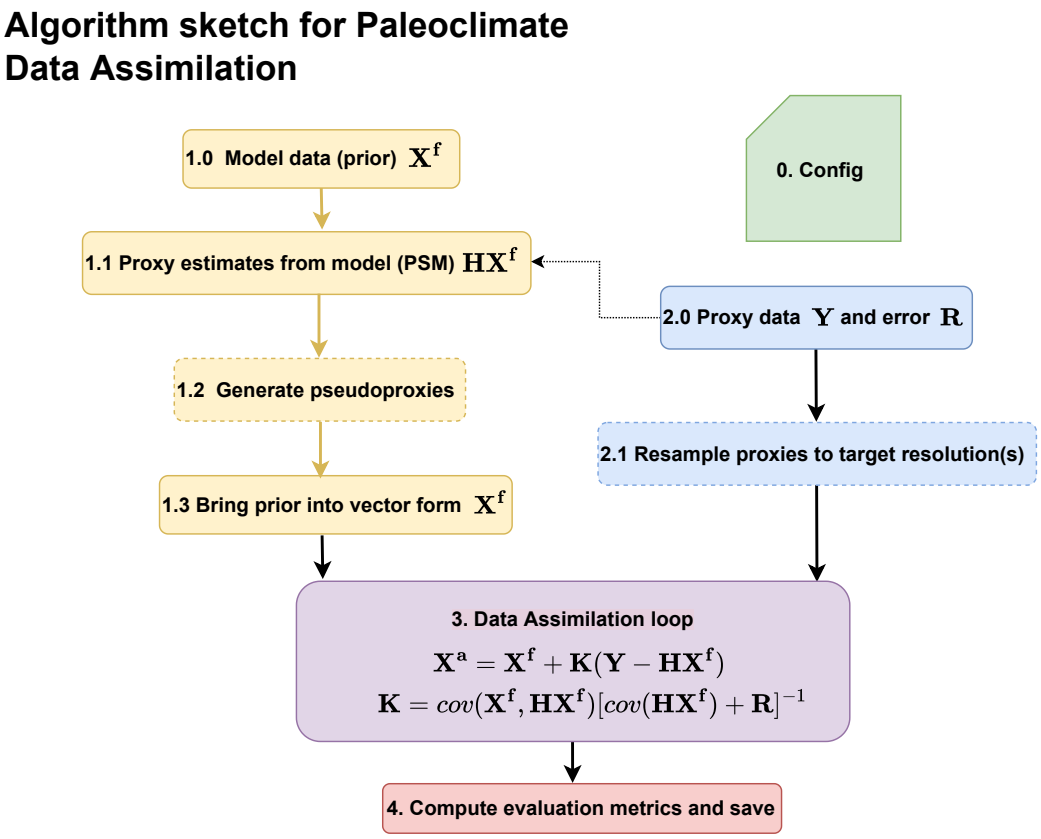

Figure 4.1: Algorithm sketch of the PaleoDA code. Dashed boxes indicate optional steps depending on the configuration and the dashed arrow indicates the input of PSM-relevant metadata. The numbers in the sketch are referred to in the text, although not all steps are explicitly outlined. A more detailed version containing more substeps can be found in Figure A.1.

and measurement uncertainties. This understanding of PSMs follows Dee et al. (2015), however where the boundaries between the compartments are drawn is a matter of definition. For instance, cave processes could also be attributed to the environment instead of the archive.
Dating uncertainty of the proxy records is not considered, because for the time period of the last two millennia studied in this project, the dating uncertainties are assumed to be relatively small. In addition, the multi-time scale DA approach outlined later will be less sensitive to inexact dating.

4.1.1 Speleothem δ^{18}O

For converting model δ^{18}O into the δ^{18}O signal recorded by calcite and aragonite speleothems the PDB-conversion, infiltration, height, karst-filtering and fractionation are described. For a comprehensive review of all processes affecting oxygen-isotope in speleothems see Lachniet (2009). Note, that the approach described here is different from Comas-Bru et al. (2019) and followed in Bühler et al. (2021), Bühler et al. (2022), and Ramos et al. (2022), where both model and proxy values are converted. The Kalman filter formalism requires the observation operator to capture all additional conversions of the prior values towards observation space.

PDB to SMOW conversion

Speleothem δ^{18}O is usually given in the PDB standard, whereas simulated precipitation water

is given in the SMOW standard. The conversion formula is found for instance in Coplen et al. (1983).

$$\delta^{18}\mathrm{O}_{\mathrm{PDB}} = \frac{\delta^{18}O_{\mathrm{SMOW}} - 30.91‰}{1.03091} \tag{4.1}$$

Infiltration/Precipitation weighting
For correctly representing $\delta^{18}\mathrm{O}_{\ prec}$ on an annual scale we can not simply compute the yearly mean $\delta^{18}\mathrm{O}$ from monthly values. The infiltration, denoted *inf*, which occurred each month needs to be accounted for. Thus a yearly mean based on the monthly infiltration is computed.

$$\delta^{18}\mathrm{O}' = \frac{\sum \mathrm{inf} \cdot \delta^{18}O_p}{\sum \mathrm{inf}} \tag{4.2}$$

The infiltration is computed as the difference of precipitation and evaporation.

$$\mathrm{inf} = \mathrm{precipitation} - \mathrm{evaporation} \tag{4.3}$$

In the case the evaporation from a model is not available (see table 3.1), the evaporation is approximated from the latent heat *LH*. The conversion equation states as follows (Allen et al., 2022).

$$\mathrm{evaporation} = \frac{\mathrm{LH}}{2.45\,\mathrm{MJ\,kg^{-1}}} \tag{4.4}$$

Latent heat is given in units of $\mathrm{MJ\,m^{-2}\,T^{-1}}$. Infiltration, precipitation, and evaporation need to be converted into a common unit for both to be comparable. I choose mm/month.
The calculation of weighted yearly mean in PaleoDA might be objected against because the observation operator $\mathcal{H}$ is supposed to act on the same prior state vector as the one that is assimilated. Here $\mathcal{H}$ acts on monthly values, although yearly means for instance for temperature, which are not weighted, are assimilated. This is an approximation, which is useful to decrease the influence of proxies which are biased towards specific months. An example are speleothem records from the South American Monsoon Region, which grow mostly during December, January and February. For a regional climate reconstruction of that region, it can make sense to explicitly assimilate seasonal climate means.

Height correction
The real topographical height at a cave location and the topographical height of the nearest climate model grid cell might differ considerably. Due to the height effect on the isotopic composition of precipitation, which is described by the isotopic lapse rate, the simulated $\delta^{18}\mathrm{O}$ value is biased. This bias can be corrected via a simple linear relationship to the height difference Δh and the isotopic lapse rate l which is usually given in $‰/100m$.

$$\delta^{18}\mathrm{O}_{\mathrm{height\ corrected}} = \delta^{18}\mathrm{O} - \Delta h \cdot l \tag{4.5}$$

The lapse rate might vary considerably regionally and unfortunately, the literature on this topic is sparse. Reasons for variability in the lapse rate might be local-scale climate, mountain geometry, and morphology Brian and Fan (2012). Here we assume a lapse rate of $-0.28‰/100m$ (Poage and Chamberlain, 2001). If temperature-dependent fractionation is to be considered, an environmental lapse rate of $-0.5\,K/100m$ is applied to the simulated temperature (Roedel and Wagner, 2017).

Karst Filter

The water which is infiltrating the soil above a cave does not drop into the cave directly as it first needs to pass the karst system. The karst storage effect for so-called drip water is a complex process, which can be simulated with an aquifer recharge model.
To that end, the incoming $\delta^{18}O$ signal is convolved with a Green's function g that depends on the time t and the mean transit time τ which is characteristic for that aquifer. It has the effect of a low pass filter which filters out short-term variability in the climate signal.

$$\delta^{18}O_{\text{after karst filter}} = g(t) * \delta^{18}O \tag{4.6}$$

The Green's function is defined as

$$g(t) = \begin{cases} \frac{1}{\tau} e^{-t/\tau}, & t > 0 \\ 0, & \text{otherwise} \end{cases} \tag{4.7}$$

The transit time can differ between different caves. For instance, Bunker cave in western Germany the transit time was found to be 3.4 years (Kluge et al., 2010), whereas for Villars cave in central France up to 11.1 years, depending on the location in the cave, were estimated (Jean-Baptiste et al., 2019). Nonetheless, transit times are not available for most caves. Bühler et al. (2022) have shown that 2.5 years can be used as a global value for the transit time.

Fractionation

Finally, the effect of isotopic fractionation between water and calcite/aragonite is simulated. Equilibrium isotopic fractionation is defined by the the fractionation factor α, which is calculated via the involved isotopic ratios $\delta_{A/B}$ for the involved phases.

$$\alpha_{A-B} = \frac{1000 + \delta_A}{1000 + \delta_B} \tag{4.8}$$

$$\Rightarrow \alpha_{A-B} \cdot (1000 + \delta_B) - 1000 = \delta_A \tag{4.9}$$

Fractionation is a temperature-dependent process which needs to be empirically quantified for the type of karst mineralogies involved (Calcite and Aragonite). Many formulas have been inferred from both lab-grown and real cave-speleothems. While labs can test a larger temperature range, they still pose an artificial environment. The differences between the fractionation formulas, in comparison to the effect introduced by model biases in simulated $\delta^{18}O$, is small. A comparison which formula suits the model and speleothem data best thus remains inconclusive. I chose to use the formulas that are recommended by the SISAL working group in Comas-Bru et al. (2019).
Fractionation factors are usually given in their logarithmic form. As the fractionation temperature the simulated annual mean temperature nearest to the cave location is chosen. In the PaleoDA code, optionally also the mean simulation temperature instead of the varying temperature can be set, such that a model bias is corrected, but the covariance to other grid cells in the Kalman gain is not affected.
For calcite I use the formula from Tremaine et al. (2011):

$$ln(\alpha) = \frac{16.10(10^3 T^{-1}) - 24.6}{1000}, \tag{4.10}$$

and for aragonite the formula from Grossman and Ku (1986) as reformulated in Lachniet (2015):

$$ln(\alpha) = \frac{18.34(10^3 T^{-1}) - 31.954}{1000}. \tag{4.11}$$

For calcite, this results in the final fractionation formula

$$\delta^{18}\mathrm{O}_{\text{after fractionation}} = (\delta^{18}\mathrm{O} + 1000) \cdot \exp(16.1/T - 24.6/1000) - 1000. \tag{4.12}$$

This formula is structurally the same as used in Dee et al. (2015) and originally proposed in Wackerbarth et al. (2012), with the difference that the PDB to SMOW standard conversion has already been performed in the first step.

4.1.2 Ice core δ^{18}O

As for the speleothem PSM I follow the PRYSM publication (Dee et al., 2015) for δ^{18}O captured by ice cores from climate model δ^{18}O . PRYSM and its publicly available python package summarize the extensive previous research that hat been undergone to understand the climate signal captured by ice cores, especially with respect to the complex processes of firn diffusion and ice core compaction. I only present the formulas for the main mechanisms. All equations can be found in Section 3.1 of Dee et al. (2015). This PSM has been used in PaleoDA studies as Steiger et al. (2017) and Zhu et al. (2020). Recently, a different PSM that also accounts for precipitation intermittency during the year has been proposed by Casado et al. (2020).

Precipitation weighting
As for speleothems, $\delta^{18}\mathrm{O}_{\,prec}$ can be computed as an annual mean by taking into account how much water has precipitated in each month. In contrast to the cave locations, evaporation is assumed to be small in comparison to precipitation and therefore not considered.

$$\delta^{18}\mathrm{O}' = \frac{\sum \mathrm{prec} \cdot \delta^{18}O_p}{\sum \mathrm{prec}} \tag{4.13}$$

Height correction
The same isotopic lapse rate as for speleothems is applied. This effect is more relevant for ice cores than for speleothems, as more of them are found in extreme locations (for instance in the Himalaya in Asia).

Compaction and Diffusion
The archive model of the ice core PSM consists of simulating the effects of compaction and diffusion. Compaction is simulated using the mean annual temperature and snow accumulation rate, based on the yearly precipitation. However, as stated by the PRYSM authors this effect will be negligible for short time scales as the last centuries. A depth-age profile is established by converting the initially even spacing in time of the original time series into depth spacing. *Diffusion* affects how the external climate signal is transferred down an ice core, which is a process that varies over depth according to local diffusivity. The diffused isotopic signal is simulated as a convolution with a gaussian kernel G

$$\delta^{18}\mathrm{O}_{diff} = G * \delta^{18}\mathrm{O} \tag{4.14}$$

where the kernel with standard deviation/diffusion length σ is

$$G = \begin{cases} \frac{1}{\sigma\sqrt{2\pi}} e^{\frac{-z^2}{2\sigma^2}}, & t > 0 \\ 0, & \text{otherwise} \end{cases} \tag{4.15}$$

The PRYSM authors propose not simplifying the calculation by assuming σ as constant but computing it step-wise given the local diffusion length at each depth, which depends on temperature and density. As this calculation also requires an estimate for the diffusivity of water

vapour, ambient pressure is another required variable for the ice core PSM. As sea level pressure is available only for two out of five simulations, and the effect of varying pressure is negligible in the context of PaleoDA for the last millennium, I decided to use the fixed average sea level pressure of 1013.25 millibars.

4.1.3 Pre-assessment of the speleothem and ice core PSM

Understanding the climate proxies that are to be assimilated is a crucial requisite for PaleoDA. This means knowing how to relate a simulated climate signal to the one observed in a climate archive. Many existing PaleoDA call for better PSMs to improve the reconstructions, because often simple linear regressions as presented in the next chapter are used. In my project the assimilated climate variable, δ^{18}O , is already available in the simulations. In this section, I discuss to what extent more comprehensive PSMs are meaningful when δ^{18}O is already available.
In offline PaleoDA, the aim of the PSM is to be provided an ensemble range of simulated values for each observation, which is characterised by its mean and standard deviation due to the assumption of normality underlying the Kalman Filter. As the prior ensemble is static, it is not important to match the true climate signal in time. PSM components as the karst filter or firn diffusion are not affecting the mean value of this range of values, hence they have no effect on the innovation part of the Kalman equations. Still, they are likely to act as low-pass filters and suppress short-term variability and hence the standard deviation of the range of values provided by the model simulation. This is relevant in the sense that it a) reduces the prior standard deviation (uncertainty) provided by the model and b) might affect the covariance relationship of the observation estimates to the other grid cells. Furthermore, an infiltration/precipitation weighted yearly mean for δ^{18}O will covary less with the regular annual mean for temperature and precipitation. Hence the effect of a proxy in the DA is reduced. A similar effect is expected when simulating karst fractionation, where the δ^{18}O variable is mixed with the time-varying annual mean temperature. However, this covariance decrease can be avoided by using one constant mean annual temperature. The choice of PSM thus also affects how much an observation influences the overall reconstruction. A lowered influence can be considered more realistic, although then the reconstruction might rely strongly on the (static) prior simulation. The question of how the reconstructions and underlying covariance patterns are affected by PSM choices is not properly addressed in existing PaleoDA literature. Some publications, as Dee et al. (2016) and Steiger et al. (2017) touch upon the issue by plotting how the mean covariance-distance relationship is changed for different PSMs.
A way to avoid this issue at first is to assimilate proxy record and model anomalies and not use PSM parts that alter the covariance structure. This will be discussed in Section 4.8, where the concept of assimilating anomalies instead of mean values is presented.

4.1.4 Calibration via linear regressions (Statistical PSM)

An alternative to the physics based PSM described in the previous sections is the so called statistical PSM. It can be applied to all types of different climate archives and can thus be considered an all-purpose weapon. In my project, it was also considered to use it, but rejected due to the considerations that are outlined in this section. The idea is to calibrate the proxy records to an instrumental dataset via a linear regression, most often performed with temperature over the 20th century. This approach has been performed used in the LMR (Hakim et al., 2016; Tardif et al., 2019) and in PHYDA (Steiger et al., 2018) which are mainly based on tree ring proxy records. In a first step, each proxy record p_i is regressed on the nearest available instrumentally measured variables X_i (e.g. temperature). An often used calibration temperature dataset is the Berkeley Earth observational temperature dataset (Rohde and Hausfather, 2020). Proxy records and instrumental data are converted into anomalies with respect to a shared time

period.

$$p_i = \alpha_i + \beta_i X_i + \epsilon_i \tag{4.16}$$

α_i and β_i are the resulting regression parameters and ϵ is the residual. The regression parameters from the calibration period can then be used for the statistical PSM on other time periods, where the same linear relationship is assumed to hold: $\mathcal{H}(\mathbf{X}_i^f) = \alpha_i + \beta_i \mathbf{X}_i^f$. The square of the residual is taken as the proxy error: $\mathbf{R}_i = \epsilon_i^2$.
For the data of this project, only ice cores qualify for the statistical PSM. Speleothem growth is irregular and for the relatively short instrumental period not enough data points would be available to compute a meaningful linear regression.
In the PaleoDA instrumental period reconstruction by Steiger et al. (2017), the authors compared the assimilation of ice core δ^{18}O via the PRYSM ice core PSM described in Section 4.1.2 and the statistical PSM which uses the simulated temperature instead of δ^{18}O . In spite of this "variable detour", they found the statistical PSM to be better suited according to global error metrics. However, I do not think this conclusion is useful for this thesis for three reasons.

- In the instrumental Berkeley Earth dataset, temperatures at the poles are only present from the year 1956 A.D on. The linear calibration is based on few values.
- Linear regression over that short time period is difficult due to non-climatic noise present in the records, which leads to small regression slopes.
- The regional mean temperature reconstructions in Steiger et al. (2017) seem to be almost not affected by the proxy records (compare Figure 12 and 14 of the publication).

To demonstrate the implications of the statistical PSM, in Figure 4.2 the regression slopes, residuals, and resulting Kalman gains are shown. Most ice cores have regression slopes close to zero and far below the spatial slope empirically found for specific regions, as $0.67 \pm 0.02‰ ^\circ C^{-1}$ for Greenland (Johnsen et al., 1989). However, in the Kalman Filter the regression slope is not used directly, but weighted relatively to the observation error variance. A large regression slope a only leads to a large Kalman Gain if the residual ϵ is small:

$$\mathbf{K} = \frac{cov(\mathbf{X}^f, \mathcal{H}(\mathbf{X}^f))}{cov(\mathcal{H}(\mathbf{X}^f), \mathcal{H}(\mathbf{X}^f)) + R} = \frac{a \cdot cov(\mathbf{T}^f, \mathbf{T}^f)}{a^2 \cdot cov(\mathbf{T}_i^f, \mathbf{T}_i^f) + \epsilon_i^2} \tag{4.17}$$

Conversely, also small regression slopes can lead to large Kalman gains. Both effects can be seen in the right panel of Figure 4.2.
Although the trend of larger Kalman gains for proxy records with larger slopes is recognisable, also proxy records with regression slopes close to zero have large Kalman gains and thus influence the reconstruction more than other proxy records. The resulting Kalman gains go up to four, meaning that a positive δ^{18}O anomaly of one in an ice core proxy record is converted to a local 4K temperature increase in the DA. Some records even have negative regression slopes and thus negative local Kalman gains, which is physically unplausible. Due to this inconclusive situation, I chose not to use the statistical PSM for ice cores. The statistical PSM might become a viable option when at a later stage climate archives with a more conclusive correlation to instrumental temperature data are incorporated.

4.2 Observation error variance

This section corresponds to box 2.0 in Figure 4.1.

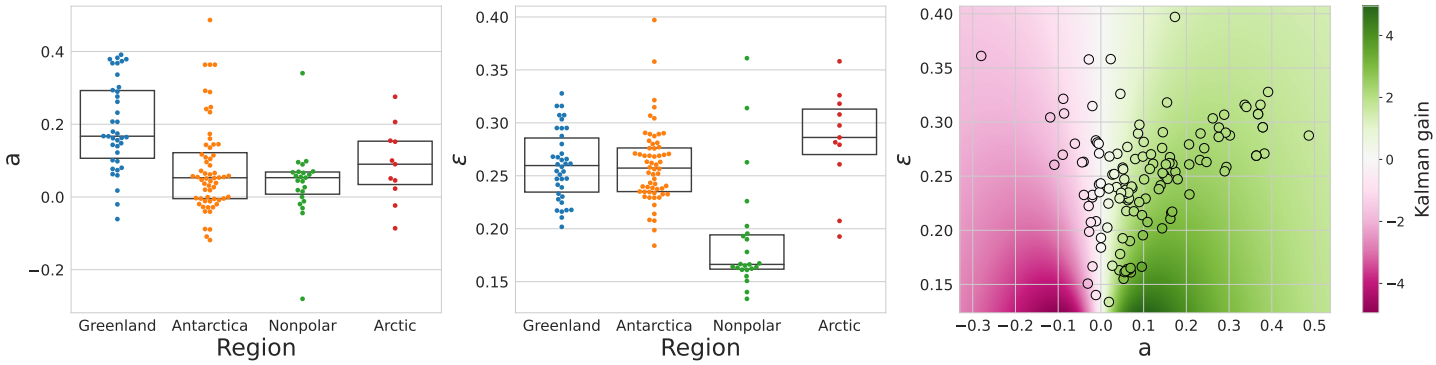

Figure 4.2: In the left panel the regression slopes for the Iso2k ice cores from different regions with the Berkeley Earth dataset is shown. The central panel shows the corresponding residuals. The resulting Kalman gain in case of an annual temperature variance of 1.5K^2 is shown as a function of regression slope and error.

In DA, one central number is the uncertainty estimate associated with an observation. In the Kalman Filter, the uncertainty covariance matrix $\mathbf{R}$ serves for weighting the covariance between the prior field and the observation estimates. In PaleoDA the proxy uncertainties have been defined in different ways. Studies using the statistical PSM, e.g. Steiger et al. (2018) and Tardif et al. (2019) assume the regression residual to capture all uncertainties, whereas in studies based on absolute values, e.g. Steiger et al. (2017) the instrumental measurement uncertainty was defined equally for all records. Okazaki and Yoshimura (2017) and Shoji et al. (2022) chose a proxy error which corresponds to a fixed signal-to-noise variance (see the next section 4.3). In tree ring based reconstructions for the second half of the last millennium Franke et al. (2017), Franke et al. (2020), and Valler et al. (2019) introduce a spatial representativeness error which takes into account that the natural variability in the area of a model grid cell. This idea has also been used in a reconstruction for the deglaciation over Greenland (Badgeley et al., 2020). Adding more errors automatically decreases the influence of climate proxies on the reconstruction.
The LGM reconstruction by Tierney et al. (2020) and LGM to Holocene reconstruction by Osman et al. (2021) found that the proxy uncertainties provided by the employed marine sediment PSMs were too large. The authors then resorted to dividing the proxy errors by a post-hoc factor, which they determined via the calibration to proxy data that was not included in the DA, to give more weight to the proxies.
These different examples show, that the observation uncertainty $\mathbf{R}$ is a rather unconstrained value in PaleoDA. The PaleoDA code allows setting different proxy errors and testing the sensitivity of the reconstruction to these values. The ambiguity of choosing the right proxy record error gets more complicated when expanding the method to multiple time steps. Should other proxy record uncertainties be chosen when the records represents a multi-year average instead of an annual average?
The observation error is related to the fundamental topic of estimating how much signal-to-noise is contained in a proxy signal, an area of active research which is also relevant for the next section 4.3 about pseudoproxy experiments.

4.3 Pseudoproxy experiments

This section corresponds to box 1.2 in Figure 4.1.

A useful tool for testing the theoretical performance of a PaleoDA reconstruction prior to using real data are so-called Pseudoproxy Experiments (PPE). The concept, which was initially

proposed in Mann and Rutherford (2002) and comprehensively reviewed in Smerdon (2012) consists of creating artificial observational data with noise from climate model simulations for specific locations. PPEs enable exploring the effects of uncertainties and spatial and temporal sampling of a proxy network on CFRs.
In PPEs, the true state from which the observations and the prior are sampled is known. The conditions of PPEs can be considered optimal, because the distribution from which the measurements and the prior are sampled is the same. The assumption of unbiasedness of the mean values and the covariance patterns holds. Thus, the reconstruction skill can be quantified with respect to the true state with common error metrics (Section 4.3.1). They are also useful when the model from which pseudoproxy records are generated from is different to the one that is used as a prior. This setup enables studying the effect of model biases, both in the mean state and the covariance pattern.
The proxy record time series after adding noise are characterized by their signal-to-noise ratio (SNR). The SNR is defined as the ratio of standard deviations of the true time series $\mathbf{T}$ and the noise time series $\mathbf{N}$ (Smerdon, 2012).

$$\mathrm{SNR} = \sqrt{\frac{\mathrm{var}(\mathbf{T})}{\mathrm{var}(\mathbf{N})}} \tag{4.18}$$

In the case of uncorrelated noise and signal, the SNR is related to the correlation r between the noise time series $\mathbf{T} + \mathbf{N}$ through the following equation.

$$\mathrm{SNR} = \frac{r}{\sqrt{1 - r^2}} \tag{4.19}$$

Most PaleoDA studies using pseudoproxies add white noise, which is also the standard assumed in my experiments. Although this is the standard procedure in PaleoDA, real proxies are considered to have more complex noise structures that change the spectral characteristics of the proxy signal. An alternative would be assuming red noise as also performed in Steiger et al. (2014). However, in offline DA the state estimates and errors are not influenced by each other, such that I chose to only test white noise.
For performing PPEs the SNR value for proxy records needs to be fixed, such that a random noise time series fulfilling equation 4.18 can be generated. The variance of the noise then corresponds to the proxy record error. The SNR contained in different types of climate archives is an area of active research. Many PaleoDA studies performing PPEs refer to Wang et al. (2014) for setting an SNR of 0.45 as a realistic value, although this study mostly studied tree rings which are calibrated on instrumental data. Rehfeld et al. (2018) and Reschke et al. (2019) studied the signal content of temperature proxy records on millennial time scales resulting in SNRs ranging from 0.05 to 0.5. In a recent model-data comparison for speleothems in the Amazon region over the last millennium, Orrison et al. (2022) found that an SNR of 0.5 underestimates the signal content of speleothems.

4.3.1 Evaluation metrics for pseudoproxy experiments

In the following, evaluation metrics commonly used for evaluating reconstructed time series $\hat{x}_i$ consisting of $i \, \epsilon \, [1, \ldots n]$ data points are defined. The metrics can be applied for PPEs, where the true target timeseries x_i is precisely known. They can either be computed for each grid cell and then be plotted as maps, or be averaged globally to summarize the skill of a reconstruction to one single value. A more comprehensive discussion of these metrics can be found in Cook et al. (1994). Except for the correlation no significance testing can be performed. In the following temporal means are denoted by overbars.

Pearson correlation (Corr)
The correlation captures how well the reconstructed and true signal covary. The covariance is weighted by the variances of the two individual signals.

$$\text{Corr} = \frac{\sum_{i=1}^{n}[(\hat{x}_i - \overline{\hat{x}})(x_i - \overline{x})]^2}{\sum_{i=1}^{n}(\hat{x}_i - \overline{\hat{x}})^2 \sum_{i=1}^{n}(x_i - \overline{x})^2} \tag{4.20}$$

The correlation spans the values -1 to 1. It effectively measures the phase coincidence of reconstructed and true time series which is better for values close to 1. It is not affected by biases in the mean value. Sometimes the correlation is also given in terms of its squared value r^2 which then spans from 0 to 1.

Root mean square error (RMSE)
The root mean square value computes the mean squared error between true and reconstructed time series and it thus defined as

$$\text{RMSE} = \sqrt{\frac{\sum_{i=1}^{n}(\hat{x}_i - x_i)^2}{n}}. \tag{4.21}$$

The RMSE can take values from 0 to ∞. Low values indicate better reconstruction skill. The RMSE is a very common tool in climate model evaluation. Another closely related error function is the mean absolute error, which calculates the mean of the absolute difference between reconstruction and truth.

Coefficient of efficiency (CE)
The CE is a metric which derives from the RMSE, but also takes into account the variance of the true time series. It is defined as

$$\text{CE} = 1 - \frac{\sum_{i=1}^{n}(\hat{x}_i - x_i)^2}{\sum_{i=1}^{n}(x_i - \overline{x})^2} \tag{4.22}$$

The coefficient of efficiency takes values from $-\infty$ to 1. Values larger than zero are interpreted as skill, because then the RMSE is truly small in comparison to the variance of the true signal. The CE value thus rewards a closer phase, amplitude and mean value in the reconstruction.

Reduction of error (RE)
A metric similar to the CE is the reduction of error. It aims to describe if a reconstruction is better than the mean climatology provided by the prior x_p.

$$\text{RE} = 1 - \frac{\sum_{i=1}^{n}(\hat{x}_i - x_i)^2}{\sum_{i=1}^{n}(x_i - \overline{x_p})^2} \tag{4.23}$$

Like the CE, the RE can take values from $-\infty$ to 1. The reconstruction is better than the uninformed mean climatology if the RE is larger than zero. Note, that if the prior and the truth are generated from the same climate model, RE and CE are equal. This score is relevant when using a different climate model as data assimilation targets and priors.

4.4 Enhancements for the PaleoDA reconstruction

The steps explained are performed on the prior state vector, and thus correspond to box 1.3 in Figure 4.1.

4.4.1 Augmenting the state vector

The iterative application of the Kalman Filter requires applying the observation operator $\mathcal{H}$ at every time step. In the offline approach, the renewed application of the observation operator is not necessary, because the ensemble of prior observation estimates is calculated once in the beginning and reused at each time step. However, this is not the case for the multi-time scale approach described in Section 4.5. To avoid a renewed application of the observation operator, the observation estimates are appended to the state vector. This is called *augmenting the state vector* in DA. As is shown below, this approach is mathematically valid for linear observation operators. The augmented state vector technique can be used when the aim is to reconstruct only the global mean temperature. An estimate of global mean temperatures can be assimilated directly instead of assimilating full climate fields. The decreased state vector size results in less costly computations[1]. Note the two following caveats. Primarily, the assimilated global mean value and the mean from the assimilated field will be different if covariance localization (see Section 4.4.2), is applied. Second, the observation operator as applied in Ensemble Kalman Filters is often not linear, and hence using the assimilated observation estimates is an approximation.

Theorem 3. Assimilating a value that can be computed via a linear operator $\mathbf{A}$ from the prior state vector $\mathbf{X}^f$ is equivalent to computing this value from the assimilated, posterior state vector $\mathbf{X}$.

Proof
$\mathbf{A}$ is applied to the assimilated state vector obtained via the Ensemble Kalman filter equation. The crux is using the linearity of the covariance and $\mathbf{A}$ operator.

$$\mathbf{AX} = \mathbf{A}(\mathbf{X}^f + \mathbf{K}(\mathbf{y} - \mathbf{HX}^f) \tag{4.24}$$

$$= \mathbf{AX}^f + \mathbf{A}\text{cov}(\mathbf{X}^f, \mathbf{HX}^f)\left[\frac{\mathcal{H}\mathbf{X}'^f(\mathbf{HX}'^f)^T}{N_e - 1} + \mathbf{R}\right]^{-1}(\mathbf{y} - \mathbf{HX}^f) \tag{4.25}$$

$$= \mathbf{AX}^f + \text{cov}(\mathbf{AX}^f, \mathbf{HX}^f)\left[\frac{\mathcal{H}\mathbf{X}'^f(\mathbf{HX}'^f)^T}{N_e - 1} + \mathbf{R}\right]^{-1}(\mathbf{y} - \mathbf{HX}^f) \tag{4.26}$$

This last equation is equal to the case, in which $\mathbf{A}$ is applied to the state vector before the assimilation, the observation estimates are unaffected by $\mathbf{A}$ because $\mathbf{A}\mathcal{H}\mathbf{X}^f = \mathcal{H}\mathbf{X}^f$[2].
Exactly the same holds for the perturbation Kalman gain from equation 2.51, and for the posterior error covariance 2.17 because of the linearity of the covariance.

Corollary
Directly assimilating the global mean value (for instance of temperature) is equivalent to assimilating the whole climate field and then computing the global mean.

Proof Assume the gridded climate field $\mathbf{T}$ is described by a matrix $\mathbf{T}_{ij}$. The index i denotes the central latitude and the index j the central longitude of each grid box.
The global mean GM for this field can be calculated by taking into account the latitudinal average weights $\mathbf{w}_i$ and the total number of grid cells.

$$\text{GM}(\mathbf{T}) = \frac{1}{N_{lats} \cdot N_{lons}} \sum_{i}^{N_{lats}} \mathbf{w}_i \sum_{j}^{N_{lons}} \mathbf{T}_{ij} \tag{4.27}$$

[1] The prior observation estimates still need to be assimilated for the innovation part of the Kalman Filter equation.

[2] Strictly speaking, the state vectors in both approaches are not equal because in one case the state vector is the augmented state vector. This is only a notational formality omitted here for the sake of brevity.

The summation is a linear operator, thus calculating the global mean is also a linear operation and theorem 3 applies. It becomes even clearer if the climate field is flattened and written as a simple vector with $N_{lats} \cdot N_{lons}$ entries. Then, the global mean can be written as a vector $\mathbf{A}$ of shape $1 \cdot (N_{lats} \cdot N_{lons})$ where each entry is equal to the appropriate latitudinal weight divided by the total number of grid boxes.

4.4.2 Covariance localization

A popular technique to enhance the Ensemble Kalman Filter is covariance localization. It can be used as an option in the PaleoDA code developed for this thesis. Covariance localization addresses the issue of spurious covariances provided by the prior, which are long-ranging correlations between the prior field and the observation locations. If they are considered to be erroneous, they should not influence the reconstruction. The covariance matrix $\mathbf{P}^f$ in the EnKF is multiplied by a localization matrix $\mathbf{L}$ which takes into account the geographical distance between locations on earth. $\mathbf{L}$ has the purpose of dampening long-ranging correlations. For creating the localization matrix, typically a Gaspari-Cohn decorrelation function of fifth order is used (Gaspari and Cohn, 1999) (p.748). It has a cut-off radius after which the function is set to zero and is isotropic, meaning that correlations are treated equally in all directions. The multiplication of $\mathbf{P}^f$ and $\mathbf{L}$ is performed element-wise (a Hadamard/Schur product), which is denoted by a $\circ$ in the Kalman gain formulation.

$$\mathbf{K} = \mathbf{L} \circ \mathbf{P}^f \mathcal{H}^T (\mathcal{H}(\mathbf{L} \circ \mathcal{P}^f)\mathcal{H}^T + \mathbf{R})^{-1} \tag{4.28}$$

Application in different EnKFs

Most EnKF variants never calculate the explicit prior covariance matrix for efficiency reasons, which is a problem for the application of covariance localization. It can be used directly in the EnSRF with serial observation treatment (Whitaker and Hamill, 2002) and has been used this way in various PaleoDA studies, e.g.Hakim et al. (2016) and Tardif et al. (2019). As shown in Section 2.5 this method is orders of magnitude slower than assimilating all observations at once. The serial EnSRF is prone to instabilities when combined with covariance localization (Nerger, 2015). Tierney et al. (2020) optimized the implementation of covariance localization by using the EnSRF (PaleoDA version) (see Section 2.4.3) in combination with two separate localisation matrices, one for $\mathbf{P}^f \mathcal{H}^T$ and one for the observation estimates in $\mathcal{H}\mathbf{P}^f \mathcal{H}^T$. This type of covariance localization is the method implemented for this thesis, which is slower than the unlocalized EnKFs because of additional calculations of the Hadamard product[3]. Another way to use covariance localization is to employ the stochastic EnKF with perturbed observations (Section 2.4.1), where $\mathbf{P}^f$ appears in the equations. The ETKF and ESTKF can not be localized directly. Ott et al. (2004) developed an alternative implementation with serial observation treatment which allows for localization. See Okazaki et al. (2021) for an application of the localized ETKF in PaleoDA.

Localization radius

The central parameter of the Gaspari-Cohn decorrelation function is the *localisation radius*, after which the covariance is set to zero. This radius is an arbitrary value which requires empirical justification. It can be set in the PaleoDA code configuration of this thesis. PaleoDA studies defined a localization radius via the comparison of reconstructions with varying localization radii to instrumental data (Tardif et al., 2019) or external proxy data (Osman et al., 2021; Tierney et al., 2020). They found very large radii between 12,000 and 25,000 km to be optimal. Valler et al. (2019) hypothesised that zonal atmosphere correlation lengths should be larger

[3] In combination with the regular matrix product, the Hadamard product is not associative and commutative. In the context of localization in the Ensemble Kalman Filter this has been studied by Petrie (2008), where the approximation of associativity and commutativity, which would improve efficiency, has proven to be inadequate.

than meridional ones and applied a non-isotropical decorrelation function with two different radii, but did not find improvements.

Arguments against covariance localization
The authors of PHYDA argue against using covariance localization, because of little gains, additional justification needed for the localisation radius and the fact that in offline DA ensemble sizes can be selected large enough to avoid spurious correlations[4]. In Parsons et al. (2021) different localization radii have been tested for PPEs with different climate models and it was found that the reconstruction skill is best for either a very long localization radius or not using localization at all. They found the use of multi-model-ensembles (see Section 4.7) to be a more robust way to limit teleconnections.

4.4.3 Covariance inflation

Another method used to enhance DA is covariance inflation (Vetra-Carvalho et al., 2018). In numerical weather prediction, it is common that the prior ensemble has too little prior uncertainty due to the posterior uncertainty being reduced in each DA step, especially for small ensemble sizes. As a consequence, new observations do not influence the estimate any longer. Covariance inflation circumvents this problem by inflating the prior covariance (uncertainty) of the ensemble members, for instance via a multiplicative factor m for each ensemble member $\mathbf{X}_i$: $\mathbf{X}_i = m(\mathbf{X}_i - \overline{\mathbf{X}}) + \overline{\mathbf{X}}$. This results in an inflated posterior uncertainty, such that observations can again influence the estimates. For the offline DA approach, where the prior estimate is not cycled in time and the same prior is used in each time step, this approach is not meaningful. To the best of my knowledge, it has not been applied in PaleoDA.

4.5 Multi-time scale PaleoDA

This section is related to box 2.1, 1.3 and 3 in Figure 4.1.

The basic PaleoDA algorithm assimilates proxy record data at a fixed time step. The aim of my thesis is to incorporate speleothem and ice core climate archives. Chiefly in the case of speleothems, these types of archives do not provide annual means, but a filtered signal that captures the mean climate conditions over a multitude of years. For speleothems from SISALv2, most chronologies have median time resolutions of multiple years. Apart from annual ice cores, Iso2k also contains decadally and centennially dated ice core records. (see Figure 3.2). It is not adequate to treat this kind of proxy record data as annual means as the usual PaleoDA algorithm assumes. A simple approach to circumvent this problem consists of binning the data for multiple years, and reconstructing the climate with the resolution of these bins. This approach has been used in the LGM to Holocene reconstructions by Osman et al. (2021), where a 200 year binning has been chosen due to the low resolution of the marine sediment proxies they assimilated. For the last millennium, both high- and low-resolution proxy records are available. However, the LMR and PHYDA rely solely on annual proxies. The annual PaleoDA algorithm of these projects also have the characteristic of producing reconstructions with low multidecadal and centennial variability in comparison to other CFR techniques (Neukom et al., 2019a) (see Figure 1 of that publication). The shortcomings of the annual algorithm have been acknowledged by Steiger and Hakim (2016). Steiger and Hakim proposed an extension of the algorithm to enable multi-time scale reconstructions. In the following, I present and discuss this approach, named SH-2016, and a recent adaptation in Erb et al. (2022), named Erb-2022, before describing the adaptation I have implemented for this thesis in the next section.

[4]Originally, covariance localization was designed for numerical weather prediction, where the DA is performed online with a small number of ensemble members (≈ 10)

$$\mathbf{X}^f = \begin{pmatrix} \mathbf{X}_{120} \\ \mathbf{X}_{50} \\ \dots \\ \mathbf{X}_{930} \end{pmatrix} \Rightarrow \overbrace{\begin{pmatrix} \mathbf{X}_{120} & \mathbf{X}_{121} & \dots & \mathbf{X}_{120+bs} \\ \mathbf{X}_{50} & \mathbf{X}_{51} & \dots & \mathbf{X}_{50+bs} \\ \dots & \dots & \dots & \dots \\ \mathbf{X}_{930} & \mathbf{X}_{931} & \dots & \mathbf{X}_{931+bs} \end{pmatrix}}^{\text{block size}} \Big\} N_y \text{ ensemble members}$$

Figure 4.3: Illustration of how the previously assumed prior state estimation vector, consisting of a random collection of climate fields, is extended into a matrix form which also contains the subsequent years. Each $\mathbf{X}_i$ corresponds to the mean climate field of one simulation year, the index denotes the year of the simulation. The $\mathbf{X}_i$ could also be depicted explicitly as a vector, thus rendering the matrix three-dimensional. In the multi-time scale DA, rows of the matrix are averaged over several years in order to assimilate multiyear means.

4.5.1 The SH-2016 multi-time scale DA algorithm

The essence lies in extending the annual prior state vector, which in Offline DA consists of a random selection of simulation years to a prior state matrix, in which also the subsequent years to these climate states are stored. This idea is depicted in Figure 4.3. With that prior matrix, multi-year means can be assimilated instead of only annual means. SH-2016 propose that each proxy record can be assimilated at its own temporal resolution. Thus, the proxy records only add information on appropriate time-scales to the reconstruction. The key assumption is that a low-resolution proxy record represents the climate state mean over n years centred on its dating points. The concept of serial proxy assimilation, presented in Section 2.3 is used. Each proxy record is assimilated one after another, updating the n-year mean which is calculated from the rows of the prior matrix. This also requires calculating prior observation estimates $\mathcal{H}(\mathbf{X})$ averaged over these years. After the assimilation of each n-year mean, the anomalies from this mean are added back. The algorithm also offers the advantage, that the covariances in the Kalman gains are computed from the multi-year averages instead of the annual means, thus being *time scale appropriate*. Depending on the climate model simulation, the covariance structure can be different on longer time scales. SH-2016 found an improved representation of longer-than-annual variability in the reconstruction for PPEs.

Limitations

The main problem of SH-2016 is the slowness of the algorithm. Serial proxy assimilation, paired with repeated mean-anomaly decompositions of the prior matrix is very slow. To reduce the computational cost SH-2016 only demonstrated their algorithm with pseudoproxies for the global mean temperature and the AMOC index. Furthermore, the size of the prior state matrix is limited with respect to the number of consecutive years it can contain (length in x-direction). For each proxy to be assimilated freely at its respective time scale, the matrix would need to have as many columns as there are years to reconstruct. However, when only one single simulation is used for the prior, this reduces the number of rows and thus the ensemble size to one. Therefore, a block size which defines the largest time scale that can be assimilated in the reconstruction is set. This then causes the problem of discontinuities at the block edges, for instance when the prior matrix has block size 50 but a decadal proxy record dated at year 49 of this block is assimilated. As suggested by the authors, a solution consists in using multiple climate simulations as a prior, such that each row of the prior matrix is given by one model. This would bring the approach closer to the concept of *transient* offline DA, however, the five climate model simulations available in my project are not sufficient to provide representative covariances.

Adapted implementation in Erb-2022
The idea of SH-2016 was used in this recent reconstruction of the last 12,000 years. To improve speed and reduce memory consumption, instead of a prior matrix a transient prior vector consisting of consecutive years is constructed (see Section 2.6.4). The smallest time scale is decadal and proxy records are assimilated at once instead of serially. Due to the way the prior is constructed, the covariances in the Kalman gain are computed from multi-decadal observation estimates (from the running mean over the prior vector) and the decadal prior ensemble. This is the main difference to SH-2016, where the time scale of observation estimates and prior members in the covariance is the same. I do not use this approach because using a transient prior is not necessary for the last millennium and using same time scale covariances is more natural.

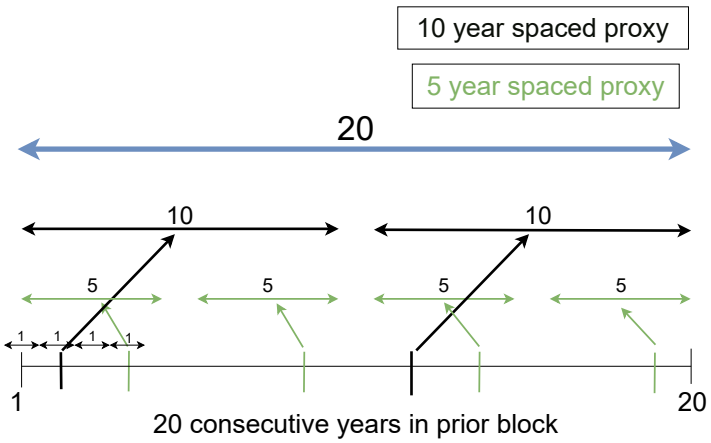

Figure 4.4: Illustration of assigning proxy records records which represent 5 and 10 years to time scale blocks inside a 20-year block. The (sub)blocks are represented by horizontal arrows. Observational data from climate archives is usually not spaced evenly in time as shown here.

4.5.2 Adapted implementation of the SH 2016-Algorithm

My main idea is to assimilate proxies not serially, but in subblocks for each time scale. The algorithm goes through the entire time period block and subblockwise. Hence, the time scales that are to be reconstructed need to be fixed beforehand. This will allow the algorithm to be orders of magnitude faster. These subblocks can be all time scales that fit into the largest time scales (e.g. 1,5 and 10 years if the largest time scale is 20 years). The largest time scale is called block size *bs*. However, it would be a coarse approach to automatically assign proxy records to these blocks by simple binning. Furthermore, there is the border discontinuity problem due to how the prior matrix is constructed. It is necessary to define a resampling procedure to preprocess the proxies and assign the observations to the subblocks. The situation is visualized in Figure 4.4.

Resampling scheme for the proxies

This section corresponds to box 2.1 in Figure 4.1.

I use a resampling route that consists of five steps. Steps 2 to 4 are inspired by the MakeEquidistant function of the Paleospec R package (github.com/EarthSystemDiagnostics/paleospec).

1. Estimating the resolution of a proxy record
2. Upsampling proxy record to annual resolution
3. Filtering against aliasing

4. Downsampling to target resolution

5. Masking gaps in the resampled time series

Estimating the resolution of a proxy record
It is necessary to set a resolution for each proxy record. However, for ice core and speleothem climate archives it is not directly clear which time scale is precisely captured due to filtering processes, also without consideration of dating uncertainties. It is often not known to researchers doing model-data comparison, if a proxy record with a dating represents a time average or a snapshot and what the effective temporal resolution of a proxy record is (Brierley and Rehfeld, 2014). To estimate an individual resolution for each record I resort to the median resolution of each proxy record time series. The median resolutions of all speleothem and ice core records are plotted in Figure 3.2. In the adapted SH-2016 algorithm, the time scales are fixed in the beginning, such that the median proxy record resolution has to be rounded to the nearest time scale in the set of predefined time scales. In the following, that individual proxy record resolution is called the target resolution. The PaleoDA code also allows reusing records on all time scales larger and equal to the target resolution (option: `reuse`). For example, if the predefined time scales are 1,5,10, and 20 years, a proxy record with target resolution 5 years is also resampled to its 10 and 20-year averages and used on these time scales.

Upsampling proxy records to annual resolution
The proxy record time series is resampled to annual resolution. This step is performed with the `.resample.interpolate` method from the Python package `xarray`. For the interpolation of non-present data points, the PaleoDA code can use nearest neighbour or linear interpolation. The former has the advantage of conserving the multi-year mean.

Filtering against aliasing
To safeguard the resampled time series against aliasing effects from frequencies higher than the desired target resolution, the upsampled signal is filtered with a Butterworth filter. The cut-off frequency is defined by the target resolution. The `signal.butter` and `signal.filtfilt` methods from the scipy-package are used to ensure that the resulting signal is not shifted in phase.

Downsampling to target resolution
The upsampled and filtered time series is resampled to the target resolution by computing the target resolution mean. The resampled time series are labelled with the leftmost entries of each interval.

Masking gaps in the resampled time series
The resampling procedure might introduce artificial data where the original proxy record time series has a large gap without available data. This can be the case for the speleothems which have decadal to centennial growth hiatuses. Therefore in the last step, the resampling algorithm goes through the original time series and detects gaps which are larger than x times the target resolution. These gaps are then masked with NANs in the resampled time series. The gap factor x can be set in the PaleoDA configuration.

4.6 Preparation of the prior state matrix

Given the number of desired ensemble members N_e and the largest time scale bs, the prior matrix is created from randomly selected simulation years and their bs(block size) subsequent

years. The prior matrix is augmented with the observation estimates $\mathcal{H}\mathbf{X}$. For the multi-time scale assimilation it is crucial that the observation estimates are also updated.

4.6.1 Assimilating the resampled proxies over multiple time scales

To assimilate the proxy records over multiple time scales, the entire time series, e.g. the last millennium is decomposed into blocks of bs consecutive years. The algorithm loops over these blocks. For each block, the prior state matrix is decomposed into one bs-year mean and bs anomalies. The algorithm looks up the proxy record values with resolution bs for the current timestamp and updates the bs-year mean of the prior matrix. Then the algorithm goes down to finer resolutions. For the subblocks, the subblock means are assimilated until finally the annual proxies are treated. The algorithm goes from the largest to the smallest time scale. SH-2016 tested their algorithm also for the other direction, going from small to large resolutions, and found statistically identical results. A visualization of the multi-time scale DA loop can be found in the full algorithm sketch in Figure A.1.

4.6.2 Advantages and limitations of the adapted multi-time scale PaleoDA algorithm

In comparison to SH-2016, resampling the proxy records drastically reduces the number of calculations, especially the anomaly-mean decompositions of the prior matrix, which constitute a costly operation. Although this way the algorithm's speed is close to the annual version, the absolute flexibility with regard to reconstructing all possible proxy time scales has been lost. However, a set of resolutions adapted to most proxy record resolutions can be chosen. The multi-time scale approach could also be used to deal with the chronological uncertainties of proxy records. It remains to be tested if the multi-time scale algorithm also improves the temporal variability of reconstructions as shown by SH-2016, or if the principle advantage lies in the ability to assimilate proxy records which are not annually resolved. The option to reuse proxies on multiple time scales can be used to give more weight to the proxy records. The adapted SH-2016 algorithm contains even more different tuning configurations than before. These configurations need to be justified and the sensitivities to these choices tested.

4.7 Single and multi-model prior ensembles

This section is related to box 1.0 and 1.3 in Figure 4.1.

Single-model ensembles
In Section 3.1, the five different isotope-enabled model simulations that are available for this study were presented. The natural approach is to create a separate prior from each of them and then compare the influence of the prior in the different reconstructions. The code proceeds by loading all variables which are to be assimilated from a simulation and computing the annual mean from the monthly values. The code also offers the option to compute seasonal means for specific months instead of annual months in order to study the influence of seasonal biases in reconstructions, see for instance Erb et al. (2022), Steiger et al. (2018), Tardif et al. (2019), and Zhu et al. (2020). The proxy estimates ($\overline{\mathcal{H}\mathbf{X}^f}$) are calculated with the configured PSM options. From these annual means, the prior ensemble is created by selecting randomly N_e years (sampling without replacement). Usually, N_e is chosen to be 100 for millennial simulations as a good trade-off between capturing the model covariance structure and not making the computation too costly.

Multi-model ensembles
The multi-model ensemble (MME) approach consists of combining prior ensemble members from different climate simulations. Such an MME reconstruction is different from taking the mean from multiple reconstructions with different single-model priors[5]. MMEs have been explored in a recent study working with pseudoproxies (Parsons et al., 2021) and applied to real data in the LGM surface temperature reconstruction (Annan et al., 2022). Parsons et al. (2021) found that MMEs have better reconstruction skill than single-model ensembles. The central motivation of using an MME is twofold. First, the range of covered values by an MME, and thus the uncertainty of the reconstruction is larger and possibly more realistic, especially when working in absolute space (see Section 4.8). last millennium simulations are tuned towards stability, the range of simulated values provided by a single-model is small. However, models can differ quite substantially in their simulated regional δ^{18}O values (Bühler et al., 2022), such that combining them provides a larger range of values. Second, the MME provides a more diverse covariance structure with more spatial degrees of freedom. Teleconnections in the covariance pattern will be weighted according to their shared prevalence in all climate models. To create an MME ensemble, the single-model approach described above is adapted.

1. In a preprocessing step the climate model simulations are regridded to a common grid, for instance with the Python `xESMF`-package. I regridded the models to both the lowest and highest resolution of the available models.

2. The data is loaded and averaged for each model separately as described above.

3. If the anomaly option in the PaleoDA code is set, the model data is debiased by subtracting the mean over a specific period.

4. The priors matrices for each model are concatenated into one MME.

4.8 Assimilation of anomalies vs absolute values

This section is related to the boxes 1.1, 1.3, and 2.0 in Figure 4.1.

In PaleoDA, either absolute values or anomalies can be assimilated. Both options are configurable in the PaleoDA code. Assimilating anomalies is a convenient way to avoid model biases and use models only as covariance structure providers. Nonetheless, this requires that the proxies are debiased over a time period shared by all proxies, which reduces the number of proxies that can be used in the reconstruction. The covariance structure provided by the model prior and the prior observation estimates is not affected by subtracting means from both values due to the definition of the covariance. However, the innovation part of the Kalman Filter is different.
In the anomaly approach, the mean observation estimate from the static prior will be close to zero (or can actively be enforced to be zero[6]), such that the innovation consists solely of the climate signal provided by the proxy. In the absolute value approach, the mean value as simulated by the model is still important. Large model-proxy differences can have a strong effect on the reconstruction, especially when a bias is only present in one variable as δ^{18}O , but not temperature and precipitation. Most reconstructions, including LMR (Hakim et al., 2016) and PHYDA (Steiger et al., 2018) assimilate anomalies because the employed statistical PSM is calibrated on instrumental temperature anomalies. Few PaleoDA studies have assimilated absolute values. For instance, the LGM reanalysis Tierney et al. (2020) consists of one single assimilation step,

[5]The MME approach is also different from the transient offline assimilation approach described previously, because the prior is not changing through time.
[6]As the prior consists of N_e randomly selected simulations years, the mean of this random selection will not be exactly zero. The ensemble is thus zero-centered again.

and thus anomaly assimilation is not possible. The deglaciation reconstruction by Osman et al. (2021) also works with absolute values. In the last millennium reconstruction by Shoji et al. (2022), which uses isotope-enabled GCMs, the authors argue against assimilating anomalies because their PSMs required absolute values, which is also the case for the speleothem and ice core PSM in this thesis. Although methodologically inconsistent with the observation operator $\mathcal{H}$, it is also conceivable to simply subtract the mean after applying the PSM to the absolute values and finally perform anomaly assimilation. This way, the PSM-modified covariance structure is used. Therefore in the PaleoDA code, if the anomaly assimilation option is set, the anomalies are computed after applying the PSM.

4.9 Monte Carlo Scheme for the PaleoDA algorithm

In the LMR (Hakim et al., 2016), a Monte Carlo scheme is used to account for uncertainty in the proxies and priors. The method consists of repeating the reconstruction a specific number of times with a different random selection of N_y ensemble members and only a fraction of the proxies, e.g. 75%. The remaining, not assimilated proxies can be used for validation. A Monte Carlo procedure is also implemented as an option in the PaleoDA package, where a fraction (or a desired absolute number) is applied to the number of proxies available at each reconstructed time scale. However, in the experiments performed for this thesis, the proxy record fraction option will not be used due to the small number of available proxy records. Only the prior will be resampled, as this proved to improve the evaluation metrics for PPEs.

Chapter 5

Validation of the PaleoDA framework

In this chapter, the PaleoDA framework presented in Section 4 is validated such that it can be applied meaningfully to the proxy record data in the next chapter. First, I perform a model data comparison to detect model-data differences. Then, I investigate the influence of the prior model in form of the averaging kernel. and perform pseudoproxy experiments with different PSM settings to estimate possible reconstruction skill. I expand on pseudoproxy experiments using different models as a target (for the pseudoproxies) and a prior to investigate the effect of model biases in the covariance structure. Furthermore, multi-model ensembles are tested as priors. Finally, I evaluate the temporal variability of multi-time scale pseudoproxy reconstructions.

5.1 Model-data median comparison

A basic assumption of the Kalman Filter is that the prior state estimate is unbiased. Biases affect the CFRs in two ways, in the mean state of the observation estimates ($\mathcal{H}\mathbf{X}^f$) for the innovation part of the Kalman Filter equations and in the covariance structure for the Kalman gain. While the latter is more difficult to estimate, the mean state bias can be straightforwardly visualized for individual proxy record locations. In Figure 5.1, the median difference between model priors and proxy records is shown for the two climate archive databases. It presents a qualitative assessment of all five climate models. The median instead of the mean has been chosen to diminish the influence of potential outliers. The simulated δ^{18}O values have been converted using all PSM options described in Section 4.1.1. The adjustments that the PSMs performs on the median state mainly stem from the height correction and the fractionation and to a small extent from the infiltration/precipitation weighting. The model-data median value comparison for the individual models, including the correlation coefficients can be found in the Appendix Figures B.4 and B.5.
The Figures 5.1 (a,b) show, that the simulated values are too depleted in the low-to-mid latitudes and too enriched at the poles. This pattern is also consistent for the individual models. Especially for the speleothems, close locations can have model biases with different signs, see for instance the proxy records in South West Australia or in Central America. Absolute model biases are generally larger for the ice core locations. The proxy record medians (see Appendix Figure B.3) also exhibit large median state differences for geographically close proxy records. The PSM is not able to reproduce these heterogeneities. The second panel (c,d) shows that the interquartile range of simulated δ^{18}O values is more homogenous at the speleothem locations in comparison to the ice core locations. Despite the better absolute closeness for the speleothem record values, the third panel (e,f) shows that the correlation between simulated and recorded δ^{18}O values is better for the ice cores than for the speleothems. For the ice core records, the regression slopes are closer to the desired value of 1 and the confidence intervals of the regres-

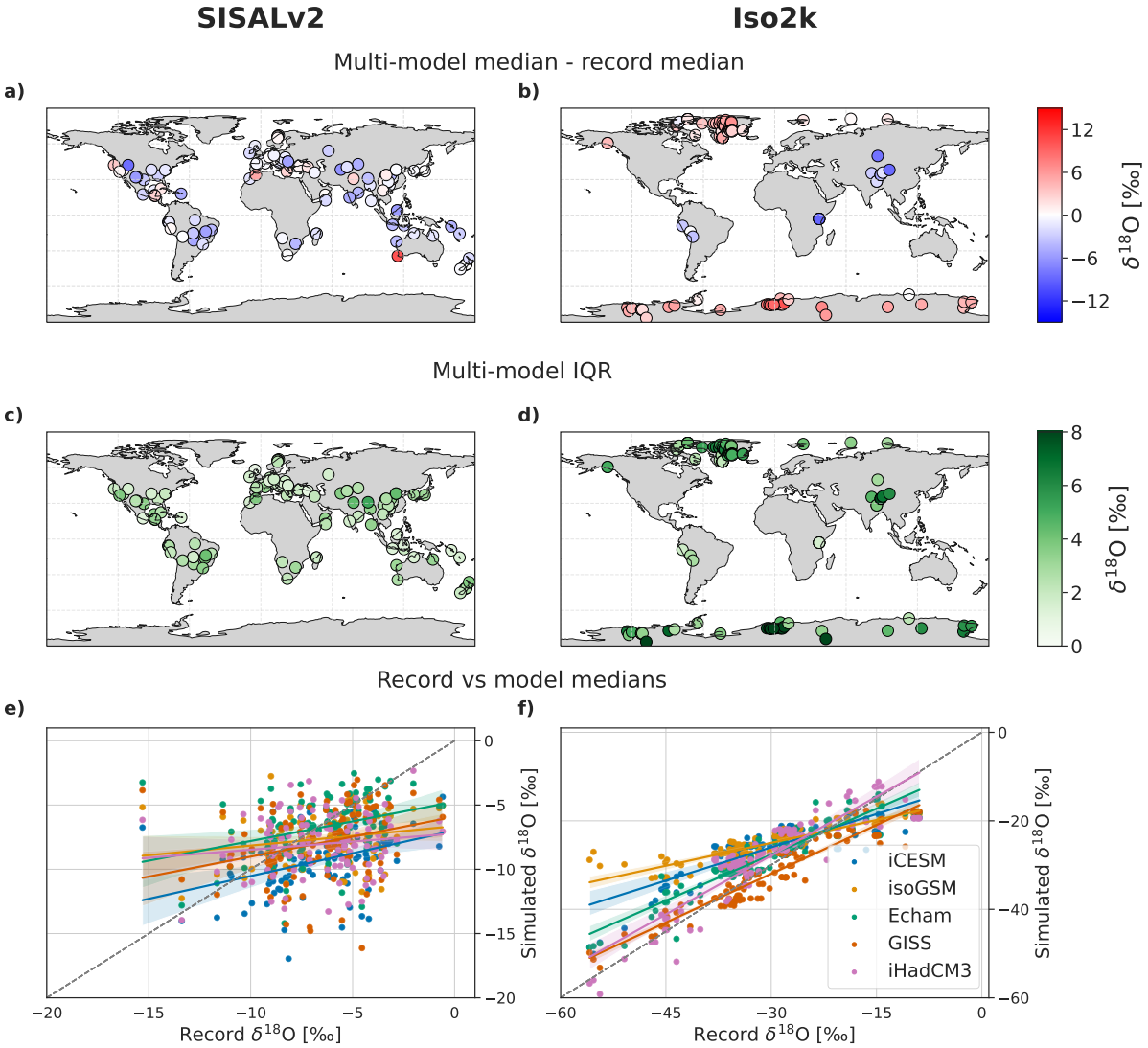

Figure 5.1: Individual comparison of the simulated δ^{18}O values , which have been converted using the speleothem and ice core PSMs, to the median of the proxy record time series. All values are given in ‰. The proxy records have been limited to the time period of the climate model simulations (850-1850CE). The left column shows the analysis for the selected speleothem records from SISALv2 and the right column for the ice cores from Iso2k. The first row shows the bias of the median of all models (a,b). Blue indicates, that the model median (including the PSM conversion) is too depleted, while red indicates that the models are too enriched in δ^{18}O in comparison to the proxy records. The second rows shows the interquartile range of all simulated δ^{18}O values (c,d) and in the third row the proxy record median δ^{18}O is plotted against the value of the individual simulations. The correlation of the simulated to measured values is indicated by the coloured lines and the respective shadings, which show the 95% confidence interval. The model-data comparison for the individuals model is shown in the appendix Figures B.4 and B.5, where also the exact correlation coefficients (including confidence intervals) are documented.

sions are smaller. The isoGSM model stands out due to a lack of depletion at the pole locations and consequently only has a regression slope of 0.34 (Appendix Figure B.5). There is no model that clearly outperforms the others for reproducing both speleothem and ice core δ^{18}O and that should thus be preferred as a PaleoDA prior. It is important to underline, that the model-data differences can be either a consequence of a real model bias, or of a too-simplified PSM which does not represent local process properly. Disentangling this problem is not obvious and not intended here. However, in particular for the speleothem locations, I assume that cave specific processes which are not represented by the speleothem PSM lead to large differences to the simulated precipitation δ^{18}O . Thus, the reconstruction of climate anomalies instead of mean values, as outlined in Section 4.8, is expected to be more reliable, although the assimilation of absolute values will also be tested.

5.2 Assessment of the influence of the prior

To estimate the influence of the proxy record observations on the reconstructions, the area of the averaging kernel (Section 2.6.4) is visualized for the surface temperature, δ^{18}O and precipitation in Figure 5.2. Here, the unmodified δ^{18}O value (no PSM) at all speleothem and proxy records have been taken. Only annual means have been used. The proxy error was set uniformly to $0.5‰^2$. This analysis presents a best-case scenario, which is not available in real proxy record reconstructions. Overall, the patterns differ considerably across the models. Regions that are consistently influenced in all models and variables are regions with many close proxy records as the northern part of South America, South Asia and the Northern Atlantic. Furthermore, remote regions without available proxy records as the low-latitude oceanic regions (especially the Pacific) are strongly influenced. This is the case in particular for precipitation. The amplitude varies between the models, as can for instance be seen in the temperature and precipitation over South America. For temperature, the influence of δ^{18}O measurements is strongest in the iHadCM3 model, which is also reflected in the global mean value of 1.08, while the other models have values between 0.6 and 0.75. This can translate into a stronger influence of δ^{18}O measurements on temperature during the DA. Furthermore, the iHadCM3 temperature field shows a remarkably continental structure. For the δ^{18}O fields, a strong influence over the Sahara region is apparent in the iCESM and the isoGSM model, although this region is void of proxy records. All models consistently show negative values for the central Pacific. The weakest response is found for the GISS model (global mean 0.24), where also Antarctica is visibly less affected by the proxy records. For precipitation, the strongest response to the records can be found in the low latitudes, especially in the Pacific. In the GISS model, checkerboard like artefacts are visible, especially over tropical South America. The area of the averaging kernel fields from the separate speleothem and ice core locations (Appendix B.6,B.7) reveal that overall the influence of the speleothem locations is stronger than the ice core locations. In some regions like Europe, northern Asia and Greenland, the areas of the averaging kernels have opposite signs when using only the speleothem or the ice core locations.

5.3 Pseudoproxy experiments

PPEs (Section 4.3) have been performed to test the possible reconstruction skill in a best-case scenario, in which all selected proxy record locations (217) provide annual mean δ^{18}O values. The SNR has been set to 0.5 and the experiment has been repeated 10 times with a varying selection of 100 prior ensemble members. Here, only annual, and no multi-time scale DA has been performed. The experiments have also been performed using the speleothem and ice core locations separately.
Figure 5.3 shows the skill scores for PPEs with δ^{18}O from the iCESM model in three experiments. The Corr and CE metrics are used to quantify the reconstruction skill (see Section

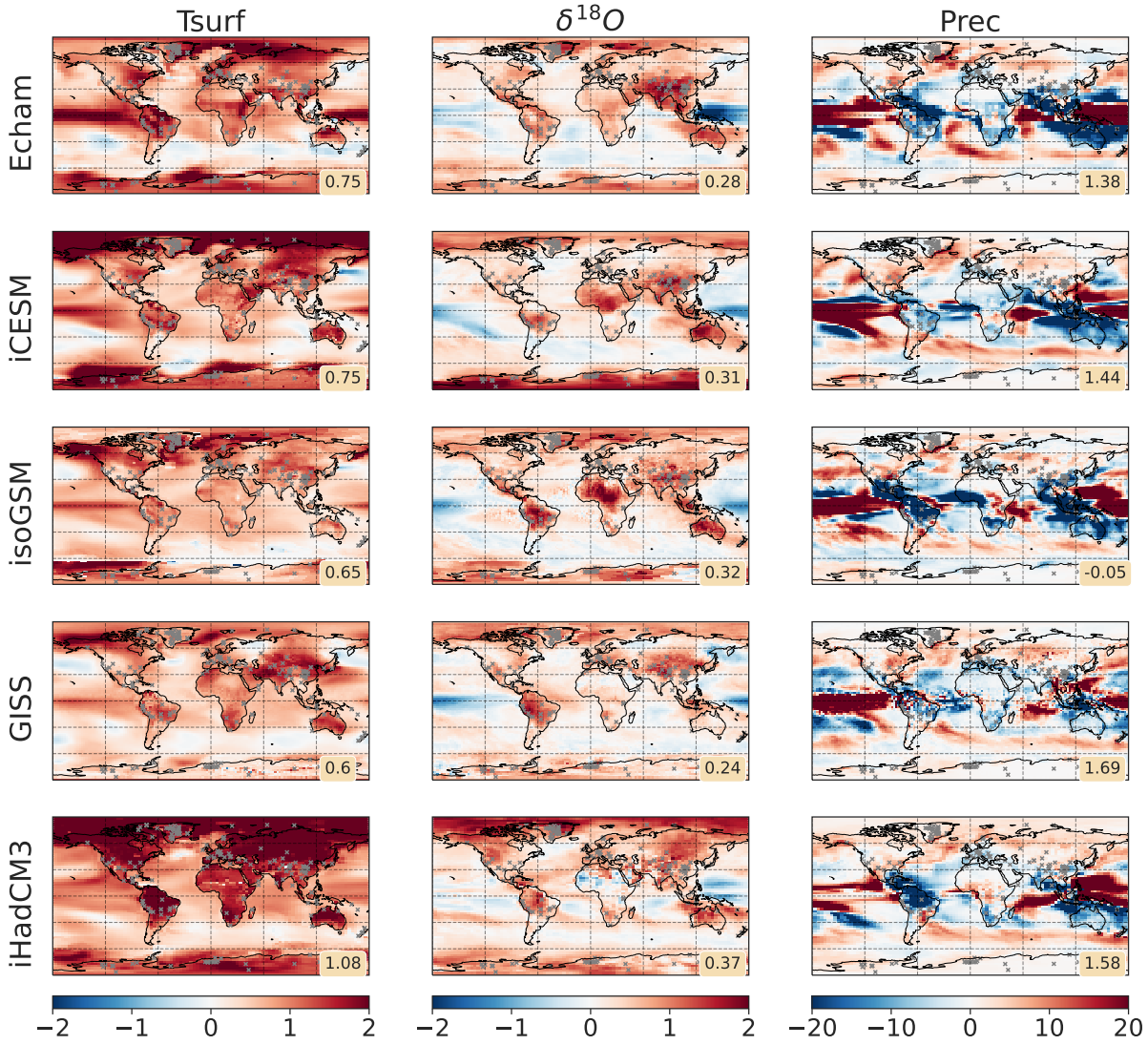

Figure 5.2: Visualization of the relationship of the simulated δ^{18}O at the proxy record locations to the surface temperature, δ^{18}O and precipitation at all model grid cells. The Kalman gain is computed from the entire climate simulation runs and then summed up for each model grid cell, resulting in a metric similar to the *area of the averaging kernel*. A measurement error variance of $0.5‰^2$ has been assumed. The proxy record locations are indicated by grey x-markers. The number in the lower right corner of each subplot is the global mean value of the metric. The maps using the speleothem and the ice core records separately can be found in the Appendix Figures B.6 and B.7.

4.3.1). A CE score of zero means that the error variance is larger than the variance of the true time series.
In the first experiment (a), for the pseudoproxies the annual δ^{18}O values from the grid cell closest to each proxy record location have not been modified further by a PSM. The best skill scores are achieved for all three climate variables in the low-latitude oceans and in proximity to proxy record locations, especially over Greenland, South East Asia, and the Northern Part of South America. Globally and regionally, the temperature is reconstructed better from δ^{18}O than the δ^{18}O field itself (0.31 vs 0.24 for $\overline{\text{CE}}$), while for precipitation the skill is the lowest ($\overline{\text{CE}} = 0.21$).
In the second experiment (b), the pseudoproxy values of δ^{18}O have been further modified by the *PSM light* configuration, which comprises fractionation and infiltration weighting for the speleothem locations and infiltration weighted δ^{18}O values for the ice core locations. This only leads to a slight reduction in skill for all variables ($\Delta\overline{\text{CE}}$ between -0.03 and -0.04). The regional patterns look similar to experiment (a). With the PSM light, the ice core locations reconstruct the polar regions better than the speleothem locations (Appendix Figure B.8 and B.8). Although the speleothems perform better in the low latitudes, the ice core experiments, which also involve some locations in South America, Asia and Africa also provide notable reconstruction skill in these regions, especially for the Pacific.
In the third experiment (c), the effect of the karst filter, firn diffusion, and ice compaction on the reconstruction skill has been further tested. This configuration is called the *full PSM*. The karst filter simply convolutes the δ^{18}O signal, whereas the full ice core PSM involves more modifications of the δ^{18}O signal as it also uses the accumulation of rainfall. The noise of the pseudoproxies has been added before the application of these filtering effects. Though there is still correlation to the true climate field, the CE is more than halved and approaching zero. The reconstruction skill is particularly reduced at the ice core locations at the poles, which also becomes clear when looking at the results of the same experiments only using the speleothem or ice core locations (Appendix Figure B.8 and B.8). The ice core PPE with the full PSM leads to $\overline{\text{CE}}$ values of 0.00 and 0.01. This contrasts to the effect of the karst filter on the speleothem pseudoproxy records, in which the skill reduction is smaller ($\overline{\text{CE}} = 0.07$ - 0.12). The experiments should still provide some reconstruction skill, at least near the proxy record locations. The ice core PSM thus requires a more thorough analysis, which has not been performed here.

5.4 Investigation of inter-model biases and multi-model ensembles

The experiments in Section 5.3 involved pseudoproxy records and prior ensemble members from the iCESM model, thus the same model. Having five different isotope-enabled last millennium simulations available, I also tested how the different models, and a combination of them in the form of MMEs can be used to reconstruct other (target) models. The target models, from which the pseudoproxy experiments are sampled, represent the true distribution, while priors from other models have different mean states and covariances. The MMEs are always created from simulation years of the non-target models, thus excluding the target simulation. The same PSM light configuration as in Section 5.3 has been used for the 217 pseudoproxy record locations. To focus on the more interesting covariance differences of the models with respect to each other, I performed a simple mean value debiasing by subtracting the local mean value for each model grid cell. Hence, only climate anomalies are reconstructed. The results of these experiments are shown in Figure 5.4. The reconstruction skill is summarized in the form of global means of the RMSE, RE and Corr. The RE metric is similar to the CE used previously, with the difference that it compares the reconstruction error variance to the error variance of the mean of the uninformed prior (see Section 4.3.1).
The experiments demonstrate a reduced skill when not using the same model for the prior and the target. Although the global mean of the local correlations is still positive for all

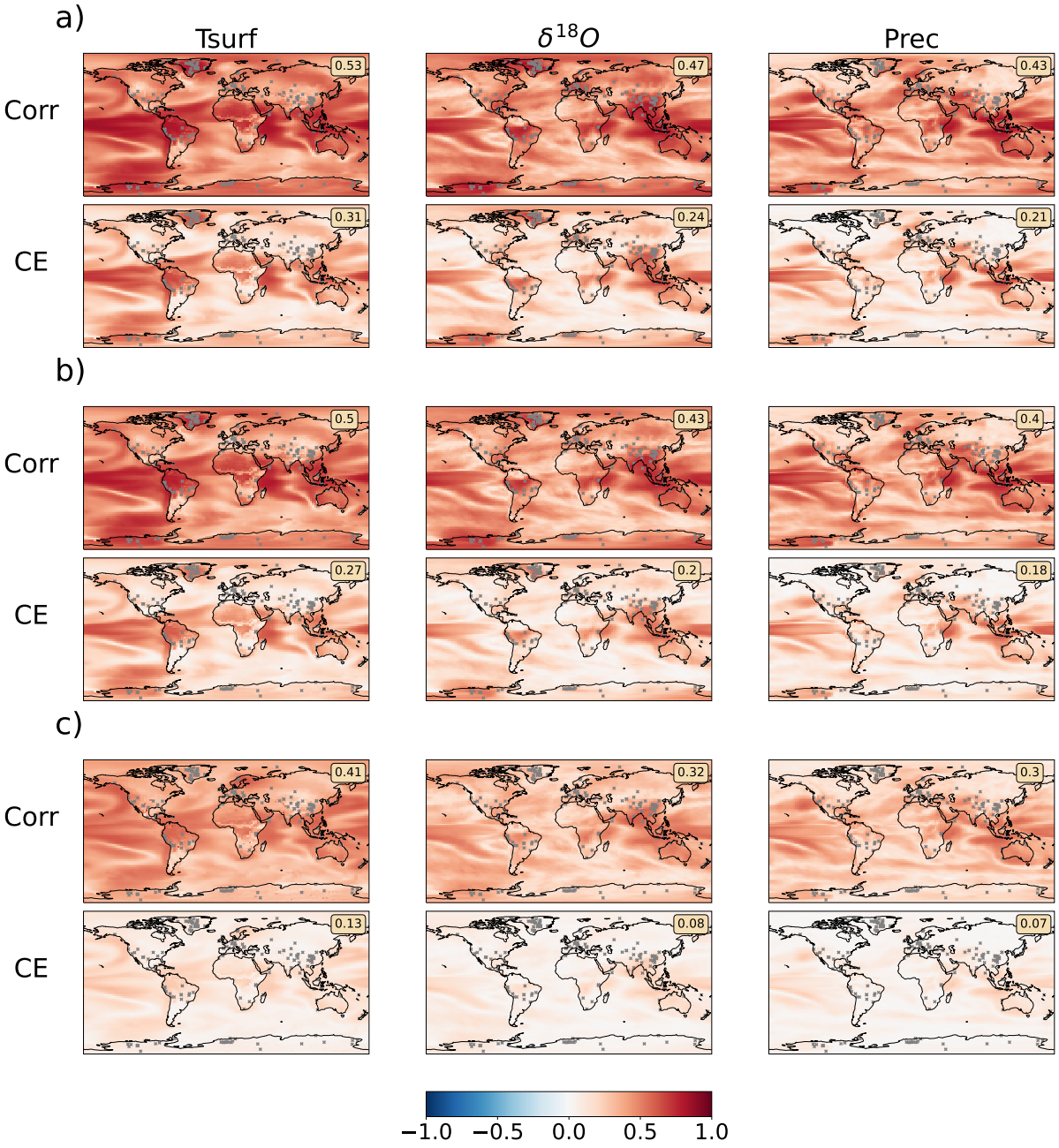

Figure 5.3: Skill scores of PPEs for reconstructing the climatic fields of the iCESM simulation from the simulated δ^{18}O at the speleothem and ice core record locations. The skill is measured with the correlation and CE metrics with respect to the truth. The global mean of the metrics is annotated in the upper right corner. The significance of the correlations is not indicated because almost all local correlations are significant ($p<0.05$). The pseudoproxies are created with an SNR of 0.5, which is applied to the simulated δ^{18}O time series before further modifications by the PSMs. In a), the annual mean δ^{18}O at the proxy record locations is used for the pseudoproxies. In b), the pseudoproxies are altered by precipitation weighting and fractionation for the speleothem pseudoproxies and infiltration weighting for the ice core pseudoproxies. In c), the pseudoproxies from b) are additionally modified by the karst filter for speleothems and firn diffusion and compaction for the ice cores.

reconstructions, the RE is close to zero or even negative when not using the target model as a prior. Only 4 out of 25 such experiments have a positive RE score, which means that the reconstruction yields a smaller error variance with respect to the truth than would the mean of the prior, which is not informed by any measurements. The MME ranks among the first two non-target priors for all experiments and metrics. However, the difference is small and the skill is close to the other models. Clearer improvements can be seen for the correlation where the scores differ more than for other metrics. It is noticeable, that the experiments with the same model as prior-target yield different skill scores, depending on the model. The ranking between models also depends on which skill score is used. On the one hand, the reconstruction of GISS and isoGSM yields the smallest root mean square errors, on the other hand, they also have smaller RE and correlation scores.

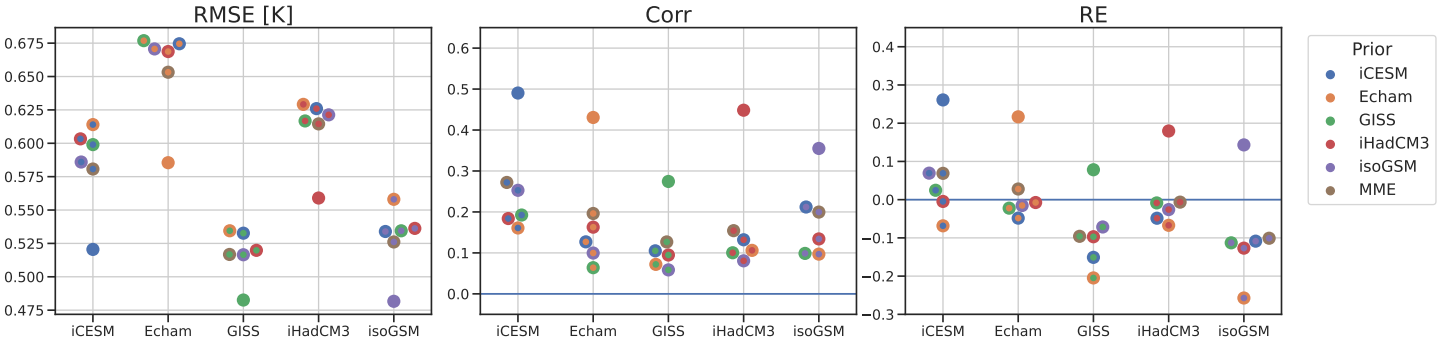

Figure 5.4: Global mean of skill metrics for PPEs in which the climate models were used as priors to reconstruct the temperature fields of other target models (on the x-axis, denoted also by inner color of circles). The speleothem and ice core δ^{18}O pseudoproxy records have been generated from the target model with an SNR of 0.5 (without the karst filter and firn diffusion). The left panel shows the Root Mean Square Error of the reconstructions (the lower, the better), the central panel the correlation (the higher, the better) and the right panel the reduction of error (the higher, the better).

The same evaluation metrics have been computed for the reconstructed global mean temperature (GMT) to investigate if despite of the low local skill, the global mean temperature is reconstructed better. These results are shown in Figure 5.5. Although the RMSE score is not directly comparable to Figure 5.4, it is clear that the reconstruction skill of global mean temperature is better for Corr and RE. The RE is positive for 16 out of 25 experiments using non target models as the prior. Still, the difference to the experiments where target and prior come from the same model is evident.

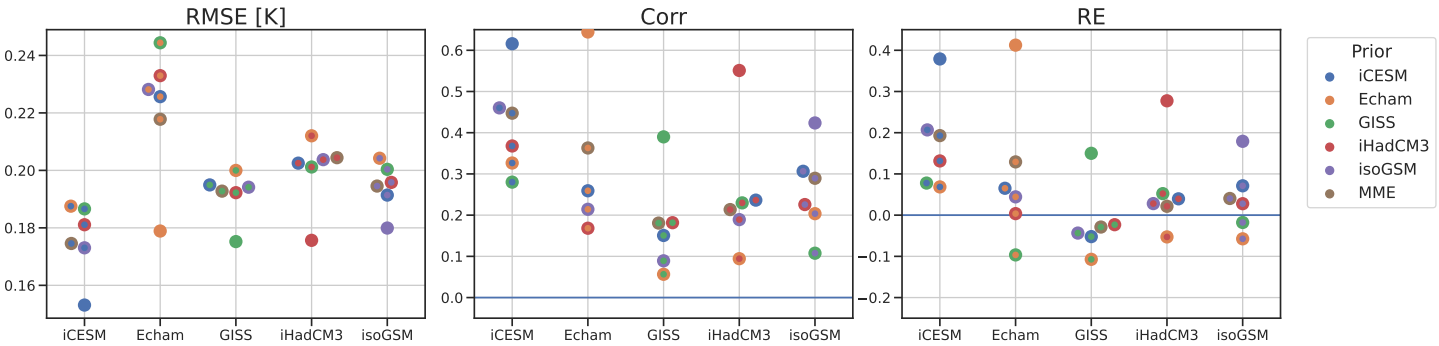

Figure 5.5: Reconstruction skill for global mean temperature using different target and prior models. Error metrics as in Figure 5.4.

5.5 Variability of multi-time scale pseudoproxy reconstructions

Until this point, the PPEs used pseudoproxy records with annual resolution. The PPEs carried out in Section 5.4 are now repeated using pseudoproxies which are computed as multi-year means and thus simulate representation on longer than annual time scales. Here I focus solely on the variability of the reconstructed GMT using pseudoproxy records on various time scales. The question is if using proxy records on different, longer than annual temporal resolutions improves the representation of long-term climate variability.
The power spectral densities (PSD) of the reconstructed global mean temperatures for iHadCM3 using different time scales are shown in Figure 5.6.
To use the same number of data points in each reconstruction, the multi-time scale experiments used an accordingly reduced number of pseudoproxy locations. The total number of data points for a 1000 year reconstruction using $1, \ldots, n$ resolutions res_i is calculated as $1000 \times$ number of locations $\times \sum_i^N \frac{1}{\text{res}_i}$. The target power spectrum of the original simulation has the typical form of a red spectrum with more variability on decadal to centennial scales than on annual scales. It ranges from 10^{-2} to 10^0 [K^2year]. The figure clearly shows, that experiments using multiple time scales improve the reconstruction of decadal to centennial variability. In contrast to the annual time scale experiment, which results in a flat spectrum with underestimated long-term variability, the multi-time scale experiments increase variability on multidecadal time scales, resulting in a red spectrum. The annual time scale experiment has also been repeated using 200 instead of 100 pseudoproyxy locations, hence double the number of data points to test if the result is improved by more data points. The resulting power spectrum (label 1_ many) also lacks longterm variability in the GMT spectrum. Figure 5.6 shows the results for the iHadCM3 model. The experiment has also been repeated using the four other climate models. In all experiments, the reconstructions using only annual pseudoproxy records resulted in a multi-decadal to centennial variability that is one order of magnitude too low, while multi-time scale pseudoproxy records resulted in a PSD closer to the truth (not shown). A similar result is found when looking at the global mean PSD of each local temperature (Figure 5.7). The multi-time scale experiments better reproduce larger variability on multi-decadal to centennial time scales. Additionally, an offset of all reconstructions to the original simulation can be seen for all periods, also for the annual periods which have a more similar spectral amplitude in the PSD for the GMT. This simple analysis involves the local temperature for all local grid cells, thus also grid cells far away from the influence of proxy records as the oceans. An analysis of the local PSDs for specific regions and continents has not been performed here.

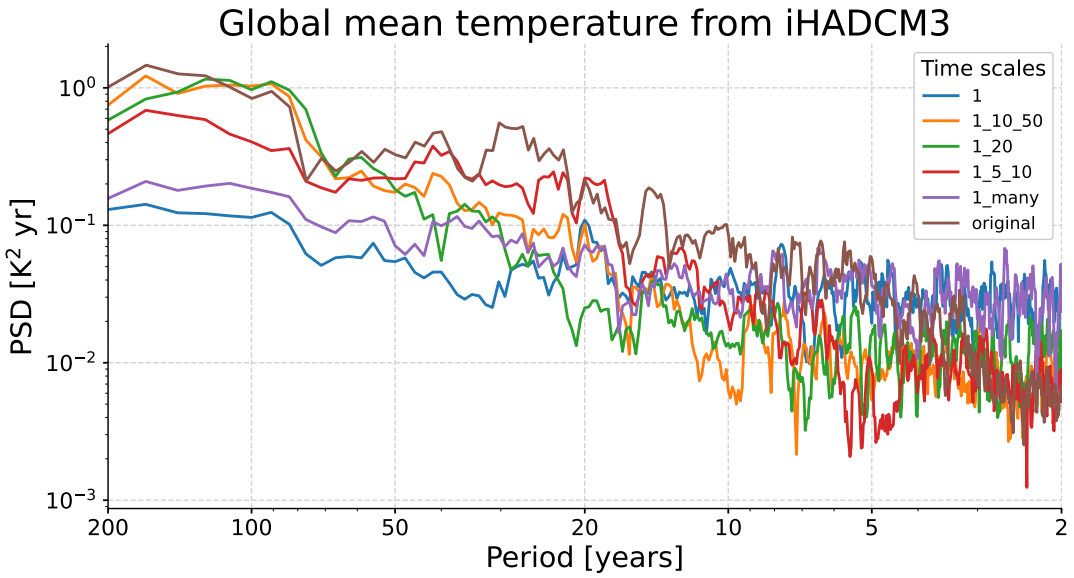

Figure 5.6: Power spectral densities of reconstructed global mean temperature using pseudoproxies on multiple time scales. The model that has been used as a prior and target is iHADCM3. The pseudoproxies have been generated from δ^{18}O with an SNR of 0.5 and the PSM-light configuration for the simulated δ^{18}O at 100 proxy record locations. The noise has been added to the pseudo proxy records after averaging the time series to the higher time scales. The lines show the resulting spectra when using different time scales, the brown line shows the GMT PSD of the target simulation. The annual experiment has been repeated with a doubled number of pseudoproxy record locations (1_many). The spectra have been generated with the multi-taper method of the Pyleoclim package (Khider et al., 2022). The GMT curves have been detrended, but not standardized, which is important to compare the absolute variability of each time series.

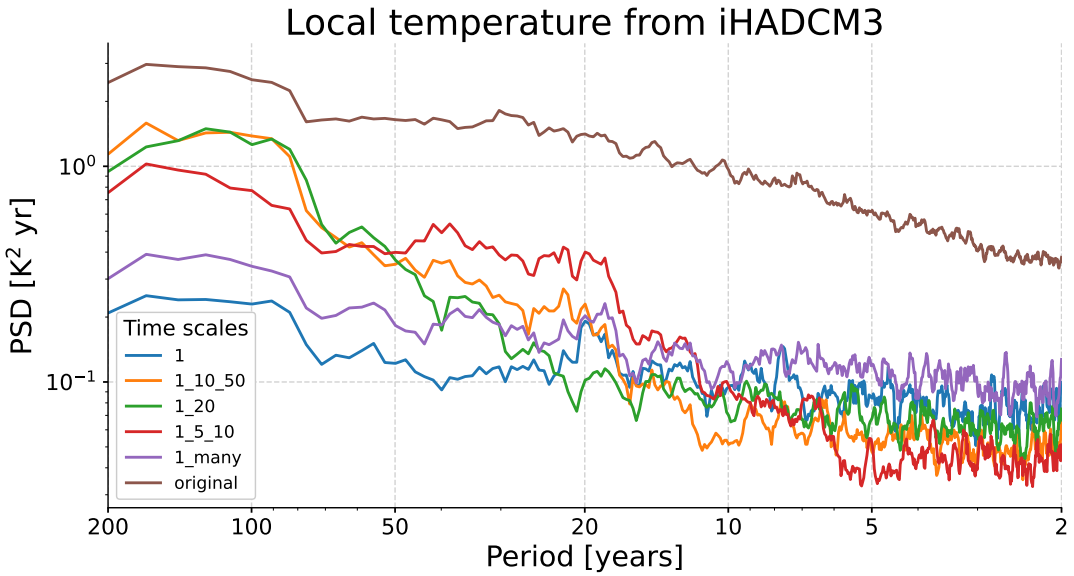

Figure 5.7: Global mean of the PSDs for each model grid cell (area-weighted). Same experimental configuration as in Figure 5.6.

Chapter 6

Application of multi-time scale PaleoDA to proxy record data

This chapter is dedicated to the application of the multi-time scale PaleoDA framework to speleothem and ice core proxy record data from the SISALv2 and Iso2k database. In the first section, the focus is laid on the global mean time series of reconstructed temperature and also precipitation. In the second section, I perform a local temperature and precipitation reconstruction for the region of tropical South America. The reconstructions are compared to existing reconstructions, in particular the version 2.1 of the Last Millennium Reanalysis (LMR) (Hakim et al., 2016; Tardif et al., 2019) and the Paleo Hydrodynamics Data Assimilation product (PHYDA) (Steiger et al., 2018). To distinguish the reconstructions obtained in this thesis, they are given the name **DAISIM**(Data Assimilation with Isotopes recorded by Speleothems and Ice cores on Multiple time scales).

6.1 A global multi-time scale PaleoDA reconstruction for the last millennium

I performed global temperature and precipitation anomaly reconstructions for the years 800-1999CE using all climate models separately and in form of an MME. The GISS model has been excluded from the MME due to the drift in δ^{18}O (Section 3.1). The reconstruction of absolute values was initially tested, but lead to extreme variations in global-mean temperature of several degrees and have therefore not been pursued further (not shown). The climate anomaly reconstructions used the 18th century mean value as a reference period for both the proxy records and the climate model priors. This century of the pre-industrial period has been selected because many speleothems and ice cores from the SISALv2 and Iso2k database have at least one sample measurement there. For the multi-time scale reconstructions, a wide range of time scales has been set, namely 1,5,10,20,50 and 100 years. The individual time scale of each of the 108 speleothem and 109 ice core records is inferred from the median time resolution of each record by the PaleoDA algorithm. The proxy records have been reused on all time scales larger than their median resolution. The resampling was done with nearest neighbour interpolation (Section 4.5.2). The resampled proxy record time series were masked with NANs for the parts, where the original time series does not have any records for a period of 3 times the median resolution (gap masking factor=3). The observation error variance was set to $0.5‰^2$ uniformly for all records independent of the time scale, which is larger than the measurement uncertainties stored in the SISALv2 database in order to account for the unclear representativity of a proxy record for the entire grid cell of the climate models. The PSM light configuration (precipitation weighting and infiltration weighting + fractionation) has been used for calculating the δ^{18}O observation estimates ($\overline{\mathcal{H}\mathbf{X}^f}$) and taking into account the seasonal and local effects. The full

PSM configuration, which further modifies the local $\delta^{18}O$ was judged not necessary for these types of experiments. Further, the mean value of the 18th century has been subtracted from the observation estimates. This way, changes in the covariance pattern that follow from the PSM remain, while model biases in the mean state become irrelevant. For each prior, the experiment is repeated 10 times with 100 randomly selected ensemble members using all available proxy records at each repetition.

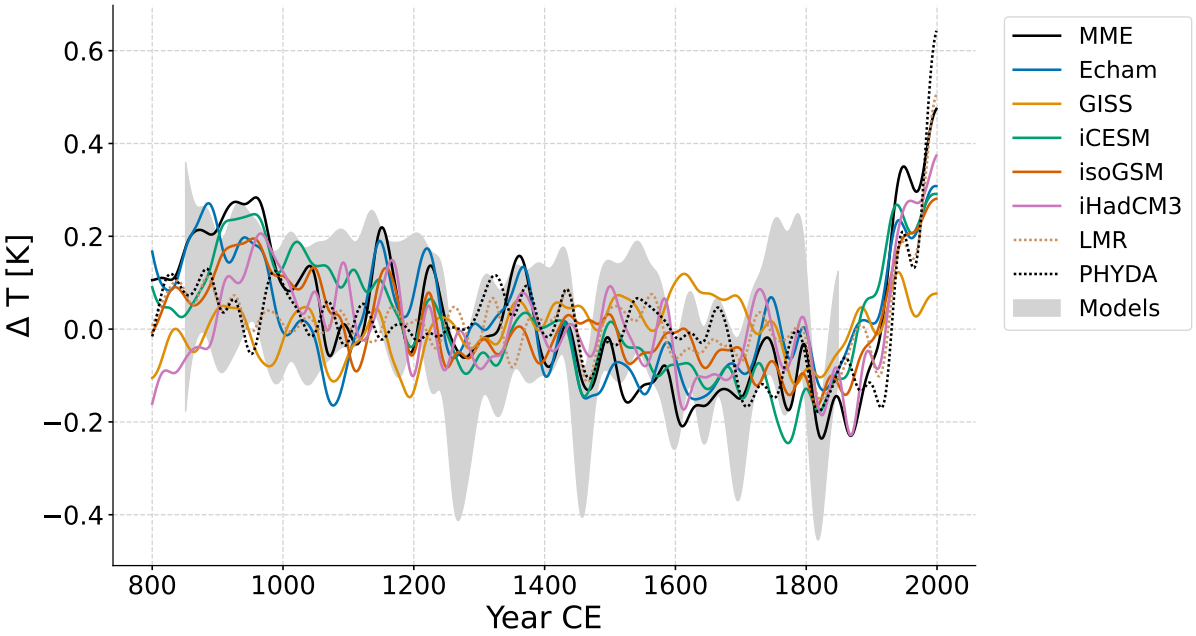

Figure 6.1: GMT anomalies from multi-time scale reconstructions using different models as priors. The MME excludes the GISS model. Furthermore, the GMT from LMR and PHYDA and the GMT from the climate model simulations (mean±standard deviation) are visualized. The reference period for the anomaly calculation is chosen as 851-1849CE, because these years are covered by all climate model simulations. The dotted lines show the GMT anomalies from LMR and PHYDA. Uncertainties are shown separately in Figure 6.2. The time series have been low-pass filtered with a 50 year Butterworth filter for better visibility and because the used climate proxy records are expected to represent multi-decadal variations better than annual variations.

The low-pass filtered GMT anomaly curves are presented in Figure 6.1. Overall, a *hockey stick* form can be recognised in DAISIM, with a cooling trend of 0.2-0.4K during the last millennium. The cooling starts around 900CE, where the reconstructions indicate a small warm plateau. The minimum of the cooling is reached in the 18th and 19th century and is followed by a subsequent strong warming of up to 0.6K. The reconstruction using the GISS model as a prior stands out due to its smaller fluctuations and missing global warming during the 20th century. The most pronounced peaks of the curves are shared across all DAISIM reconstructions. In comparison to the LMR and PHYDA reconstructions, the temperature variability in DAISIM is more pronounced. Their relative amplitudes are two to three times higher. Apart from the pronounced global warming in the 20th century, peaks/troughs that coincide across DAISIM, LMR, PHYDA, and the model simulations can be seen at the beginning and end of the 15th century and at the beginning of the 19th century. The amplitudes of the temperature changes depend on the model that is used a prior. The highest peaks are found in the iHadCM3 and the MME reconstruction. Remarkably, the temperature anomaly obtained from the MME at times exceed the anomalies from the single climate models, especially in the 20th century.
To better assess the contributions of both climate archive types, speleothems and ice cores,

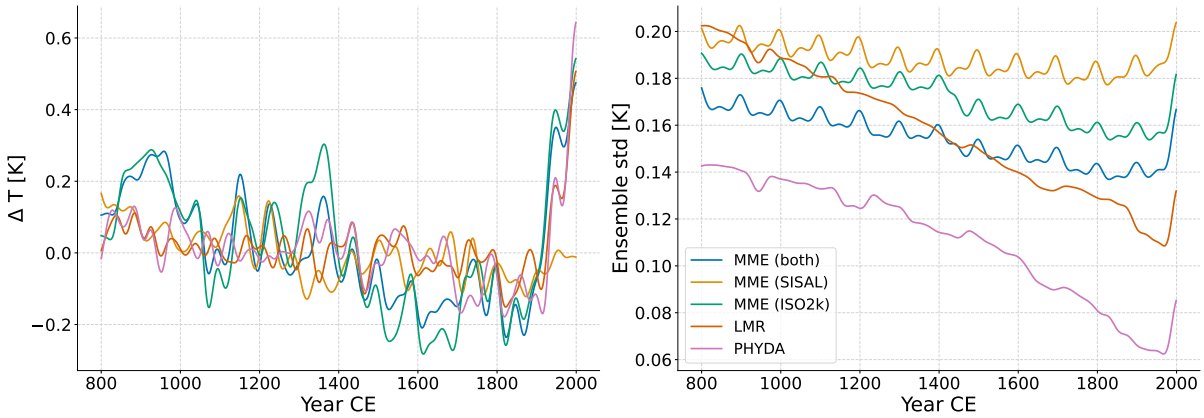

Figure 6.2: The reconstructed GMTs from the individual and joint SISAL (speleothems) and Iso2k (ice cores) databases in comparison to the LMR and PHYDA reconstructions are shown in the left panel. The uncertainties of the reconstructions are shown in the right panel. The periodicity is an artefact from the prior block in the multi-time scale approach. The time series have been low-pass filtered with a 50 year Butterworth filter.

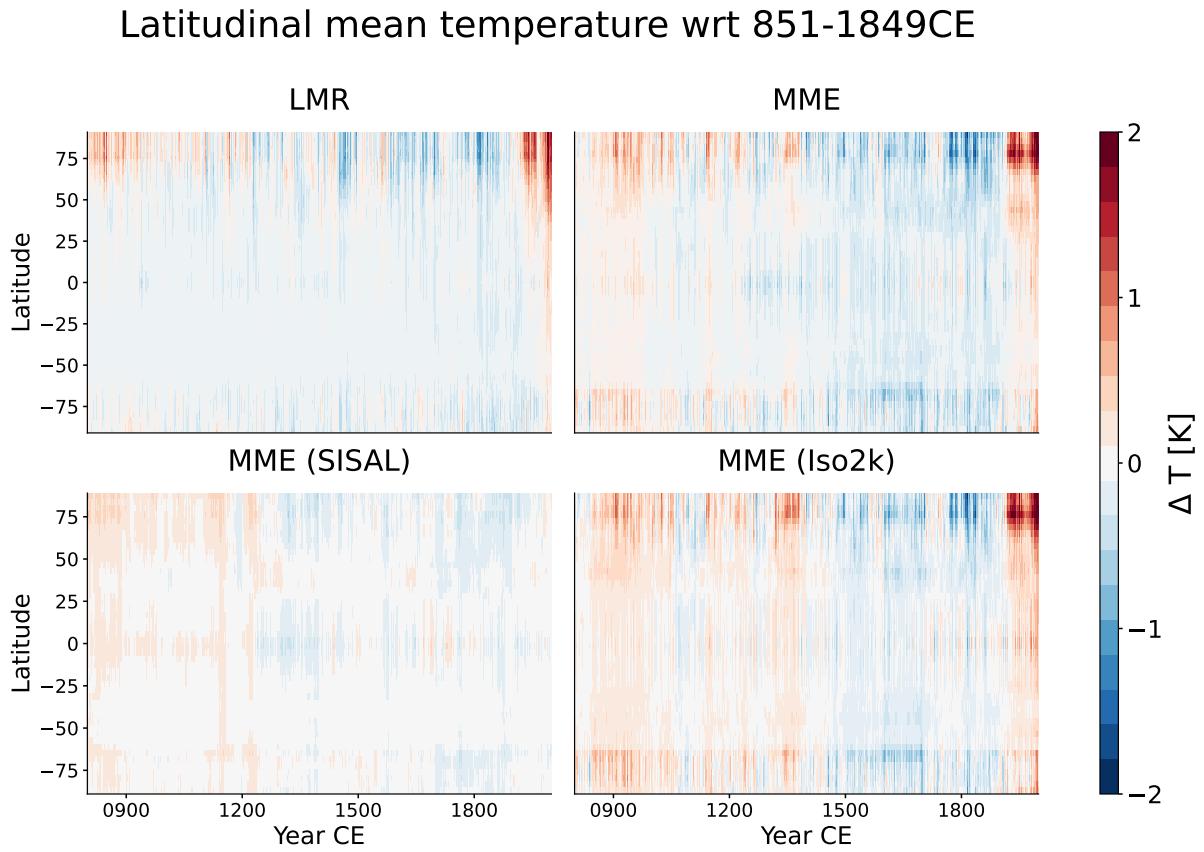

Figure 6.3: Latitudinal mean temperature anomalies over time (Hovmöller diagram). The upper left panel shows the LMR reconstruction, the upper right panel the results from the MME reconstruction using both the speleothems and ice cores. The lower panel show the reconstructions using only speleothems (SISAL) and ice cores (Iso2k). In comparison to Figure 6.1 and 6.2, the time series have not been filtered. The apparent coarser resolution of MME in comparison to LMR stems from the multi-time scale approach. 851-1849CE was used as the reference period.

the reconstructed GMTs have also been reconstructed from both archive types separately. The resulting GMT curves for the MME and their uncertainties are presented in Figure 6.2. It is apparent, that the ice cores have a stronger influence on the reconstructed GMT than the speleothems over the entire last millennium. Except for the 16th and 17th century, the GMT from ice cores is closer to the overall reconstruction than the GMT from speleothems. The speleothem records do not reproduce the global warming trend of the current warm period (CWP). The evolution of the latitudinal mean temperature is shown in Figure 6.3. The largest temperature anomalies over the last millennium and the CWP can be found in the high latitudes of the northern hemisphere. The MME reconstructions also show some synchronous, but less pronounced, temperature variability in the low-to-mid-latitudes, whereas in in the LMR most temperature variability happens almost exclusively in the high latitudes of the northern hemisphere. The similarity of the reconstructions using only the ice cores and all proxy records is also evident in these diagrams, but the speleothem only reconstruction also does exhibit some temperature variability over the last millennium. The reconstruction uncertainty/error (Figure 6.2), which is defined as the standard deviation of the posterior ensemble, ranges from 0.14 to 0.20K and is more similar to the LMR reconstructions than the PHYDA reconstruction whose uncertainty ranges from 0.06 to 0.14K. The uncertainties of all reconstructions inversely follow the trend of how many proxy records are available, which is expected from the theory of the Kalman Filter. The uncertainty increase at the end of the 20th century, were many proxy records end, also reflects this relationship. The uncertainties for the single-model prior reconstructions lie in the same range and show similar trends, but are up to 0.04K smaller than the MME estimates (not shown). A striking feature of the MME uncertainty is a centennial periodicity, which stems from the prior matrix in the multi-time scale algorithm, because the largest time scale has been set to 100 years. In the single model prior reconstructions, this periodicity is most visible for the iHadCM3 prior.

To assess the similarity of the GMT curves, the Pearson correlation coefficients of the curves have been computed and visualized in Figure 6.4. The correlations have been computed separately for the pre-industrial period (PI) before the onset of global warming (800-1850CE), and the CWP (1850-1999CE). I did not detrend the time-series on purpose to see if the cooling and warmings trend are reproduced consistently, although this violates the assumption of stationarity that is underlying correlation. The assessment performed here is primarily of qualitative nature. For a more quantitative assessment of the trends other statistical instruments should be used. The values for the GISS model confirm the apparent lack of similarity to the other curves, both for the PI and the CWP, in spite of the detrending that has been performed to reduce the δ^{18}O drift in the GISS simulation. Of the DAISIM reconstructions, the MME, MME_iso, iCESM and isoGSM reconstructions are most similar to LMR and PHYDA with correlations between 0.46 and 0.51. The similarity of the MME using all proxy records and the MME only using the ice cores (MME_iso) in Figure 6.2 is reflected by a high correlation value of 0.92 (95% confidence interval 0.91-0.93). LMR and PHYDA, which are based on the same proxy record data but use different climate models as priors, have a GMT correlation is 0.61 (0.57-0.65). During the CWP, due to the global warming trend, the not-detrended correlations are larger. The MME ensemble based on ice core data only has the best correlation with respect to the instrumental Berkeley Earth (BE) (Rohde and Hausfather, 2020) time series (0.8, 0.73-0.85) after PHYDA and LMR, which have a correlation of 0.89 (0.86-0.92) and 0.92 (0.90-0.94). The MME has a very high correlation of 0.99 (0.99-0.99 due to rounding) to the ice core data only reconstruction.

The local correlations between the MME and the LMR reconstruction are shown in Figure 6.5 for the PI and the CWP. During the PI, both climate fields are most similar over Greenland, West and East Antarctica as well as the Arctic. This is also the case when the local time series are detrended (not shown). The largest patches of dissimilar climate fields with non-significant correlations can be found in Asia and in the central Pacific. In the CWP, the dissimilar patch over Asia disappears. Regions without significant correlation can still be found in the Northern

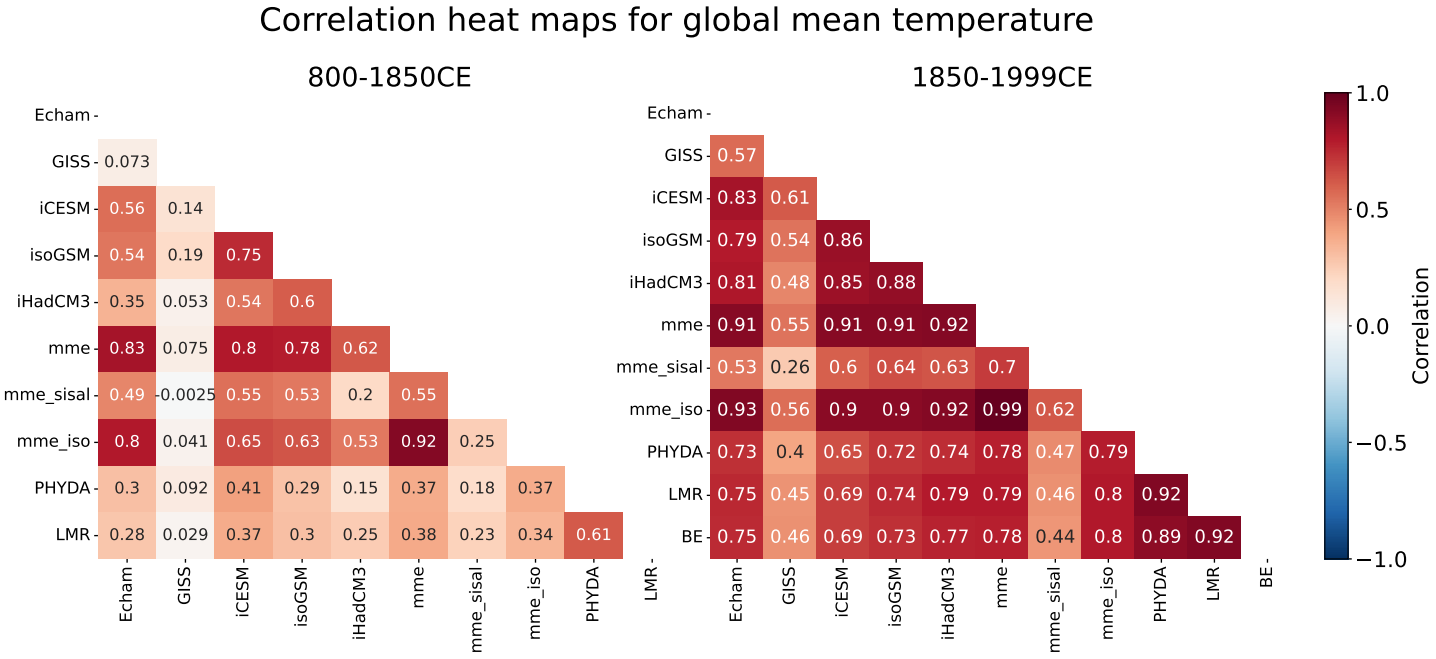

Figure 6.4: Heat map visualizing the correlation between the time series in Figure 6.1 and 6.2. The correlations are computed separately for the PI (left panel) and the CWP (right panel). The time series have not been detrended to assess similarity including the cooling and warming trends. No filtering of the signals has been performed. The CWP evaluation also includes the correlation with the observational GMT from the Berkeley Earth dataset (BE) (Rohde and Hausfather, 2020). mme_sisal and mme_iso refer to the multi-model ensemble reconstructions with the separate SISALv2 and Iso2k database records. The 95% confidence intervals of the correlations can be found in Appendix Figure B.10.

.

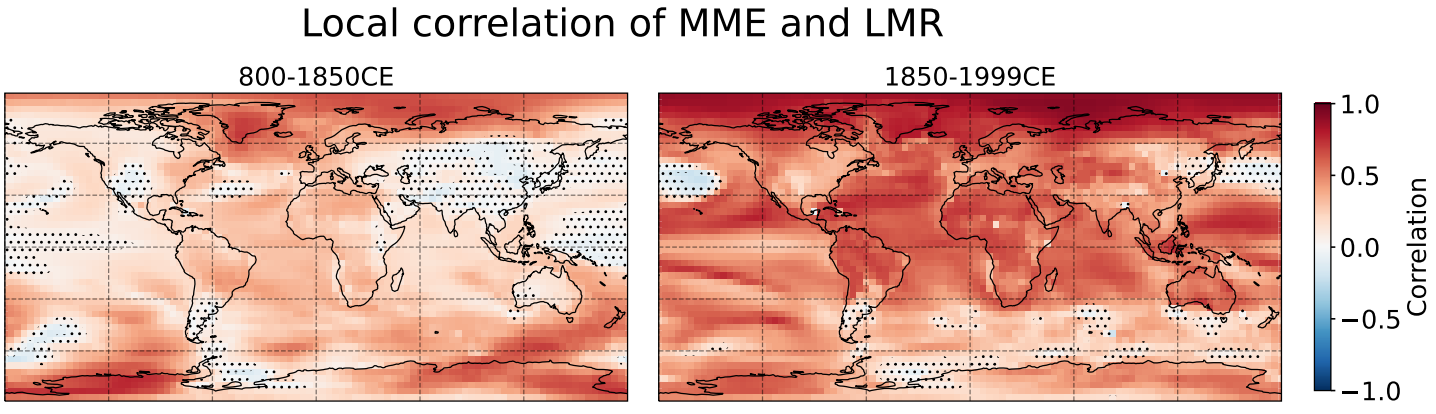

Figure 6.5: Correlation fields between the MME reconstruction (using both databases) and the LMR. The left panel shows the correlation for the PI (800-1850CE) and the right panel for the CWP (1850-1999CE). The local time series have not been filtered. The time series have not been detrended. The stippling indicates non-significant correlations (p>0.05).

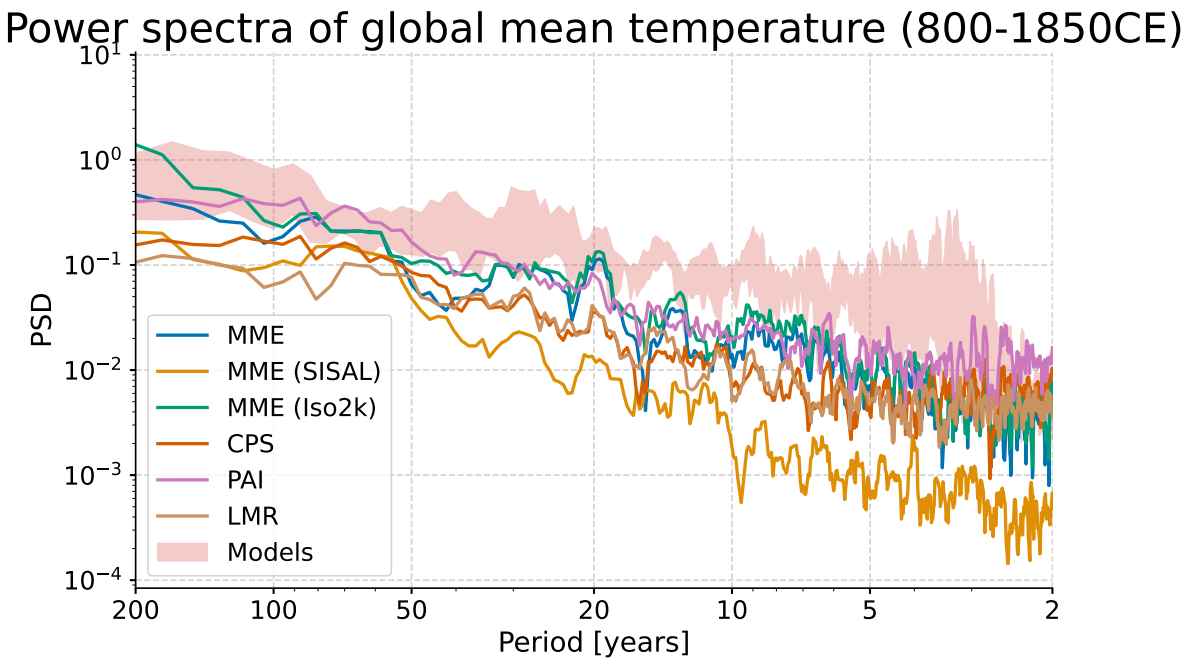

Figure 6.6: Power spectral densities of the DAISIM-MME reconstructions, LMRv2.1 and two reconstructions included in Neukom et al. (2019a), CPS and PAI. CPS (composite plus scaling) uses only annually resolved proxy records, whereas PAI (pairwise comparison) also uses non-annually resolved proxy records. The red shading indicates the range of spectra of the climate simulations used as priors. The spectra have been generated by applying the multitaper method to the non-standardized, detrended GMTs in the time period from 800 to 1850. The peak between 2 and 5 years for the models maily stems from the ECHAM5 simulation.

Pacific and close to the Antarctic circle.
To investigate the spectral composition of the reconstructed GMTs, the power spectral densities (PSD) of the DAISIM-MME reconstructions are plotted aside the LMR and two reconstructions from Neukom et al. (2019a) in Figure 6.6. The Figure also contains the PSD range of the last millennium simulations used as priors. The Neukom et al. (2019a) reconstructions are based on (almost) the same proxy record data as LMR [1], but use different CFR methods.
All PSD curves have a red spectrum, meaning that variability increases with period length. On all displayed time scales, the climate model priors exhibit most variability. The MME speleothem reconstruction has the least variability for annual to decadal time scales. However, this lack of variability is expected because many speleothems are used on longer than annual time scales. Exempt this reconstruction, the GMT from LMR has the least variability for decadal to centennial time scales. Here, only two other reconstructions from Neukom et al. (2019a) are shown for better visibility, but the lack of decadal-to-centennial variability is also visible in comparison to their other reconstructions. The PSD of the MME for decadal to centennial time scales provides a middle ground between the most and least variable reconstructions from Neukom et al. (2019a).

The curves of reconstructed global mean precipitation are shown in Figure 6.7. They also follows a hockey stick like curve over the last millennium, although the handle seems flat. A decrease in precipitation as for temperature over the last millennium is not noticeable by eye. The amplitudes of the precipitation peaks from the reconstructions performed in this thesis are

[1] Neukom et al. (2019a) contains the first version of LMR, while here the LMR version 2.1 is displayed. It uses an extended proxy record database similar to the one used by the PHYDA reconstruction (Steiger et al., 2018).

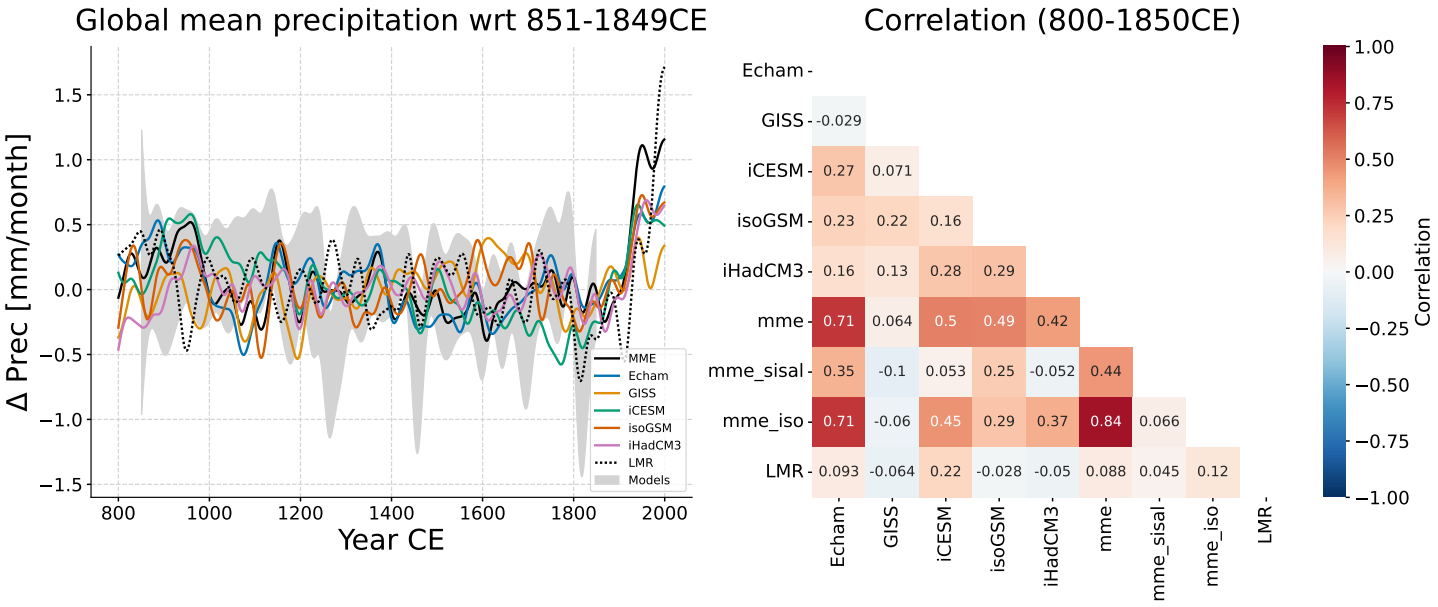

Figure 6.7: The left figure shows the global mean precipitation anomaly of the DAISIM reconstructions, LMR and the climate model simulations. The anomaly period is chosen as 851-1849CE. The time series have been low pass filtered with a 50 year Butterworth filter. The right figure shows the correlation heat map for the period 800-1850CE. The confidence intervals of the correlations can be found in Appendix Figure B.11.

more similar to the LMR reconstruction than for temperature. However, the signal phases are more different from each other, as indicated by the low correlation values in the corresponding correlation table. As for temperature, the signal from the MME is more similar to the MME based on ice cores only than on speleothems (correlation of 0.84 (0.82-0.86) against 0.44 (0.39-0.49)).

6.2 Reconstructions of temperature and precipitation in tropical South America

To give an example of the characteristics of reconstructed regional climate (anomaly) fields, the temperature and precipitation fields over tropical South America have been reconstructed separately. This region is particularly interesting for studying the potential benefits of incorporating speleothems into last millennium CFRs. The PAGES2k database, on which the PHYDA and LMR reconstructions are based, only contains few proxy records from that region, mainly tree data from the Southern Cone. Speleothems from South America are known to capture the history of variability of the South American Monsoon system, which governs the amount of rainfall in that region (Novello et al., 2018). Therefore, an anomaly reconstruction only using proxy records from that region is performed for the period 500-1999CE. Again, the 18th century is the reference period for the anomaly reconstruction. The starting point is set 500CE due to the availability of various records in that region even before 800CE. The reconstruction is based on 11 speleothems from South America, 7 from Central America and the Quelcaya ice core record. Except for the annually dated Quelcaya record, which represents annual variation in $\delta^{18}O$, the proxy records are uniformly resampled to 10 year means using the resampling technique for the multi-time scale DA. The proxy record error variance is set to $0.2‰^2$, thus smaller than in the global experiment because the proxy records are used on less timescales.
The results are compared to the LMR reconstructions, which provides both temperature and precipitation fields. The Southern Cone region below 57°S is not studied due to the lack of

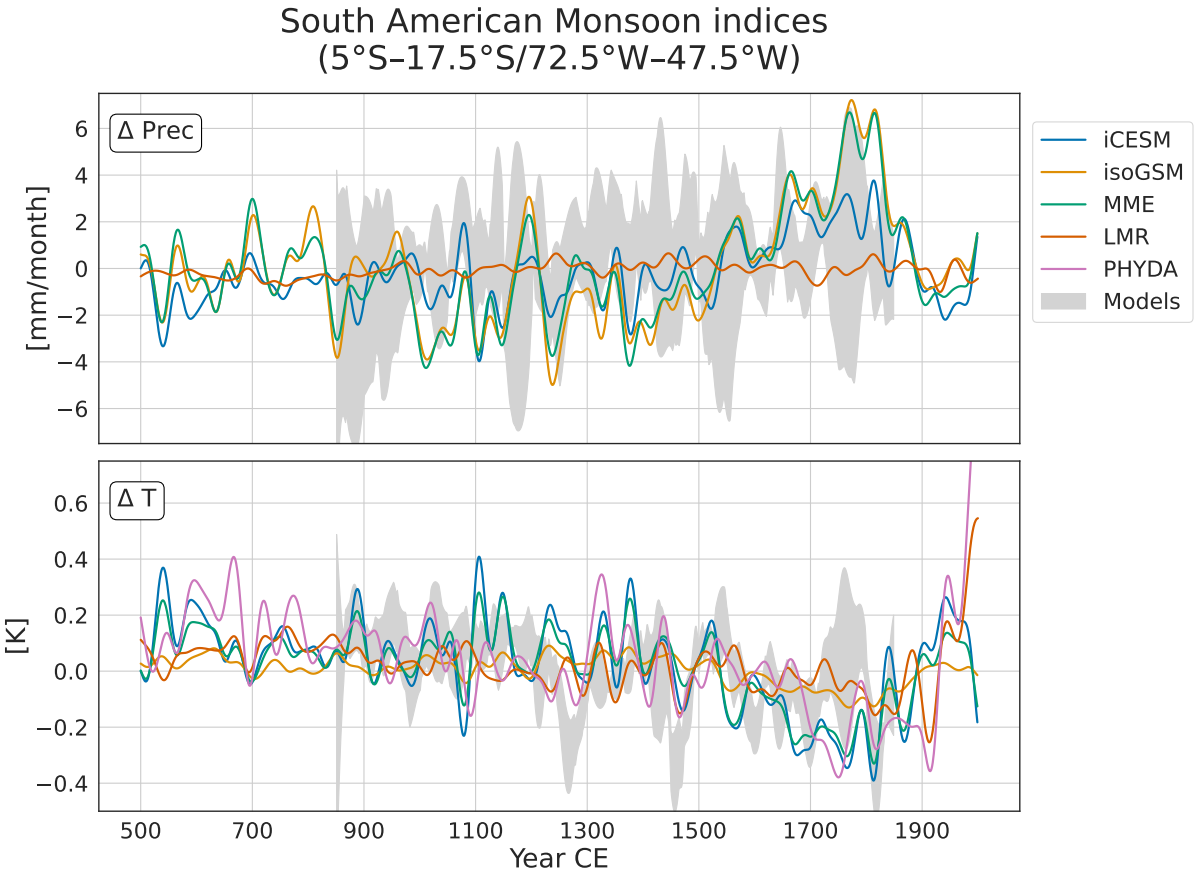

Figure 6.8: Mean precipitation anomaly (upper panel) and temperature anomaly (lower panel) for the core monsoon region as defined in Vuille et al. (2012) from three DAISIM reconstructions (iCESM, isoGSM, MME), LMR, PHYDA and the climate model simulations (mean±standard deviation). The PHYDA reconstruction does not provide precipitation fields and is thus not included in the first panel. The reference period is 851-1849CE.

speleothem and ice core proxy records in that region. Although it is in part included in the figures, it is not discussed in the analysis here.

To asses changes in rainfall over tropical South America during the last 1500 years, a simple index for the intensity of the South American Monsoon is defined as in Vuille et al. (2012). It is calculated as the mean rainfall over the core region of the South American Monsoon (5° S - 17° S/72.5° W - 47.5° W) (see the blue box in Figure 6.9). Figure 6.8 presents the precipitation and temperature anomalies from that region using iCESM and isoGSM, which are the models of highest spatial resolution, and the MME (excluding GISS). The MME uses climate fields regridded to the resolution of isoGSM. The figure also shows the precipitation anomaly reconstructed by the LMR, which is almost unchanged during the last millennium.

The reconstructions performed for this thesis indicate a pronounced wet phase in the core monsoon region from the 16th until the 19th century, the so-called Little Ice Age (LIA). IsoGSM exhibits the largest amplitudes in the precipitation anomaly signal of up to 5mm/month. The model simulations do not show a clear wet period during the LIA.

For the temperature anomaly of that region, during the LIA a cooling can be recognised for all reconstructions (~ -0.25K), although it is almost indistinguishable for the LMR reconstruction. In contrast, the PHYDA temperature reconstruction indicates a stronger LIA cooling. The reconstructed temperature fluctuates less for the isoGSM model and more for iCESM and the MME, which is the opposite of the situation for precipitation. The MME and iCESM reconstructions indicate warm phases from the 12th until the 14th century.

The temperature anomaly for the region in the simulations follow the simulated GMT, which is mainly influenced by the imposed volcanic forcing and seen in form of troughs for instance in the 13th, 15th and 19th century. The exceptionally strong 1815 eruption of Mount Tambora in Indonesia is also visible in the reconstructions for the core monsoon region.

6.2.1 Centennial temperature and precipitation fields

To investigate the climate over tropical South America further, the centennial mean temperature and precipitation fields are visualized in Figure 6.9 and 6.10. The corresponding fields from LMR, which do not exhibit much variation, can be found in Appendix B.12 and B.13. The LMR suggests little changes in precipitation and temperature during the last millennium. In contrast, the DAISIM-MME reconstruction has more spatially and temporally variable patterns. According to that reconstruction, the period from the 16th until the 19th century was cooler than the 800-1850CE mean for each region except for the north eastern tip of Brazil (Nordeste), which shows a particular behaviour. This region appears cooler than the millennial mean until 900CE. The closest proxy record shows a strong δ^{18}O depletion during that period. The precipitation anomaly field is less homogenous than the temperature anomaly field. The MME reconstruction indicates that tropical South America was drier in the period from 500-1500CE and then went into a wetter phase until the 20th century. The peak of the wet phase occurred during the 18th century, which was wetter than the mean for almost all the continental parts of tropical South America and Central America. According to the MME reconstruction, the Nordeste was wetter than the mean from 500-900CE, a pattern similar but more spatially extended than the cold anomaly for temperature during that period. The 11th century is the only century apart from the 20th century, in which dry conditions over all tropical South America prevailed. For the climatic anomalies over the oceans surrounding the land mass, different patterns for temperature and precipitation are evident. Whereas temperature changes have the same sign for the land and the ocean, the patterns are more complex for precipitation. Dry conditions over land were accompanied by wetter conditions in the equatorial eastern Pacific and vice versa. For instance, during the peak terrestrial wet phase of the 18th century, the eastern equatorial Pacific was drier than average.
In the Figures 6.9 and 6.10, the proxy record anomalies which have been drawn on the climate anomaly fields help interpreting the results. They often show a dipole between the proxy records from the northern/eastern part of tropical South America and the southern/western part. In the reconstructions of temperature and precipitation, this dipole is mostly reflected in form of the anomaly over north-eastern Brazil. This follows the common interpretation of δ^{18}O in precipitation: More depleted δ^{18}O values are interpreted as stronger rainfall and colder temperatures. However, the record in the northern part of Brazil near the mouth of the Amazon river stands out the reconstructed fields. This exceptionality is also visible in the reconstruction of the δ^{18}O fields (Figure 6.11) in a less pronounced form. This reconstruction also exemplifies, how the δ^{18}O proxy record anomalies are converted into δ^{18}O anomalies of smaller amplitude by the EnKFs due to the proxy and model errors, as well as the PSMs.

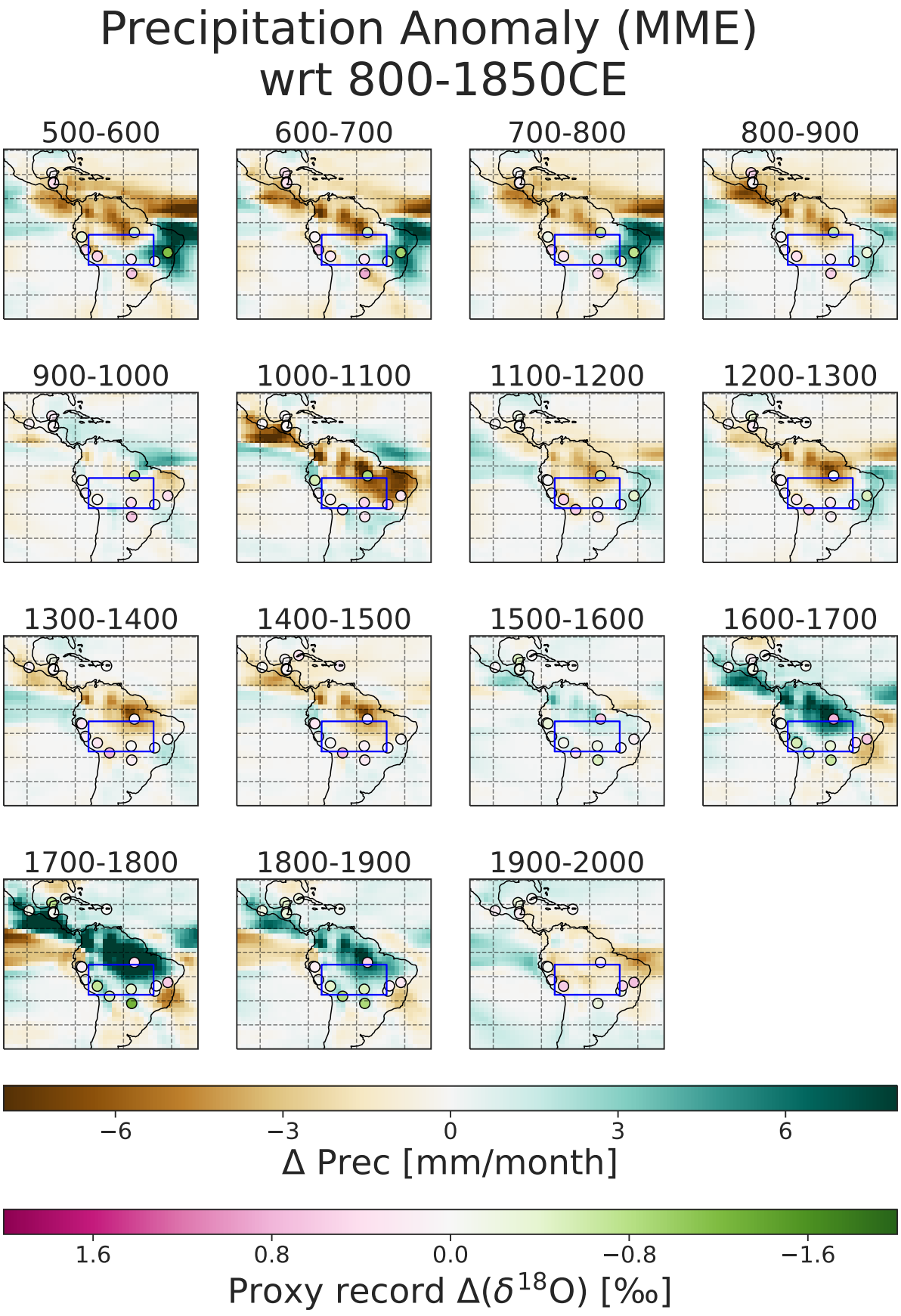

Figure 6.9: Centennial mean precipitation anomaly fields for tropical South America from the 6th to the 20th century using the MME. The dots indicate the available proxy records during the centuries and their colour the centennial mean anomaly with respect to the reference period of 851-1849CE. The values of the colorbar go from positive to negative values to facilitate the interpretation in terms of precipitation (more depleted values equal more precipitation). The blue box is the core monsoon region as defined in Vuille et al. (2012).

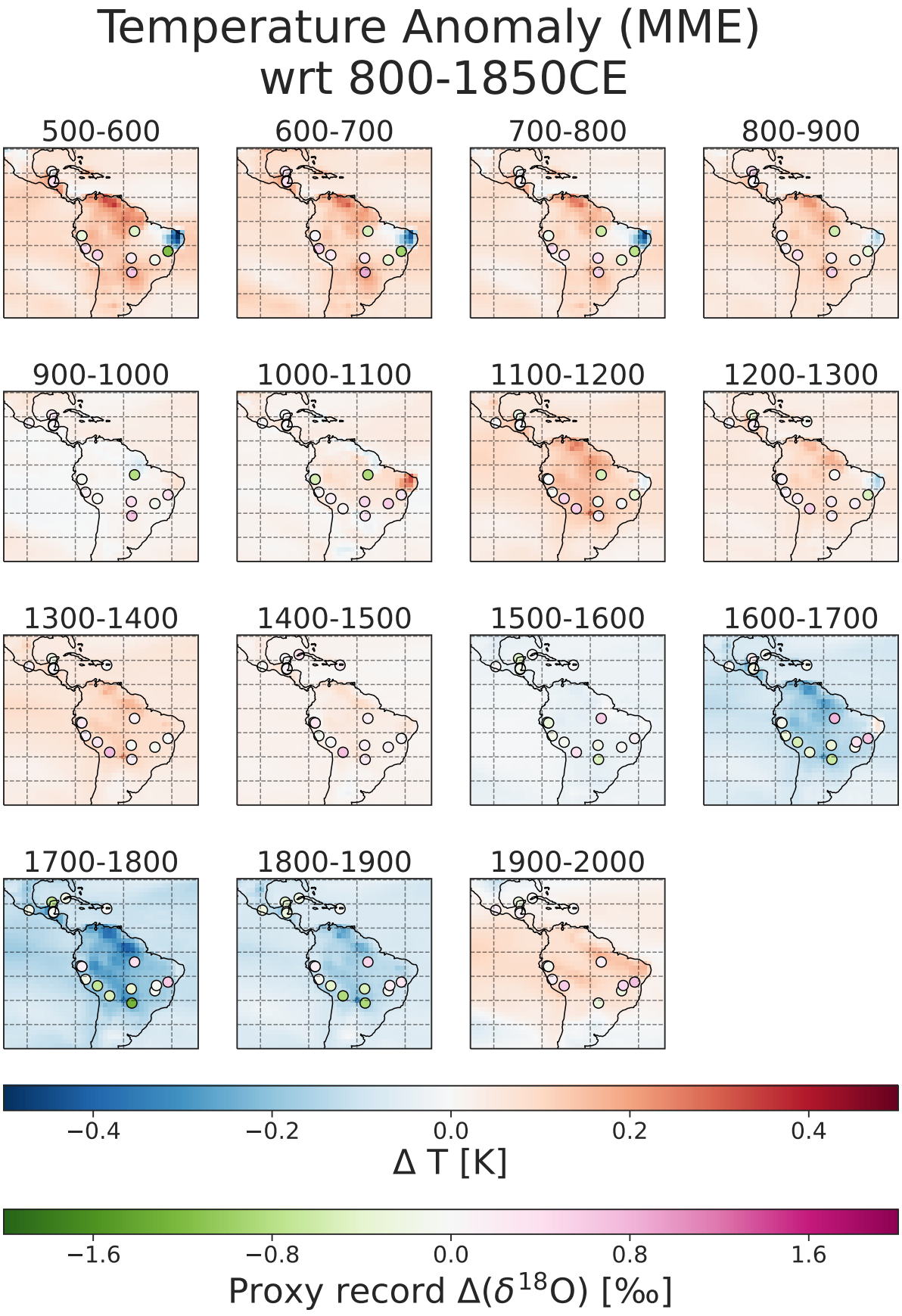

Figure 6.10: Centennial mean temperature anomaly fields for tropical South America from the 6th to the 20th century using the MME. Note, that in comparison to Figure 6.9 the colorbar for the proxy record anomalies is reversed, in order to facilitate their interpretation (more depleted values equal colder temperatures).

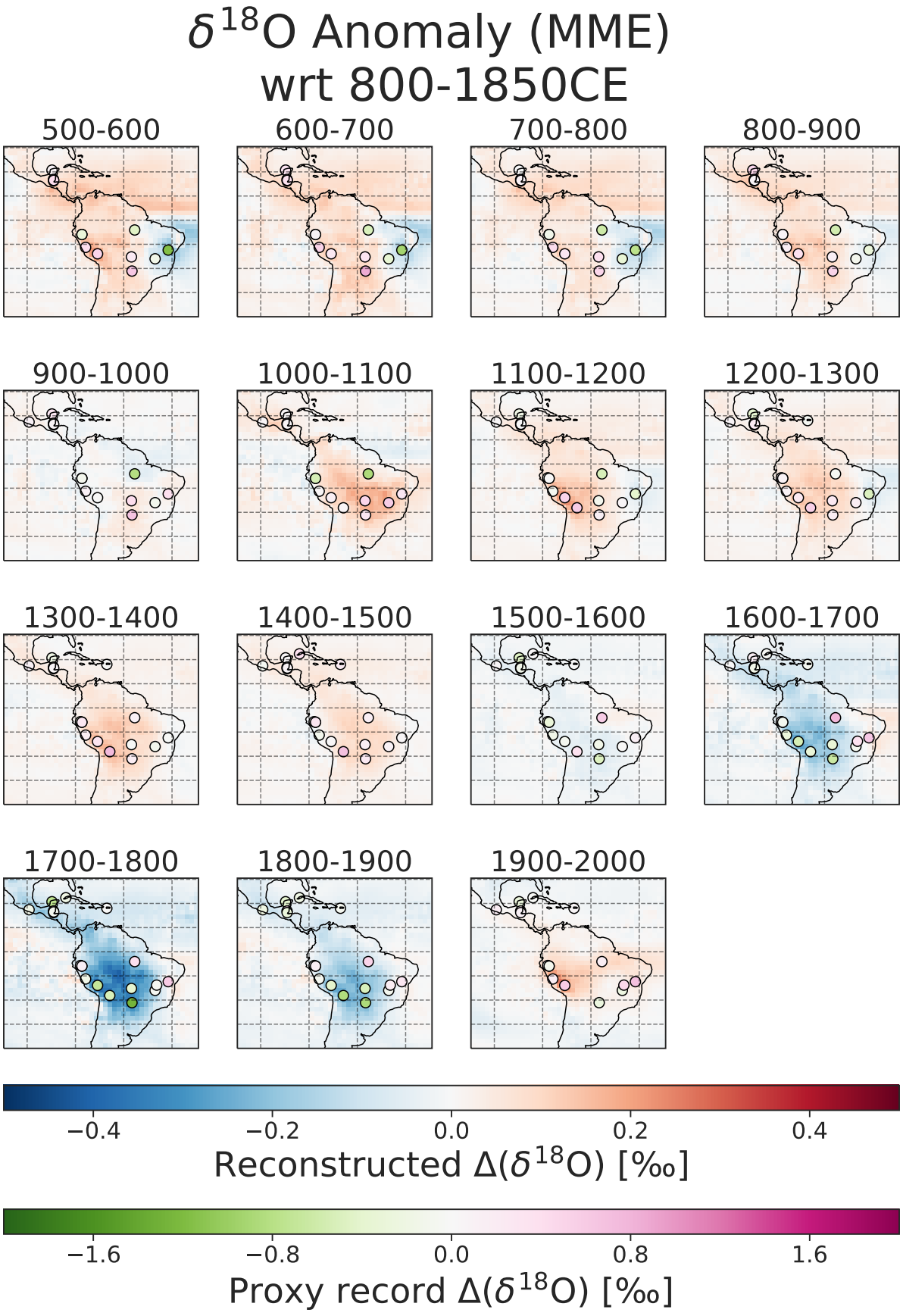

Figure 6.11: Centennial mean δ^{18}O anomaly fields for tropical South America from the 6th to the 20th century using the MME. Note the differing ranges for the proxy record values and the δ^{18}O field. The different ranges and colormaps have been chosen for illustrating that the large proxy record anomalies are not reflected in amplitude by the reconstruction.

Chapter 7

Discussion

7.1 Characteristics of reconstructed temperature and precipitation

The reconstructed GMT anomalies from DAISIM for the period 800-2000CE exhibit the well-established patterns of a long-term cooling trend which reaches its lowest point in the period of the LIA in the 16th to 19th century (Figures 6.1, 6.2 and 6.3). The cooling is reverted by a sharp increase since the onset of the CWP in the 19th century. This pattern was reproduced consistently by all model priors, except for the reconstruction using the GISS model, which reproduces neither the cooling nor the warming. Although the model priors are simulations for the years 850 to 1850CE, they can thus be used to reproduce the global warming trend. The model priors serve as covariance structure providers in the offline PaleoDA scheme. The reconstructed cooling trend is part of a global cooling which started during the mid-Holocene (8000BP) (Gulev et al., 2021; Marcott et al., 2013). DAISIM indicates a relatively warm phase around 900-1000CE, which would fit into the nowadays refuted narrative of the Medieval Climate Anomaly(MCA) as a globally warm period (Neukom et al., 2019a). However, there is only little proxy data available during that period ($\sim$ 30 proxy records per year) and this period just marks the beginning of the DAISIM reconstructions. While it would have also been possible to use the available speleothem and ice core data for reconstructing the climate signal from the year 0CE onwards, there are even fewer available proxy records before 800CE. Although the terms Medieval Climate Anomaly and Little Ice Age are used in this thesis to describe periods of the climate during the last millennium, a cautionary use of these terms is advised. Neukom et al. (2019a) showed, that in contrast to the CWP, there were no warm and cold periods that occurred at the same time on the whole planet during the last millennium.

The GMT changes in DAISIM appear disproportionately strong in amplitude in comparison to PHYDA and in particular the LMR (Figures 6.1, 6.2 and 6.3), which suggests temperature changes of 0.1-0.2K instead of 0.4K. It is important to note, that the LMR stands out in comparison to other reconstructions of the last millennium, for instance from Neukom et al. (2019a) (see their Figure 1), that do exhibit temperature variation amplitudes similar to or even larger than DAISIM. LMR and PHYDA are calibrated on instrumental data which follows the warming signal of the CWP and then use the obtained statistical relationship for the PSM over the whole last millennium. This calibration method might decrease the impact of proxy data further back in time[1]. The Hovmöller diagrams of the latitudinal mean temperature (Figure 6.3) show, that the largest changes in temperature can be found in the high latitudes, and that the cooling trend

[1]It is noticeable, that LMR which only uses the anomalies from 1951-1980 for the calibration shows smaller temperature variations than PHYDA, which calibrates the proxy record data from 1920-2000. The precise methodologies employed by PHYDA and LMR have not been compared systematically yet, such that my hypothesis remains to be tested.

in the GMT is mainly caused by temperature changes at the poles. The DAISIM reconstructions also exhibit larger temperature variations in the low-to-mid-latitudes, which are less visible in the LMR. In the LMR, larger temperature variations occur mainly in the high latitudes of the northern hemisphere. It can be summarized, that the GMT anomalies in DAISIM are realistic, and thus comparable to existing reconstructions. This result encourages incorporating the ice core and speleothem proxy record data into reconstructions based on the PAGES2k database. It will then be possible to estimate, to what extent the sharp increases and declines reconstructed by DAISIM are sustained or refuted by other types of climate archives. The DAISIM temperature fields are most similar to the LMR across Greenland and West Antarctica (Figure 6.5). The large correlations could be rooted in a proxy record data overlap of DAISIM and LMR, which also uses some ice core records from these regions. However, LMR uses a calibration of ice core δ^{18}O to temperature instead of the δ^{18}O values in the DA, such that a similarity does not necessarily have to arise. To confirm the hypothesis of the similarity due to a proxy data overlap, a careful investigation of the reconstructions in these regions is required. One should also compare the difference of using the statistical calibration of δ^{18}O to temperature and δ^{18}O directly for these regions. Such a comparison has been performed with simulated ice core data by Dee et al. (2016), who found similar reconstructions for both PSM types in the high latitudes.

The reconstructed precipitation changes during the last millennium are more similar in amplitude range for the LMR and the reconstructions (Figure 6.7). However, as expected there is less temporal coherence, which is also noticeable between the reconstructions using different model priors. Precipitation changes are often more regionally constrained and less uniform than temperature changes. The mean decorrelation lengths of simulated δ^{18}O to precipitation in the climate models are typically shorter than the decorrelation lengths for temperature (not shown). The difficulty of reconstructing precipitation is also reflected in the decreased reconstruction skill of the PPEs in comparison to reconstructing temperature and δ^{18}O fields (Figure 5.3). Interpreting the resulting precipitation curves thus has to be done with caution. The LMR reconstruction can not be considered a good baseline, because the employed proxy record data from PAGES2k primarily reflects temperature and not precipitation changes. To enhance the DAISIM reconstruction of hydroclimate, a natural choice would consist of using more climate archive types from the Iso2k hydroclimate archive database (Konecky et al., 2020), which for instance comprises proxies such as δ^{18}O from wood or lake sediments. Proxies of hydroclimate can be difficult to interpret. Depending of the archive type, they often not only reflect precipitation, but also soil moisture changes, thus the combined effect of precipitation, evapotranspiration, and soil water processes (Consortium, 2017). Therefore, variables better suited for hydroclimate reconstructions as the Palmer Drought Severity Index (PDSI) and the Standardized Precipitation Evapotranspiration Index (SPEI) have been developed, which are also included in the PHYDA last millennium reconstruction instead of precipitation. Reconstructing these would permit a comparison to the hydroclimatic fields from PHYDA.

To perform a more meaningful reconstruction of precipitation changes, I have laid the focus on a regional reconstruction over tropical South America. It is an archetypical region for speleothem studies, as speleothem records from numerous caves have been sampled and published and the availability of other climate archives, especially in the center of the continent, is limited. Speleothems from tropical South America are considered reliable archives of intensity changes of the South American Summer Monsoon (SASM), which leads to a pronounced wet season during the months of December, January, and February (Zhou and Lau, 1998). DAISIM found an increased wetting during the LIA, with a peak during the 18th century for both the core monsoon region and the northern part of South America (Figures 6.8 and 6.9). This result concords with studies that interpreted single-or multiple speleothem records (Bird et al., 2011; Campos et al., 2019; Deininger et al., 2019; Orrison et al., 2022; Vuille et al., 2012), thus in part

the same records as used for DAISIM. The key difference is, that the PaleoDA method allows for a CFR, which enhances the interpretation of proxy record data. The mentioned studies also see the speleothem records as indicators of a marked dry period during the MCA, especially in the 11th and 12th centuries. The DAISIM reconstructions for South America support this hypothesis, though it is better visible in the negative precipitation anomaly fields for parts of northern and central South America than for the core monsoon region. Looking into the time periods associated with the MCA and the LIA shows, that the dry and wet phases were not homogeneous over the whole continent. The north-eastern part of Brazil (Nordeste) stands out, which is also reflected in the δ^{18}O dipole between eastern and western South American records and that has been discussed extensively in the literature (Deininger et al., 2019; Novello et al., 2018). Changes in the hydroclimate of tropical South America have been attributed to changes in the SASM, which are driven by latitudinal displacements of the Intertropical Convergence Zone (ITCZ) (Vuille et al., 2012) and the South Atlantic Convergence Zone (SACZ). The variability of the latter has been taken as an explanation in variations of the δ^{18}O dipole between eastern and western South American records (Novello et al., 2018). The LMR reconstruction stands in strong contrast to the DAISIM precipitation anomalies for South America, as it suggests only very little precipitation variability over the whole continent and the core monsoon region (Figures 6.8 and B.12). This result primarily reflects the lack of proxy record data from the region in the PAGES2k database LMR uses. LMR uses proxy records from Central America, the Quelcaya ice core record from the Andes, and tree data from the Southern Cone. Future PaleoDA studies building on DAISIM could strengthen these assumptions by explicitly assimilating climate indices for the ITCZ and SACZ position, as well as by assimilating also more climate variables of the atmospheric conditions, for instance sea level pressure.

Speleothems from South America are usually not interpreted in terms of temperature changes. However, PaleoDA also allows for the straightforward reconstruction of temperature from the South American records (Figure 6.8 and 6.10). During the LIA (16th-19th century), DAISIM exhibits a pronounced decrease in temperature for both the core monsoon region and the northern and central parts of South America(Figures 6.8 and 6.10). The preceding centuries showed warmer conditions, especially the 12th century, which could be seen as the MCA for that region. The δ^{18}O dipole is reflected in form of colder conditions in the Nordeste from the 6th until the 10th century. The reconstructed spatial patterns reveal a possible issue of the PaleoDA method in terms of spatial variability. The centennial anomalies of the single record in the north of Brazil (Paraiso cave) do not fit into the reconstructed climate fields if depletion of δ^{18}O is interpreted as decreased temperature or increased precipitation. The dipole pattern over the Nordeste could have been expected to extend further north and west. The Paraiso cave lies in a special location. The precipitation at the cave location comes predominantly from the tropical Atlantic, whereas the western and southern regions of tropical South America receive precipitation that has undergone more processes in the lowlands (Wang et al., 2017). Having more proxy records in the western and southern parts of tropical South America might bias the reconstruction toward the anomalies recorded in these regions.

It would also be particularly interesting to see if the covariance structures in the climate model simulations support the δ^{18}O dipole over South America. The EnKF uses the spatial covariance of the model simulations to spread the information from proxy records to nearby locations and provides a fit of the model and the proxy data. It can be supposed that it tends to produce spatially too homogeneous climate fields. Reduced spatial diversity by the EnKF in PaleoDA has not been assessed systematically yet. However, it has been mentioned in the Holocene reconstruction by Erb et al. (2022) (see the outstanding proxy record anomalies in their Figures 9 and 10), or in the study of spatial temperature correlations of last millennium reconstructions by Bakker et al. (2022) (see their Figure 6). Investigating and potentially improving the spatial heterogeneity of CFRs obtained through PaleoDA with the EnKF might be an opportunity to justify the use of covariance localization, which limits the influence of distanced proxy records

and would thus also limit the influence of regions which have more proxy records than others. The spatial homogeneity of reconstructed fields could be quantified in terms of the spatial degrees of freedom (Bretherton et al., 1999) and how these are limited by the degrees of freedom in the prior simulations.
The DAISIM-CFRs of tropical South America demonstrate the potential of incorporating speleothem records into CFRs. However, DAISIM only represents a prototype of what could be even more insightful reconstructions. DAISIM could be further refined by making use of data from PAGES2k and Iso2k data that has not been used to obtain a more complete and reliable picture of the climatic changes on the continent. For instance, a lot of tree data is available for the Southern Cone, which is also data that the LMR used. The Southern Cone has not been considered here because of the lack of speleothem and ice core data. It is noticeable, that it is one of the few regions where the MME and LMR reconstructions do not have a significant correlation for both the PI and CWP (Figure 6.5). According to the area of the averaging kernel (Figure 5.2), this region is less influenced by the speleothem and ice core locations than the rest of South America. With its large variety of available climate archives, the South American continent could also make an ideal test bed to study the fundamental issue of distinguishing the effects of dynamic and thermodynamic changes on hydroclimate. An important caveat in all the DAISIM reconstructions, which will also be discussed in the following section, is that no systematic sensitivity tests concerning the defined proxy record error and time scales have been performed. However, these prototype global and regional reconstructions imply, that meaningful multi-time scale reconstructions with the ice core and speleothem proxy records are possible.

7.2 Influence of speleothem and ice core records on the last millennium reconstructions

The correlation analysis showed, that the reconstructed GMT and precipitation signal is mainly influenced by the ice core records (Figure 6.5). This is also reflected in the uncertainty/estimation error, which is smaller for the reconstruction from ice cores (Figure 6.2). This does not support the hypothesis, that the speleothems could contribute more information because they are spatially better distributed, whereas the available ice core records are mainly clustered around specific locations such as Greenland and West Antarctica. First and foremost, I suspect the larger influence of the ice cores to be a consequence of larger anomalies in the signal of the ice cores. In the Hovmöller diagrams of the latitudinal mean temperature (Figure 6.3), the DAISIM-MME reconstruction based on ice cores exhibits larger temperature fluctuations than the speleothem reconstruction, both for the high and the low latitudes. The diagrams of both LMR and DAISIM reveal, that the largest temperature changes over the last millennium can be found at the poles. The cooling trend in the GMT over the last millennium is thus also mostly a phenomenon recorded at the poles. Due to the phenomenon of polar amplification, the poles are more sensitive to changes in the GMT. Hence, ice cores from these regions may be better recorders of these changes than remote speleothems in the low-to-mid latitudes. The ice cores are also crucial for reconstructing the temperature increase during the 20th century in DAISIM, which cannot be reconstructed by using solely the speleothems. This is probably due to the locations of the speleothems, their lower temporal resolution and thus fewer available data points. However, dismissing the speleothems as proxy records for reconstructing global climate changes would not do them justice. The Hovmöller diagrams (Figure 6.3) show, that in the low-and-mid latitudes temperature changes are indeed reconstructed. Regionally, the reconstructed precipitation changes over tropical South America are an example of what could not have been reconstructed using ice core data alone. The global MME Iso2k reconstruction is not able to reproduce the pronounced precipitation over tropical South America during the LIA and MCA (not shown).
Furthermore, I see the possibility that the MME experiment disproportionally favoured the

ice core records due to how it was conducted. First, an important, yet fairly unconstrained, variable in the experiments is the error variance attributed to the proxy record time series. In the global reconstruction, it has been set uniformly to $0.5‰^2$ due to a lack of better constraints. This value is larger than most measurement uncertainties provided by the databases. In the Kalman Filter, the observation error is weighted relative to the variance of the PSM-converted δ^{18}O. δ^{18}O is more variable at the poles. Hence, a globally fixed proxy error is less relevant there, which could lead to an increased influence of the ice cores. The lack of constraints for the proxy record error is currently a limiting factor in PaleoDA (when not using the statistical PSM). Second, in the multi-time scale approach here, proxy records have been reused on all time scales larger than their median resolution by computing the respective multi-year mean to give more weight to the limited proxy record data. As most ice core records are of annual resolution, they have been effectively used more often than the more coarsely resolved speleothems. Sensitivity tests for quantifying the effect of reusing the proxy records, and which time scales are adequate need to be performed. The DAISIM reconstruction only presents one realization out of a diverse set of options. Multi-timescale PaleoDA is still in its very early phase and has not been employed for the last millennium before.

Before the application of the PaleoDA framework to the real proxy data, a preliminary analysis in form of PPEs (Figures 5.3, B.9 and B.8) and the area of the averaging kernel (Figures 5.2, B.6, and B.7) was performed. This analysis did not indicate, that using the ice core locations would have such a larger impact. The question thus is, how the DAISIM reconstructions and the PPEs could be reconciled in future studies.

The main shortcoming of the PPEs, which were also meant to validate the PaleoDA framework as such, is that they were not adapted to the real temporal and spatial availability of the proxy record data. A realistic simulation with PPEs would need to take into account the time scales of the individual proxy records and at which time proxy records are actually available.

Furthermore, the pseudoproxies need to be created via realistic PSMs. The PPEs involved speleothems and ice core PSMs on varying levels of complexity. However, the results from pseudoproxies created with the compaction and firn diffusion as in Dee et al. (2015) were inconclusive due to a total lack of reconstruction skill. In consequence, the ice core PSM has not been employed in the DAISIM reconstructions, where only a slight modification of the simulated δ^{18}O via the precipitation weighting was performed. In its practical use, the ice core PSM also showed to be prone to numerical instabilities and thus needs a reevaluation. Only two PaleoDA studies have used this particular ice core PSM. It was employed in the pseudoproxy study by Dee et al. (2016) alongside PSMs for other climate archives. The authors assumed a small, non-realistic proxy record error. No fundamental flaws with the ice core PSM seemed to occur. Steiger et al. (2017) also used the ice core PSM with δ^{18}O from ice cores and isotope-enabled simulations for the CWP, but were not able to reconstruct the global warming trend. The authors did not test if using the simulated δ^{18}O without the PSM would have led to better results. In the PPEs performed here, the use of the full speleothem PSM, including the karst fractionation and filtering process, for pseudoproxies produced more promising results than the ice core PSM. By selecting data points on non-annual time scales it could be used to simulate the low-temporal resolution of speleothem records.

An important aspect of PSMs not touched upon in this thesis is their use to inhibit seasonal biases on the reconstruction via a modification of the local covariance to annual mean values. Some proxy records represent seasonal means instead of annual means, and it has been hypothesised that Holocene temperature reconstructions, e.g. Marcott et al. (2013) are affected by these. For instance, the speleothem records from South America used for DAISIM are mainly created during the summer monsoon season (Bradley, 2015). This effect is accounted for by the monthly precipitation and infiltration weighting for the calculation of annual δ^{18}O, but the sea-

son during which a proxy record could also be set explicitly. For the observation operator this would mean only using specific months in the calculation of the annual mean $\delta^{18}O$. This way, PaleoDA becomes a great tool for artificially testing the influence of specific seasonal means on the annual reconstructions, as performed by Erb et al. (2022). Future studies using speleothems and ice cores should look explicitly into potential seasonal biases of the proxy records and how precipitation and infiltration weighting compares to the explicit setting of months for the seasonal means.

In their general use in PaleoDA, PSMs have the purpose of representing the relationship of the simulated climate variables to the proxy record observations for both the mean and the covariance. In the anomaly reconstructions performed here, the importance of the PSM is restricted to the covariance relationship. It is unclear if in the case of isotope-enabled model simulations, the covariance relationship to simulated temperature and precipitation has to be further altered by the PSM, which would especially be the case when filtering effects are incorporated. Furthermore, the PSM should also be connected to the proxy record error variance mentioned earlier as is required by the Kalman Filter (Equation 2.3), and not be set arbitrarily. To fulfil these needs, I conclude that specialized PSMs focused on the application in PaleoDA need to be developed. In PaleoDA, it is more important to reproduce the spatial covariance than to represent the local process of a cave/ice core location. Once commensurate PSMs, proxy errors, and time scales for the proxy records have been established, it would make sense to perform PPEs to mimic real reconstructions. Then, the original question of how different archive types contributed to the reconstruction could be more meaningfully answered. For instance, the proxy record and prior influence could be investigated by means of the Kalman gains for each location, the area of the averaging kernel or a new statistical approach proposed by Harris et al. (2021), which characterizes the added value of proxy records in PaleoDA reconstruction by statistically comparing the prior and posterior distributions. In addition, it should be studied how many records are necessary and which degree of spatial independence between them is needed to meaningfully reconstruct global means and climate fields.

To conclude this section, the sensitivity tests of using speleothem and ice core records separately reveal that the impact of speleothem and ice core records on the reconstruction is yet to be understood. The correlation and Hovmöller diagram analysis show a pronounced contrast between the real reconstructions and the PPEs. Reconciling them by refined PPEs will help in understanding both, and the underlying mechanisms of PaleoDA better. However, it remains to be estimated if the model priors provide climate variations that are sufficiently temporally and spatially variable to perform such PPEs.

7.3 Temporal variability of the climate reconstructions

Climatologists' understanding of Earth's climate variability is based on climate proxy records, reconstructions, and model simulations. A key task lies in finding mechanisms to understand the represented climate variability, and assessing how differences between models, reconstructions and proxy records can be reconciled. Therefore, it is essential to understand how climate variability is reconstructed by a CFR method such as offline PaleoDA with the EnKF and if the method has spectral artefacts. This aspect of PaleoDA has not been systematically assessed yet. However, in the GMT reconstructions presented by Neukom et al., 2019a, it is apparent that the PaleoDA reconstruction has the lowest variability on decadal to centennial time scales compared to other CFR techniques.
A central motivation behind this thesis was the incorporation of speleothems and ice cores into PaleoDA reconstructions to gain a more realistic representation of climate variability on decadal to centennial time scales. The lack of decadal to centennial variability in climate simulations

compared to climate archives has been demonstrated in numerous independent studies as Bühler et al. (2022), Ellerhoff et al. (2022), and Laepple and Huybers (2014). Here, I focused more on the temporal variability of GMT than the local variability at the individual model grid cells, although the reported model-data mismatch especially refers to the latter. The DAISIM reconstruction using both speleothems and ice cores reproduced larger GMT variability on decadal to centennial time scales compared to the LMR (Figure 6.6). However, this result seems to stem mainly from the ice core records, as the GMT reconstruction based only on the speleothem records lacked variability on all time scales. The speleothems might have contributed to variability at the local level, which has not been investigated here.

Extending the annual PaleoDA algorithm to a multi-time scale algorithm, which was a basic necessity for the incorporation of non-yearly resolved proxy records represented an ideal opportunity to look into the reconstructed variability with PPEs. Simple PPEs reusing pseudoproxies on various time scales clearly demonstrated, that the incorporation of pseudoproxy records on longer-than-annual timescales improved the representation of decadal to centennial variability on both the local and global level (Figures 5.6 and 5.7). This finding contradicts the idea, that information about the spectrum of temperature is already carried by the annual proxy records in PaleoDA, corroborating the hypothesis by Steiger and Hakim (2016), who initially developed the concept of multi-time scale PaleoDA. To strengthen the findings, the experiments should be repeated using a more diverse set of possible proxy record locations and by varying the proxy record error, which was set as realistically large here. In addition, a set of possible time scales on which proxy records can be used should be tested to identify critical time scales where the multi-time scale approach does make a difference. Future studies with additional comparison to the spectra of the proxy records are required to determine how local variability is translated into local and global climate variability in the PaleoDA-algorithm. Apart from these sensitivity tests, a more mathematical investigation of the differences in the covariance structure on various time scales could be attempted to better comprehend the multi-time scale algorithm.

The lack of investigation on the topic of climate variability in PaleoDA reconstructions is manifest. Although the Holocene temperature reconstruction by Erb et al. (2022) used a multi-time scale PaleoDA approach to enable more temporal variability in the reconstruction, the authors did not assess the reconstructed variability. Multi-time scale PaleoDA is a field that needs yet to be established and also justified. In contrast, there are studies investigating the reconstructed temporal climate variability for other CFR methods. For instance, Smerdon et al. (2016) looked into the local scaling coefficients for pseudoproxy reconstructions produced by regression-based methods. Nilsen et al. (2018) assessed the performance of the Bayesian Hierarchical Model BARCAST by performing statistical tests on the spectral characteristics of reconstructed time series.

The results presented here shed first light on how offline PaleoDA with the EnKF influences the reconstructed temporal variability as a CFR method. Making use of the multi-time scale approach and ice core and proxy record data, the PaleoDA reconstructed larger climate variability than existing PaleoDA reconstructions. The reconstruction of variability is a topic of fundamental importance, which needs to be elucidated further. In light of the fact, that more PaleoDA reconstructions are now aiming at transient climate periods with a prior ensemble which changes through time, a thorough assessment for a climatically stable period as the last millennium is imperative for understanding the reconstructed spectral characteristics better.

7.4 Model biases, inter-model differences, and the stationary covariance pattern in offline PaleoDA

The discrepancies in the mean state between the proxy records and the model priors were found to be of up to two digits (in ‰) for individual proxy records and thus judged too large for the EnKF (Figure 5.1). The studies by Bühler et al. (2022) and Heiser et al. (2021), which worked

on the same proxy record data[2] to perform model-data comparison, did not rate the biases as large because they looked at the global mean of the biases. The difference in judgement comes from the sensitivity of the EnKF to mean state biases at individual proxy record locations. For instance, a mean bias of $\sim 10‰$ at one proxy record location would be sufficient to shift the reconstructed temperature by several degrees in this region. A meaningful reconstruction of GMT is particularly inhibited if the proxy record with such an offset to the simulated values is only available for some years of the reconstruction period, which would lead to large artificial jumps in the reconstructed signal when this record is not available. Neither a particular PSM configuration (especially the height correction or fractionation), nor a specific model prior or a multi-model ensemble could avoid at least some large local δ^{18}O biases. The anomaly reconstruction performed here provides a simple way of dealing with the mean value bias, although it does introduce the necessity of a time period in which all proxy records have a value. It also adds additional uncertainty because not all proxy records precisely span the whole reference period, here chosen to be the 18th century. In the end, the anomaly reconstruction is similar to the anomaly reconstructions in LMR and PHYDA, which use periods during the 20th century as the reference period due to how the statistical calibration of the proxy record data is done. The last millennium is a stable period, in which an anomaly reconstruction is easily justifiable. For the reconstruction of transient climate, Erb et al. (2022) used a similar approach of reconstructing anomalies with respect to a reference period. For a single-time fit of the LGM, Annan et al. (2022) employed a more advanced debiasing technique based on Empirical Orthogonal Functions to center the model priors on the proxy record data, which could serve as a debiasing reference in future PaleoDA studies.

Biases in the mean simulated state, which could also reflect a shortcoming of the employed PSMs, are not the only type of bias which might distort the reconstructions. The employed models have different covariance structures for the climate variables at the grid cells. The covariance bias is more difficult to quantify and visualize than the mean bias. Furthermore, the proxy record and observational δ^{18}O records from the instrumental period are sparse, which impedes establishing a target δ^{18}O covariance pattern which the model priors should reproduce. Nonetheless, the experiments performed in this thesis illustrate the impacts of differences in the covariance patterns and the different overall response to measurements of δ^{18}O in the DA. As an example, the reconstructed GMT curves show, that the iHadCM3 model leads to larger temperature anomalies than the other model priors (Figure 6.1). This finding is in line with the global area of the averaging kernel analysis (Figure 5.2), where iHadCM3 exhibited the strongest temperature response to potential δ^{18}O measurements. The reason for this effect, which might be connected to the known bias of overestimated local evaporation (Table 3.1) needs to be elaborated on. Such inter-model differences in the covariance are also apparent in the reconstructed temperature and precipitation changes over the core monsoon region in tropical South America (Figure 6.8). For instance, iCESM has a stronger temperature response than isoGSM, while the opposite is the case for precipitation. This effect is also visible in the area of the averaging kernel for that region (Figure 5.2). A more precise assessment using proxy locations only from that region and the covariances on the right time scales is needed to further substantiate this connection.

To balance out covariance biases of the individual model priors, MMEs were employed. Their use was motivated by the PPEs performed by Parsons et al. (2021), who calculated that multi-model ensembles have more spatial degrees of freedom and consequently more spatially diverse covariance patterns. The reconstructed GMT and monsoon indices suggest that the MME follows the model prior which reconstructs the strongest variations. At times, the resulting curves also surpass the reconstructions based on the individual models in amplitude. These counter-

[2]The mentioned studies did not select exactly the same speleothem and ice core records.

intuitive results demonstrate that the MME is not straightforward to interpret and not simply a mid-way between different climate model priors. However, the MME used here only consisted of 4 models due to the exclusion of GISS, which is rather small in comparison Parsons et al. (2021) who used 9 different models. Future studies could profit from using more isotope-enabled climate simulations. They would need to take into account the similarity of climate models from the same model family to avoid biased covariance structures. Considerations for the appropriate selection of MME members can be found in the LGM PaleoDA reconstruction by Annan et al. (2022). Making use of MMEs can now be considered good practice in PaleoDA. MMEs have been used in the recent ENSO last millennium reconstruction by Sanchez et al. (2021) and the LGM reconstruction by Annan et al. (2022). However, as in the DAISIM experiments, these studies did not specifically investigate the benefit of the MME in their reconstructions. At least, the use of multiple models and MMEs emphasises the importance of assessing how much a reconstruction depends on a specific prior, thus improving the reliability of the reconstructions.

Besides applying MME to the proxy data, I applied them in PPEs employing different target and prior models. The MMEs only led to small improvements in comparison to the single model priors (Figures 5.4 and 5.5). A similar result was also found by Parsons et al. (2021), who used pseudoproxies of temperature and not δ^{18}O. However, the authors showed, that the MME is particularly beneficiary for regions that are remote of usual terrestrial proxy record locations, as the oceans, which is an aspect I have not looked into. The target-prior PPEs are a great tool to investigate the inter-model differences as such. They can be seen as a simulation of the bias relationship between climate model priors and the real climate system. The local skill is remarkably low when not using the same model as prior and target, despite the anomaly reconstruction, which is unaffected by the mean bias (Figure 5.4 and 5.5). This kind of experiment could be seen as a testbed for evaluating debiasing schemes. Perhaps, the pseudoproxy records from the target simulation contain enough information, such that the covariances from the prior model could be debiased to give better reconstruction skill. A study performing PPEs to study the effect of various PSMs by Dee et al. (2016) has performed such a bias correction in variance. However, the method applied there requires that the true distribution in form of the target model is known entirely and is thus impractical for real proxy data. The authors concluded, that PaleoDA reconstructions could be more sensitive to model biases than imprecise PSMs. Making use of five different isotope-enabled models for the assimilation of the speleothem and ice core proxy records could enable finding a variance debiasing scheme, which improves the reconstruction skill of the non-target prior models. This scheme could then also be applied to real data to produce more reliable PaleoDA reconstructions. The GISS simulation showed a particular bias and proved to be unsuited for the global PaleoDA, due to little similarity to the reconstructions from other prior (Figure 6.4). An explanation could be the δ^{18}O drift over Antarctica and how it has been detrended here (Section 3.1). It has not been tested, if only using the first 300 years of the simulation, which seem to be without the drift, or another detrending technique leads to more sensible reconstructions. The detrended δ^{18}O values over Antarctica should only affect observation estimates from that region. Another test could thus consist of performing reconstructions with all climate model priors without assimilating any proxy records from Antarctica.

A question closely related to the topic of varying covariance structures in the different models is if the stationary covariance that is used by the PaleoDA algorithm is always suited. During the CWP, it can be hypothesised that the covariance structure changes, although this would need to be tested statistically. At least, it was possible to reproduce the global warming trend with the covariance structure from the last millennium simulations, which do not incorporate the global warming of the CWP. However, it is important to keep in mind, that using the same covariance over the entire last millennium to interpolate the climate fields is only an approximation, which

might not be appropriate for specific periods and regions. Whereas with DAISIM this possible caveat has not been studied, a recent reconstruction of ENSO for the last millennium from corals by Sanchez et al. (2021) found an unexpected covariance bias artefact. For the period of strong volcanic activity at the beginning of the 19th century, the signal recorded from corals in different regions of the Pacific could only be reconciled by the PaleoDA reconstruction when specific simulation years without the teleconnections influenced by ENSO were selected for the prior. This suggests that selecting specific prior ensemble members instead of taking a random sample might improve offline EnKF, also for a supposedly stable period as the last millennium. In a purely technical study with a simple Lorenz model, Sun et al. (2022) propose an analog offline EnKF that goes into that direction. It preselects its ensemble members for each time step given an error metric. The technique could be tested with the target-prior model PPEs from GCM simulations to evaluate if the model priors offer enough choice in variability to effectively improve the reconstruction. However, this method might not be easily expandable to the multi-time scale approach implemented for DAISIM.

To summarize this section of the discussion, it can be said that performing PaleoDA experiments with different isotope-enabled models imply the need for a better understanding of the simulated δ^{18}O values and their covariance relationship to other variables. Hence, further multi-model data comparison is necessary.

7.5 Central tasks for future PaleoDA reconstructions

The multi-timescale PaleoDA algorithm presented and applied in this thesis is a versatile method with many different options. The obtained reconstructions can be tuned by doing sensitivity tests and cross-validated using external data, for instance, proxy records that are not used on purpose during the reconstruction. In the first place, this tuning should be avoided. It can easily lead to circular arguments and it is tempting to aim for reductions in an error metric without deeper physical and mathematical reasoning. For research following up on this project, I recommend finding methods to tackle the following four central issues, which have been touched upon in the discussion and are summarized in the following. Assessing them will also help in answering the scientific questions that have been raised at the beginning of this thesis better.

1. **Realistic uncertainty assessment.** The δ^{18}O observation error associated with each proxy record should be constrained realistically by calibrating it to the employed PSM and the associated time scale. The proxy error should also reflect the SNR that is estimated for a proxy record type. This task is especially relevant when the δ^{18}O proxy records incorporated for DAISIM will be assimilated alongside more proxy data with different PSM types. In addition, the uncertainties provided by the prior ensembles, ideally provided by an ensemble of climate models should be examined. In sum, the reconstructed climate estimates should be understood better in terms of uncertainties and thus become more reliable.

2. **Time scales and dating uncertainty.** In the multi-time scale approach, each proxy record needs to be attributed a time scale over which it is assumed to represent a mean value. This should be done in a physically sound way and not be based only on the provided record resolution. Furthermore, it needs to be justified if proxy records are to be reused on multiple time scales and if dating uncertainty of proxy records needs to be considered separately.

3. **Quantifying the covariance structure and the influence of observations.** While visualizing the Kalman gain for each proxy record at each reconstruction time scale of the reconstruction is not practical, some metric summarizing the effect of the observations,

for instance from specific archive types, regions or time scales could improve the understanding of how the PaleoDA method reconstructs climate fields. This type of assessment is also necessary for evaluating to what extent the simulated δ^{18}O needs to be modified by a PSM to reproduce realistic spatial covariance relationships for speleothem and ice core records.

4. **Debiasing the model prior.** Establishing a method for centering the model prior(s) on the proxy record data in a commensurate way is required to reduce the influence of model biases on the reconstruction, not only for the mean state but also for the static covariance structure used by the offline PaleoDA algorithm.

Chapter 8

Conclusion

Offline PaleoDA has been used with data from isotope-enabled climate models and speleothem and ice core proxy records to reconstruct global climate fields for the last millennium. This combination of δ^{18}O proxy and model data had not been assimilated with PaleoDA before. To that end, I flexibilized the existing annual PaleoDA algorithm introduced by Hakim et al. (2016) for the incorporation of proxy records on multiple time scales by adapting the method proposed by Steiger and Hakim (2016). After testing different mathematical solutions of the EnKF, the PaleoDA algorithm has been implemented in an optimized way, such that climate fields can be reconstructed with limited computational resources. The EnKF makes use of the covariance between simulated δ^{18}O and simulated variables as temperature and precipitation in order spread information provided by the δ^{18}O proxy records to the grid cells of the climate fields. To render simulated and recorded δ^{18}O comparable, PSMs for speleothems and ice cores have been implemented and tested. Due to large differences in the mean states of proxy and model data, climate anomalies instead of absolute values have been reconstructed, which limits the importance of the PSMs to the covariance relationship.
The developed framework has been applied to speleothem δ^{18}O from the SISALv2 database and ice core δ^{18}O from the Iso2k database, yielding climate signals which are comparable to existing reconstructions. On the global scale, the influence of speleothem records remained inconclusive. The regional reconstruction of temperature and precipitation over tropical South America demonstrated the utility of speleothems. The results indicate strong changes in hydroclimate in the region during the last millennium which are not present in other reconstructions, but have been suggested by proxy record studies. The multi-timescale reconstruction of GMT shows an increased decadal to centennial variability in comparison to existing, single-time scale PaleoDA. Pseudoproxy experiments suggest that assimilating proxy records on longer than annual time scales improves the representation of this long-term variability. PaleoDA reconstructions using more proxy records will enable an investigation of local climate variability to compare it to the variability simulated by climate models.
The multi-timescale PaleoDA algorithm offers many configuration options. Future research will need to evaluate the sensitivity to uncertainties in the proxy records, PSMs, climate models, and their inherent biases to produce more reliable statistical estimates of past climate changes. PaleoDA is not a black box but a method with clear mechanisms, which can be difficult to follow due to the temporal and spatial sparsity of available proxy records. Developing standards for the assessment of PaleoDA reconstructions will improve understanding of how the reconstructed climate signal, its uncertainty, and variability depend on model priors and proxy data. PaleoDA is a promising method in the field of paleoclimatology. It enables the reconstruction of full climate fields for all climate variables which are provided by a model simulation and thus enhances the interpretation of proxy record signals. Its deployment for a wide range of climatic periods is already in full swing and the importance of better understanding and constraining the limitations of PaleoDA can thus hardly be overestimated.

Bibliography

Aeschbach-Hertig, Werner and D. Kip Solomon (2013). "Noble Gas Thermometry in Groundwater Hydrology". In: *The Noble Gases as Geochemical Tracers*. Ed. by Pete Burnard. Advances in Isotope Geochemistry. Berlin, Heidelberg: Springer, pp. 81–122. DOI: 10.1007/978-3-642-28836-4_5.

Ahmed, Moinuddin et al. (May 2013). "Continental-Scale Temperature Variability during the Past Two Millennia". In: *Nature Geoscience* 6.5 (5), pp. 339–346. DOI: 10.1038/ngeo1797.

Allen, Richard et al. (2022). *Crop Evapotranspiration - Guidelines for Computing Crop Water Requirements - FAO Irrigation and Drainage Paper 56*. FAO - Food and Agriculture Organization of the United Nations Rome, 1998.

Andersen, K. K. et al. (Sept. 2004). "High-Resolution Record of Northern Hemisphere Climate Extending into the Last Interglacial Period". In: *Nature* 431.7005 (7005), pp. 147–151. DOI: 10.1038/nature02805.

Andrews, Angus (June 1968). "A Square Root Formulation of the Kalman Covariance Equations." In: *AIAA Journal* 6.6, pp. 1165–1166. DOI: 10.2514/3.4696.

Annan, J. D. and J. C. Hargreaves (July 10, 2012). "Identification of Climatic State with Limited Proxy Data". In: *Climate of the Past* 8.4, pp. 1141–1151. DOI: 10.5194/cp-8-1141-2012.

Annan, James et al. (Feb. 15, 2022). "A New Global Climate Reconstruction for the Last Glacial Maximum". In: *Climate of the Past Discussions*, pp. 1–20. DOI: 10.5194/cp-2022-12.

Atsawawaranunt, Kamolphat et al. (Sept. 14, 2018). "The SISAL Database: A Global Resource to Document Oxygen and Carbon Isotope Records from Speleothems". In: *Earth System Science Data* 10.3, pp. 1687–1713. DOI: 10.5194/essd-10-1687-2018.

Augustin, Laurent et al. (June 2004). "Eight Glacial Cycles from an Antarctic Ice Core". In: *Nature* 429.6992 (6992), pp. 623–628. DOI: 10.1038/nature02599.

Badgeley, Jessica A. et al. (July 28, 2020). "Greenland Temperature and Precipitation over the Last 20000 Years Using Data Assimilation". In: *Climate of the Past* 16.4, pp. 1325–1346. DOI: 10.5194/cp-16-1325-2020.

Bakker, Pepijn et al. (Nov. 24, 2022). "Internal Climate Variability and Spatial Temperature Correlations during the Past 2000 Years". In: *Climate of the Past* 18.11, pp. 2523–2544. DOI: 10.5194/cp-18-2523-2022.

Barkmeijer, J. et al. (2003). "Forcing Singular Vectors and Other Sensitive Model Structures". In: *Quarterly Journal of the Royal Meteorological Society* 129.592, pp. 2401–2423. DOI: 10.1256/qj.02.126.

Bhend, J. et al. (May 31, 2012). "An Ensemble-Based Approach to Climate Reconstructions". In: *Climate of the Past* 8.3, pp. 963–976. DOI: 10.5194/cp-8-963-2012.

Bird, Broxton W. et al. (May 24, 2011). "A 2,300-Year-Long Annually Resolved Record of the South American Summer Monsoon from the Peruvian Andes". In: *Proceedings of the National Academy of Sciences* 108.21, pp. 8583–8588. DOI: 10.1073/pnas.1003719108.

Bishop, Craig H. et al. (Mar. 1, 2001). "Adaptive Sampling with the Ensemble Transform Kalman Filter. Part I: Theoretical Aspects". In: *Monthly Weather Review* 129.3, pp. 420–436. DOI: 10.1175/1520-0493(2001)129⟨0420:ASWTET⟩2.0.CO;2.

Bradley, Raymond (2015). *Paleoclimatology. Reconstructing Climates of the Quaternary.* Elsevier.

Brady, E. et al. (2019). "The Connected Isotopic Water Cycle in the Community Earth System Model Version 1". In: *Journal of Advances in Modeling Earth Systems* 11.8, pp. 2547–2566. DOI: 10.1029/2019MS001663.

Breitenmoser, P. et al. (Mar. 11, 2014). "Forward Modelling of Tree-Ring Width and Comparison with a Global Network of Tree-Ring Chronologies". In: *Climate of the Past* 10.2, pp. 437–449. DOI: 10.5194/cp-10-437-2014.

Brennan, M. Kathleen and Gregory J. Hakim (Feb. 15, 2022). "Reconstructing Arctic Sea Ice over the Common Era Using Data Assimilation". In: *Journal of Climate* 35.4, pp. 1231–1247. DOI: 10.1175/JCLI-D-21-0099.1.

Bretherton, Christopher S. et al. (July 1, 1999). "The Effective Number of Spatial Degrees of Freedom of a Time-Varying Field". In: *Journal of Climate* 12.7, pp. 1990–2009. DOI: 10.1175/1520-0442(1999)012⟨1990:TENOSD⟩2.0.CO;2.

Brian, H. and M. Fan (Dec. 1, 2012). "Variability of the Isotopic Lapse Rate across the Mountain Ranges in Wyoming". In: 2012, T21E–2610.

Brierley, Chris and Kira Rehfeld (Oct. 2014). "Paleovariability: Data Model Comparisons". In: *Past Global Changes Magazine* 22.2, pp. 102–102. DOI: 10.22498/pages.22.2.102.

Brown, R.G. and P.Y.C. Hwang (2012). *Introduction to Random Signals and Applied Kalman Filtering.* John Wiley & Sons, Inc.

Bühler, Janica C. et al. (May 5, 2021). "Comparison of the Oxygen Isotope Signatures in Speleothem Records and iHadCM3 Model Simulations for the Last Millennium". In: *Climate of the Past* 17.3, pp. 985–1004. DOI: 10.5194/cp-17-985-2021.

Bühler, Janica C. et al. (July 13, 2022). "Investigating Stable Oxygen and Carbon Isotopic Variability in Speleothem Records over the Last Millennium Using Multiple Isotope-Enabled Climate Models". In: *Climate of the Past* 18.7, pp. 1625–1654. DOI: 10.5194/cp-18-1625-2022.

Burgers, Gerrit et al. (June 1, 1998). "Analysis Scheme in the Ensemble Kalman Filter". In: *Monthly Weather Review* 126.6, pp. 1719–1724. DOI: 10.1175/1520-0493(1998)126⟨1719:ASITEK⟩2.0.CO;2.

Campos, J. L. P. S. et al. (July 28, 2019). "Coherent South American Monsoon Variability During the Last Millennium Revealed Through High-Resolution Proxy Records". In: *Geophysical Research Letters* 46.14, pp. 8261–8270. DOI: 10.1029/2019GL082513.

Casado, Mathieu et al. (Aug. 25, 2020). "Climatic Information Archived in Ice Cores: Impact of Intermittency and Diffusion on the Recorded Isotopic Signal in Antarctica". In: *Climate of the Past* 16.4, pp. 1581–1598. DOI: 10.5194/cp-16-1581-2020.

Colose, Christopher M. et al. (Aug. 23, 2016a). "Hemispherically Asymmetric Volcanic Forcing of Tropical Hydroclimate during the Last Millennium". In: *Earth System Dynamics* 7.3, pp. 681–696. DOI: 10.5194/esd-7-681-2016.

— (Apr. 15, 2016b). "The Influence of Volcanic Eruptions on the Climate of Tropical South America during the Last Millennium in an Isotope-Enabled General Circulation Model". In: *Climate of the Past* 12.4, pp. 961–979. DOI: 10.5194/cp-12-961-2016.

Comas-Bru, Laia et al. (Aug. 9, 2019). "Evaluating Model Outputs Using Integrated Global Speleothem Records of Climate Change since the Last Glacial". In: *Climate of the Past* 15.4, pp. 1557–1579. DOI: 10.5194/cp-15-1557-2019.

Comas-Bru, Laia et al. (Oct. 27, 2020). "SISALv2: A Comprehensive Speleothem Isotope Database with Multiple Age–Depth Models". In: *Earth System Science Data* 12.4, pp. 2579–2606. DOI: 10.5194/essd-12-2579-2020.

Consortium, PAGES Hydro2k (Dec. 20, 2017). "Comparing Proxy and Model Estimates of Hydroclimate Variability and Change over the Common Era". In: *Climate of the Past* 13.12, pp. 1851–1900. DOI: 10.5194/cp-13-1851-2017.

Cook, Edward R. et al. (1994). "Spatial Regression Methods in Dendroclimatology: A Review and Comparison of Two Techniques". In: *International Journal of Climatology* 14.4, pp. 379–402. DOI: 10.1002/joc.3370140404.

Coplen, Tyler B. et al. (Mar. 1983). "Comparison of Stable Isotope Reference Samples". In: *Nature* 302.5905, pp. 236–238. DOI: 10.1038/302236a0.

Dalaiden, Quentin et al. (Apr. 8, 2020). "How Useful Is Snow Accumulation in Reconstructing Surface Air Temperature in Antarctica? A Study Combining Ice Core Records and Climate Models". In: *The Cryosphere* 14.4, pp. 1187–1207. DOI: 10.5194/tc-14-1187-2020.

Dance, S. L. et al. (2007). "Unbiased Ensemble Square Root Filters". In: *PAMM* 7.1, pp. 1026505–1026506. DOI: 10.1002/pamm.200700603.

Dansgaard, W. (1964). "Stable Isotopes in Precipitation". In: *Tellus* 16.4, pp. 436–468. DOI: 10.1111/j.2153-3490.1964.tb00181.x.

Dee, S. et al. (2015). "PRYSM: An Open-Source Framework for PRoxY System Modeling, with Applications to Oxygen-Isotope Systems". In: *Journal of Advances in Modeling Earth Systems* 7.3, pp. 1220–1247. DOI: 10.1002/2015MS000447.

Dee, Sylvia et al. (2020). "Enhanced North American ENSO Teleconnections During the Little Ice Age Revealed by Paleoclimate Data Assimilation". In: *Geophysical Research Letters* 47.15, e2020GL087504. DOI: 10.1029/2020GL087504.

Dee, Sylvia G. and Nathan J. Steiger (2022). "ENSO's Response to Volcanism in a Data Assimilation-Based Paleoclimate Reconstruction Over the Common Era". In: *Paleoceanography and Paleoclimatology* 37.3, e2021PA004290. DOI: 10.1029/2021PA004290.

Dee, Sylvia G. et al. (2016). "On the Utility of Proxy System Models for Estimating Climate States over the Common Era". In: *Journal of Advances in Modeling Earth Systems* 8.3, pp. 1164–1179. DOI: 10.1002/2016MS000677.

Deininger, Michael et al. (Mar. 2019). "Late Quaternary Variations in the South American Monsoon System as Inferred by Speleothems—New Perspectives Using the SISAL Database". In: *Quaternary* 2.1 (1), p. 6. DOI: 10.3390/quat2010006.

Dirren, Sébastien and Gregory J. Hakim (Feb. 2005). "Toward the Assimilation of Time-Averaged Observations". In: *Geophysical Research Letters* 32.4, n/a–n/a. DOI: 10.1029/2004GL021444.

Dubinkina, Svetlana et al. (Dec. 2011). "Testing a Particle Filter to Reconstruct Climate Changes over the Past Centuries". In: *International Journal of Bifurcation and Chaos* 21.12, pp. 3611–3618. DOI: 10.1142/S0218127411030763.

Ellerhoff, Beatrice et al. (2022). "Contrasting State-Dependent Effects of Natural Forcing on Global and Local Climate Variability". In: *Geophysical Research Letters* 49.10, e2022GL098335. DOI: 10.1029/2022GL098335.

Emile-Geay, Julien et al. (July 11, 2017). "A Global Multiproxy Database for Temperature Reconstructions of the Common Era". In: *Scientific Data* 4.1 (1), p. 170088. DOI: 10.1038/sdata.2017.88.

Erb, Michael P. et al. (Dec. 15, 2022). "Reconstructing Holocene Temperatures in Time and Space Using Paleoclimate Data Assimilation". In: *Climate of the Past* 18.12, pp. 2599–2629. DOI: 10.5194/cp-18-2599-2022.

Evans, M. N. et al. (Sept. 15, 2013). "Applications of Proxy System Modeling in High Resolution Paleoclimatology". In: *Quaternary Science Reviews* 76, pp. 16–28. DOI: 10.1016/j.quascirev.2013.05.024.

Evensen, Geir (1994). "Sequential Data Assimilation with a Nonlinear Quasi-Geostrophic Model Using Monte Carlo Methods to Forecast Error Statistics". In: *Journal of Geophysical Research: Oceans* 99.C5, pp. 10143–10162. DOI: 10.1029/94JC00572.

Evensen, Geir et al. (2022). *Data Assimilation Fundamentals: A Unified Formulation of the State and Parameter Estimation Problem*. Springer Textbooks in Earth Sciences, Geography and Environment. Cham: Springer International Publishing. DOI: 10.1007/978-3-030-96709-3.

Franke, Jörg et al. (Dec. 2017). "A Monthly Global Paleo-Reanalysis of the Atmosphere from 1600 to 2005 for Studying Past Climatic Variations". In: *Scientific Data* 4.1, p. 170076. DOI: 10.1038/sdata.2017.76.

Franke, Jörg et al. (June 18, 2020). "The Importance of Input Data Quality and Quantity in Climate Field Reconstructions – Results from the Assimilation of Various Tree-Ring Collections". In: *Climate of the Past* 16.3, pp. 1061–1074. DOI: 10.5194/cp-16-1061-2020.

Gaspari, Gregory and Stephen E. Cohn (1999). "Construction of Correlation Functions in Two and Three Dimensions". In: *Quarterly Journal of the Royal Meteorological Society* 125.554, pp. 723–757. DOI: 10.1002/qj.49712555417.

Goosse, H. et al. (May 13, 2010). "Reconstructing Surface Temperature Changes over the Past 600 Years Using Climate Model Simulations with Data Assimilation". In: *Journal of Geophysical Research* 115.D9, p. D09108. DOI: 10.1029/2009JD012737.

Goosse, Hugues et al. (Aug. 2006). "Using Paleoclimate Proxy-Data to Select Optimal Realisations in an Ensemble of Simulations of the Climate of the Past Millennium". In: *Climate Dynamics* 27.2-3, pp. 165–184. DOI: 10.1007/s00382-006-0128-6.

Goosse, Hugues et al. (Dec. 1, 2012). "The Role of Forcing and Internal Dynamics in Explaining the "Medieval Climate Anomaly"". In: *Climate Dynamics* 39.12, pp. 2847–2866. DOI: 10.1007/s00382-012-1297-0.

Grossman, Ethan L and Teh-Lung Ku (Jan. 1, 1986). "Oxygen and Carbon Isotope Fractionation in Biogenic Aragonite: Temperature Effects". In: *Chemical Geology: Isotope Geoscience section*. Calibration of the Phanerozoic Time Scale 59, pp. 59–74. DOI: 10.1016/0168-9622(86)90057-6.

Gulev, S. K. et al. (Aug. 16, 2021). "Changing State of the Climate System". In: Cambridge University Press, pp. 287–422. DOI: 10.1017/9781009157896.004.

Hakim, Gregory J. et al. (2016). "The Last Millennium Climate Reanalysis Project: Framework and First Results". In: *Journal of Geophysical Research: Atmospheres* 121.12, pp. 6745–6764. DOI: 10.1002/2016JD024751.

Harris, Trevor et al. (July 3, 2021). "Evaluating Proxy Influence in Assimilated Paleoclimate Reconstructions—Testing the Exchangeability of Two Ensembles of Spatial Processes". In: *Journal of the American Statistical Association* 116.535, pp. 1100–1113. DOI: 10.1080/01621459.2020.1799810.

Heiser, Yannick et al. (Mar. 4, 2021). *Comparison of Isotopic Signatures in Ice Core and Speleothem Records to an Isotope Enabled Climate Model Simulation for the Last Millennium*. other. pico. DOI: 10.5194/egusphere-egu21-8661.

Houtekamer, P. L. and Herschel L. Mitchell (Mar. 1, 1998). "Data Assimilation Using an Ensemble Kalman Filter Technique". In: *Monthly Weather Review* 126.3, pp. 796–811. DOI: 10.1175/1520-0493(1998)126⟨0796:DAUAEK⟩2.0.CO;2.

— (Jan. 1, 2001). "A Sequential Ensemble Kalman Filter for Atmospheric Data Assimilation". In: *Monthly Weather Review* 129.1, pp. 123–137. DOI: 10.1175/1520-0493(2001)129⟨0123:ASEKFF⟩2.0.CO;2.

Huntley, Helga S. and Gregory J. Hakim (Nov. 1, 2010). "Assimilation of Time-Averaged Observations in a Quasi-Geostrophic Atmospheric Jet Model". In: *Climate Dynamics* 35.6, pp. 995–1009. DOI: 10.1007/s00382-009-0714-5.

Jean-Baptiste, P. et al. (Aug. 1, 2019). "Tritium Dating of Dripwater from Villars Cave (SW-France)". In: *Applied Geochemistry* 107, pp. 152–158. DOI: 10.1016/j.apgeochem.2019.06.005.

Johnsen, S. J. et al. (1989). "The Origin of Arctic Precipitation under Present and Glacial Conditions". In: *Tellus B* 41B.4, pp. 452–468. DOI: 10.1111/j.1600-0889.1989.tb00321.x.

Jones, P. D. and M. E. Mann (June 2004). "Climate over Past Millennia". In: *Reviews of Geophysics* 42.2. DOI: 10.1029/2003RG000143.

Kalman, R. E. (Mar. 1, 1960). "A New Approach to Linear Filtering and Prediction Problems". In: *Journal of Basic Engineering* 82.1, pp. 35–45. DOI: 10.1115/1.3662552.

Katz, Richard W. and Barbara G. Brown (July 1, 1992). "Extreme Events in a Changing Climate: Variability Is More Important than Averages". In: *Climatic Change* 21.3, pp. 289–302. DOI: 10.1007/BF00139728.

Kaufman, Darrell S. and Nicholas P. McKay (Apr. 26, 2022). "Technical Note: Past and Future Warming – Direct Comparison on Multi-Century Timescales". In: *Climate of the Past* 18.4, pp. 911–917. DOI: 10.5194/cp-18-911-2022.

Kettner, Andreas Martin and Mario Paolone (Sept. 2017). "Sequential Discrete Kalman Filter for Real-Time State Estimation in Power Distribution Systems: Theory and Implementation". In: *IEEE Transactions on Instrumentation and Measurement* 66.9, pp. 2358–2370. DOI: 10.1109/TIM.2017.2708278. arXiv: 1702.08262.

Khider, Deborah et al. (2022). "Pyleoclim: Paleoclimate Timeseries Analysis and Visualization With Python". In: *Paleoceanography and Paleoclimatology* 37.10, e2022PA004509. DOI: 10.1029/2022PA004509.

King, J. M. et al. (2021). "A Data Assimilation Approach to Last Millennium Temperature Field Reconstruction Using a Limited High-Sensitivity Proxy Network". In: *Journal of Climate*. DOI: 10.1175/JCLI-D-20-0661.1.

Kirtman, Ben et al. (2013). "Projections and Predictability". In: *Climate Change 2013: The Physical Science Basis. Contribution of Working Group 1 to the Fifth Assessment Report of the Intergovernmental Panel on Climate Change*. Cambridge: Cambridge Univ. Press.

Kluge, Tobias et al. (Sept. 2010). "Assessing the Use of 3H-3He Dating to Determine the Subsurface Transit Time of Cave Drip Waters". In: *Isotopes in Environmental and Health Studies* 46.3, pp. 299–311. DOI: 10.1080/10256016.2010.503893. pmid: 20812118.

Konecky, Bronwen L. et al. (Sept. 23, 2020). "The Iso2k Database: A Global Compilation of Paleo-δ^{18}O and δ^{2}H Records to Aid Understanding of Common Era Climate". In: *Earth System Science Data* 12.3, pp. 2261–2288. DOI: 10.5194/essd-12-2261-2020.

Lachniet, Matthew S. (Mar. 1, 2009). "Climatic and Environmental Controls on Speleothem Oxygen-Isotope Values". In: *Quaternary Science Reviews* 28.5, pp. 412–432. DOI: 10.1016/j.quascirev.2008.10.021.

— (Nov. 2015). "Are Aragonite Stalagmites Reliable Paleoclimate Proxies? Tests for Oxygen Isotope Time-Series Replication and Equilibrium". In: *Geological Society of America Bulletin* 127.11-12, pp. 1521–1533. DOI: 10.1130/B31161.1.

Laepple, Thomas and Peter Huybers (Nov. 25, 2014). "Ocean Surface Temperature Variability: Large Model–Data Differences at Decadal and Longer Periods". In: *Proceedings of the National Academy of Sciences* 111.47, pp. 16682–16687. DOI: 10.1073/pnas.1412077111.

Leeuwen, Peter Jan van (June 1, 1999). "Comment on "Data Assimilation Using an Ensemble Kalman Filter Technique"". In: *Monthly Weather Review* 127.6, pp. 1374–1377. DOI: 10.1175/1520-0493(1999)127⟨1374:CODAUA⟩2.0.CO;2.

LeGrande, Allegra N. and Gavin A. Schmidt (2006). "Global Gridded Data Set of the Oxygen Isotopic Composition in Seawater". In: *Geophysical Research Letters* 33.12, p. L12604. DOI: 10.1029/2006GL026011.

Lewis, S. C. and A. N. LeGrande (Oct. 13, 2015). "Stability of ENSO and Its Tropical Pacific Teleconnections over the Last Millennium". In: *Climate of the Past* 11.10, pp. 1347–1360. DOI: 10.5194/cp-11-1347-2015.

Liu, Huaran et al. (2017). "A Systematic Comparison of Particle Filter and EnKF in Assimilating Time-Averaged Observations". In: *Journal of Geophysical Research: Atmospheres* 122.24, pp. 13, 155–13, 173. DOI: 10.1002/2017JD026798.

Liu, Zhengyu et al. (Aug. 26, 2014). "The Holocene Temperature Conundrum". In: *Proceedings of the National Academy of Sciences* 111.34, E3501–E3505. DOI: 10.1073/pnas.1407229111.

Malevich, Steven B. et al. (2019). "Global Core Top Calibration of δ18O in Planktic Foraminifera to Sea Surface Temperature". In: *Paleoceanography and Paleoclimatology* 34.8, pp. 1292–1315. DOI: 10.1029/2019PA003576.

Mann, Michael E. and Scott Rutherford (May 15, 2002). "Climate Reconstruction Using 'Pseudoproxies'". In: *Geophysical Research Letters* 29.10, pp. 139-1-139–4. DOI: 10.1029/2001GL014554.

Mann, Michael E. et al. (Apr. 1998). "Global-Scale Temperature Patterns and Climate Forcing over the Past Six Centuries". In: *Nature* 392.6678 (6678), pp. 779–787. DOI: 10.1038/33859.

Marcott, Shaun A. et al. (Mar. 8, 2013). "A Reconstruction of Regional and Global Temperature for the Past 11,300 Years". In: *Science* 339.6124, pp. 1198–1201. DOI: 10.1126/science.1228026.

Matsikaris, A. et al. (Jan. 15, 2015). "On-Line and off-Line Data Assimilation in Palaeoclimatology: A Case Study". In: *Climate of the Past* 11.1, pp. 81–93. DOI: 10.5194/cp-11-81-2015.

Maybeck, Peter S. (2022). *Stochastic Models, Estimation, and Control, Volume 3 - 1st Edition*. Academic Press.

Molteni, F. (Jan. 1, 2003). "Atmospheric Simulations Using a GCM with Simplified Physical Parametrizations. I: Model Climatology and Variability in Multi-Decadal Experiments". In: *Climate Dynamics* 20.2, pp. 175–191. DOI: 10.1007/s00382-002-0268-2.

Nerger, Lars (May 1, 2015). "On Serial Observation Processing in Localized Ensemble Kalman Filters". In: *Monthly Weather Review* 143.5, pp. 1554–1567. DOI: 10.1175/MWR-D-14-00182.1.

Nerger, Lars et al. (July 2012). "A Unification of Ensemble Square Root Kalman Filters". In: *Monthly Weather Review* 140.7, pp. 2335–2345. DOI: 10.1175/MWR-D-11-00102.1.

Neukom, Raphael et al. (Aug. 2019a). "Consistent Multidecadal Variability in Global Temperature Reconstructions and Simulations over the Common Era". In: *Nature Geoscience* 12.8 (8), pp. 643–649. DOI: 10.1038/s41561-019-0400-0.

Neukom, Raphael et al. (July 2019b). "No Evidence for Globally Coherent Warm and Cold Periods over the Preindustrial Common Era". In: *Nature* 571.7766 (7766), pp. 550–554. DOI: 10.1038/s41586-019-1401-2.

Nilsen, Tine et al. (June 29, 2018). "Assessing the Performance of the BARCAST Climate Field Reconstruction Technique for a Climate with Long-Range Memory". In: *Climate of the Past* 14.6, pp. 947–967. DOI: 10.5194/cp-14-947-2018.

Novello, V. F. et al. (2018). "Two Millennia of South Atlantic Convergence Zone Variability Reconstructed From Isotopic Proxies". In: *Geophysical Research Letters* 45.10, pp. 5045–5051. DOI: 10.1029/2017GL076838.

Okazaki, Atsushi and Kei Yoshimura (Apr. 20, 2017). "Development and Evaluation of a System of Proxy Data Assimilation for Paleoclimate Reconstruction". In: *Climate of the Past* 13.4, pp. 379–393. DOI: 10.5194/cp-13-379-2017.

— (Aug. 27, 2019). "Global Evaluation of Proxy System Models for Stable Water Isotopes With Realistic Atmospheric Forcing". In: *Journal of Geophysical Research: Atmospheres* 124.16, pp. 8972–8993. DOI: 10.1029/2018JD029463.

Okazaki, Atsushi et al. (2021). "Revisiting Online and Offline Data Assimilation Comparison for Paleoclimate Reconstruction: An Idealized OSSE Study". In: *Journal of Geophysical Research: Atmospheres* 126.16, e2020JD034214. DOI: 10.1029/2020JD034214.

Orrison, Rebecca et al. (Sept. 2, 2022). "South American Summer Monsoon Variability over the Last Millennium in Paleoclimate Records and Isotope-Enabled Climate Models". In: *Climate of the Past* 18.9, pp. 2045–2062. DOI: 10.5194/cp-18-2045-2022.

Osman, Matthew B. et al. (Nov. 2021). "Globally Resolved Surface Temperatures since the Last Glacial Maximum". In: *Nature* 599.7884 (7884), pp. 239–244. DOI: 10.1038/s41586-021-03984-4.

Ott, Edward et al. (Jan. 1, 2004). "A Local Ensemble Kalman Filter for Atmospheric Data Assimilation". In: *Tellus A: Dynamic Meteorology and Oceanography* 56.5, pp. 415–428. DOI: 10.3402/tellusa.v56i5.14462.

Parsons, Luke A. et al. (2021). "Do Multi-Model Ensembles Improve Reconstruction Skill in Paleoclimate Data Assimilation?" In: *Earth and Space Science* 8.4, e2020EA001467. DOI: 10.1029/2020EA001467.

Peixoto, Jose P. and Abraham H. Oort (1992). *Physics of Climate*. New York: American Institute of Physics.

Perkins, W. A. and G. J. Hakim (2021). "Coupled Atmosphere–Ocean Reconstruction of the Last Millennium Using Online Data Assimilation". In: *Paleoceanography and Paleoclimatology* 36.5, e2020PA003959. DOI: 10.1029/2020PA003959.

Petrie, Ruth Elizabeth (2008). "Localization in the Ensemble Kalman Filter".

Poage, Michael A. and C. Page Chamberlain (Jan. 1, 2001). "Empirical Relationships Between Elevation and the Stable Isotope Composition of Precipitation and Surface Waters: Considerations for Studies of Paleoelevation Change". In: *American Journal of Science* 301.1, pp. 1–15. DOI: 10.2475/ajs.301.1.1.

Ramos, R. D. et al. (2022). "Constraining Clouds and Convective Parameterizations in a Climate Model Using Paleoclimate Data". In: *Journal of Advances in Modeling Earth Systems* 14.8, e2021MS002893. DOI: 10.1029/2021MS002893.

Rehfeld, Kira et al. (Feb. 2018). "Global Patterns of Declining Temperature Variability from the Last Glacial Maximum to the Holocene". In: *Nature* 554.7692 (7692), pp. 356–359. DOI: 10.1038/nature25454.

Reschke, Maria et al. (Mar. 26, 2019). "Empirical Estimate of the Signal Content of Holocene Temperature Proxy Records". In: *Climate of the Past* 15.2, pp. 521–537. DOI: 10.5194/cp-15-521-2019.

Rodgers, Clive D. (July 17, 2000). *Inverse Methods For Atmospheric Sounding: Theory And Practice*. World Scientific. 256 pp. Google Books: Xv7sCgAAQBAJ.

Roedel, Walter and Thomas Wagner (2017). *Physik unserer Umwelt: Die Atmosphäre*. Berlin, Heidelberg: Springer. DOI: 10.1007/978-3-662-54258-3.

Rohde, Robert A. and Zeke Hausfather (Dec. 17, 2020). "The Berkeley Earth Land/Ocean Temperature Record". In: *Earth System Science Data* 12.4, pp. 3469–3479. DOI: 10.5194/essd-12-3469-2020.

Sanchez, Sara C. et al. (Mar. 1, 2021). "Climate Model Teleconnection Patterns Govern the Niño-3.4 Response to Early Nineteenth-Century Volcanism in Coral-Based Data Assimilation Reconstructions". In: *Journal of Climate* 34.5, pp. 1863–1880. DOI: 10.1175/JCLI-D-20-0549.1.

Shoji, Satoru et al. (May 2022). "Impact of Proxies and Prior Estimates on Data Assimilation Using Isotope Ratios for the Climate Reconstruction of the Last Millennium". In: *Earth and Space Science* 9.5. DOI: 10.1029/2020EA001618.

Sjolte, Jesper et al. (Sept. 11, 2020). "Seasonal Reconstructions Coupling Ice Core Data and an Isotope-Enabled Climate Model – Methodological Implications of Seasonality, Climate Modes and Selection of Proxy Data". In: *Climate of the Past* 16.5, pp. 1737–1758. DOI: 10.5194/cp-16-1737-2020.

Smerdon, Jason E. (2012). "Climate Models as a Test Bed for Climate Reconstruction Methods: Pseudoproxy Experiments". In: *WIREs Climate Change* 3.1, pp. 63–77. DOI: 10.1002/wcc.149.

Smerdon, Jason E. et al. (Mar. 1, 2016). "Model-Dependent Spatial Skill in Pseudoproxy Experiments Testing Climate Field Reconstruction Methods for the Common Era". In: *Climate Dynamics* 46.5, pp. 1921–1942. DOI: 10.1007/s00382-015-2684-0.

Sorenson, H. W. (July 1970). "Least-Squares Estimation: From Gauss to Kalman". In: *IEEE Spectrum* 7.7, pp. 63–68. DOI: 10.1109/MSPEC.1970.5213471.

Steiger, Nathan and Gregory Hakim (June 24, 2016). "Multi-Timescale Data Assimilation for Atmosphere–Ocean State Estimates". In: *Climate of the Past* 12.6, pp. 1375–1388. DOI: 10.5194/cp-12-1375-2016.

Steiger, Nathan J. et al. (Jan. 1, 2014). "Assimilation of Time-Averaged Pseudoproxies for Climate Reconstruction". In: *Journal of Climate* 27.1, pp. 426–441. DOI: 10.1175/JCLI-D-12-00693.1.

Steiger, Nathan J. et al. (2017). "Climate Reconstruction Using Data Assimilation of Water Isotope Ratios from Ice Cores". In: *Journal of Geophysical Research: Atmospheres* 122.3, pp. 1545–1568. DOI: 10.1002/2016JD026011.

Steiger, Nathan J. et al. (May 22, 2018). "A Reconstruction of Global Hydroclimate and Dynamical Variables over the Common Era". In: *Scientific Data* 5.1 (1), p. 180086. DOI: 10.1038/sdata.2018.86.

Steiger, Nathan J. et al. (Oct. 2021). "ENSO-driven Coupled Megadroughts in North and South America over the Last Millennium". In: *Nature Geoscience* 14.10 (10), pp. 739–744. DOI: 10.1038/s41561-021-00819-9.

Stevenson, S. et al. (2019). "Volcanic Eruption Signatures in the Isotope-Enabled Last Millennium Ensemble". In: *Paleoceanography and Paleoclimatology* 34.8, pp. 1534–1552. DOI: 10.1029/2019PA003625.

Storch, Hans von (2000). "Combining Paleoclimatic Evidence and GCMS by Means of Data Assimilation Through Upscaling and Nudging (Datun)". In:

Strang, Gilbert (2006). *Linear Algebra and Its Applications*. Belmont, CA: Thomson, Brooks/Cole.

— (2007). *Computational Science and Engineering*. Vol. 791. Wellesley-Cambridge Press Wellesley.

Sun, Haohao et al. (2022). "An Analog Offline EnKF for Paleoclimate Data Assimilation". In: *Journal of Advances in Modeling Earth Systems* 14.5, e2021MS002674. DOI: 10.1029/2021MS002674.

Tardif, Robert et al. (July 5, 2019). "Last Millennium Reanalysis with an Expanded Proxy Database and Seasonal Proxy Modeling". In: *Climate of the Past* 15.4, pp. 1251–1273. DOI: 10.5194/cp-15-1251-2019.

Tejedor, E. et al. (2021a). "Global Temperature Responses to Large Tropical Volcanic Eruptions in Paleo Data Assimilation Products and Climate Model Simulations Over the Last Millennium". In: *Paleoceanography and Paleoclimatology* 36.4, e2020PA004128. DOI: 10.1029/2020PA004128.

Tejedor, Ernesto et al. (Mar. 23, 2021b). "Global Hydroclimatic Response to Tropical Volcanic Eruptions over the Last Millennium". In: *Proceedings of the National Academy of Sciences* 118.12. DOI: 10.1073/pnas.2019145118. pmid: 33798096.

Tierney, Jessica E. and Martin P. Tingley (June 23, 2015). "A TEX86 Surface Sediment Database and Extended Bayesian Calibration". In: *Scientific Data* 2.1 (1), p. 150029. DOI: 10.1038/sdata.2015.29.

— (2018). "BAYSPLINE: A New Calibration for the Alkenone Paleothermometer". In: *Paleoceanography and Paleoclimatology* 33.3, pp. 281–301. DOI: 10.1002/2017PA003201.

Tierney, Jessica E. et al. (2019). "Bayesian Calibration of the Mg/Ca Paleothermometer in Planktic Foraminifera". In: *Paleoceanography and Paleoclimatology* 34.12, pp. 2005–2030. DOI: 10.1029/2019PA003744.

Tierney, Jessica E. et al. (Aug. 2020). "Glacial Cooling and Climate Sensitivity Revisited". In: *Nature* 584.7822 (7822), pp. 569–573. DOI: 10.1038/s41586-020-2617-x.

Tierney, Jessica E. et al. (Oct. 18, 2022). "Spatial Patterns of Climate Change across the Paleocene–Eocene Thermal Maximum". In: *Proceedings of the National Academy of Sciences* 119.42, e2205326119. DOI: 10.1073/pnas.2205326119.

Tindall, J. C. et al. (Feb. 21, 2009). "Stable Water Isotopes in HadCM3: Isotopic Signature of El Niño–Southern Oscillation and the Tropical Amount Effect". In: *Journal of Geophysical Research* 114.D4, p. D04111. DOI: 10.1029/2008JD010825.

Tippett, Michael K. et al. (July 1, 2003). "Ensemble Square Root Filters". In: *Monthly Weather Review* 131.7, pp. 1485–1490. DOI: 10.1175/1520-0493(2003)131⟨1485:ESRF⟩2.0.CO;2.

Tremaine, Darrel M. et al. (Sept. 2011). "Speleothem Calcite Farmed in Situ: Modern Calibration of δ18O and δ13C Paleoclimate Proxies in a Continuously-Monitored Natural Cave System". In: *Geochimica et Cosmochimica Acta* 75.17, pp. 4929–4950. DOI: 10.1016/j.gca.2011.06.005.

Tuan Pham, Dinh et al. (Oct. 1, 1998). "A Singular Evolutive Extended Kalman Filter for Data Assimilation in Oceanography". In: *Journal of Marine Systems* 16.3, pp. 323–340. DOI: 10.1016/S0924-7963(97)00109-7.

Valler, Veronika et al. (Aug. 2, 2019). "Impact of Different Estimations of the Background-Error Covariance Matrix on Climate Reconstructions Based on Data Assimilation". In: *Climate of the Past* 15.4, pp. 1427–1441. DOI: 10.5194/cp-15-1427-2019.

Vetra-Carvalho, Sanita et al. (Jan. 1, 2018). "State-of-the-Art Stochastic Data Assimilation Methods for High-Dimensional Non-Gaussian Problems". In: *Tellus A: Dynamic Meteorology and Oceanography* 70.1, pp. 1–43. DOI: 10.1080/16000870.2018.1445364.

Vuille, M. et al. (Aug. 23, 2012). "A Review of the South American Monsoon History as Recorded in Stable Isotopic Proxies over the Past Two Millennia". In: *Climate of the Past* 8.4, pp. 1309–1321. DOI: 10.5194/cp-8-1309-2012.

Wackerbarth, A. et al. (Nov. 5, 2012). "Simulated Oxygen Isotopes in Cave Drip Water and Speleothem Calcite in European Caves". In: *Climate of the Past* 8.6, pp. 1781–1799. DOI: 10.5194/cp-8-1781-2012.

Wang, J. et al. (Jan. 6, 2014). "Evaluating Climate Field Reconstruction Techniques Using Improved Emulations of Real-World Conditions". In: *Climate of the Past* 10.1, pp. 1–19. DOI: 10.5194/cp-10-1-2014.

Wang, Xianfeng et al. (Jan. 2017). "Hydroclimate Changes across the Amazon Lowlands over the Past 45,000 Years". In: *Nature* 541.7636 (7636), pp. 204–207. DOI: 10.1038/nature20787.

Werner, M. (2010). "Modelling Stable Water Isotopes: Status and Perspectives". In: *EPJ Web of Conferences* 9, pp. 73–82. DOI: 10.1051/epjconf/201009005.

Werner, M. et al. (Feb. 17, 2016). "Glacial–Interglacial Changes in $H_2{}^{18}O$, HDO and Deuterium Excess – Results from the Fully Coupled ECHAM5/MPI-OM Earth System Model". In: *Geoscientific Model Development* 9.2, pp. 647–670. DOI: 10.5194/gmd-9-647-2016.

Whitaker, Jeffrey S. and Thomas M. Hamill (July 1, 2002). "Ensemble Data Assimilation without Perturbed Observations". In: *Monthly Weather Review* 130.7, pp. 1913–1924. DOI: 10.1175/1520-0493(2002)130⟨1913:EDAWPO⟩2.0.CO;2.

Yoshimura, K. et al. (2008). "Historical Isotope Simulation Using Reanalysis Atmospheric Data". In: *Journal of Geophysical Research: Atmospheres* 113.D19. DOI: 10.1029/2008JD010074.

Zhou, Jiayu and K-M. Lau (May 1998). "Does a Monsoon Climate Exist over South America?" In: *Journal of Climate* 11.5, pp. 1020–1040. DOI: 10.1175/1520-0442(1998)011⟨1020:DAMCEO⟩2.0.CO;2.

Zhu, Feng et al. (2020). "Resolving the Differences in the Simulated and Reconstructed Temperature Response to Volcanism". In: *Geophysical Research Letters* 47.8, e2019GL086908. DOI: 10.1029/2019GL086908.

Zhu, Feng et al. (Feb. 8, 2022). "A Re-Appraisal of the ENSO Response to Volcanism with Paleoclimate Data Assimilation". In: *Nature Communications* 13.1 (1), p. 747. DOI: 10.1038/s41467-022-28210-1.

Appendix A

Detailed flowchart of the PaleoDA code

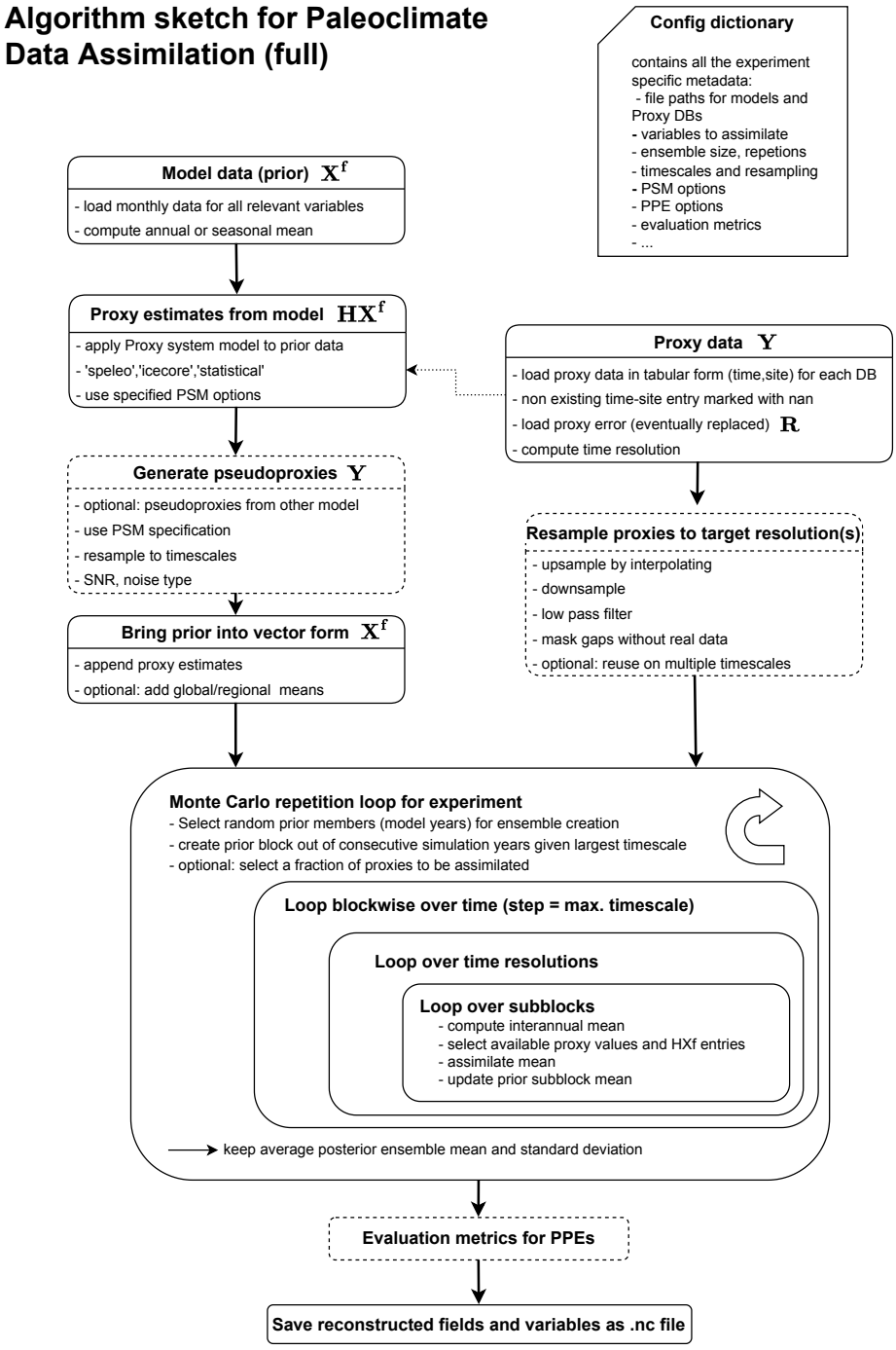

Figure A.1: Algorithm sketch for PaleoDA code developed for this thesis (see 4.1 for the simplified version). Dashed boxes indicate optional steps dependent of the configuration and the dashed arrow indicates the input of proxy metadata for the PSM. The reconstruction can be comprehensively configured with a configuration dictionary. Practical examples and detailed descriptions of all options can be found in the public repository https://github.com/mchoblet/paleoda.

Appendix B

Additional figures

B.1 GISS drift (Section 3.1)

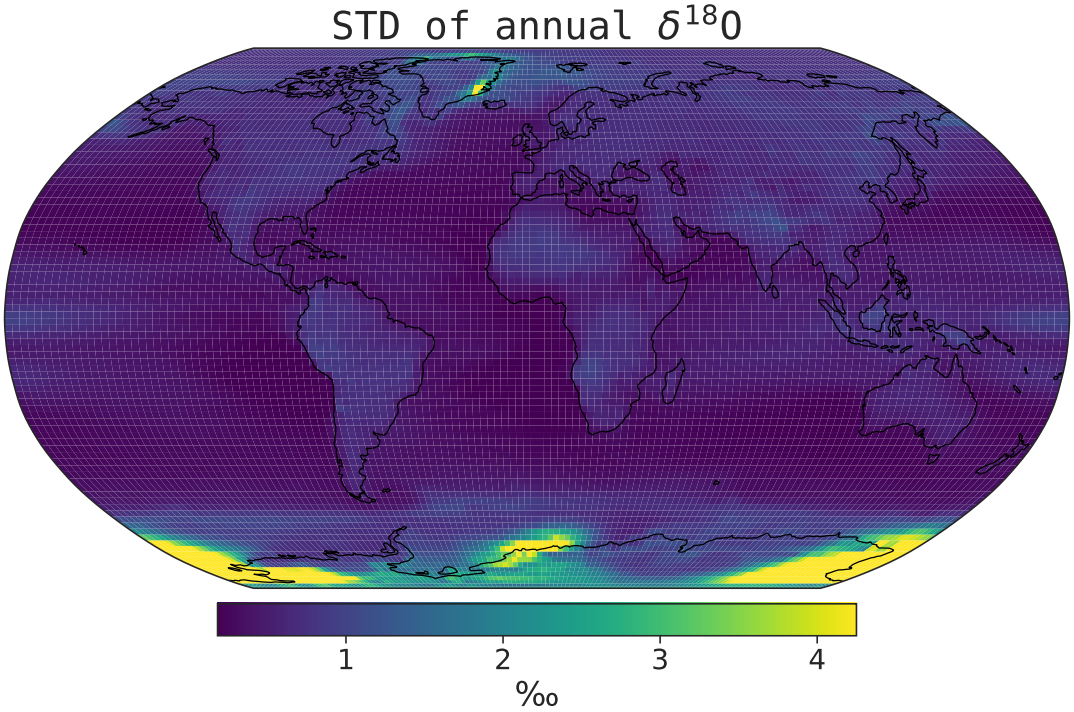

Figure B.1: Standard deviation of the annual mean δ^{18}O from the GISS last millennium simulation (see Table 3.1). The extreme values in the west and the east of Antarctica, and the eastern coast of Greenland indicate a model artefact.

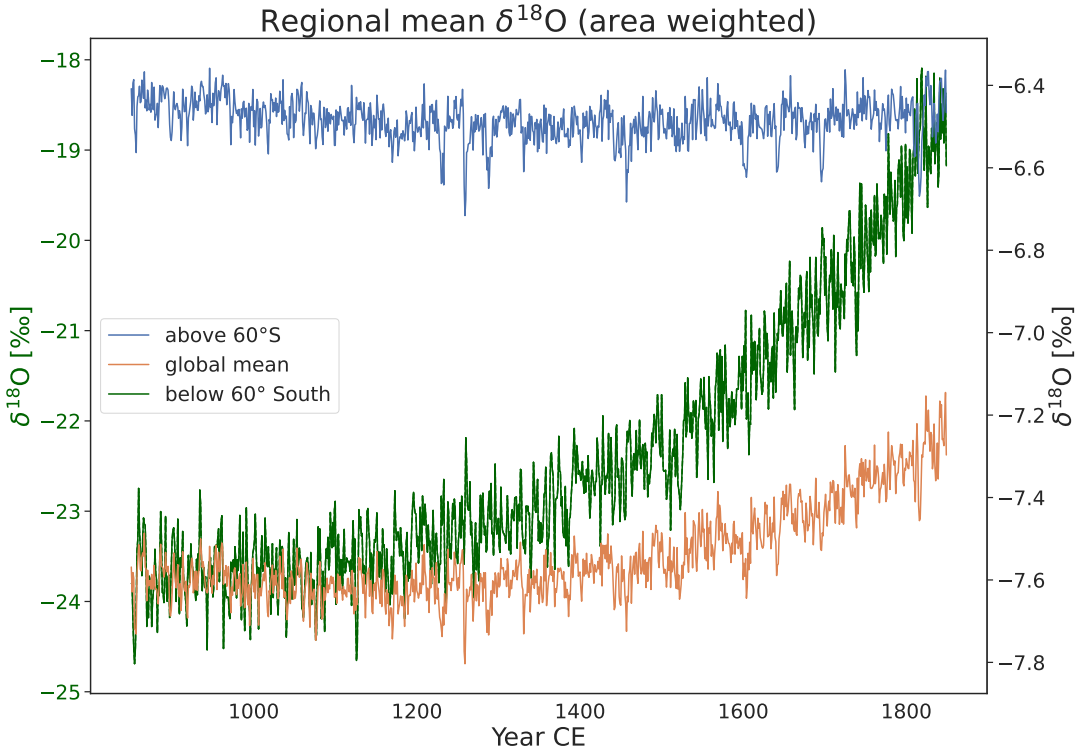

Figure B.2: Visualization of the δ^{18}O drift in the GISS last millennium simulation. The left axis refers to the green curve, which is the mean δ^{18}O for all grid cells south of 60°S (range -25 to -18 ‰). The right axis refers to the blue and orange curves, which represent the global mean and the mean of all grid cells above 60°S (range -7.8 to - 6.4 ‰).

B.2 Model data comparison (Section 5.1)

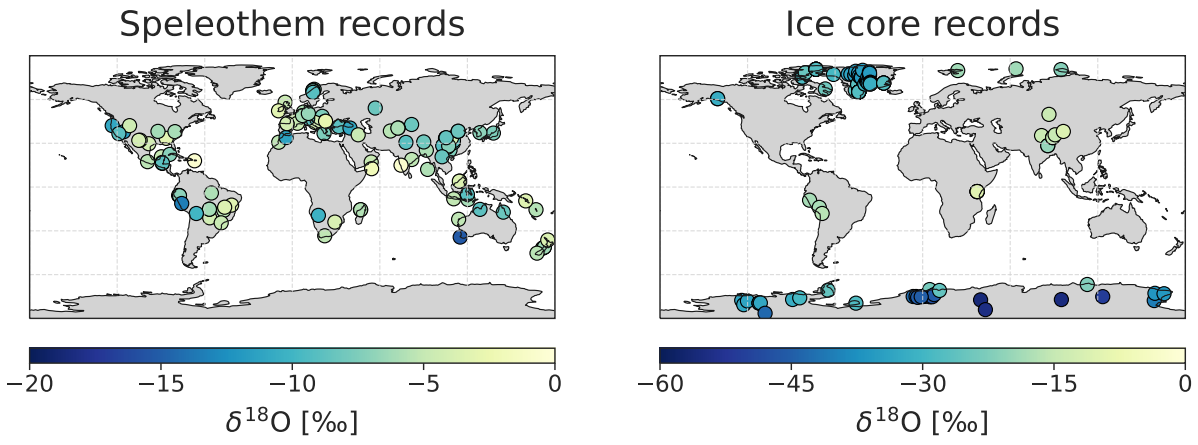

Figure B.3: Median δ^{18}O value of the selected proxy records from SISALv2 (left panel, speleothem records) and Iso2k (right panel, ice core records) for the period 850-1850CE.

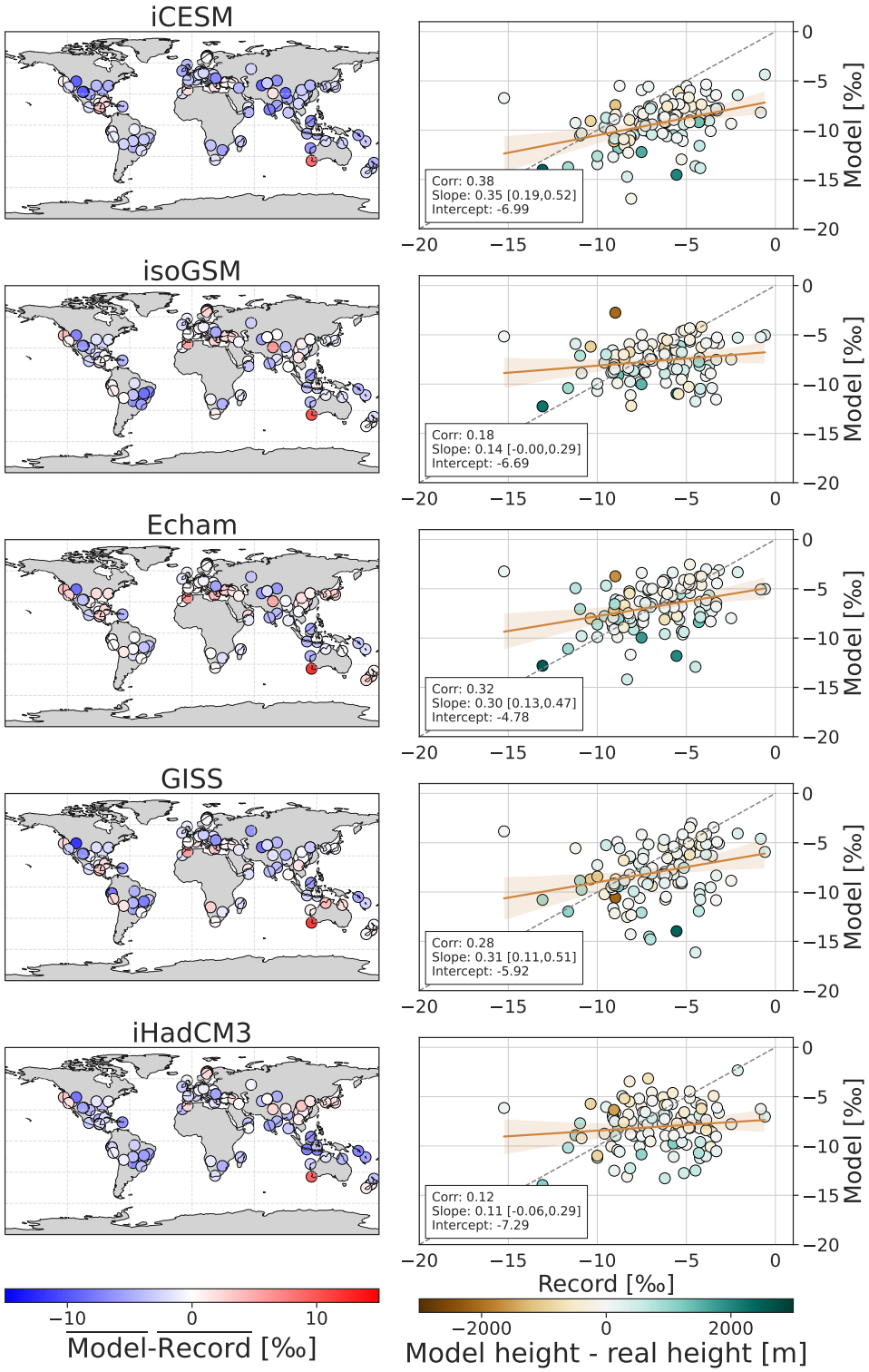

Figure B.4: Comparison of the median PSM converted $\delta^{18}O$ values from the climate models to the proxy record medians for the SISALv2 records (850-1850CE). In the left column, the model bias is indicated by color for the individual records and in the right column the simulated medians are plotted against the proxy record medians. The colour in the dots indicates the height difference of the respective model grid cell to the elevation of the proxy record locations. The colored lines indicate the correlation and the 95% confidence interval.

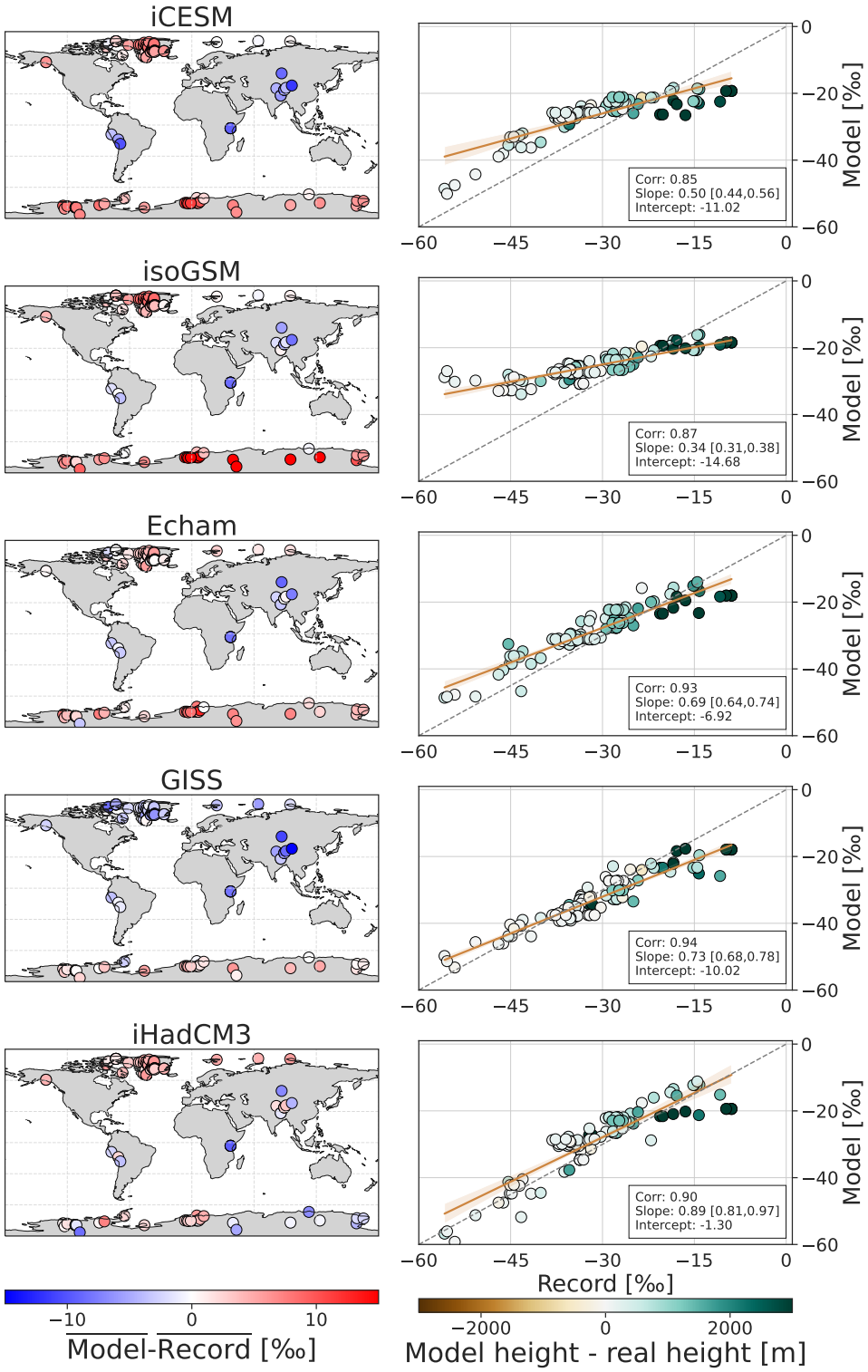

Figure B.5: Difference of PSM converted simulated δ^{18}O values to the ice core records, as in Figure B.4.

B.3 Area of the averaging kernel (Section 5.2)

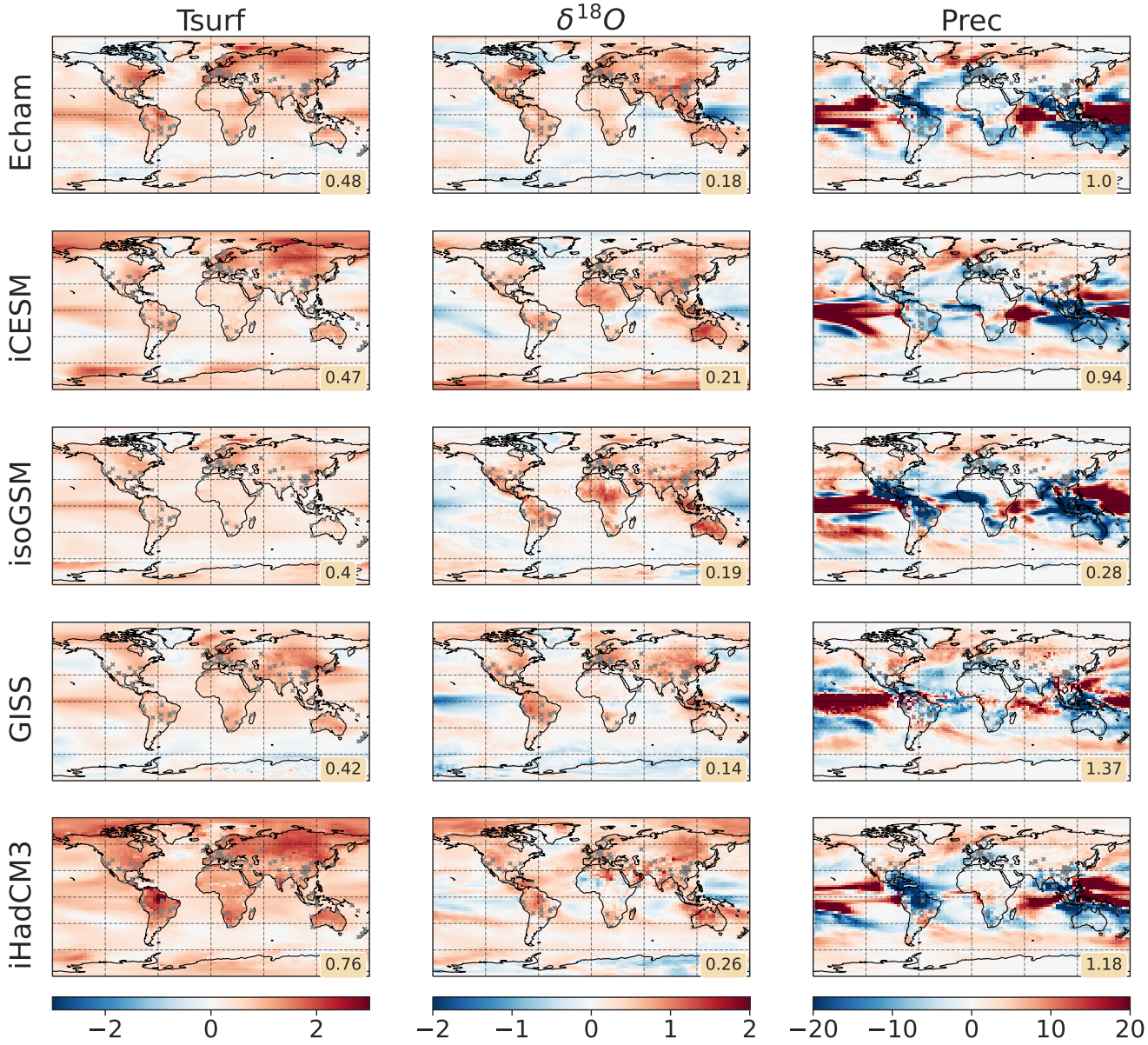

Figure B.6: Area of the averaging kernel (Kalman gain summed up for each grid cell) using the annual δ^{18}O at the selected SISALv2 speleothem locations and assuming a proxy error variance of $0.5‰^2$. The proxy record locations are indicated by grey x-markers. The global mean value is written in the box in the lower right corner.

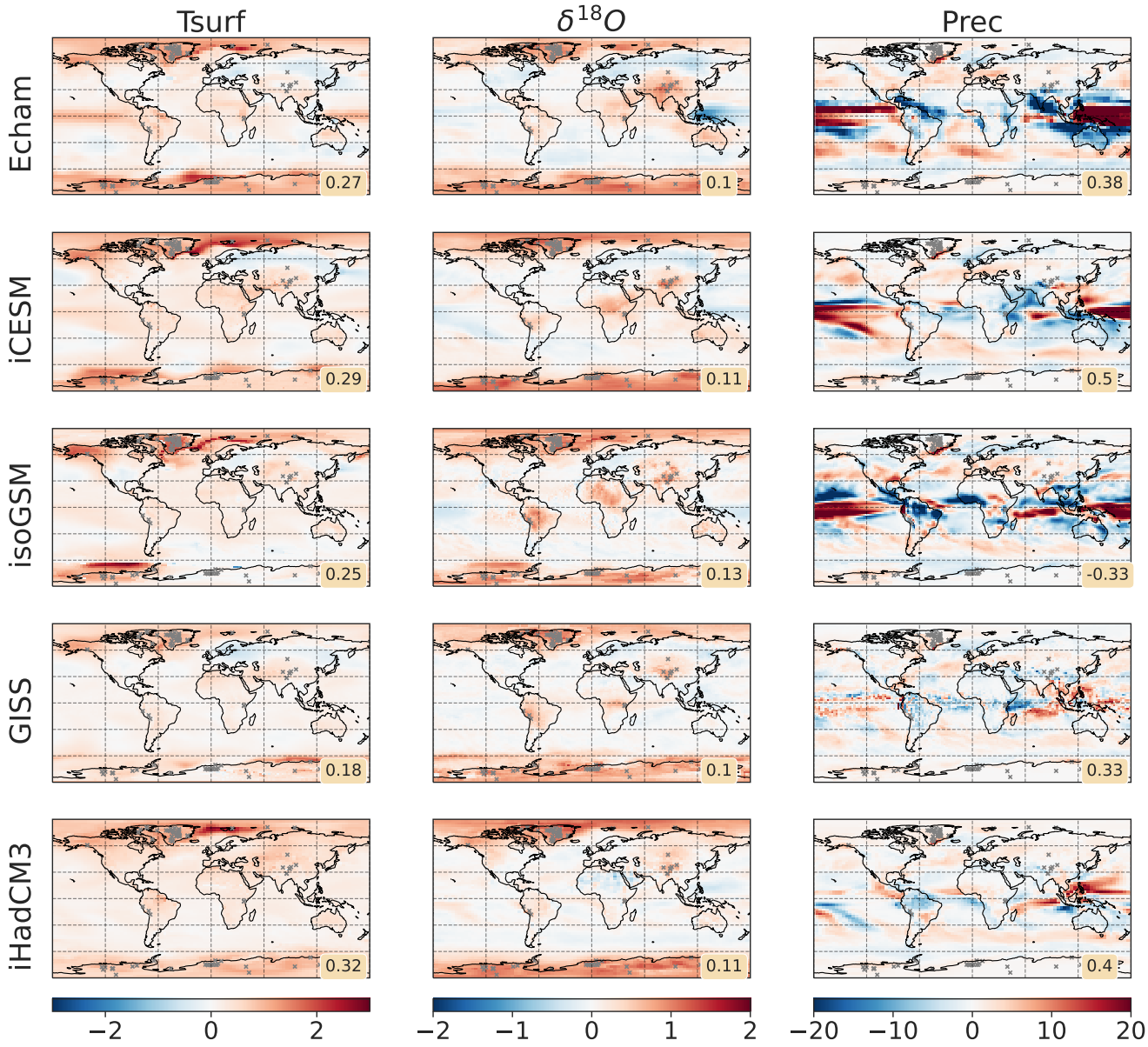

Figure B.7: As Figure B.6 for δ^{18}O at the selected Iso2k ice core locations.

B.4 Pseudoproxy experiments (Section 5.3)

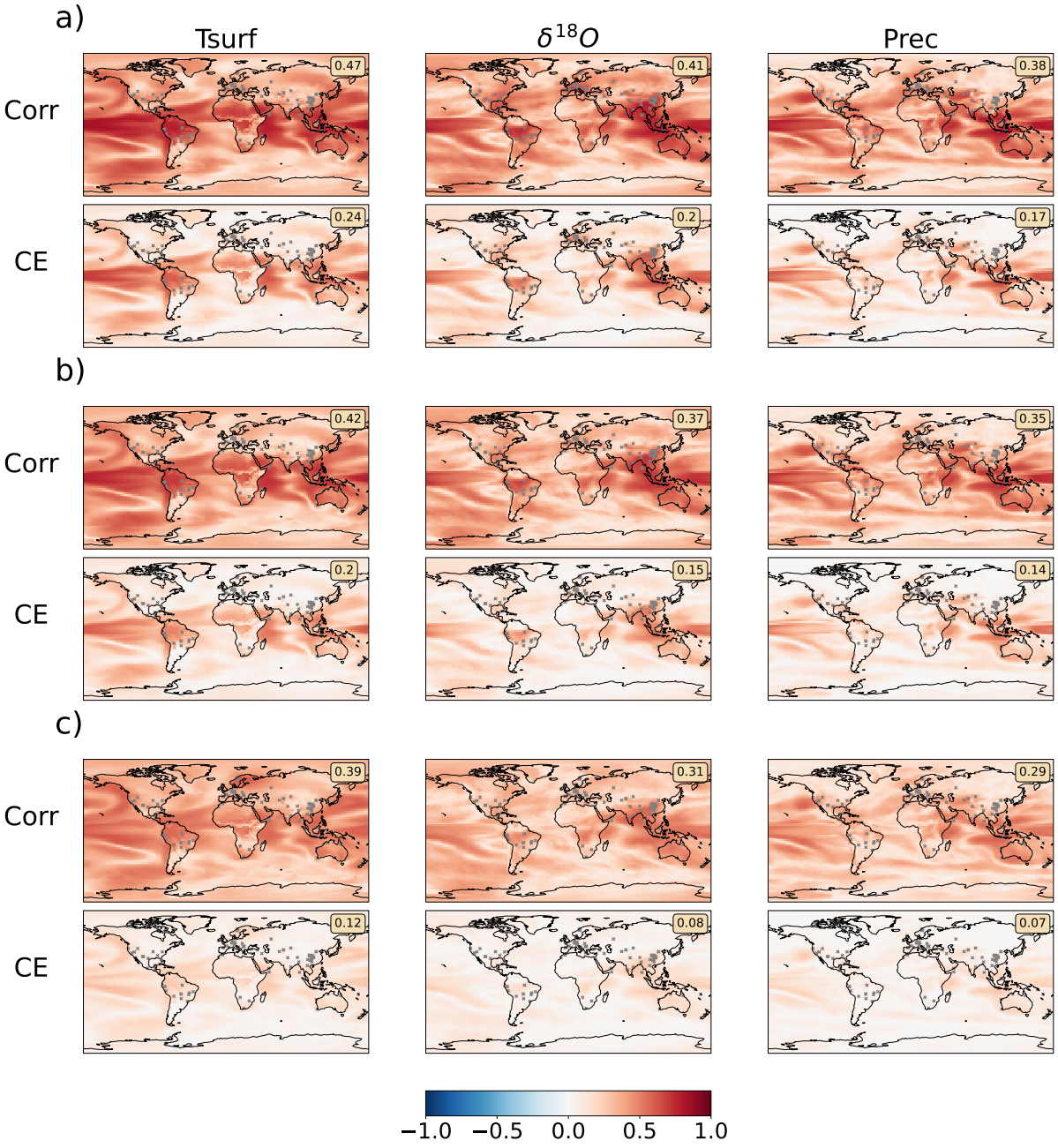

Figure B.8: Skill scores of Pseudoproxy experiments for reconstructing the climatic fields of the iCESM simulation from the simulated δ^{18}O at the speleothem locations. The global mean of the skill metrics is annotated in the upper right corner. The pseudoproxies are created with a SNR of 0.5, which is applied to the simulated δ^{18}O time series before further modifications by the PSMs. In a), the annual mean δ^{18}O at the proxy record locations is used for the pseudoproxies. In b), the pseudoproxies are altered by infiltration weighting and fractionation for the speleothem pseudoproxies. In c), the pseudoproxies from b) are additionally modified by the karst filter.

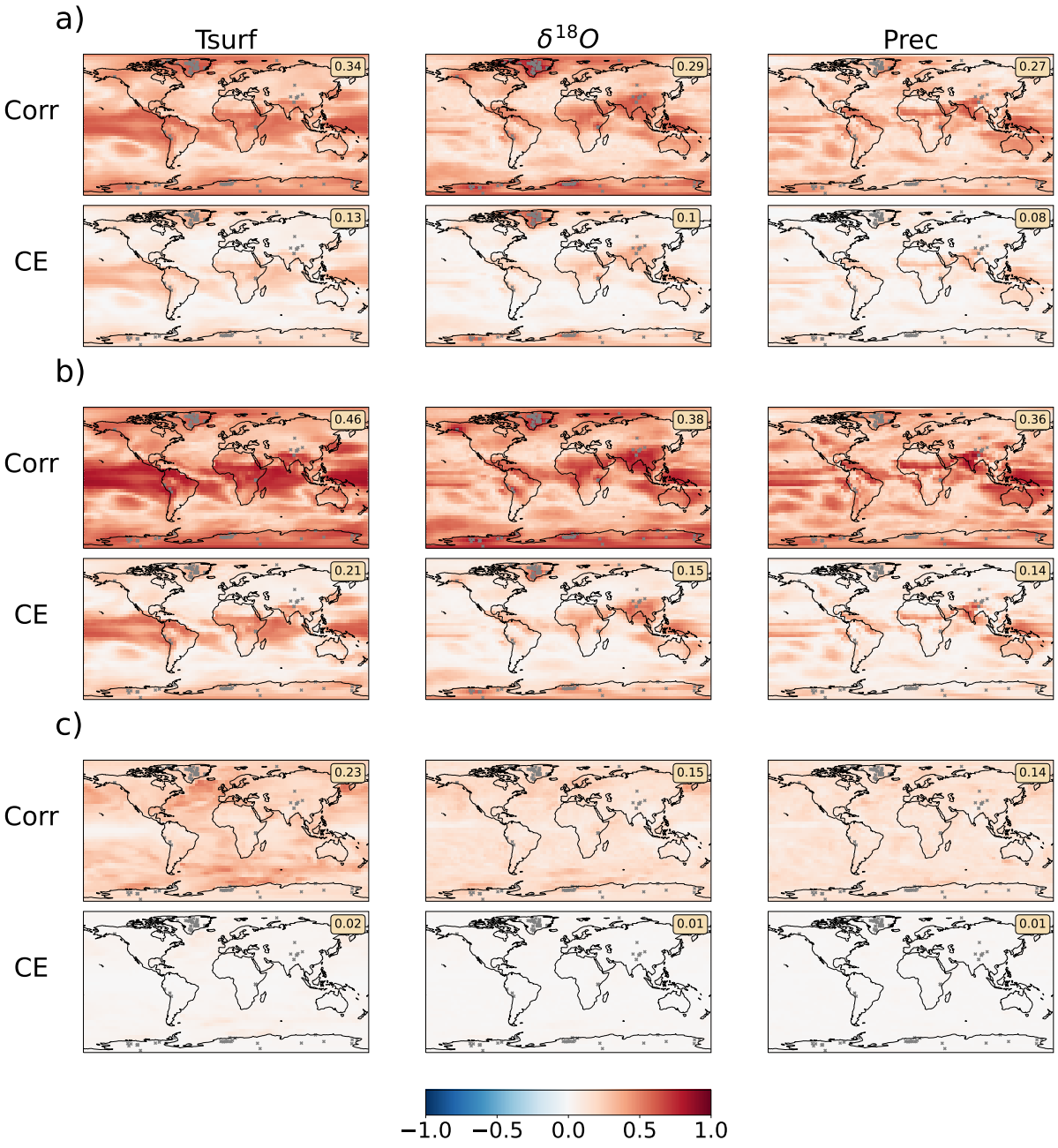

Figure B.9: As Figure B.8 for the selected Iso2k ice core records. In b) the δ^{18}O from the ice core record locations is modified by precipitation weighting and in c) the signal is further modified by firn diffusion and compaction for the ice cores.

B.5 Correlation analysis including the confidence intervals (Section 6.1)

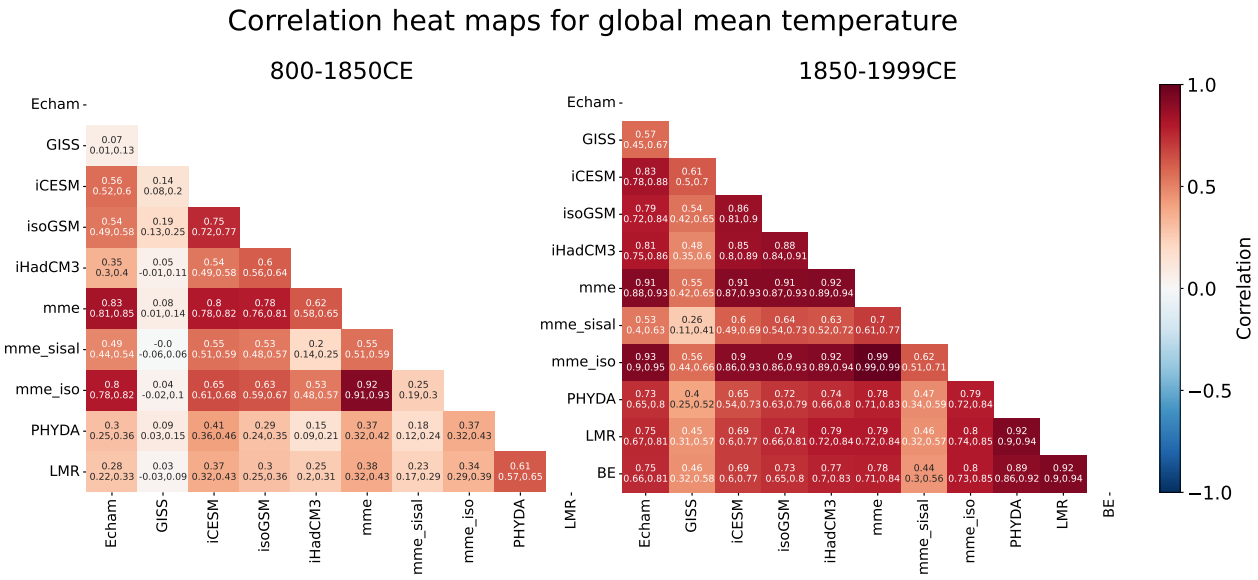

Figure B.10: Heat map visualizing the correlation between the time series in Figure 6.1 and 6.2. The upper value in each cell is the correlation coefficient, and the two lower values indicate its 95% confidence interval. The correlations are computed separately for the PI (left panel) and the CWP (right panel). The time series have not been detrended to assess similarity including the cooling and warming trends. No filtering of the signals has been performed. The CWP evaluation also includes the correlation with the observational global mean temperature from the Berkeley Earth dataset (BE). mme_sisal and mme_iso refer to the multi-model ensemble reconstructions with the separate SISALv2 and Iso2k database records.

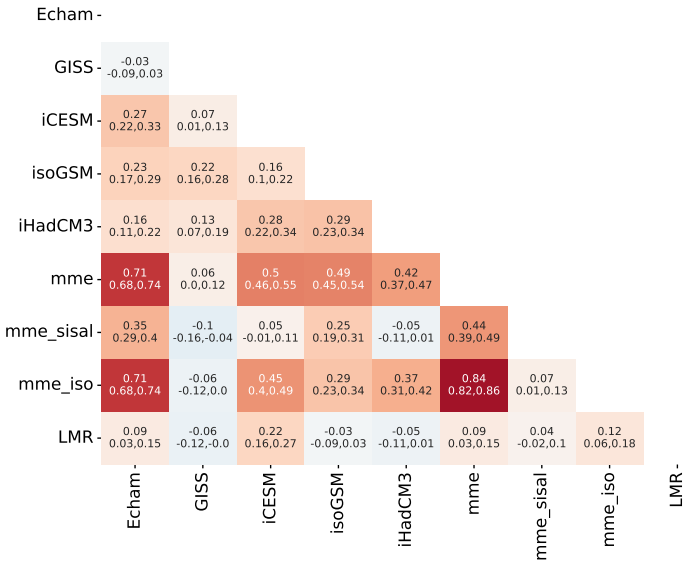

Figure B.11: Correlation heat map for global mean precipitation during the period 800-1850CE (Figure 6.7). The upper value in each cell is the correlation coefficient, and the two lower values indicate its 95% confidence interval.

B.6 Centennial mean anomalies for tropical South America from LMR (Section 6.2)

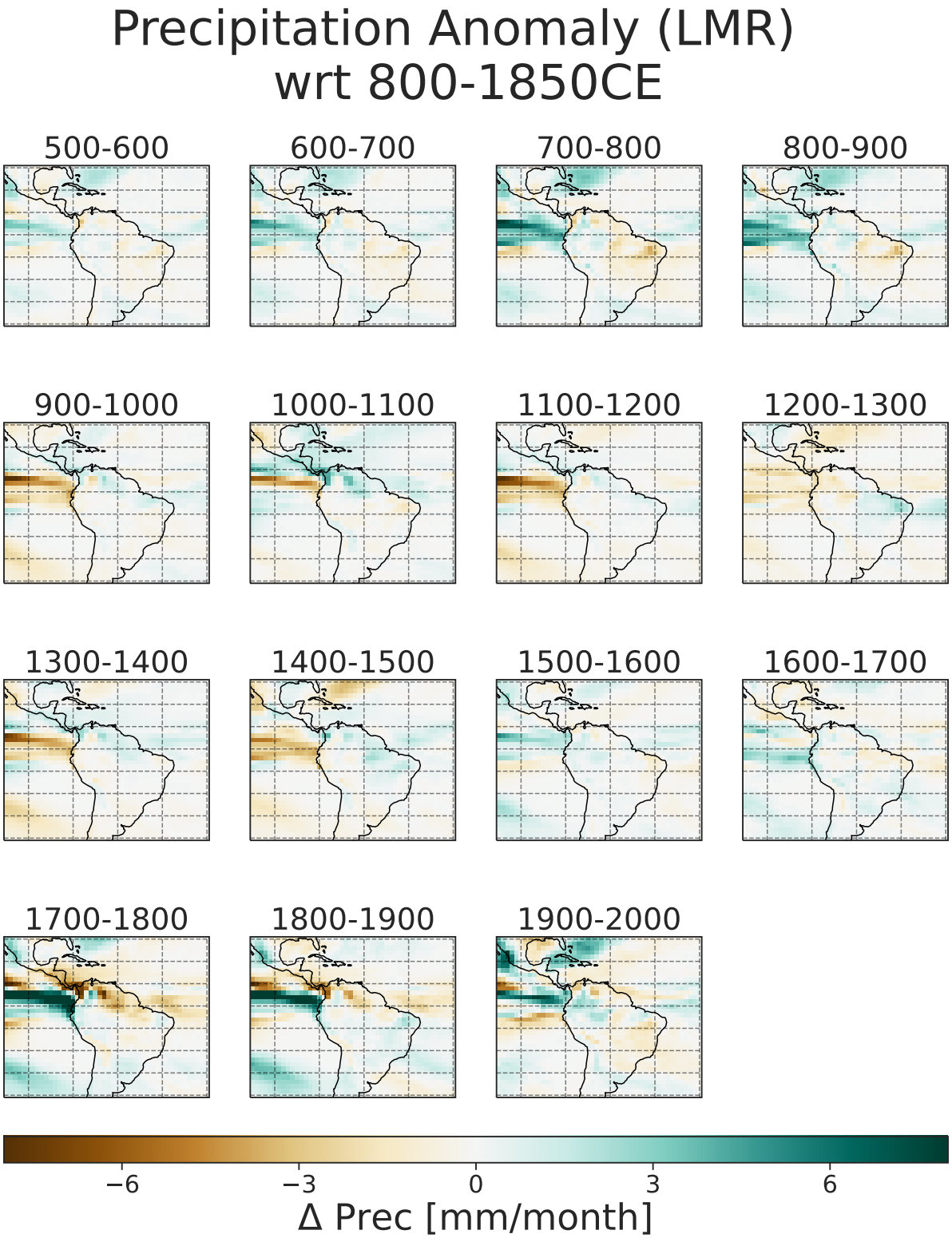

Figure B.12: Centennial mean precipitation anomaly fields for tropical South America from the 6th to the 20th century in the Last Millennium Reanalysis (Hakim et al., 2016).

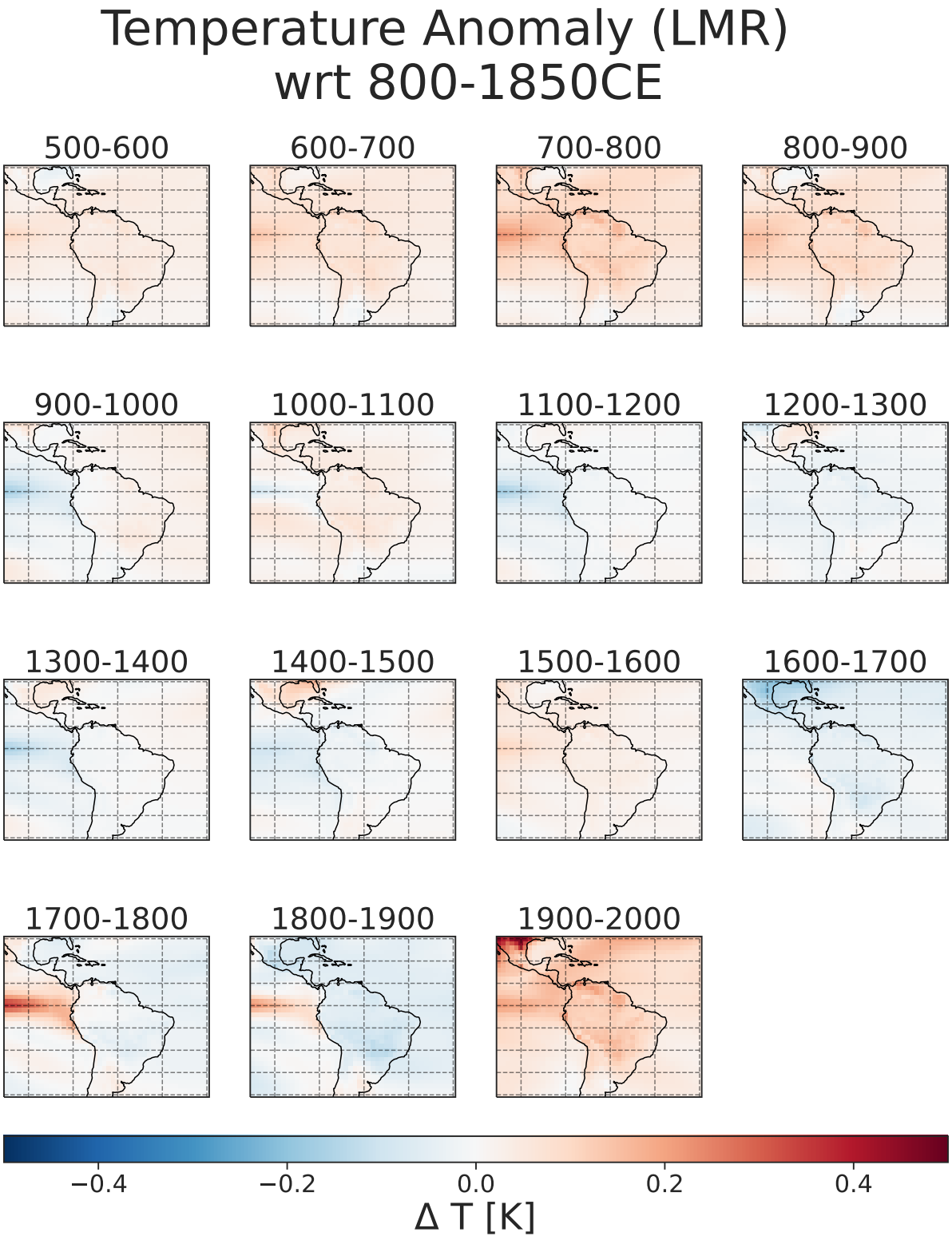

Figure B.13: Centennial mean temperature anomaly fields for tropical South America from the 6th to the 20th century in the Last Millennium Reanalysis (Hakim et al., 2016).

Appendix C

Matrix calculations fact sheet

This appendix section briefly reviews basic matrix calculation concepts (without proofs) which are used for the derivations of the Ensemble Kalman Filter formulas. This is only a small subset of many fascinating matrix decompositions and theorems. For the reader interested to learn more about Linear Algebra and its matrix representation, I recommend textbooks as Strang (2006) and Strang (2007). The respective lecture recordings are available via MIT OpenCourseWare. These resources also served as the primary source for this fact sheet.

Matrix definition
An n×m matrix $\mathbf{A}$ is a rectangular array which consists of n rows and m columns, in case its entries are real values it can be written as $\mathbf{A} \epsilon \mathbf{R}^{n \times m}$.
A matrix can be written in form of its entries as

$$\mathbf{A} = (a_{ij}) \tag{C.1}$$

where $i \epsilon 1, \ldots, n$ denotes the rows and $j \epsilon 1, \ldots, m$ the columns. It is called a square matrix if $n = m$.
The addition and subtraction of matrices is associative and commutative, whereas the multiplication of matrices is associative and distributive, but not commutative.
A matrix is called *diagonal* if it only has nonzero entries on its entries. A lower/upper *triangular* matrix only contains nonzero values in the part below/above its diagonal (including the diagonal).

Transpose of a matrix
The transpose of a matrix $\mathbf{A}$ is obtained by inverting its rows and columns:

$$\mathbf{A}^T = (a_{ij})^T = (a_{ji}) \tag{C.2}$$

where $i \epsilon 1, \ldots, n$ and $j \epsilon 1, \ldots, m$. The transpose of a product of matrices $(\mathbf{AB})^T$ is $\mathbf{B}^T \mathbf{A}^T$.

Symmetric matrices
A matrix $\mathbf{S}$ is symmetric if

$$\mathbf{S} = \mathbf{S}^T. \tag{C.3}$$

The product of any matrix $\mathbf{A}$ with its transpose, $\mathbf{AA}^T$ is a symmetric matrix. Symmetric matrices are positive semidefinite.

Inverse of a matrix
The inverse of a matrix $\mathbf{A} \epsilon \mathbf{R}^{n \times m}$ is denoted by the superscript -1. $\mathbf{A}^{-1}$ is the matrix which multiplied with $\mathbf{A}$ results in the identity matrix $\mathbf{I}$, a diagonal matrix which only consists of ones.

$$\mathbf{A}\mathbf{A}^{-1} = \mathbf{I} \tag{C.4}$$

The inverse of a matrix is unique. In case $\mathbf{A}$ is not a square matrix one must distinguish between the left and right inverse of a matrix, else it is the same matrix.
Matrices which have such an inverse and are thus invertible are also called *non singular*, whereas noninvertible matrices are called *singular*.
The inverse of a product of matrices $(\mathbf{AB})^{-1}$ is $(\mathbf{B}^{-1}\mathbf{A}^{-1})$.
A matrix is called *orthogonal* if its inverse is equal to its transpose: $\mathbf{A}^{-1} = \mathbf{A}^T$.

Facts about a non singular $n \times n$ matrix A

1. The rows and columns of $\mathbf{A}$ are independent, meaning that they cannot be obtained from one another through linear combinations (the matrix is said to have full rank).
2. The determinant of $\mathbf{A}$ is not zero.
3. All eigenvalues of $\mathbf{A}$ are nonzero.
4. $\mathbf{A}^T\mathbf{A}$ is symmetric and strictly positive definite.
5. $\mathbf{A}$ has n positive singular values.

Sherman-Morrison-Woodbury Formula
This matrix identity states that for matrices $\mathbf{A} \epsilon \mathbb{R}^{n \times n}$, $\mathbf{U} \epsilon \mathbb{R}^{n \times k}$,$\mathbf{V} \epsilon \mathbb{R}^{k \times n}$ and $\mathbf{C} \epsilon \mathbb{R}^{k \times k}$ the following equality holds

$$(\mathbf{A} + \mathbf{UCV}^T)^{-1} = \mathbf{A}^{-1} - \mathbf{A}^{-1}\mathbf{U}(\mathbf{C}^{-1} + \mathbf{VA}^{-1}\mathbf{U})^{-1}\mathbf{VA}^{-1}. \tag{C.5}$$

Eigenvalues and vectors
$\mathbf{A}$ has the nonzero eigenvector $\mathbf{x}$ with the corresponding scalar eigenvalue λ if

$$\mathbf{Ax} = \lambda\mathbf{x}. \tag{C.6}$$

$\mathbf{A}^T$ has the same eigenvectors and eigenvalues as $\mathbf{A}$.

Eigenvalue decomposition (EVD)
A square matrix $\mathbf{A} \epsilon \mathbf{R}^{n \times n}$ which has n linearly independent eigenvectors can be de decomposed into its eigenvector matrix $\mathbf{S}$ (the columns are eigenvectors of A) and its eigenvalue matrix Λ, which is a diagonal matrix with the Eigenvalues as its entries.

$$\mathbf{A} = \mathbf{S}\Lambda\mathbf{S}^{-1} \tag{C.7}$$

When $\mathbf{A}$ is a symmetric matrix, its eigenvectors and hence $\mathbf{S}$ are orthogonal. EVD can be used for instance for finding the inverse of a matrix, because it has the same eigenvectors and the inverse eigenvalues.

$$\mathbf{A}^{-1} = \mathbf{S}\Lambda^{-1}\mathbf{S}^{-1} \tag{C.8}$$

Positive (semi) definite matrices
A matrix $\mathbf{A}\epsilon\mathbf{R}^{n\times n}$ is said to be *positive semidefinite* if

$$x\mathbf{A}x^T \geq 0 \text{ for all } x\,\epsilon\,\mathbf{R}^{n\times 1}\backslash\{0\} \tag{C.9}$$

$$\text{All its eigenvalues are non negative} \tag{C.10}$$

Both definitions are equivalent and hence only one of both is required to be shown for positive semidefiniteness of a matrix. A matrix is said to be *positive definite* if the inequality is strictly non-negative and all eigenvalues are positive.

Singular Value Decomposition (SVD)
Any real matrix $\mathbf{A}\,\epsilon\,\mathbf{R}^{m\times n}$ can be decomposed into a set of of orthogonal and diagonal matrices.

$$\mathbf{A} = \mathbf{U}\mathbf{\Sigma}\mathbf{V}^T \tag{C.11}$$

where $\mathbf{U}\epsilon\mathbf{R}^{m\times n}$ and $\mathbf{V}\epsilon\mathbf{R}^{n\times n}$ are orthogonal matrices and $\mathbf{\Sigma}\epsilon\mathbf{R}^{n\times n}$ is a diagonal matrix which contains the singular values σ_i of $\mathbf{A}$. The squared eigenvalues are the Eigenvalues of the matrix $\mathbf{A}^T\mathbf{A}$.

Matrix square roots
The matrix square root $\mathbf{X}$ of $\mathbf{A}$ is a matrix that fulfils

$$\mathbf{X}\mathbf{X}^T = \mathbf{A}. \tag{C.12}$$

Cholesky factorisation
Any symmetric and positive definite matrix can be decomposed into the product of a lower triangular matrix $\mathbf{C}$ with its transpose, which is an upper triangular matrix.

$$\mathbf{A} = \mathbf{C}\mathbf{C}^T \tag{C.13}$$

Appendix D

Derivation of the Kalman Filter

D.1 Derivation of the optimal Kalman gain (Equation 2.16)

The proof can be performed straightforwardly from Bayes' theorem using multivariate normal distributions. However, it involves a lot of notational overhead. I therefore follow a different, yet mathematically equivalent approach which is presented in Brown and Hwang (2012). The derivation as used here also gives more intuition for other calculations performed in this thesis. I start by showing the expression for the posterior error covariance $\mathbf{P}$ in Equation 2.18 starting from its basic definition and using Equation 2.15 for the posterior state estimate. The final goal is to find the expression for $\mathbf{K}$ that minimizes $\mathbf{P}$.

$$\begin{aligned}
\mathbf{P} &= \mathbb{E}[(\mathbf{x}-\hat{\mathbf{x}})(\mathbf{x}-\hat{\mathbf{x}})^T] && \text{(D.1)}\\
&= \mathbb{E}[(\mathbf{x}-\mathbf{x}^f-\mathbf{K}(\mathbf{y}-\mathbf{H}\mathbf{x}^f))(\mathbf{x}-\mathbf{x}^f-\mathbf{K}(\mathbf{y}-\mathbf{H}\mathbf{x}^f))^T] && \text{(D.2)}\\
&= \mathbb{E}[((\mathbf{x}-\mathbf{x}^f-\mathbf{K}(\mathbf{H}\mathbf{x}+\mathbf{v}-\mathbf{H}\mathbf{x}^f))(\mathbf{x}-\mathbf{x}^f-\mathbf{K}(\mathbf{H}\mathbf{x}+\mathbf{v}-\mathbf{H}\mathbf{x}^f))^T] && \text{(D.3)}\\
&= \mathbb{E}[[(\mathbf{I}-\mathbf{K}\mathbf{H})(\mathbf{x}-\mathbf{x}^f)-\mathbf{K}\mathbf{v}][(\mathbf{I}-\mathbf{K}\mathbf{H})(\mathbf{x}-\mathbf{x}^f)-\mathbf{K}\mathbf{v}]^T] && \text{(D.4)}\\
&= \mathbb{E}[[(\mathbf{I}-\mathbf{K}\mathbf{H})(\mathbf{x}-\mathbf{x}^f)(\mathbf{x}-\mathbf{x}^f)^T(\mathbf{I}-\mathbf{K}\mathbf{H})^T-(\mathbf{I}-\mathbf{K}\mathbf{H})(\mathbf{x}-\mathbf{x}^f)\mathbf{K}^T\mathbf{v}^T && \text{(D.5)}\\
&\quad -\mathbf{K}\mathbf{v}(\mathbf{x}-\mathbf{x}^f)^T(\mathbf{I}-\mathbf{K}\mathbf{H})^T+\mathbf{K}\mathbf{v}(\mathbf{v})^T\mathbf{K}^T] && \text{(D.6)}\\
& && \text{(D.7)}
\end{aligned}$$

This equation can be simplified using the fact that $\mathbf{K}$ and $\mathbf{H}$ are constant matrices and can thus be pulled out of the expected value operator. Furthermore, the observation error $\mathbf{v}$ and the estimation error $\mathbf{x}-\mathbf{x}^f$ are uncorrelated, such that $\mathbb{E}[(\mathbf{x}-\mathbf{x}^f)\mathbf{v}^T)]=0$. We use the linear properties of the expected value to split the equation into parts and use the definitions of $\mathbf{P}$ and $\mathbf{R}$.

$$\begin{aligned}
\mathbf{P} &= (\mathbf{I}-\mathbf{K}\mathbf{H})\,\mathbb{E}[[(\mathbf{x}-\mathbf{x}^f)(\mathbf{x}-\mathbf{x}^f)^T](\mathbf{I}-\mathbf{K}\mathbf{H})^T-(\mathbf{I}-\mathbf{K}\mathbf{H})\,\mathbb{E}[(\mathbf{x}-\mathbf{x}^f)\mathbf{v}^T]\mathbf{K}^T && \text{(D.8)}\\
&\quad -\mathbf{K}\,\mathbb{E}[\mathbf{v}(\mathbf{x}-\mathbf{x}^f)^T](\mathbf{I}-\mathbf{K}\mathbf{H})^T+\mathbf{K}\,\mathbb{E}[\mathbf{v}\mathbf{v}^T]\mathbf{K}^T && \text{(D.9)}\\
&= (\mathbf{I}-\mathbf{K}\mathbf{H})\mathbf{P}^f(\mathbf{I}-\mathbf{K}\mathbf{H})^T+\mathbf{K}\mathbf{R}\mathbf{K}^T && \text{(D.10)}
\end{aligned}$$

The next step consists of finding the specific solution for $\mathbf{K}$ that minimizes $\mathbf{P}$ which can be done by factoring the equation into the parts which are linear and quadratic in $\mathbf{K}$.

$$\begin{aligned}
\mathbf{P} &= \mathbf{P}^f-\mathbf{K}\mathbf{H}\mathbf{P}-\mathbf{P}^f(\mathbf{K}\mathbf{H})^T+\mathbf{K}\mathbf{H}\mathbf{P}^f(\mathbf{K}\mathbf{H})^T+\mathbf{K}\mathbf{R}\mathbf{K}^T && \text{(D.11)}\\
&= \mathbf{P}^f-\mathbf{K}\mathbf{H}\mathbf{P}-\mathbf{P}^f(\mathbf{K}\mathbf{H})^T+\mathbf{K}(\mathbf{H}\mathbf{P}^f\mathbf{H}^T+\mathbf{R})\mathbf{K}^T && \text{(D.12)}
\end{aligned}$$

The term in brackets, which is quadratic in $\mathbf{K}$ is a sum of symmetric matrices. Knowing that this term is positive definite[1], we can use the fact that a Cholesky decomposition with a triangular matrix $\mathbf{S}$ exists such that the term can be written as

$$\mathbf{S}\mathbf{S}^T := \mathbf{H}\mathbf{P}^f\mathbf{H}^T + \mathbf{R} \tag{D.13}$$

$\mathbf{S}$ will not be calculated explicitly, we only need to know that this kind of matrix exists. Hence, we can write the equation for $\mathbf{P}$ in a quadratic form using a matrix $\mathbf{A}$, which we need to find to find the Kalman gain $\mathbf{K}$.

$$\mathbf{P} = \mathbf{P}^f + (\mathbf{K}\mathbf{S} - \mathbf{A})(\mathbf{K}\mathbf{S} - \mathbf{A})^T - \mathbf{A}\mathbf{A}^T = \mathbf{P}^f + \mathbf{K}\mathbf{S}\mathbf{A}^T - \mathbf{A}\mathbf{S}^T\mathbf{K}^T + \mathbf{K}\mathbf{S}\mathbf{S}^T\mathbf{K} \tag{D.14}$$

Comparing the last equation to Equation D.12, we see that

$$\mathbf{K}\mathbf{S}\mathbf{A}^T + \mathbf{A}\mathbf{S}^T\mathbf{K}^T = \mathbf{K}\mathbf{H}\mathbf{P}^f + \mathbf{P}^f\mathbf{H}^T. \tag{D.15}$$

This is fulfilled if

$$\mathbf{A} = \mathbf{P}^f\mathbf{H}^T(\mathbf{S}^T)^{-1} \tag{D.16}$$

and

$$\mathbf{A}^T = \mathbf{S}^{-1}\mathbf{H}(\mathbf{P}^f)^T. \tag{D.17}$$

As for minimizing Equation D.14 it is required that $\mathbf{K}\mathbf{S} = \mathbf{A}$, we finally get the desired expression for the Kalman gain $\mathbf{K}$.

$$\mathbf{K} = \mathbf{A}\mathbf{S}^{-1} = \mathbf{P}^f\mathbf{H}(\mathbf{S}^T)^{-1}\mathbf{S}^{-1} = \mathbf{P}^f\mathbf{H}(\mathbf{S}\mathbf{S}^T)^{-1} = \mathbf{P}^f\mathbf{H}(\mathbf{H}\mathbf{P}^f\mathbf{H}^T + \mathbf{R})^{-1} \tag{D.18}$$

D.2 Proof of corollary to the Kalman Filter theorem (Equation 2.18)

To show the alternative formulation of the posterior error covariance, we start from equation D.12 and plug in the optimal Kalman gain (Equation 2.16).

$$\begin{aligned}
\mathbf{P} &= \mathbf{P}^f - \mathbf{K}\mathbf{H}\mathbf{P} - \mathbf{P}^f(\mathbf{K}\mathbf{H})^T + \mathbf{K}\mathbf{H}\mathbf{P}^f(\mathbf{K}\mathbf{H})^T + \mathbf{K}\mathbf{R}\mathbf{K}^T && \text{(D.19)}\\
&= \mathbf{P}^f - \mathbf{K}\mathbf{H}\mathbf{P}^f - \mathbf{P}^f\mathbf{H}^T\mathbf{K}^T + \mathbf{K}(\mathbf{H}\mathbf{P}^f\mathbf{H}^T + \mathbf{R})\mathbf{K}^T && \text{(D.20)}\\
&= \mathbf{P}^f - \mathbf{K}\mathbf{H}\mathbf{P}^f - \mathbf{P}^f\mathbf{H}^T\mathbf{K}^T + \mathbf{P}^f\mathbf{H}^T(\mathbf{H}\mathbf{P}^f\mathbf{H}^T + \mathbf{R})^{-1}(\mathbf{H}\mathbf{P}^f\mathbf{H}^T + \mathbf{R})\mathbf{K}^T && \text{(D.21)}\\
&= \mathbf{P}^f - \mathbf{K}\mathbf{H}\mathbf{P}^f - \mathbf{P}^f\mathbf{H}^T\mathbf{K}^T + \mathbf{P}^f\mathbf{H}^T\mathbf{K}^T && \text{(D.22)}\\
&= (\mathbf{I} - \mathbf{K}\mathbf{H})\mathbf{P}^f && \text{(D.23)}
\end{aligned}$$

D.3 Proof of the alternative Kalman Filter formulation (Equation 2.23)

We can show that $(\mathbf{P}^f)^{-1} + \mathbf{H}^T\mathbf{R}^{-1}\mathbf{H}$ is the inverse of $\mathbf{P}$ by multiplying both expressions. For reasons of clarity we introduce the definition $\mathbf{A} := (\mathbf{H}\mathbf{P}^f\mathbf{H}^T + \mathbf{R})$

[1] Covariance matrices are by definition positive *semi* definite. For using Cholesky decomposition we need to assume strict positive definiteness. In a real world scenario, an eigenvalue of exactly zero is practically excluded and hence this is a good assumption. The covariance matrices could also be tailored to be positive definite.

$$\begin{aligned}
\mathbf{P}^{-1}\mathbf{P} &= ((\mathbf{P}^f)^{-1} + \mathbf{H}^T\mathbf{R}^{-1}\mathbf{H})(\mathbf{I} - \mathbf{K}\mathbf{H})\mathbf{P}^f && \text{(D.24)}\\
&= ((\mathbf{P}^f)^{-1} + \mathbf{H}^T\mathbf{R}^{-1}\mathbf{H})(\mathbf{P}^f - \mathbf{P}^f\mathbf{H}^T(\mathbf{H}\mathbf{P}^f\mathbf{H}^T + \mathbf{R})^{-1}\mathbf{H}\mathbf{P}^f) && \text{(D.25)}\\
&= ((\mathbf{P}^f)^{-1} + \mathbf{H}^T\mathbf{R}^{-1}\mathbf{H})(\mathbf{P}^f - \mathbf{P}^f\mathbf{H}^T\mathbf{A}^{-1}\mathbf{H})\mathbf{P}^f && \text{(D.26)}\\
&= \mathbf{I} - \mathbf{H}^T\mathbf{A}^{-1}\mathbf{H}\mathbf{P}^f + \mathbf{H}^T\mathbf{R}^{-1}\mathbf{H}\mathbf{P}^f - \mathbf{H}^T\mathbf{R}^{-1}\mathbf{H}\mathbf{P}^f\mathbf{H}^T\mathbf{A}^{-1}\mathbf{H}\mathbf{P}^f && \text{(D.27)}\\
&= \mathbf{I} + \mathbf{H}^T[-\mathbf{A}^{-1} + \mathbf{R}^{-1} - \mathbf{R}^{-1}\mathbf{H}\mathbf{P}^f\mathbf{H}^T\mathbf{A}^{-1}]\mathbf{H}\mathbf{P}^f && \text{(D.28)}\\
&= \mathbf{I} + \mathbf{H}^T[-\mathbf{I} + \mathbf{R}^{-1}\mathbf{A} - \mathbf{R}^{-1}\mathbf{H}\mathbf{P}^f\mathbf{H}^T]\mathbf{A}^{-1}\mathbf{H}\mathbf{P}^f && \text{(D.29)}\\
&= \mathbf{I} + \mathbf{H}^T[-\mathbf{I} + \mathbf{R}^{-1}(\mathbf{H}\mathbf{P}^f\mathbf{H}^T + \mathbf{R}) - \mathbf{R}^{-1}\mathbf{H}\mathbf{P}^f\mathbf{H}^T]\mathbf{A}^{-1}\mathbf{H}\mathbf{P}^f && \text{(D.30)}\\
&= \mathbf{I} + \mathbf{H}^T[-\mathbf{I} + \mathbf{I}]\mathbf{A}^{-1}\mathbf{H}\mathbf{P}^f && \text{(D.31)}\\
&= \mathbf{I} + \mathbf{H}^T[\mathbf{0}]\mathbf{A}^{-1}\mathbf{H}\mathbf{P}^f && \text{(D.32)}\\
&= \mathbf{I} && \text{(D.33)}
\end{aligned}$$

The alternative formulation of the Kalman gain is derived from the initial formula for $\mathbf{K}$ (Equation 2.16) by inserting $\mathbf{P}\mathbf{P}^{-1} = \mathbf{I}$ and $\mathbf{R}\mathbf{R}^{-1} = \mathbf{I}$ and using the equation for the inverse of $\mathbf{P}$.

$$\begin{aligned}
\mathbf{K} &= \mathbf{P}^f\mathbf{H}^T(\mathbf{H}\mathbf{P}^f\mathbf{H}^T + \mathbf{R})^{-1} && \text{(D.34)}\\
&= \mathbf{P}\mathbf{P}^{-1}\mathbf{P}^f\mathbf{H}\mathbf{R}^{-1}\mathbf{R}(\mathbf{H}\mathbf{P}^f\mathbf{H}^T + \mathbf{R})^{-1} && \text{(D.35)}\\
&= \mathbf{P}(\mathbf{P}^{f^{-1}} + \mathbf{H}^T\mathbf{R}^{-1}\mathbf{H})\mathbf{P}^f\mathbf{H}\mathbf{R}^{-1}(\mathbf{H}\mathbf{P}^f\mathbf{H}^T\mathbf{R}^{-1} + \mathbf{R}\mathbf{R}^{-1})^{-1} && \text{(D.36)}\\
&= \mathbf{P}(\mathbf{I} + \mathbf{H}^T\mathbf{R}^{-1}\mathbf{H}\mathbf{P}^f)\mathbf{H}\mathbf{R}^{-1}(\mathbf{H}\mathbf{P}^f\mathbf{H}^T\mathbf{R}^{-1} + \mathbf{I})^{-1} && \text{(D.37)}\\
&= \mathbf{P}(\mathbf{H}^T\mathbf{R}^{-1}\mathbf{H}^T\mathbf{R}^{-1^{-1}} + \mathbf{H}^T\mathbf{R}^{-1}\mathbf{H}\mathbf{P}^f)\mathbf{H}\mathbf{R}^{-1}(\mathbf{H}\mathbf{P}^f\mathbf{H}^T\mathbf{R}^{-1} + \mathbf{I})^{-1} && \text{(D.38)}\\
&= \mathbf{P}\mathbf{H}^T\mathbf{R}^{-1}(\mathbf{I} + \mathbf{H}\mathbf{P}^f\mathbf{H}\mathbf{R}^{-1})(\mathbf{I} + \mathbf{H}\mathbf{P}^f\mathbf{H}^T\mathbf{R}^{-1})^{-1} && \text{(D.39)}\\
&= \mathbf{P}\mathbf{H}^T\mathbf{R}^{-1} && \text{(D.40)}\\
& && \text{(D.41)}
\end{aligned}$$

Appendix E

Equivalence of the serial Kalman Filter

Proof

The serial Kalman Filter (Section 2.3) is mentioned in classic textbooks as Maybeck (2022) and Brown and Hwang (2012), but only intuitive arguments are provided for proving the equality to the original Kalman Filter. To the best of my knowledge, a rigorous proof can only be found in the recent publication by Kettner and Paolone (2017), whose steps I elaborate on[1]. We start by showing the equality of the posterior error covariance matrix $\mathbf{P}$ using its inverse[2]. We assume that the measurement error covariance $\mathbf{R}$ is a diagonal matrix, where each entry j is the observation variance corresponding to measurement j:

$$\mathbf{R} = \begin{bmatrix} R_1 & & \\ & \ddots & \\ & & R_n \end{bmatrix}$$

If the inverses are equal then also the matrices as such are equal[3], thus it needs to be shown that

$$\mathbf{P}^{-1} = \mathbf{P}_n^{-1} = \mathbf{P}_{n-1}^{-1} + \mathbf{H}_n^T \mathbf{R}_n^{-1} \mathbf{H}_n. \tag{E.1}$$

This is done by writing $\mathbf{R}$ and $\mathbf{H}$ as block matrices, which is simple due to the diagonality of $\mathbf{R}$. Recall, that the observation operator $\mathbf{H}$ is an $N_y \times N_x$ matrix, and hence each row $\mathbf{H}_j$ corresponds to one measurement, in $\mathbf{H}^T$ each column.

$$\mathbf{P}^{-1} = (\mathbf{P}^f)^{-1} + \mathbf{H}^T \mathbf{R}^{-1} \mathbf{H} \tag{E.2}$$

$$= (\mathbf{P}^f)^{-1} + \left(\begin{array}{c|c|c} \mathbf{H}_1{}^T & \dots & \mathbf{H}_n{}^T \end{array} \right) \left(\begin{array}{c|c|c} \mathbf{R}_1^{-1} & & \\ \hline & \ddots & \\ \hline & & \mathbf{R}_n^{-1} \end{array} \right) \left(\begin{array}{c} \mathbf{H}_1 \\ \hline \dots \\ \hline \mathbf{H}_n \end{array} \right) \tag{E.3}$$

$$= (\mathbf{P}^f)^{-1} + \mathbf{H}_1{}^T \mathbf{R}_1^{-1} \mathbf{H}_1 + \dots + \mathbf{H}_n{}^T \mathbf{R}_n^{-1} \mathbf{H}_n \tag{E.4}$$

$$\tag{E.5}$$

[1] The fact that this is a publication about optimizing electrical grids is yet another demonstration of the versatility of the Kalman Filter.

[2] As in the derivations before, we assume the covariance matrices all to be strictly positive definite which is a necessary and sufficient condition for the inverse to exist.

[3] By inverse we mean both right and left inverse, as these are equal for square matrices.

As the prior covariance $(\mathbf{P}^f)^{-1}$ is by definition equal to $\mathbf{P}_0$ in the serial Kalman Filter, we recognise the recursive definition of $\mathbf{P}_n^{-1}$.

$$\mathbf{P}^{-1} = \mathbf{P}_0{}^{-1} + \mathbf{H}_1^T\mathbf{R}_1^{-1}\mathbf{H}_1 + \cdots + \mathbf{H}_n^T\mathbf{R}_n^{-1}\mathbf{H}_n \tag{E.6}$$
$$= \mathbf{P}_1^{-1} + \mathbf{H}_2^T\mathbf{R}_2^{-1}\mathbf{H}_2 + \cdots + \mathbf{H}_n^T\mathbf{R}_n^{-1}\mathbf{H}_n \tag{E.7}$$
$$= \mathbf{P}_{n-1}^{-1} + \mathbf{H}_n^T\mathbf{R}_n^{-1}\mathbf{H}_n \quad \square \tag{E.8}$$

The second part of the proof consists of showing that the posterior state vectors are equal, which means that

$$\mathbf{x} = \mathbf{x}_n \tag{E.9}$$
$$\hat{\mathbf{x}}^f + \mathbf{K}(\mathbf{y} - \mathbf{H}\hat{\mathbf{x}}^f) = \hat{\mathbf{x}}_{n-1}^f + \mathbf{K}_n(\mathbf{y}_n - \mathbf{H}_n\hat{\mathbf{x}}_{n-1}^f). \tag{E.10}$$

We start by rewriting the last equation as

$$\mathbf{K}\mathbf{y} + (\mathbf{I} - \mathbf{K}\mathbf{H})\hat{\mathbf{x}}^f = \mathbf{K}_n\mathbf{y}_n + (\mathbf{I} - \mathbf{K}_n\mathbf{H}_n)\hat{\mathbf{x}}_{n-1} \tag{E.11}$$
$$\tag{E.12}$$

and explicitly state the recursion on the right hand side to bring into into the form of sums and products.

$$= \mathbf{K}_n\mathbf{y}_n + (\mathbf{I} - \mathbf{K}_n\mathbf{H}_n)\mathbf{x}_{n-1} \tag{E.13}$$
$$= \mathbf{K}_n\mathbf{y} + (\mathbf{I} - \mathbf{K}_n\mathbf{H}_n)\mathbf{K}_{n-1}\mathbf{y}_{n-1} + (\mathbf{I} - \mathbf{K}_n\mathbf{H}_n)(\mathbf{I} - \mathbf{K}_{n-1}\mathbf{H}_{n-1})\mathbf{x}_{n-2} \tag{E.14}$$
$$= \mathbf{K}_n\mathbf{y}_n + (\mathbf{I} - \mathbf{K}_n\mathbf{H}_n)\mathbf{K}_{n-1}\mathbf{y}_{n-1} + (\mathbf{I} - \mathbf{K}_n\mathbf{H}_n)(\mathbf{I} - \mathbf{K}_{n-1}\mathbf{H}_{n-1})\mathbf{K}_{n-2}\mathbf{y}_{n-2} \tag{E.15}$$
$$+ (\mathbf{I} - \mathbf{K}_n\mathbf{H}_n)(I - \mathbf{K}_{n-1}\mathbf{H}_{n-1})(\mathbf{I} - \mathbf{K}_{n-2}\mathbf{H}_{n-2})\mathbf{X}_{n-3} + \ldots \tag{E.16}$$
$$= \mathbf{K}_n\mathbf{y}_n + \sum_{i=1}^{n-1}\prod_{j=i+1}^{n}(\mathbf{I} - \mathbf{K}_j\mathbf{H}_j)\mathbf{K}_i\mathbf{y}_i + \prod_{i=1}^{n}(\mathbf{I} - \mathbf{K}_i\mathbf{H}_i)\mathbf{x}_0 \tag{E.17}$$

Recalling the equality of the prior state vector, $\mathbf{x}_0 = \mathbf{x}^f$, and comparing this to Equation E.12, we recognise similar terms whose equality can be shown.

$$(\mathbf{I} - \mathbf{K}\mathbf{H})\mathbf{x}^f = \prod_{i=1}^{n}(\mathbf{I} - \mathbf{K}_i\mathbf{H}_i)\mathbf{x}^f \tag{E.18}$$

and

$$\mathbf{K}\mathbf{y} = \mathbf{K}_n\mathbf{y}_n + \sum_{i=1}^{n-1}\prod_{j=i+1}^{n}(\mathbf{I} - \mathbf{K_j}\mathbf{H_j})\mathbf{K_i}\mathbf{y_i}$$

The first equality follows straight from the equality of $\mathbf{P}$ and $\mathbf{P}_n$ that we have shown previously, because $\mathbf{P}_n$ then can also be written in a recursive way.

$$\begin{aligned}
\mathbf{P} = (\mathbf{I} - \mathbf{K}\mathbf{H})\mathbf{P}^f = \mathbf{P}_n &= (\mathbf{I} - \mathbf{K}_n\mathbf{H}_n)\mathbf{P}_{n-1} \\
&= \prod_{i=1}^{n}(\mathbf{I} - \mathbf{K}_i\mathbf{H}_i)\mathbf{P}_0 \\
&= \prod_{i=1}^{n}(\mathbf{I} - \mathbf{K}_i\mathbf{H}_i)\mathbf{P}_f \\
\Rightarrow (\mathbf{I} - \mathbf{K}\mathbf{H}) &= \prod_{i=1}^{n}(\mathbf{I} - \mathbf{K}_i\mathbf{H}_i) \\
(\mathbf{I} - \mathbf{K}\mathbf{H})\mathbf{x}^f &= \prod_{i=1}^{n}(\mathbf{I} - \mathbf{K}_i\mathbf{H}_i)\mathbf{x}^f \quad \square
\end{aligned}$$

For showing the second equality, we first rewrite the product term in terms of prior error covariances by introducing them as an identity matrix into the equation. One recognises the recursive formulation of $\mathbf{P}$ and that most terms actually vanish.

$$\prod_{j=i+1}^{n} (\mathbf{I} - \mathbf{K}_j \mathbf{H}_j) = \prod_{j=i+1}^{n} (\mathbf{I} - \mathbf{K}_j \mathbf{H}_j) \mathbf{P}_{j-1} \mathbf{P}_{j-1}^{-1} \tag{E.19}$$

$$= \prod_{j=i+1}^{n} \mathbf{P}_j \mathbf{P}_{j-1}^{-1} \tag{E.20}$$

$$= \mathbf{P}_n \mathbf{P}_i^{-1} \tag{E.21}$$

This relationship and the alternative formulation of the Kalman Gain from Equation 2.23, $\mathbf{K}_i = \mathbf{P}_i {\mathbf{H}_i}^T \mathbf{R}_i^{-1}$, are then used to get closer to the desired formulation.

$$\mathbf{K}_n \mathbf{y}_n + \sum_{i=1}^{n-1} \prod_{j=i+1}^{n} (\mathbf{I} - \mathbf{K}_j \mathbf{H}_j) \mathbf{K}_i \mathbf{y}_i \tag{E.22}$$

$$= \mathbf{K}_n \mathbf{y}_n + \sum_{i=1}^{n-1} \mathbf{P}_n \mathbf{P}_i^{-1} \mathbf{K}_i \mathbf{y}_i \tag{E.23}$$

$$= \mathbf{K}_n \mathbf{y}_n + \mathbf{P}_n \sum_{i=1}^{n-1} \mathbf{P}_i^{-1} \mathbf{K}_i \mathbf{y}_i \tag{E.24}$$

$$= \mathbf{K}_n \mathbf{y}_n + \mathbf{P}_n \sum_{i=1}^{n-1} \mathbf{P}_i^{-1} \mathbf{P}_i {\mathbf{H}_i}^T \mathbf{R}_i^{-1} \mathbf{y}_i \tag{E.25}$$

$$= \mathbf{P}_n {\mathbf{H}_n}^T \mathbf{R}_n^{-1} \mathbf{y}_n + \mathbf{P}_n \sum_{i=1}^{n-1} {\mathbf{H}_i}^T \mathbf{R}_i^{-1} \mathbf{y}_i \tag{E.26}$$

$$= \mathbf{P}_n \sum_{i=1}^{n} {\mathbf{H}_i}^T \mathbf{R}_i^{-1} \mathbf{y}_i \tag{E.27}$$

Again, we can use the fact that $\mathbf{R}$ is diagonal and that $\mathbf{H}_i$ corresponds to one row of $\mathbf{H}$, such that the last equation can be written in terms of the full matrices of the nonserial formulation.

$$= \mathbf{P}_n \mathbf{H}^T \mathbf{R}^{-1} \mathbf{y} \tag{E.28}$$

$$= \mathbf{P} \mathbf{H}^T \mathbf{R}^{-1} \mathbf{y} \tag{E.29}$$

$$= \mathbf{K} \mathbf{y} \quad \square \tag{E.30}$$

Appendix F

Derivations of the Ensemble Square Root Kalman Filter formulations

In the following the steps required for deriving the different solutions of the square root formulation of the Ensemble Kalman Filter (Section 2.4.2 and Table 2.1) are performed. The notation follows Vetra-Carvalho et al. (2018) who present the different solutions without elaborating on the precise steps for obtaining them.

F.1 Ensemble Transform Kalman Filter (ETKF)

This method was introduced in Bishop et al. (2001) and is called the Ensemble Transform Kalman Filter, because the estimates of observations from the model are transformed into the so called error space. This is done by $\mathbf{TT}^T$ in Equation 2.46 using the Sherman-Morrison-Woodbury formula. This simplifies the calculation of inverses (for instance of $\mathbf{F}^{-1}$), To bring the original term for $\mathbf{TT}^T$ into the right form, identity matrices of the according shape are inserted into the equation.

$$\mathbf{TT}^T = (\mathbf{I} - \mathbf{S}^T\mathbf{F}^{-1}\mathbf{S}) \tag{F.1}$$
$$= \mathbf{I} - \mathbf{IS}^T(N_e - 1)\mathbf{R} + \mathbf{SIS}^T \tag{F.2}$$
$$= \mathbf{I} - \mathbf{IS}^T((N_e - 1)\mathbf{R} + \mathbf{SIS}^T)\mathbf{SI} \tag{F.3}$$

The Sherman-Morrison-Woodbury formula states that for matrices $\mathbf{A}\,\epsilon\,\mathbf{R}^{n\times n}$, $\mathbf{U}\,\epsilon\,\mathbf{R}^{n\times k}$,$\mathbf{V}\,\epsilon\,\mathbf{R}^{k\times n}$ and $\mathbf{C}\,\epsilon\,\mathbf{R}^{k\times k}$ the following equality holds

$$(\mathbf{A} + \mathbf{UCV}^T)^{-1} = \mathbf{A}^{-1} - \mathbf{A}^{-1}\mathbf{U}(\mathbf{C}^{-1} + \mathbf{VA}^{-1}\mathbf{U})^{-1}\mathbf{VA}^{-1} \tag{F.4}$$

Recognising $\mathbf{A}^{-1} = \mathbf{I}$, $\mathbf{C} = (N_e - 1)\mathbf{R}$, $\mathbf{V} = \mathbf{S}$ and $\mathbf{U} = \mathbf{S}^T$ we rewrite the equation as

$$\mathbf{TT^T} = \left[\mathbf{I} - \frac{\mathbf{S^T R^{-1} S}}{\mathbf{N_e - 1}}\right]^{-1} \tag{F.5}$$
$$\tag{F.6}$$

We have used that the inverse of the identity is the identity itself. This new formulation of $\mathbf{TT}^T$ is the starting point of the ETKF. The next step consists of doing an eigenvalue decomposition of the inverse of the this term. As $(\mathbf{TT}^T)^{-1}$ is by construction a symmetric matrix, the Eigenvector matrix $\mathbf{U}$ is orthogonal. The Eigenvalue matrix $\mathbf{\Sigma}$ is by definition a diagonal matrix. Hence, we can directly get the matrix square root $\mathbf{T}$ from the square root of the Eigenvalues. Regaining the term $\mathbf{TT}^T$ without the inverse becomes simple as it reduces to inverting the Eigenvalue matrix $\mathbf{\Sigma}$.

$$(\mathbf{T}\mathbf{T}^T)^{-1} = \mathbf{U}\Sigma\mathbf{U}^T \tag{F.7}$$
$$\Rightarrow \mathbf{T}\mathbf{T}^T = (\mathbf{U}^T)^{-1}\mathbf{\Sigma}^{-1}\mathbf{U}^{-1} \tag{F.8}$$
$$= \mathbf{U}\mathbf{\Sigma}^{-1}\mathbf{U}^T \tag{F.9}$$
$$= \mathbf{U}\mathbf{\Sigma}^{-\frac{1}{2}}\mathbf{\Sigma}^{-\frac{1}{2}}\mathbf{U}^T \tag{F.10}$$
$$= \mathbf{U}\mathbf{\Sigma}^{-\frac{1}{2}}\mathbf{U}^T\mathbf{U}\mathbf{\Sigma}^{-\frac{1}{2}}\mathbf{U}^T \tag{F.11}$$
$$= \mathbf{U}\mathbf{\Sigma}^{-\frac{1}{2}}\mathbf{U}^T(\mathbf{U}\mathbf{\Sigma}^{-\frac{1}{2}}\mathbf{U}^T)^T \tag{F.12}$$
$$\Rightarrow \mathbf{T} = \mathbf{U}\mathbf{\Sigma}^{-\frac{1}{2}}\mathbf{U}^T \tag{F.13}$$
$$\tag{F.14}$$

For this method, the matrix $\mathbf{T}$ is directly the perturbation weight matrix $\mathbf{W}'$ (Equation 2.48). We get the mean weight vector $\overline{\mathbf{w}}$ (Equation 2.48) from the alternative Kalman gain notation (Equation 2.23) using the ensemble formulation and the decomposition from above.

$$\mathbf{K} = \mathbf{P}\mathbf{H}^T\mathbf{R}^{-1} \tag{F.15}$$
$$= \frac{1}{N_e - 1}\mathbf{X}'^f\mathbf{T}\mathbf{T}^T(\mathbf{X}'^f)^T\mathbf{H}^T\mathbf{R}^{-1} \tag{F.16}$$
$$= \mathbf{X}'^f\frac{1}{N_e - 1}\mathbf{U}\mathbf{\Sigma}^{-1}\mathbf{U}^T\mathbf{S}^T\mathbf{R}^{-1} \tag{F.17}$$

Therefore, taking into account the innovation $\mathbf{d} = (\mathbf{y} - \overline{\mathcal{H}\mathbf{X}^f})$ we get for $\overline{\mathbf{w}}$ in Equation 2.48

$$\overline{\mathbf{w}} = \frac{1}{N_e - 1}\mathbf{U}\mathbf{\Sigma}^{-1}\mathbf{U}^T\mathbf{S}^T\mathbf{R}^{-1}\mathbf{d} \tag{F.18}$$

Alternative formulation

Computing $\mathbf{S}^T\mathbf{R}^{-1}\mathbf{S}$ can be prone to rounding errors, which is why an alternative formulation has been proposed by Dance et al. (2007).
It starts from the same equation as the ETKF

$$\mathbf{T}\mathbf{T}^\mathbf{T} = \left(\mathbf{I} - \frac{\mathbf{S}^\mathbf{T}\mathbf{R}^{-\mathbf{1}}\mathbf{S}}{\mathbf{N_e} - \mathbf{1}}\right)^{-1} \tag{F.19}$$
$$\tag{F.20}$$

The matrix $\mathbf{S}$ is redefined to $\tilde{\mathbf{S}}$.

$$\tilde{\mathbf{S}} = \frac{1}{\sqrt{N_e - 1}}\mathbf{R}^{-\frac{1}{2}}\mathbf{S} \tag{F.21}$$

.
Performing a singular value decomposition of $\tilde{\mathbf{S}}^T$, the matrix square root $\mathbf{T}$ is obtained.

$$\tilde{\mathbf{S}}^T = \mathbf{U}\tilde{\mathbf{\Sigma}}\tilde{\mathbf{V}}^T \tag{F.22}$$
$$\Rightarrow \mathbf{T}\mathbf{T}^T = (\mathbf{I} + \mathbf{U}\tilde{\mathbf{\Sigma}}\tilde{\mathbf{V}}^T(\mathbf{U}\tilde{\mathbf{\Sigma}}\tilde{\mathbf{V}}^T)^T) \tag{F.23}$$
$$= (\mathbf{U}\mathbf{U}^T + \mathbf{U}\tilde{\Sigma}\tilde{\mathbf{V}}^T\mathbf{V}\tilde{\mathbf{\Sigma}}\tilde{\mathbf{U}}^T) \tag{F.24}$$

where $\mathbf{U}$ and $\mathbf{V}$ are unitary and hence also orthogonal matrices. This simplifies to

$$\mathbf{T}\mathbf{T}^T = \mathbf{U}(\mathbf{I} + \mathbf{\Sigma}\mathbf{\Sigma}^T)\mathbf{U}^T \tag{F.25}$$
$$= \mathbf{U}(\mathbf{I} + \mathbf{\Sigma}\mathbf{\Sigma}^T)^{-\frac{1}{2}}\mathbf{U}^T\mathbf{U}(\mathbf{I} + \mathbf{\Sigma}\mathbf{\Sigma}^T)^{-\frac{1}{2}}\mathbf{U}^T \tag{F.26}$$
$$\Rightarrow \mathbf{T} = \mathbf{U}(\mathbf{I} + \mathbf{\Sigma}\mathbf{\Sigma}^T)^{-\frac{1}{2}}\mathbf{U}^T \tag{F.27}$$

which is equal to the weight matrix $\mathbf{W}'$ (Equation 2.48).
Following steps similar as for the regular ETKF, we get

$$\mathbf{K} = \mathbf{P}\mathbf{H}^T\mathbf{R}^{-1} \tag{F.28}$$
$$= \frac{1}{N_e - 1}\mathbf{X}'\mathbf{T}\mathbf{T}^T\mathbf{X}'^T\mathbf{H}^T\mathbf{R}^{-1} \tag{F.29}$$
$$= X'\frac{1}{\sqrt{N_e - 1}}\mathbf{U}(\mathbf{I} + \mathbf{\Sigma}\mathbf{\Sigma}^T)\mathbf{U}^T\frac{\mathbf{S}^T\mathbf{R}^{-\frac{1}{2}}}{\sqrt{N_e - 1}}\mathbf{R}^{-\frac{1}{2}} \tag{F.30}$$
$$= X'\frac{1}{\sqrt{N_e - 1}}\mathbf{U}(\mathbf{I} + \mathbf{\Sigma}\mathbf{\Sigma}^T)\mathbf{U}^T\tilde{\mathbf{S}}^T\mathbf{R}^{-\frac{1}{2}} \tag{F.31}$$
$$= \mathbf{X}'\frac{1}{\sqrt{N_e - 1}}\mathbf{U}(\mathbf{I} + \mathbf{\Sigma}\mathbf{\Sigma}^T)\mathbf{U}^T\mathbf{U}\tilde{\mathbf{\Sigma}}\tilde{\mathbf{V}}^T\mathbf{R}^{-\frac{1}{2}} \tag{F.32}$$
$$= \mathbf{X}'\frac{1}{\sqrt{N_e - 1}}\mathbf{U}(\mathbf{I} + \mathbf{\Sigma}\mathbf{\Sigma}^T)\tilde{\mathbf{\Sigma}}\tilde{\mathbf{V}}^T\mathbf{R}^{-\frac{1}{2}}, \tag{F.33}$$

such that the mean weigh vector (Equation 2.48) is

$$\overline{\mathbf{w}} = \frac{1}{\sqrt{N_e - 1}}\mathbf{U}(\mathbf{I} + \mathbf{\Sigma}\mathbf{\Sigma}^T)\tilde{\mathbf{\Sigma}}\tilde{\mathbf{V}}^T\mathbf{R}^{-\frac{1}{2}}\mathbf{d}. \tag{F.34}$$

F.2 Ensemble Square Root Kalman Filter (ENSRF)

The decomposition presented here follows the reformulation of Vetra-Carvalho et al. (2018).
Starting from

$$\mathbf{T}\mathbf{T}^T = (\mathbf{I} - \mathbf{S}^T\mathbf{F}^{-1}\mathbf{S}^T) \tag{F.35}$$

the inverse of the matrix $\mathbf{F}$ is formulated in terms of an EVD. As $\mathbf{F}$ is a symmetric matrix, the Eigenvector matrix is an orthogonal matrix.

$$\mathbf{F}^{-1} = \mathbf{U}\mathbf{\Lambda}^{-1}\mathbf{U}^T \tag{F.36}$$
$$= \mathbf{U}\mathbf{\Lambda}^{-\frac{1}{2}}\mathbf{\Lambda}^{-\frac{1}{2}}\mathbf{U}^T \tag{F.37}$$

Thus,

$$\mathbf{T}\mathbf{T}^T = \mathbf{X}'^f(\mathbf{I} - \mathbf{S}^T\mathbf{U}\mathbf{\Lambda}^{-\frac{1}{2}}\mathbf{\Lambda}^{-\frac{1}{2}}\mathbf{U}^T\mathbf{S})\mathbf{X}'^{fT} \tag{F.38}$$
$$\mathbf{T}\mathbf{T}^T = \mathbf{X}'^f(\mathbf{I} - \mathbf{G}\mathbf{G}^T)\mathbf{X}'^{fT} \tag{F.39}$$

where we have introduced the matrix $\mathbf{G} = \mathbf{S}^T\mathbf{U}\mathbf{\Lambda}^{-\frac{1}{2}}$. Next $\mathbf{G}$ is reformulated in terms of a SVD, the index s denotes that these are the unitary matrices stemming from the SVD, not the EVD.

$$\mathbf{G} = \mathbf{U}_s\mathbf{\Sigma}_s\mathbf{V}_s^T \tag{F.40}$$
$$\Rightarrow \mathbf{T}\mathbf{T}^T = \mathbf{X}'^f(\mathbf{I} - \mathbf{U}_s\Sigma_s\mathbf{V}_s^T(\mathbf{U}_s\mathbf{\Sigma}_s\mathbf{V}_s^T)^T)\mathbf{X}'^f \tag{F.41}$$
$$= \mathbf{X}'^f(\mathbf{U}_s\mathbf{U}_s^T - \mathbf{U}_s\mathbf{\Sigma}_s\mathbf{\Sigma}_s^T\mathbf{U}_s^T)\mathbf{X}'^f \tag{F.42}$$
$$= \mathbf{X}'^f\mathbf{U}_s(\mathbf{I} - \mathbf{\Sigma}_s\mathbf{\Sigma}_s^T)\mathbf{U}_s^T\mathbf{X}'^f \tag{F.43}$$
$$= \mathbf{X}'^f\mathbf{U}_s(\mathbf{I} - \mathbf{\Sigma}_s\mathbf{\Sigma}_s^T)^{\frac{1}{2}}\mathbf{U}_s\mathbf{U}_s^T(\mathbf{I} - \mathbf{\Sigma}_s\mathbf{\Sigma}_s^T)^{\frac{1}{2}}\mathbf{U}_s^T\mathbf{X}'^f \tag{F.44}$$
$$\tag{F.45}$$

As the matrix $\mathbf{\Sigma}_s\mathbf{\Sigma}_s^T$ only has values on the diagonal (the squared singular values) computing the matrix square root just consists of computing the square root of the scalars on the diagonal. One finally gets the following formulation of the perturbation weight matrix (Equation 2.48)

$$\mathbf{W}' = \mathbf{U}_s(\mathbf{I} - \mathbf{\Sigma}_s\mathbf{\Sigma}_s^T)\mathbf{U}_s^T \tag{F.46}$$

Note, that the right hand $\mathbf{U}_s^T$ is a possible, but not necessary addition, which is usually done for reasons of numerical stability (Dance et al., 2007).
For updating the means we get the weight vector (Equation 2.48) from the original Kalman gain equation by using the decomposition of the term in brackets which as performed above (Equation F.37, called $\mathbf{F}$ there).

$$\mathbf{K}\mathbf{d} = \mathbf{P}^f\mathbf{H}^T(\mathbf{H}\mathbf{P}^f\mathbf{H} + \mathbf{R})^{-1} \tag{F.47}$$
$$= \mathbf{X}'^f(\mathbf{H}\mathbf{X}')^T\mathbf{F}^{-1}\mathbf{d} \tag{F.48}$$
$$= \mathbf{X}'^f(\mathbf{H}\mathbf{X}')^T\mathbf{U}\mathbf{\Lambda}^{-1}\mathbf{U}^T\mathbf{d} \tag{F.49}$$
$$\Rightarrow \overline{\mathbf{w}} = (\mathbf{H}\mathbf{X}')^T\mathbf{U}\mathbf{\Lambda}^{-1}\mathbf{U}^T\mathbf{d} \tag{F.50}$$

F.3 Kalman gain formulation of the ENSRF

It needs to be proven that

$$\tilde{\mathbf{K}} = \mathbf{P}^f\mathbf{H}^T[\sqrt{(\mathbf{H}\mathbf{P}^f\mathbf{H}^T + \mathbf{R})}^{-1}]^T[\sqrt{(\mathbf{H}\mathbf{P}^f\mathbf{H}^T + \mathbf{R})} + \sqrt{\mathbf{R}}]^{-1} \tag{F.51}$$

is a solution of the posterior error covariance error

$$\mathbf{P} = (\mathbf{I} - \tilde{\mathbf{K}}\mathbf{H})\mathbf{P}^f(\mathbf{I} - \tilde{\mathbf{K}}\mathbf{H})^T. \tag{F.52}$$

For proofing this relationship, the authors Whitaker and Hamill (2002) refer to Andrews (1968), who formulated the original Kalman Filter covariance equations using square roots.
I follow the proof by Andrews (1968) and show how it is connected to the definition of $\tilde{\mathbf{K}}$ by Whitaker and Hamill (2002), which requires some additional steps and a unified notation to be evident.
Andrews (1968) states that the posterior perturbation can be written as

$$\mathbf{X}' = \frac{\mathbf{X}'^f}{\sqrt{N_e - 1}}\left[\mathbf{I} - \frac{\mathbf{X}'^f}{\sqrt{N_e - 1}}H(\sqrt{\mathbf{R} + \frac{\mathbf{H}\mathbf{X}'^f(\mathbf{X}'^f)^T\mathbf{H}^T}{N_e - 1}}^{T^{-1}}[(\sqrt{\mathbf{R} + \mathbf{H}\frac{\mathbf{X}'^f(\mathbf{X}'^f)^T}{N_e - 1}\mathbf{H}^T}^T + \sqrt{\mathbf{R}})]^{-1}\frac{(\mathbf{X}'^f\mathbf{H})}{\sqrt{N_e - 1}}^T\right]. \tag{F.53}$$

Using the definiton of $\tilde{\mathbf{K}}$ by this equation becomes

$$\mathbf{X}' = \mathbf{X}'^f - \tilde{\mathbf{K}}\mathbf{H}^T\mathbf{X}'^{f^T}. \tag{F.54}$$

Assuming that $\tilde{\mathbf{K}}$ is correct, we can show that by multiplying this equation with its transpose $\mathbf{X}'^T$ we gain the posterior error covariance formula.

$$\begin{aligned}
\mathbf{X}'\mathbf{X}'^T &= (\mathbf{X}'^f - \tilde{\mathbf{K}}\mathbf{H}^T\mathbf{X}'^{f^T})(\mathbf{X}'^f - \tilde{\mathbf{K}}\mathbf{H}^T\mathbf{X}'^{f^T})^T && \text{(F.55)}\\
&= (\mathbf{I} - \tilde{\mathbf{K}}\mathbf{H})\mathbf{X}'^f\mathbf{X}'^{f^T}(\mathbf{I} - \tilde{\mathbf{K}}^T\mathbf{H}^T) && \text{(F.56)}\\
\Rightarrow \mathbf{P} &= (\mathbf{I} - \tilde{\mathbf{K}}\mathbf{H})\mathbf{P}^f(\mathbf{I} - (\tilde{\mathbf{K}}\mathbf{H})^T) && \text{(F.57)}
\end{aligned}$$

Still, the correctness of $\tilde{\mathbf{K}}$ needs to be shown.
In order to proof it we first simplify the equations by defining the following quantities

$$\begin{aligned}
\mathbf{Z} &:= \frac{\mathbf{X}'^f\mathbf{H}}{N_e - 1} && \text{(F.58)}\\
\mathbf{U} &:= \sqrt{\mathbf{R} + \frac{\mathbf{H}\mathbf{X}'^f(\mathbf{X}'^f)^T\mathbf{H}^T}{N_e - 1}} = \sqrt{\mathbf{R} + \mathbf{Z}\mathbf{Z}^T} && \text{(F.59)}\\
\mathbf{V} &:= \sqrt{\mathbf{R}} && \text{(F.60)}
\end{aligned}$$

Equation F.53 becomes

$$\mathbf{X}' = \mathbf{X}'^f[\mathbf{I} - \mathbf{Z}\mathbf{U}^{T^{-1}}[\mathbf{U} + \mathbf{V})]^{-1}\mathbf{Z}^T \tag{F.61}$$

which is shown in the following algebraic exercise

$$\begin{aligned}
\mathbf{X}\mathbf{X}^T &= \mathbf{X}'^f[\mathbf{I} - \mathbf{Z}\mathbf{U}^{T^{-1}}[\mathbf{U} + \mathbf{V}]^{-1}\mathbf{Z}^T][\mathbf{X}'^f[\mathbf{I} - \mathbf{Z}\mathbf{U}^{T^{-1}}[\mathbf{U} + \mathbf{V})]^{-1}\mathbf{Z}^T]^T && \text{(F.62)}\\
&, = \mathbf{X}'^f[\mathbf{I} - \mathbf{Z}\mathbf{U}^{T^{-1}}(\mathbf{U} + \mathbf{V})^{-1}\mathbf{Z}^T + \mathbf{Z}\mathbf{U}^{T^{-1}}(\mathbf{U} + \mathbf{V})^{-1}\mathbf{Z}^T\mathbf{Z}(\mathbf{U} + \mathbf{V})^{-1^T}\mathbf{U}^{-1}\mathbf{Z}^T && \text{(F.63)}\\
&, - \mathbf{Z}(\mathbf{U} + \mathbf{V})^{-1^T}\mathbf{U}^{-1}\mathbf{Z}^T]\mathbf{X}'^{f^T}. && \text{(F.64)}
\end{aligned}$$

For means of keeping the equations simple we temporarily introduce the definition

$$\begin{aligned}
\mathbf{A} &:= \mathbf{U}^{T^{-1}}(\mathbf{U} + \mathbf{V})^{-1} && \text{(F.65)}\\
\mathbf{A}^T &= (\mathbf{U} + \mathbf{V})^{-1^T}\mathbf{U}^{-1} && \text{(F.66)}
\end{aligned}$$

in the equation above:

$$\begin{aligned}
\mathbf{X}\mathbf{X}^T &= \mathbf{X}'^f[\mathbf{I} - \mathbf{Z}\mathbf{A}\mathbf{Z}^T + \mathbf{Z}\mathbf{A}\mathbf{Z}^T\mathbf{Z}\mathbf{A}^T\mathbf{Z}^T - \mathbf{Z}\mathbf{A}^T\mathbf{Z}^T] && \text{(F.67)}\\
&= \mathbf{X}'^f[\mathbf{I} - \mathbf{Z}\mathbf{A}\mathbf{A}^{T^{-1}}\mathbf{A}^T\mathbf{Z}^T + \mathbf{Z}\mathbf{A}\mathbf{Z}^T\mathbf{Z}\mathbf{A}^T\mathbf{Z}^T - \mathbf{Z}\mathbf{A}\mathbf{A}^{-1}\mathbf{A}^T\mathbf{Z}^T] && \text{(F.68)}\\
&= \mathbf{X}'^f[\mathbf{I} - \mathbf{Z}\mathbf{A}(\mathbf{A}^{T^{-1}} - \mathbf{Z}^T\mathbf{Z} + \mathbf{A}^{-1})\mathbf{A}^T\mathbf{Z}^T] && \text{(F.69)}\\
& && \text{(F.70)}
\end{aligned}$$

We rewrite the final equation in original terms and use that $\mathbf{U}\mathbf{U}^T = \mathbf{R} + \mathbf{Z}\mathbf{Z}^T = \mathbf{V}\mathbf{V}^T + \mathbf{Z}\mathbf{Z}^T$ to get the desired result.

$$= \mathbf{X}'^f[\mathbf{I} - \mathbf{ZA}(\mathbf{U}(\mathbf{U}+\mathbf{V})^T - \mathbf{Z}^T\mathbf{Z} + (\mathbf{U}+\mathbf{V})\mathbf{U}^T)\mathbf{A}^T\mathbf{Z}^T]\mathbf{X}'^{fT} \tag{F.71}$$

$$= \mathbf{X}'^f[\mathbf{I} - \mathbf{ZA}(\mathbf{U}\mathbf{U}^T + \mathbf{U}\mathbf{V}^T - \mathbf{Z}^T\mathbf{Z} + \mathbf{U}\mathbf{U}^T + \mathbf{V}\mathbf{U}^T)\mathbf{A}^T\mathbf{Z}^T]\mathbf{X}'^{fT} \tag{F.72}$$

$$= \mathbf{X}'^f[\mathbf{I} - \mathbf{ZA}(\mathbf{U}\mathbf{U}^T + \mathbf{U}\mathbf{V}^T - \mathbf{Z}^T\mathbf{Z} + \mathbf{V}\mathbf{V}^T + \mathbf{Z}\mathbf{Z}^T + \mathbf{V}\mathbf{U}^T)\mathbf{A}^T\mathbf{Z}^T]\mathbf{X}'^{fT} \tag{F.73}$$

$$= \mathbf{X}'^f[\mathbf{I} - \mathbf{ZA}(\mathbf{U}\mathbf{U}^T + \mathbf{U}\mathbf{V}^T + \mathbf{V}\mathbf{V}^T + \mathbf{V}\mathbf{U}^T)\mathbf{A}^T\mathbf{Z}^T]\mathbf{X}'^{fT} \tag{F.74}$$

$$= \mathbf{X}'^f[\mathbf{I} - \mathbf{ZA}((\mathbf{U}+\mathbf{V})(\mathbf{U}+\mathbf{V})^T)\mathbf{A}^T\mathbf{Z}^T]\mathbf{X}'^{fT} \tag{F.75}$$

$$= \mathbf{X}'^f[\mathbf{I} - \mathbf{ZU}^{T^{-1}}(\mathbf{U}+\mathbf{V})^{-1}(\mathbf{U}+\mathbf{V})(\mathbf{U}+\mathbf{V})^T(\mathbf{U}+\mathbf{V})^{-1^T}\mathbf{U}^{-1}\mathbf{Z}^T]\mathbf{X}'^{fT} \tag{F.76}$$

$$= \mathbf{X}'^f[\mathbf{I} - \mathbf{ZU}^{T^{-1}}\mathbf{U}^{-1}\mathbf{Z}^T]\mathbf{X}'^{fT} \tag{F.77}$$

$$= \mathbf{X}'^f\mathbf{X}'^{fT} - \mathbf{X}'^f\frac{\mathbf{X}'^f\mathbf{H}}{N_e-1}(\mathbf{U}\mathbf{U}^T)^{-1}\frac{\mathbf{H}\mathbf{X}'^{fT}\mathbf{X}'^f}{N_e-1} \tag{F.78}$$

$$= \mathbf{P}^f - \mathbf{P}^f\mathbf{H}(\mathbf{H}\mathbf{P}^f\mathbf{H}^T + \mathbf{R})^{-1}\mathbf{H}\mathbf{P}^f \tag{F.79}$$

$$= (\mathbf{I} - \mathbf{KH})\mathbf{P}^f \quad \square \tag{F.80}$$

F.4 Serial ENSRF

Houtekamer and Mitchell (2001) used the explicit formulation of $\tilde{\mathbf{K}}$ in the previous section because of it's ease of implementation when treating observation serially. We have shown in Section 2.3 that treating the observations serially gives equivalent results to the original Kalman Filter, and this results also applies for the Ensemble Kalman Filter.
The matrix square roots and inverses in the mean and perturbation Kalman gain then simply reduce to scalars because $\mathbf{R}$ and $\mathbf{HPH}$ reduce to single values.
Besides efficiency gains which are discussed in Section 2.5 , the authors also used this formulation because it simplifies the application of the covariance localization, a topic that is explained in Section 4.4.2.

F.5 Ensemble Subspace transform Kalman Filter (ESTKF)

The last Ensemble square root Kalman Filter discussed in this thesis is the Error Subspace transform Kalman Filter, which is a mixture of the ETKF described previously and another Ensemble Kalman Filter not discussed here, the Singular evolutive interpolated Kalman filter (SEIK)(Tuan Pham et al., 1998) which was not tested in this thesis.
The ESTKF has been introduced by Nerger et al. (2012) in order to combine advantages of both these filters. It involves the introduction of a projection matrix into the square root equations for projecting the forecast ensemble into the so called error subspace which is of dimension N_e-1 instead of N_e without explicitely removing the mean. Depending on how small the ensemble is, this can give a speed up in comparison to the ETKF. For a comprehensive treatment of the subject and the motavation and creation of the projection matrix see Nerger et al. (2012).
The entries of the projection matrix $\mathbf{A}$ which are used for transforming the forecast ensemble are defined as

$$\mathbf{A}_{i,j} := \begin{cases} 1 - \frac{1}{\sqrt{N_e}}\frac{1}{\sqrt{N_e}+1} & \text{for } i = j, i < N_e \\ -\frac{1}{\sqrt{N_e}}\frac{1}{\sqrt{N_e}+1} & \text{for } i \neq j, i < N_e \\ -\frac{1}{\sqrt{N_e}} & \text{for } i = N_e \end{cases} \tag{F.81}$$

Before using this projection matrix, we need to first show its orthogonality $\mathbf{A}^T\mathbf{A} = \mathbf{I}$, which will make its insertion into the equation for the posterior error covariance possible.

The columns of this matrix comprise one entry $1 - \frac{1}{\sqrt{N_e}}\frac{1}{\sqrt{N_e}+1}$, $(N_e - 2)$ entries $-\frac{1}{\sqrt{N_e}}\frac{1}{\sqrt{N_e}+1}$ and one entry $-\frac{1}{\sqrt{N_e}}$ which always is the last row. It can be shown, that $\mathbf{A}$ is an orthogonal matrix by multiplying its columns with each other. For notational convenience $B := \sqrt{N_e}$ and $C := \sqrt{N_e} + 1$ are defined. The product of matrix columns a_j and a_k then is

$$a_j \cdot a_k = \begin{cases} 1 - \frac{2}{BC} + \frac{N_e-1}{(BC)^2} + \frac{1}{B^2} & \text{for } j = k \\ -\frac{2}{BC} + \frac{N_e-1}{(BC)^2} + \frac{1}{B^2} & \text{for } j \neq k \end{cases} \tag{F.82}$$

We recognise, that for the orthonormality of the columns of $\mathbf{A}$ it needs to be shown that the second equation is zero.
To that end we perform some standard algebraic transformations and plug back the terms for B and C.

$$-\frac{2}{BC} + \frac{N_e - 1}{(BC)^2} + \frac{1}{B^2} = \frac{-2BC}{(BC)^2} + \frac{(N_e - 1)}{(BC)^2} + \frac{C^2}{(BC)^2} \tag{F.83}$$

$$= \frac{-2\sqrt{N_e}(\sqrt{N_e} + 1) + (N_e - 1) + (\sqrt{N_e} + 1)^2}{\dots} \tag{F.84}$$

$$= \frac{-2N_e - 2\sqrt{N_e} + (N_e - 1) + N_e + 2\sqrt{N_e} + 1}{\dots} \tag{F.85}$$

$$= 0 \quad \square \tag{F.86}$$

Having shown the orthonormality, we can finally introduce this projection matrix into the posterior error covariance formulations.

$$\mathbf{X}'(\mathbf{X}')^T = \mathbf{X}^f\mathbf{A}\mathbf{A}^T(\mathbf{I} - \mathbf{S}^T\mathbf{F}^{-1}\mathbf{S})(\mathbf{A}\mathbf{A}^T\mathbf{X}^{f\prime})^T \tag{F.87}$$

$$\tag{F.88}$$

The term in brackets is reformulated as in the derivation of the ETKF (Equation F.6).

$$\mathbf{X}'(\mathbf{X}')^T = \mathbf{X}^f\mathbf{A}\mathbf{A}^T(\mathbf{I} - \frac{\mathbf{S}^T\mathbf{R}^{-1}\mathbf{S}}{N_e - 1})^{-1}\mathbf{A}\mathbf{A}^T X'^{f^T} \tag{F.89}$$

$$= \mathbf{X}^f\mathbf{A}(\mathbf{A}^T\mathbf{A} - \frac{\mathbf{A}^T\mathbf{S}^T\mathbf{R}^{-1}\mathbf{S}\mathbf{A}}{N_e - 1})^{-1}\mathbf{A}^T\mathbf{X}'^{f^T} \tag{F.90}$$

We introduce the definition of $\mathbf{S} := \mathbf{H}\mathbf{X}$ and denote the multiplication of the $\mathbf{X}$ with the projection $\mathbf{A}$ as $\mathbf{L}$.

$$\mathbf{T}\mathbf{T}^T = \mathbf{X}^f\mathbf{A}(\mathbf{I} - \frac{(\mathbf{X}\mathbf{A})^T\mathbf{H}^T\mathbf{R}^{-1}\mathbf{H}(\mathbf{X}\mathbf{A})}{N_e - 1})^{-1}\mathbf{A}^T\mathbf{X}'^{f^T} \tag{F.91}$$

$$= \mathbf{X}^f\mathbf{A}(\mathbf{I} - \frac{(\mathbf{H}\mathbf{L})^T\mathbf{R}^{-1}(\mathbf{H}\mathbf{L})}{N_e - 1})^{-1}\mathbf{A}^T\mathbf{X}'^{f^T} \tag{F.92}$$

From that point on, the same Eigenvalue decomposition as for the ETKF is performed (Equation F.14). The matrices $\mathbf{U}$ and $\mathbf{\Sigma}$ denote the Eigenvector and Eigenvalue matrices of $\mathbf{T}$. I directly present the results which are obtained by the same steps as for ETKF, the only difference being that here the projection matrix $\mathbf{A}$ has been introduced.

$$\mathbf{T} = \mathbf{U}\mathbf{\Sigma}^{-\frac{1}{2}}\mathbf{U}^T \tag{F.93}$$

$$\mathbf{W}' = \mathbf{A}\mathbf{T}\mathbf{A}^T = \mathbf{A}\mathbf{U}\mathbf{\Sigma}^{-\frac{1}{2}}\mathbf{U}^T\mathbf{A}^T \tag{F.94}$$

$$\overline{\mathbf{w}} = \frac{1}{\sqrt{N_e - 1}}\mathbf{A}\mathbf{U}\mathbf{\Sigma}^{-1}\mathbf{U}^T(\mathbf{H}\mathbf{L})^T\mathbf{R}^{-1}\mathbf{d} \tag{F.95}$$

Appendix G

Code and data availability

The multi-timescale PaleoDA framework developed in this thesis and the code for reproducing the figures can be found in the following public GitHub repository: https://github.com/paleovar/paleoda. It also includes Jupyter notebooks for preprocessing the model data and selecting the proxy records from the proxy databases.
The Ensemble Kalman Filters implemented in Python for this thesis are also available through a seperate GitHub repository, which focuses only on the core Data Assimilation algorithms: https://github.com/paleovar/ensemblefilters.
The simulation data of the five isotope-enabled climate simulations can be found in the Zenodo repository which accompanies the publication by Bühler et al. (2022): https://zenodo.org/record/6610684.
The SISALv2 speleothem record database is publicly available through a repository provided by the University of Reading: https://researchdata.reading.ac.uk/256/.
The Iso2k database, which provided the ice core record data used in this thesis is publicly available in a repository of the National Oceanic and Atmospheric Administration (NOAA): https://www.ncei.noaa.gov/pub/data/paleo/reconstructions/iso2k/.

Acknowledgements

I am deeply indebted to the many scientists and technicians behind the SISAL and Iso2k projects who collected and synthesized the proxy record data. My work would also not have been possible without the many people who developed the climate models and data assimilation methods that I could use.
I am extremely grateful to my supervisor Kira Rehfeld for giving me the opportunity to work in the STACY/SPACY group. The last year was a very good scientific and human experience which I really enjoyed.
I would like to thank André Butz for his openness to be my supervisor for this thesis. Thank you for the interesting suggestions on my work.
My sincere thanks to Janica Bühler for the comprehensive supervision during the last year, the many ideas and interesting discussions, as well as for the extensive proofreading.
I gratefully acknowledge the effort of Nathan Steiger, Michael Erb and Matt Osman to thoroughly answer my questions about their PaleoDA studies.
I would also like to thank Beatrice Ellerhoff, Nils Weitzel and Valdir Novello for their constant readiness to discuss my questions during the last year.
Last but not least, I would like to thank the proofreaders of this thesis, Moritz Adam, Laura Braschoß, Janica Bühler, Udo Choblet, Laura Fink, Jan Gräfje, Felix Pollak, Julian Stähle and Jonathan Wider for their valuable corrections and comments.

Declaration of authorship

Erklärung:

Ich versichere, dass ich diese Arbeit selbstständig verfasst habe und keine anderen als die angegebenen Quellen und Hilfsmittel benutzt habe.

Heidelberg, den 21.12.2022